Universidad de Oviedo
Universidá d'Uviéu
University of Oviedo

Electrical, Electronic, Computers and Systems Engineering Department

PhD Program in Energy and Process Control

PhD Thesis

3-Phase 4-Leg (3P4L) Converters Control for Massive Electric Energy Storage Systems Integration in Low Voltage Grids

by

Cristina González Moral

GIJÓN, JULY 2020

Universidad de Oviedo
Universidá d'Uviéu
University of Oviedo

Departamento de Ingeniería Eléctrica, Electrónica, de Computadores y Sistemas

Programa de Doctorado en Energía y Control de Procesos

Tesis doctoral

Control de Convertidores 3P4L para Integración de Sistemas de Almacenamiento Masivo de Energía Eléctrica en Redes de Baja Tensión

por

Cristina González Moral

GIJÓN, JULIO 2020

Universidad de Oviedo
Universidá d'Uviéu
University of Oviedo

Electrical, Electronic, Computers and Systems Engineering Department

PhD Program in Energy and Process Control

3-Phase 4-Leg (3P4L) Converters Control for Massive Electric Energy Storage Systems Integration in Low Voltage Grids

by

Cristina González Moral

Dissertation submitted in fulfillment of the requirements for the degree of Doctor of Philosophy in Electrical Engineering with International and Industrial Mentions

Advisors

Juan Manuel Guerrero Muñoz. Associate Professor. Dept. of Elec., Computer, & Systems Engineering, University of Oviedo

David Díaz Reigosa. Associate Professor. Dept. of Elec., Computer, & Systems Engineering, University of Oviedo

GIJÓN, JULY 2020

Universidad de Oviedo
Universidá d'Uviéu
University of Oviedo

Departamento de Ingeniería Eléctrica, Electrónica, de Computadores y Sistemas

Programa de Doctorado en Energía y Control de Procesos

Control de Convertidores 3P4L para Integración de Sistemas de Almacenamiento Masivo de Energía Eléctrica en Redes de Baja Tensión

por

Cristina González Moral

Tesis presentada en cumplimiento de los requisitos para el grado de Doctor en Filosofía en Ingeniería Eléctrica con Menciones Internacional y de Doctorado Industrial

Tutores

Juan Manuel Guerrero Muñoz. Profesor titular. Dpto. de Ing. Eléctrica, Electrónica, de Computadores y Sistemas, Universidad de Oviedo

David Díaz Reigosa. Profesor titular. Dpto. de Ing. Eléctrica, Electrónica, de Computadores y Sistemas, Universidad de Oviedo

GIJÓN, JULIO 2020

A Alejandro e Inés
y en especial a mis padres

Acknowledgements

Como no podía ser de otra manera, empiezo agradeciendo a mis tutores: David Díaz Reigosa y Juan Manuel Guerrero Muñoz, por todo su esfuerzo y dedicación a lo largo de estos cuatro años de tesis, en los que me han guiado y me han enseñado muchas cosas por las cuales voy a estar siempre agradecida. Agradeceros vuestra paciencia corrigiendo artículos y esta tesis, y por la oportunidad de asistir a congresos en los que poder aprender y formarme. Agradecer también a Fernando Briz, por su facilidad para transmitir conocimientos y estar siempre disponible para consultar dudas y aclarar conceptos. Muchas gracias a Daniel Fernández, porque su ayuda en el laboratorio ha sido siempre esencial para llevar a cabo todos los proyectos. Todos los miembros del grupo de investigación me habéis dedicado un tiempo que valoro inmensamente y estoy muy agradecida por haber podido pasar este tiempo aprendiendo de vosotros.

Mención muy importante se merece Carlos Rivas, mi supervisor de tesis en ELINSA. Trabajar con él ha resultado algo fácil y agradable y siempre ha sabido ser comprensivo cuando las cosas no avanzaban tan rápido como se esperaba. Hacia la empresa solo tengo palabras de agradecimiento por haberme permitido realizar esta tesis con ellos a la vez que aprendía el funcionamiento de la industria.

Agradecer por supuesto a mis amigos y compañeros de grupo: a Diego Fernández Laborda, por su inestimable ayuda que viene desde hace tantísimos años y María Martínez Gómez, que ha conseguido mantenerme sana durante estos años con su gran apoyo y sinceridad (y sus grandes consejos). Vuestra ayuda, cafés y consejos durante toda esta etapa son algo que valoro enormemente y que recordaré siempre. Gracias también a Lidia y a Marcos por su ayuda con algunos de los experimentales y a Mariam por estar siempre dispuesta a ayudar. Agradecer al resto de gente que ha pasado por el grupo por ser unos grandes compañeros: Marta, Ye Gu, Germán, Ahmed, Paul, Carlo, Mario y Chema.

Gracias también a Irene, Miguel, Sarah, Guirguis y, en general, a todas aquellas personas que han animado el día a día en la Universidad, incluidos mis compañeros del capítulo de estudiantes del IEEE (IAS/PELS/PES). Mención especial para Rosana por su alegría y por entretenernos siempre durante la comida.

Agradecer a todas las personas del Departamento de Ingeniería Eléctrica, Electrónica de Computadores y Sistemas de la Universidad de Oviedo que de alguna manera o de otra me han ayudado a llegar a este momento, ya sea mediante sus enseñanzas durante toda mi etapa formativa en la Universidad de Oviedo o ayudándome de cualquier otra manera. Especial mención aquí a Gemma por toda su ayuda administrativa, a José Ángel por estar siempre disponible para cualquier cuestión técnica del laboratorio y a Rosa por alegrarnos las mañanas con su presencia y cariño.

I would like to express my deepest gratitude to Proffesor Dražen Dujić for accepting me in the PEL research group during my PhD internship in Lausanne, Switzerland. I felt valued and included in the group, and for that and his dedication and kindness I will always be grateful. I cannot forget here the rest of the PEL members, who welcomed me with open arms and made my stay in the group something remarkable: Nathalie, Roland, Dr. Francisco, Prof. Masataka, Gabriele, Seongil, Milan, Stefan, the two Marko, Dragan, Nicolai, Milan, Ignacio, Miodrag, Yan-Kim and especially Emilien.

Agradecer también a todos mis amigos que me han apoyado siempre y me han distraido y animado cuando no veía las cosas claras en este camino largo y en muchas ocasiones complicado. Gracias también a Dolores y a Raquel y Manolo.

Finalmente quiero agradecer a mi familia todo su apoyo incondicional, el entenderme, escucharme y apoyarme siempre: a mis abuelos y tios, a mis padres, a mi hermana, a Flecha, y sobre todo a Alejandro, por estar siempre ahí.

Resumen

La necesidad de abandonar la producción eléctrica basada en combustibles fósiles altamente contaminantes está propiciando un cambio en el sistema eléctrico mundial, moviéndose de un sistema centralizado hacia una generación distribuida formada por generadores basados en energías renovables (paneles solaras, turbinas eólicas...). Una desventaja de estos sistemas es la intermitencia de la producción eléctrica. Por ejemplo, la velocidad del viento es altamente fluctuante, mientras que solo se dispone de energía solar durante el día. Esto lleva a que exista un desajuste entre la producción de energía y su consumo. Todo esto, unido a la necesidad de sistemas cada vez más estables y robustos, han aumentado el interés en sistemas de almacenamiento de energía masivos, permitiendo producir cuando sea posible y consumir cuando sea necesario.

Estos sistemas de almacenamiento de energía varían mucho en cuanto operación, capacidad y propiedades dinámicas, y cada uno se ajusta más a diferentes tipos de aplicación. Entre los sistemas existentes, las baterías suponen uno de los más atractivos en el rango de almacenamiento de capacidad media, debido a su pequeño tamaño y rápida respuesta. Las propiedades de las baterías varían mucho en función de la química, siendo una de las más atractivas las baterías de litio, por su alta eficiencia, alto voltaje nominal de celda y buena energía específica. Por todo ello, las baterías que se estudian en esta tesis son baterías de litio, más concretamente del tipo $LiFePO_4$.

La integración de energías renovables con sistemas de almacenamiento de energía, unidos a la posibilidad de conectarse a la red eléctrica general conlleva una serie de problemas que hasta la fecha solo han sido parcialmente resueltos. Si la controlabilidad de estas unidades, en términos de algoritmos de sincronización y controladores de corriente, no se maneja cuidadosamente, puede llevar a inestabilidades y fallos. Debido a esto, en los últimos años la normativa de calidad de red se ha endurecido.

Esta tesis presenta el desarrollo y control de un edificio autónomo que puede funcionar conectado a la red o aislado de ella. Incluye energías renovables, como son los paneles solares, y sistemas de almacenamiento de energía, como son las baterías. En concreto, el principal sistema de almacenamiento del edificio se basará en un pack de baterías de litio del tipo $LiFePO_4$. Estas baterías tienen unas características superiores cuando se comparan con otros tipos, sobre todo en número de ciclos de vida, energía específica y seguridad. Esta tesis lleva a cabo un estudio del comportamiento de estas baterías con la temperatura. Más concretamente, su resistencia interna se usa para estimar la temperatura de estas cuando se conectan a distintos convertidores de potencia. Hay dos tipos de convertidores principales que se pueden emparejar con baterías. El primero sería el convertidor de potencia, que conecta las baterías con el resto del sistema. El segundo sería el convertidor que ecualiza las celdas que forman la batería de tal manera que todas ellas tengan la misma tensión.

El convertidor de potencia que se encarga de generar la red del edificio, además de conectarlo o desconectarlo de la red, es un convertidor DC/AC de 3 fases y 4 ramas. Esta configuración permite una mejor controlabilidad del sistema y además permite el control de la componente homopolar que se genera cuando se conectan cargas monofásicas (como por ejemplo pantallas o electrodomésticos). De esta manera se elimina la necesidad de transformadores de baja frecuencia, generalmente grandes y pesados. En esta tesis se muestra el control básico de este sistema. Además, se propone una solución simple y fácil de implementar para manejar la saturación en convertidores de 3 fases cuando se utilizan múltiples reguladores en paralelo, lo cual es necesario para reducir el contenido armónico de la red.

Abstract

Motivated by the need of abandoning highly pollutant fossil-fuel based generation, the electric system is gradually changing to a distributed generation system, which is formed by small generation units based on renewable energy sources, as solar panels or wind turbines. One technical drawback of these renewable energy sources is the intermittence of the production. For example, wind speed is highly fluctuating, and solar energy is only produced during the daytime in the presence of the sun. Mismatches between energy production and consumption, and the need of providing reliable services, has spiked the interest in massive Energy Storage Systems to decouple energy production from its supply, producing when possible and consuming when desired.

Energy storage systems are different in terms of operation, capacity and dynamic properties, and each type is more suitable for one different application. Among the existing energy storage systems, batteries are one of the most cost-effective energy storage technologies available due to their low size and fast response for medium capacities energy storage systems.

The integration of renewable energy sources with energy storage systems and the possibility of connecting to the grid raises a series of issues that have been only partially solved. When connected to the grid, this system is seen as a distributed power generation system. If the controllability (synchronization algorithms and current controllers) of these units is not carefully managed, it can lead to grid instability or failure. Due to this, requirements for grid quality have been toughened in the last years.

This thesis presents the development and control of an autonomous building which can work connected to the grid or isolated from it. It will include renewable energy sources, as solar panels, and energy storage systems, as batteries. The main energy storage system will be a lithium battery pack, specifically made of

$LiFePO_4$ batteries. They have superior characteristics when compared to other types of batteries, as a long life cycle, specific energy and safety. In this thesis, a study of the behavior of these batteries with temperature is carried out. Specifically, the internal resistance of the batteries is used to estimate temperature when they are connected to different power converters; the power converter that connects them to the rest of the power system and the converter that keeps the cell voltages equalized.

The power converter to control the grid in the building and connect it or disconnect it from the grid is a DC/AC converter in a 3-phase, 4-legs configuration. This configuration leads to a better controllability of current and/or voltage. Not only it controls the same signal as a classical 3-phase converter, but it also controls the homopolar components generated by single-phase loads (as screen or home appliance), thus eliminating the need for heavy and bulky transformers. This thesis deals with the basic control of the converter. In addition, it provides a simple solution to manage the saturation state in a 3-phase converter when multiple regulators are parallelized for the control of different harmonics, which is required to reduce the harmonic content in the grid.

Nomenclature

$[1, a1, ..., an]$	Denominator coefficients
α_{avg}	Mean battery thermal coefficient
α_{bat}	Battery thermal coefficient
ε	Error
ε_{aa}	Quantization error
ε_{ar}	Relative error
ε_i	Current error
ε_{sat}	Error signal that produces a saturated output
ε_v	Voltage error
θ	Angular position
θ_l	Angular position of the fl reference frame
φ_{I_h}	Phase angle of the current at the hth harmonic
φ_{V_h}	Phase angle of the voltage at the hth harmonic
$[b0, b1, ..., bn]$	Numerator coefficients
C	Capacitance
e	Euler number
fl	Specific reference frame
f_r	Resonance frequency
f_{sw}	Switching frequency
h	Harmonic order
i_a	A-phase current
i_{ia}	A-phase inductor current
i_b	B-phase current
I_{bat}	Battery current
i_{ib}	B-phase inductor current
i_c	C-phase current

i_{ic}	C-phase inductor current
i_d	$d-$axis component of current complex vector
I_{DC}	DC current
i_g	Grid current
I_h	Current magnitude of the h^{th} switching harmonic
i_{iqd}	Inverter current
i_L	Inductor current
i_q	$q-$axis component of current complex vector
i^*_{iqd}	Current trajectory command
$[k]$	Actual sampling period
$[k-1]$	Previous sampling period
K_p	Proportional gain
K_i	Integral gain
L	Inductance
$\mathrm{LiCoO_2}$	Lithium-Cobalt Oxide
$\mathrm{LiFePO_4}$	Lithium Iron Phosphate
$\mathrm{LiMn_2O_4}$	Lithium-Manganese Oxide
Li-ion	Lithium-ion
M	Amplitude of a signal
m	Number of zeroes of the controller
MI	Modulation Index
N	Number of bits
n	Number of poles of the controller
NiCd	Nickel-Cadmium
NiMH	Nickel-metal hydride
R_i	Internal resitance
R_{bath}	Battery resistance at the frequency of the h^{th} harmonic component
R_{bath0}	Battery resistance at the frequency of the h^{th} harmonic component at $\mathrm{T_0}$
s	Laplace complex variable
t	Time
T	Sampling period
T_0	Room temperature
T_{bat}	Battery temperature
$\widehat{T_{\mathrm{bat}}}$	Estimated battery temperature
u	Controller output
uC_a	A-phase measured capacitor voltage

uC_b	B-phase measured capacitor voltage
uC_c	C-phase measured capacitor voltage
uC_{qd}	Measured capacitor voltage in qd reference frame
u_g	Grid voltage
u_i	Iverter voltage
u_{iqd}	Inverter voltage in qd reference frame
u_L	Inductor voltage drop
u_{l_sat}	Fraction of saturation voltage
$u_{\max}$	Maximum realizable voltage
$u_{\min}$	Minimum realizable voltage
u_{sat}	Saturated controller output
V_{bat}	Battery voltage
V_{cell}	Cell voltage
V_{DC}	DC voltage
v_{dq}	Voltage complex vector
V_h	Voltage magnitude of the hth switching harmonic
V_{out}	Power converter output voltage
X_{bath}	Battery reactance at the frequency of the hth harmonic component
Z_{bath}	Battery impedance at the frequency of the hth harmonic component

Abbreviations and Acronyms

3P4L	3-phase 4-leg
AC	Altern Current
ADC	Analog to Digital Converter
BESS	Battery Energy Storage System
BLDC	Brushless DC
BMS	Battery Management System
BPF	Band-Pass Filter
CAES	Compressed Air Energy Storage
CHP	Combined Heat and Power
DAB	Dual Active Bridge
DC	Direct Current
DER	Distributed Energy Resource
DOD	Depth Of Discharge
DPGS	Distributed Power Generation System
DSP	Digital Signal Processor
EDLC	Electric Double Layer Capacitors
EIS	Electrochemical Impedance Spectroscopy
EKF	Extended Kalman Filter
ESR	Equivalent Series Resistance
ESS	Energy Storage System
EV	Electric Vehicle
FESS	Flywheels Energy Storage Systems
FFT	Fast Fourier Transform
FSR	Full-Scale Range

IEEE	Institute of Electrical and Electronics Engineers
IR	Internal Resistance
IGBT	Insulated Gate Bipolar Transistor
IM	Induction Machine
IPM	Intelligent Power Module
IR	Internal Resistance
LFT	Line Frequency Transformer
LIB	Lithium-Ion Battery
LSB	Least Significant Bit
LFT	Line-Frequency Transformer
LUT	Look Up Table
MOSFET	Metal–Oxide–Semiconductor Field-Effect Transistor
MRF	Multiple Reference Frame
NASA	National Aeronautics and Space Administration
OCV	Open Circuit Voltage
OPEC	Organization Of the Petroleum Exporting Countries
PCB	Printed Circuit Board
PCC	Point of Common Coupling
PHES	Pumped Hydro Energy Storage
PI	Proportional-Integral
PMSM	Permanent Magnet Synchronous Machines
PR	Proportional-Resonant
PV	Photovoltaic
RC	Repetitive Controller
RES	Renewable Energy Source
RR	Realizable Reference
RTD	Resistance Temperature Detector
SCE	Switched Capacitor Equalizer
SCI	Split Capacitor Inverterr
SEI	Solid Electrolyte Interphase
SMES	Superconducting Magnetic Energy Storage
SOC	State-Of-Charge
SOGI	Second-Order Generalized Integrators
SOH	State-Of-Health
SPWM	Sinusoidal Pulse-Width Modulation
SRF	Single Reference Frame
SRM	Synchonous Reluctance Machine
SS	State Saturation

ROGI	Reduced-Order Generalized Integrators
THD	Total Harmonic Distortion
UPS	Uninterruptable Power Systems

List of Figures

List of Tables

Contents

Part I

Introduction

Chapter 1

Introduction

1.1 Background

According to NASA, the average global surface temperature has increased more than 1°C since 1880, and every decade since the 1960s has been warmer than the previous one (see Fig. 1.1). There is enough evidence to consider this as a long-term trend and to relate this increase in temperature with an increase in carbon dioxide and other greenhouse gas emissions into the atmosphere, all related to human activities [1].

In 2018, fossil fuels made up 82.7 % of total Spanish energy consumption [2]. Several governments are proposing measures to reduce the emissions, as agreed in the Paris agreement [3], which aims to stop the global temperature rise. It is clear that, in addition to raise awareness in the general public, a new technological framework is needed to reach this goal. In addition to pollution, dependence on fossil fuels is also a concern for the countries that are not part of the OPEC (Organization Of the Petroleum Exporting Countries), which holds 71.8 % of global reserves of petroleum [4].

One alternative to fossil fuels is the use of nuclear energy, which does not pollute the atmosphere. However, it raises safety (e.g. Fukushima accident) and political concerns [5]. Besides, nuclear waste must be safely stored for periods that

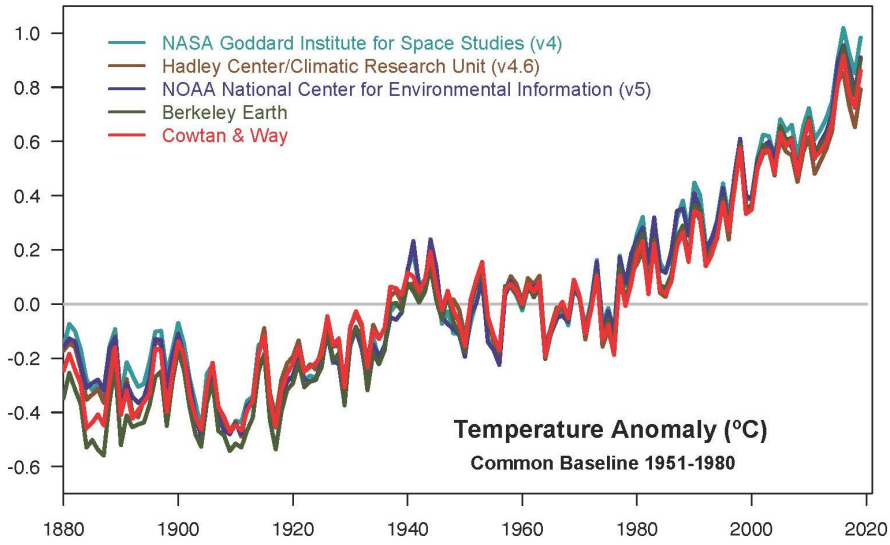

Figure 1.1: Yearly temperature anomalies with respect to the 1951-1980 mean measured by different independent research associations [1].

sometimes exceed hundreds of years [6]. Due to this, Renewable Energy Sources (RES) are preferred over nuclear energy as an alternative to fossil fuels [5].

As a conclusion, a major shift in how energy is produced and used, moving from a fossil fuel and nuclear-based energy system to a clean, low-carbon footprint and renewable energy system is needed [7]. This change is already happening; in 2019, 19 % of the energy was produced using renewable energy, and the forecast predicts that it will increase up to 38 % by 2050 [8]. In addition, in 2019 the CO_2 emissions reduced by a 1.3 % globally with respect to the previous year 2018, with the power sector leading the reduction. This figure increases up to 3.2 % if only developed countries are taken into account [9].

Examples of RES are wind, solar photovoltaic (PV), solar thermal, geothermal, hydroelectric, biomass, wave or tidal turbines, among others. Among these, hydroelectric, PV, and wind are the most mature and extended technologies [5]. By 2019, there were 1292 GW installed capacity of hydropower [10], 500 GW installed capacity of PV [11] and 597 GW installed capacity of wind energy [12].

Energy transitions take time, and a number of different issues must be solved for every different type of RES [7]. In general, the main drawbacks involve

economic, technical, institutional, and social barriers. Environmental impacts must also be taken into account (e.g. noises and presence in general of a wind farm affecting the wildlife of the area, great land requirements from a solar farm or great water requirements from hydro storage) [13, 14].

Forecasting the electricity demand involves complex processes and the use of different power plants to meet and match the instantaneous consumption [15], which is shown for a given day in Spain in Fig. 1.2. One technical drawback of RES is the intermittence of the production [16–20]. For example, wind speed is highly fluctuating, and solar energy is only produced during daytime in the presence of the sun, so the energy produced will be reduced in the event of clouds and will stop at night time. However, solar energy is less intermittent than wind [17].

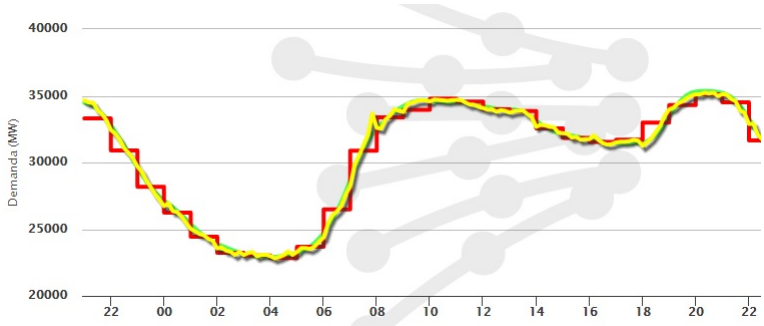

Figure 1.2: Power demand in Spain for the 5^{th} of February, 2020. The x-axis represents the time of the day and the y-axis the power demand in MW [21].

Mismatches between energy production and consumption, and the need of providing reliable services, have spiked the interest in massive Energy Storage Systems (ESS) [15] in order to decouple energy consumption from its supply [22], producing when possible and consuming when desired. It is believed that massive electricity storage is the critical technology needed for RES to become a major source of power in the grid [17]. ESS could be used for peak shaving (leveling the highest power demand peaks) or load-leveling (level all the power demand and producing only the mean energy required), leading to a better resource management and avoiding oversized power systems [22]. In Fig. 1.2, this would imply generating more energy at night time, where the valley in the demand is more pronounced and storing it to use it during peak hours.

Pumped Hydro Energy Storage (PHES) has been successfully used in the last

century for massive ESS [15,17,18]. A lot of PHES were developed in the 1970s combined with large thermal and nuclear power plants, due to their flexibility during peak hours [18]. Nowadays, there are more than 161 GW of pumped storage capacity installed worldwide, which accounts for the around 94 % of the installed global energy storage capacity [23]. Combined installed capacity of solar and wind energy represents around 1100 GW [11,12], which means that this storage capability represents only 15 % of the two most important renewable energy sources. Nevertheless, this ESS is limited to favorable geographical locations, not only topographically but also with respect to water availability [17,24]. Compressed Air Energy Storage (CAES) is also a high capacity ESS, which works similarly as PHES, changing the storage medium from water to air [25]. Although less extended than PHES, it is also a mature technology that has been used for the last 40 years. However, there are only a few commercial power plants using this technology nowadays (with a total installed power of around 535 MW), probably due to the need of already existing large underground caverns to store the compressed air in an economically viable way [25]. In general, both PHES and CAES have a bulky nature and are heavily limited by geographical locations. Thermal Energy Storage (TES) can also be used for massive energy storage, overcoming the geographical needs of the previous two ESS. However, it requires steam turbines and high temperatures of operation, which increase the cost of the installation [26].

In a medium energy scale, other ESS could be more convenient, as power-to-gas, hydrogen or battery ESS. Power-to-gas and hydrogen ESS need complex installations to generate the gases needed for the operation (hydrogen or natural gas), which on the other hand are easy to store and transport [25,27,28]. On the other hand, batteries come in a lot of different chemistries, each with different characteristics. They have a fast response and low size, so they can be placed near the loads with no special requirements [19,25,29].

Finally, for lower capacities, flywheels, supercapacitors or superconducting magnetics are reliable options. The three of them have a very fast response with high power capabilities, but flywheels lose the charge too [30] while supercapacitors have the smallest capacities [25,31]. Finally, superconductive materials are still very new technologies and need very low temperatures to operate, highly increasing the price of the system [31].

As has been explained, ESS are different in terms of operation, capacity and dynamic properties, and each type is more suitable for one different application. Batteries are one of the most cost-effective energy storage technologies available

[31, 32]. Their low size compared to other technologies, in addition to the fast response, makes them a great choice for medium capacities ESS.

In the last decades, batteries have been the focus of an extended research effort [33]. As an alternative to traditional petrol-powered cars, Electric Vehicles (EVs) are gaining popularity, thanks in part to governmental efforts. Still, increasing the energy density to reduce the volume and weight or reducing the charging times cheaply and safely while having a long life span is needed to fully substitute traditional petrol-powered cars by EV [34, 35].

Batteries are also a very convenient ESS solution in cases of medium power generation units (kW range), as PV or wind generation in zero energy buildings, connected or not to the main grid [36]. These buildings are in the trend of the "zero energy" buildings, where a balance is achieved between the energy used by the building and the one produced by its RES, or even injecting energy to the grid [36]. To achieve this zero-energy concept, batteries or other ESS are needed to balance production and consumption.

Among the different chemistries researched for batteries, Lithium-Ion Batteries (LIBs) are compact and are characterized by high specific energy, high efficiency, high capacity and long life expectancy [16, 35]. However, some of the most powerful oxides used in the cathode of lithium batteries are expensive and toxic (e.g. cobalt), while others reduce the energy density (e.g. manganese oxides or iron phosphates). Besides, LIBs are very sensitive to temperature variations [37], so its monitoring is of high importance to have reliable systems. Battery Management Systems (BMS) monitor different important parameters of the battery, such as temperature, State Of Charge (SOC) and State Of Health (SOH), protecting them against dangerous operating conditions. They also control the charge and discharge rate. In addition, BMS can include a function to equalize the different cells in a series string, protecting the cells from overvoltage/undervoltage and maximizing the energy utilization [38].

The integration of RES with ESS and the possibility of connecting to the grid raises a series of issues that have been only partially solved. When connected to the grid, this system is seen as a Distributed Power Generation System (DPGSs). If the controllability (synchronization algorithms and current controllers) of these units is not carefully managed, it can lead to grid instability or failure [39]. Due to this, requirements for grid quality have been toughened up to improve the general power quality [40]. Power quality can be defined as "Any power problem manifested in voltage, current, or frequency deviations that results in failure or misoperation of customer equipment" [41]. Transients, overvoltages,

undervoltages, power interruptions, unbalances, DC offsets and harmonics are all issues that affect the power quality of a system and may affect its stability [41].

Since the interface of DPGSs is generally based on power converters, this opens opportunities for correcting some of the power quality problems addressed, as harmonic compensation, active and reactive power control, avoid faults propagation... [42]. In addition to harmonics, zero-sequence components may appear in the system in case of single-phase unbalances. However, most four-wire systems (3-phase systems with neutral connection) use star-ungrounded or delta-connected transformers, which prevents the propagation of said components [43]. Nevertheless, Line-Frequency Transformers (LFTs), although cheap and robust, are bulky and heavy [44]. If the LFT is eliminated, the single-phase unbalance would flow into the grid in grid-connected converters. Due to this, a 4^{th} leg must be added to the classical converter to control it, thus turning the system into a 3-Phase 4-Wire system [45]. This will not only allow the control of single-phase unbalance currents in grid-tied converters, but will allow voltage unbalance control when disconnected from the main grid, caused by zero-sequence current consumption of single-phase loads.

This thesis will focus on the development of the power converter to generate a 3-phase grid for an autonomous building. For it to work independently from the grid, some kind of ESS is required. In this case, batteries are selected to be the main ESS in the building. The batteries will be part of the electrical distribution of the building and will be used to generate the grid. To do so, and given that the system will naturally include single-phase loads, a 3P4L converter is required to feed them while maintaining the required power quality levels.

1.2 Research motivation and overview

This thesis focuses on Battery ESS (BESS) monitoring techniques and power converter control to interface ESS for autonomous/zero energy buildings. The building under study will be a hybrid supplied system, including RES, as solar and wind, and an ESS to smooth the possible mismatches between generation and demand (see Fig. 1.3). In addition, there will be a biodiesel generator intended as a backup (in case of the ESS, i.e. battery, system failure), and will never be active at the same time as the battery system. The building will have two possible operation modes: grid-connected and isolated from the grid.

At a practical level, this thesis will deal with the ESS and the power converter

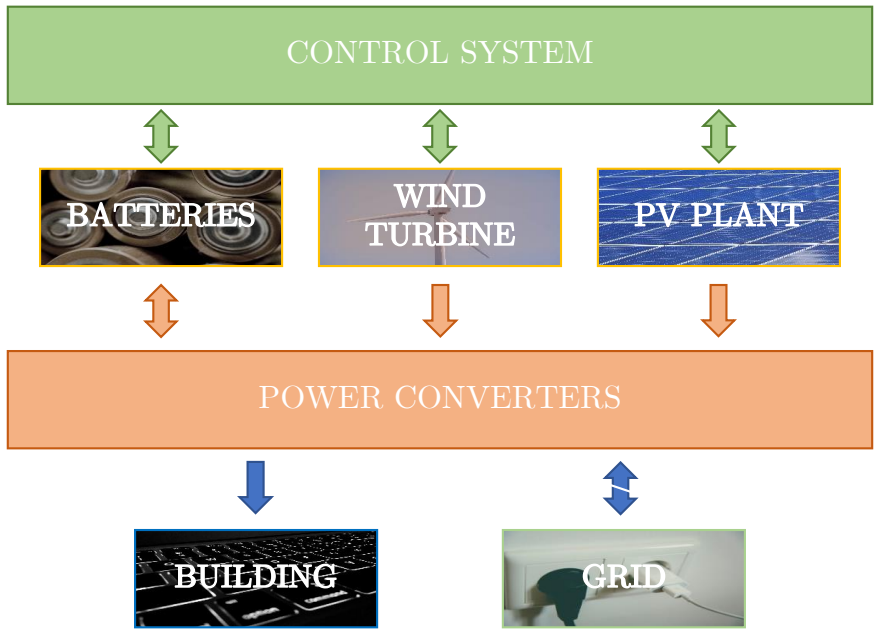

Figure 1.3: Hybrid system basic scheme.

to interface it to the rest of the system and provide power to the systems in the building(see Fig. 1.4).

The power stage scheme is shown in Fig. 1.5. The battery voltage is boosted using an interleaved DC/DC converter to meet the DC-bus requirements. Batteries can be charged from RES or from the grid (in case that the building is grid-connected). A 3P4L power converter will be used to form the grid and feed all loads in the building, i.e. three-phase/single-phase loads and linear/non-linear loads.

The physical power stage of the converter is shown in Fig 1.6. Its nominal power is 100 kW. In Fig 1.6a, the module on the left is for the DC/DC converter, while the one on the right is for the DC/AC 3-phase part. The single-phase module in the upper part of the figure is for the 4^{th} leg completing the DC/AC converter. These boards have been designed and developed during this thesis. Each power converter is controlled by a dedicated control unit. The control boards for both power converters are shown in Fig. 1.7. Each of them are identical and include a TMS320F28335 DSP from Texas Instruments [46].

Figure 1.4: Power converter (left) with the batteries (right).

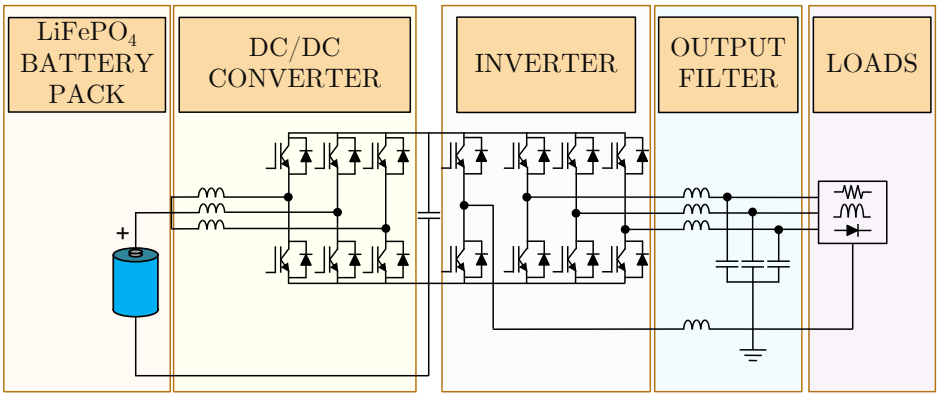

Figure 1.5: Power stage scheme.

This thesis is the result of a collaboration between the University of Oviedo and the Spanish company ELINSA "sponsored by the Oviedo Siembra Talento" program from Oviedo's city council (Spain). The converter was jointly designed between ELINSA and the University, and was then built by the company in its headquarters in La Coruña (Galicia), while the batteries were provided by the Spanish company Cegasa. The thesis will study the following issues:

(a) Power modules (b) Filters and switches

Figure 1.6: Power stage of the power converter.

Figure 1.7: Control boards for the power converters.

- **Thermal monitoring of the battery pack:** Single $LiFePO_4$ cells are studied both when connected to switching power converters and switched-capacitor equalizers, and methods to estimate its temperature are proposed. For this purpose, a reduced scale of a DC/DC converter and a battery equalizer were built. Methods to estimate the internal resistance of the battery and its further use for battery temperature estimation have been analyzed. These proposed methods do not interfere with the normal operation of the systems.

- **Control of the 3P4L inverter:** 3P4L systems are studied and a control solution for isolated grids is proposed and validated. Saturation issues that arise when several controllers work in parallel are addressed, proposing a simple solution that does not require a particular controller structure.

1.3 Outline of the document

This thesis is organized in two different blocks, one regarding the study of the ESS and the other regarding the control of the power converter:

- **Block II - Energy Storage System**
  - **Chapter 2: Introduction to storage systems.** Discusses ESS that could be used in combination with RES. Among ESS, BESS can be considered as the best choice for the main ESS in an autonomous building. BESS' characteristics depend on their chemistry. Among the different chemistries used in high capacity ESS, LIBs are the most commonly used choice due to its outstanding characteristics. This chapter explains the basics of LIBs and the different electrical models that can be used to represent them. It also stresses the problem of batteries with temperatures, showing different estimation methods. In addition, it explains the basics of BMS, focusing on cell equalization.
  - **Chapter 3: Thermal monitoring using switching harmonics.** This chapter proposes a temperature estimation method for $LiFePO_4$ batteries using the switching harmonics of the converter feeding the battery (the DC/DC converter is placed to the left in Fig. 1.6a). Temperature changes are estimated from the variation of the battery resistance at the switching frequency.
  - **Chapter 4: Battery internal resistance estimation using a battery balancing system based on switched capacitors.** This chapter proposes a battery resistance estimation method, during cell balancing, for Switched Capacitor Equalizers (SCEs). The Internal Resistance (IR) of the battery is estimated using signals produced by the SCE regular operation. The estimated IR will be used for cell temperature estimation.
- **Block III : Control techniques for power converters**

- ◇ **Chapter 5: Introduction to power converters for hybrid systems.** This chapter shows different control methods for 3P4L converters and reviews the different saturation methods proposed in the literature for correctly saturating the regulators in the case of parallel controllers.
- ◇ **Chapter 6: Realizable reference anti-windup implementation for parallel controllers in multiple reference frames**. This chapter generalizes the instantaneous realizable reference algorithm for application in parallel controller structures. The proposed anti-windup implementation allows saturation of controllers in multiple reference frames and it does not require gain tuning.
- ◇ **Chapter 7: Control of converters for smartgrids: DC/DC and 3P4L.** This chapter presents the control of the building's converter. It shows the control of the DC/DC converter to integrate the battery pack in the DC-link and the control of the 3P4L to generate the grid.

- **Chapter 8: Conclusions.** It summarizes the contributions of this thesis and outlines future research lines.
- **Appendix A: Power Converter design.** This appendix shows the design of the power converter in Fig. 1.6.
- **Appendix B: Complex vectors: reference frame transformation.** This appendix summarizes complex vectors and especially reference frame transformations.

Part II

Storage systems

Chapter 2

Introduction to energy storage systems

2.1 Introduction

There are many reasons to include ESS as part of the generation and distribution grid. They can be useful in mobile applications, like cars or planes. They are typically employed as backups in case of emergencies (e.g. hospitals) and they can help to alleviate the generation stress at peak hours in stressed electricity supply systems [17]. Besides, as state in Chapter 1, the intermittent nature of RES, as wind or solar, has spiked the interest for ESS to store the extra energy that is not consumed while produced. Following the trend towards cleaner energies, "zero energy" buildings are becoming more and more common [36]. Although they could be connected to the main grid, if their geographical location allows it, the idea is having self-sufficient buildings that can work completely isolated from the main grid. To do so, different energy sources are needed, which are normally RES with fossil fuels based generators for back-up (see Chapter 1). To not use the back-up unless it is strictly necessary, ESS are built-in to balance production and consumption [36].

Energy can be stored in different forms: electrical, electrochemical, thermal and mechanical [25, 30], from smaller to higher capacity [47]. Some of these groups can be divided into different ESS, depending on the technology, the storage

medium... [17, 19, 47]. The most typical ones are shown in Fig. 2.1).

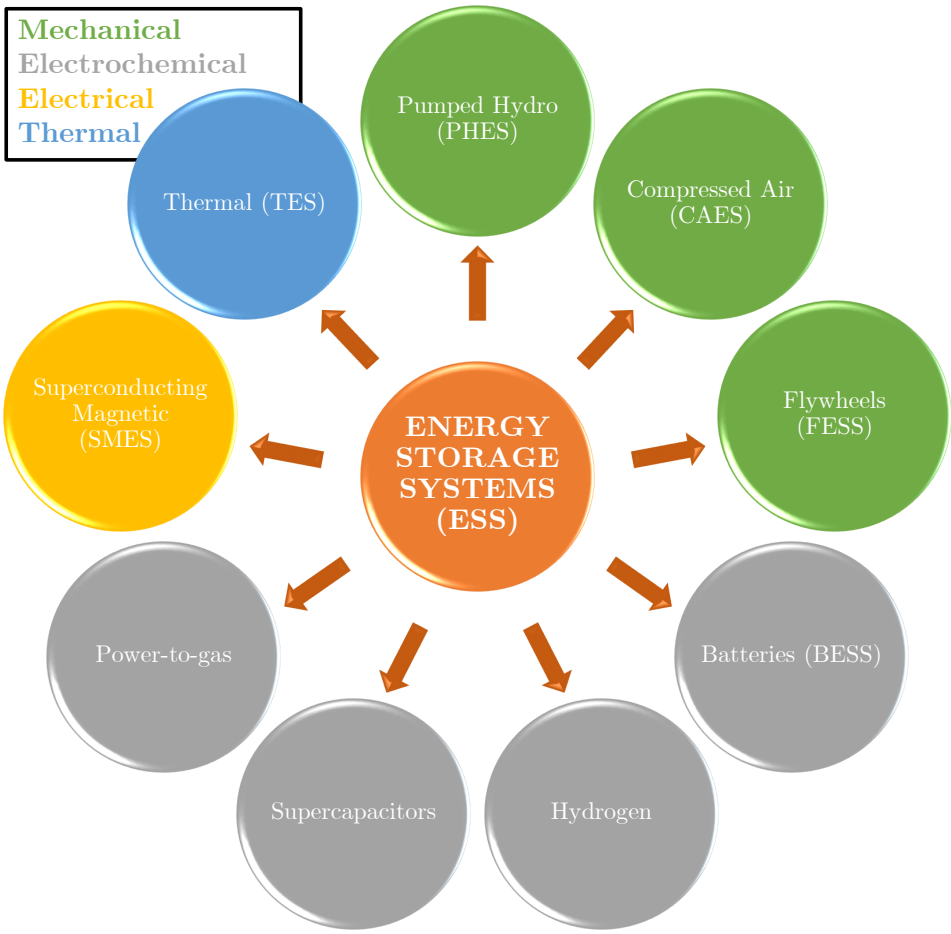

Figure 2.1: Energy storage systems for renewable energy sources.

The ESS needed for a zero-energy building (which is the objective of the thesis) is a medium-capacity ESS with good efficiency capable of maintaining the shape of the voltage in terms of magnitude and frequency [47]. It should not have special requirements in terms of geographical position or temperatures. The space requirements are not as tight as in an EV, but bulky systems are not desired. In the next sections, several ESS for RES are analyzed, stressing the pros and cons of each of them.

2.1.1 Pumped hydro

One solution that has been successfully used in the last century to reduce the peak-to-valley difference between power generation and consumption is the Pumped Hydro Energy Storage (PHES), storing potential energy through a reversible turbine/generator [17], although a separate pump and turbine can also be employed [17]. Its philosophy consists of pumping energy to a higher level reservoir when the electricity prize is cheap (there is a low demand for the energy, normally at night) and releasing it back to the lower reservoir through hydro turbines when the price increases back (there is a high power demand), generating, this way, electric power [17]. In the last decades there has also been an increased interest for variable speed pumped-storage, with the generator decoupled from the grid [18] and allowing for power control. With more than 161 GW of pumped storage capacity installed worldwide, this ESS accounts for the 94 % of the installed global energy storage capacity [23] and is, nowadays, the best solution and the most cost-effective when it comes to massive energy storage systems, with efficiencies ranging from 70 % to 80 % and reaching up to 87 % [17, 18]. As to its capabilities, they can range from few hundreds kW to more than 10 MW.

Its flexible start/stop and fast response, in addition to its ability to adapt to drastic load changes while been already a mature technology makes PHES an ideal source to pair it with RES [18, 48]. However, its special geographical needs and high amounts of water requirements make it impractical for every location [17,24]. In addition, its response time (2-5 min), although fast compared to classical technologies, is considered low compared with the majority of ESS from Fig. 2.1 [35].

2.1.2 Compressed air

Compressed air energy storage (CAES) is similar to the principle of PHES, using air instead of water as the storage medium of the potential energy [19, 25]. The energy is converted back to electric energy when expanded in a turbine [24]. This technology has been successfully used for more than 40 years [19].

Some of its advantages include the capability of storing high capacity for a long time (more than a year) with high efficiency at large scale applications. In addition, it is a low-cost system with low maintenance. Moreover, compared with PHES (which needs two tanks to transfer the water in between), only one tank is needed. Due to its dynamics, it can be used for load leveling. The main

drawback is that it is only economically effective at large scale, which makes it a great substitute of PHES in the cases where the latter is not viable [19, 25]. However, it is also limited geographically due to the need for already existing underground caverns to store the compressed air economically. In addition, as PHES, it has a lower start-up time (≈12 min) compared with the rest of the ESS in Fig. 2.1 [25].

2.1.3 Flywheels

Flywheels Energy Storage Systems (FESS), sometimes called "mechanical batteries" [19], are one of the oldest ESS [49]. They use a rotating flywheel to store electric power in the form of kinetic energy. Reversely, they discharge the power by transforming the kinetic energy in electric power employing an electric motor. Nowadays, FESS are mainly used to stabilize power generation in intermittent RES, as PV panels, in response to changes in sunshine [49–51].

The main benefits of FESS systems are their rapid response, low maintenance cost, low toxicity and longer life when compared to secondary (rechargeable) batteries [19, 30]. Their efficiency is limited by the motor/generator (Permanent Magnet Synchronous Machine (PMSM), Brushless DC (BLDC), Induction Machine (IM), Synchronous Reluctance Machine (SRM)...) and power electronics [19], but is typically very high. Some of its limitations are related to the mechanical bearings to support the rotor [50]. Besides, there is a limitation as to the maximum weight and achievable speed, the two parameters that influence the stored energy. However, the highest drawback is the friction, resulting in a loose of energy between 3 % and 20 % per hour of the total stored energy [30].

To achieve higher energy densities, new FESS with magnetic bearings were developed, with a higher speed capability in exchange for a higher cost and lower long term reliability [50, 51].

2.1.4 Thermal

Thermal Energy Storage (TES) consists of storing energy in the form of heat. TES can be classified into [52–54]:

- **Sensible heat:** heat stored by raising the temperature of a given material, either liquids (water, oil) or solids (molten salts, metals, rocks). The temperature of the storage material varies with the amount of energy stored.

- **Latent heat:** uses the energy stored in a material when it changes phase (latent heat), as when water melts from ice to water. The temperature is kept constant at the phase transition temperature. The heat transfer between the material and the environment is made through a heat-transfer fluid. This ESS is more expensive than sensible heat, but its capacity and efficiency can be higher.

The heat is transformed back to electricity in a steam turbine, generally following a Rankine cycle. For this, temperatures of over 400°C are desired to increase the efficiency of the thermal cycle [26]. The heat storage capability is highly dependent on the material. The storage medium must have high specific capacity, long term stability under thermal cycling, compatibility with its containment and low cost [52–55]. The energy can be stored up to months in both TES systems [54]. The drawbacks of the system are the need for containers to efficiently retain the heated material and the need for big spaces to store them. In addition, using a turbine to generate electricity has low efficiency (≈ 40 %) [26] which lowers the good efficiency (up to 90 %) of the storage system [54].

TES has interesting applications in commercial buildings with Combined Heat and Power (CHP) systems [55]. CHP reduces cost, energy consumption and emissions because it captures the waste heat associated with power production and can be potentially used to heat water or spaces [54, 55]. Since a CHP system operates most efficiently at a constant load, TES can help to level the intermittence of the consumption, extending the operation time and increasing the profits [55].

2.1.5 Batteries

Battery Energy Storage Systems (BESS) convert chemical energy in electrical energy. There are a lot of different kind of batteries according to the materials of the electrodes and the electrolyte [19]. They can be classified in two groups [32]:

- **Primary batteries:** Non rechargeable; the chemical reaction is non-reversible. Examples: Zinc-carbon (zinc chloride), magnesium/manganese dioxide (Mg /MnO_2) or alkaline - manganese dioxide (zinc/KOH/ MnO_2).

- **Secondary batteries:** Rechargeable; the electric energy can be converted back to chemical energy. Examples: nickel–cadmium (NiCd), Pb-acid, lithium-ion (Li-ion) or Li-ion-polymer.

Depending on the chemistry, characteristics of the battery vary, like energy density, power capability, cycling ability, cost, efficiency, pollution and life-span [31]. Their fast response makes them suitable for frequency and voltage control, but they also can provide energy for longer duration [25, 29]. They have low size and can be located near the loads, reducing system losses. As drawbacks, the initial cost is generally high and they need to be replaced every 8-10 years for the most demanding applications [25], with the exception of a few cases, as the redox flow battery [27, 56, 57]. They also require special care for storage without degrading, as a given charge and temperature. In addition, the low voltage per cell entails the need of stacking them in series to meet the requirements for massive ESS [31]. Moreover, they normally require a BMS to monitor the different parameters in the BESS, its complexity depending on the chemistry of the battery [29]. Good chemistries for massive ESS could be Li-ion, lithium-ion-polymer, redoxflow batteries, sodium-based batteries, Nickel-cadmium, Nickel-metal-hydride or Lead-acid [25].

2.1.6 Supercapacitors

Supercapacitors are Electric Double Layer Capacitors (EDLC) that store electric energy in the same way as a normal capacitor, by accumulating positive and negative charges separated by an insulating dielectric.

The capacitance in a supercapacitor can be as high as 10,000 Farads. The energy storage capability is increased due to a larger surface area using porous electrolyte [25,31]. They have high power density and high efficiency. In addition, they have long life-time, a high number of cycles and long-time energy storage (up to 10 years), with low maintenance and low safety requirements. Moreover, and in opposition to batteries, they can be stored completely discharged without degrading. Their main drawback is their low energy density [19, 30, 31].

2.1.7 Hydrogen

This ESS uses the electricity to create hydrogen by water electrolysis and is then used in fuel cells to produce electricity again [27, 58]. Hydrogen is easy to store and transport, in addition to being efficient and clean. Moreover, it can be used both in stationary and portable applications and can be stored for a long period. Fuel cells have low toxic emissions, low noise and vibrations, high efficiency, are easy to install and can be designed in a modular way [25, 27],

although they are more expensive than batteries [35]. The main drawback of this ESS is the space needed for the storage due to its low volumetric energy density, since hydrogen is the lightest chemical element [25, 47]. A solution for this is storing it in a different form, as compressed, liquefied cryogenic, cryo-compressed or solid (in the form of hydrides). However, this increases the cost and reduces the efficiency, since some of the energy would be needed to store the gas [47, 59].

2.1.8 Power-to-gas

This ESS goes one step ahead from hydrogen ESS (Section 2.1.7). Once the hydrogen is formed, CH_4 is created through an external CO or CO_2 source, called methanation [58]. This process can be consider as CO_2 recycling [28]. This resulting gas is known as substitute natural gas and can be injected in the existing distribution grids or gas storage. The extra steps needed to obtain the CH_4 makes the system more expensive and complicated. In addition, its use will free again CO_2 particles, thus being contaminant.

2.1.9 Superconducting magnetics

Superconducting Magnetic Energy Storage (SMES) stores energy in the form of a magnetic field that forms when a current flows through a superconducting coil. SMES is a very fast system when compared to mechanical storage and is a very good option for power quality maintenance, been very efficient ($\approx$95 %) [31]. The main drawback is the cost: it needs a power converter and cryogenic temperatures. It also does not maintain the charge for a long time [19, 31].

2.1.10 Conclusions

Advantages and disadvantages for the different ESS shown in Fig. 2.1 are summarized in Table 2.1.

As it has been presented, ESS are different in terms of operation, capacity and dynamic properties, and each type is more suitable for one different application. Fig. 2.2 shows the ESS presented in Table 2.1 in terms of their typical power and energy.

Batteries are one of the most cost-effective energy storage technologies available [31, 32]. Their low size compared to other methods, in addition to the fast response, makes them a great choice to be the main ESS in an autonomous

Table 2.1: Advantages and Disadvantages of Different ESS

Type	Advantages	Disadvantages
PHES (2.1.1)	High energy and long storage time	Geographical limitations, needs high amount of water. Low response time
CAES (2.1.2)	High energy and long storage time	Only economically possible at large scale and low response time
FESS (2.1.3)	High power density, quick response, long life, high efficiency	High power losses due to friction (low storage time)
TES (2.1.4)	Paired with CHP reduces cost, energy consumption and emissions	Special storage space. Trade-off in between different materials for different characteristics
Batteries (2.1.5)	Fast response, low size and high capacity	High initial cost and need for replacement every several years
Supercapacitors (2.1.6)	High power density, quick response, long storage time and high efficiency	Low energy density
Hydrogen (2.1.7)	Easy to store and transport. Efficient, clean, long storage time	Low volumetric density. Needs some form of compression. High cost
Power-to-gas (2.1.8)	Recycles CO_2	Pollution and cost
SMES (2.1.9)	Fast response and high efficiency	High cost, low storage times

building. Besides, in this kind of application there is no need for a high capacity. However, some security measures will be needed to guarantee a correct operation, as monitoring the temperature. PHES and CAES are discarded due to their high capacity and bulky nature. FESS losses the charge too quickly, while supercapacitors have low capacities. TES, power-to-gas and hydrogen would need more complex installations, although TES could be a good solution if combined with a CHP system. Finally, SMES are overly expensive.

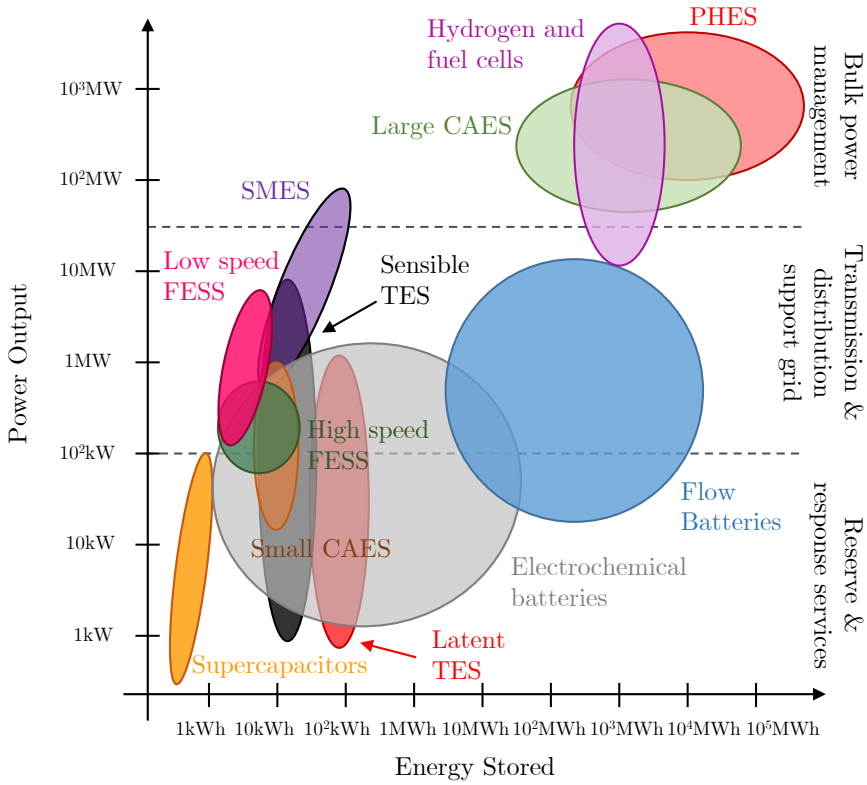

Figure 2.2: Comparison of ESS technologies in terms of storage capacity power, based on [25, 47, 53, 54].

Since there are a lot of possible battery chemistries, a bigger study than the one presented in Section 2.1.5 is carried out throughout the next Section (2.2).

2.2 Batteries

The use of battery-based Energy Storage Systems (ESS) has highly increased in the last decades [33]. They can be found in a broad range of applications, such as electric vehicles (EV) [20, 33, 60–62], smartgrids and microgrids [29, 63, 64], aerospace applications [65–67] and all kind of small appliances applications as mobile devices [67], with energy/power requirements strongly depending on the application [67].

As a remark, a *cell* can be considered as the basic electrochemical unit, been the source of the electrical energy by conversion of chemical energy. A *battery*, on the other hand, consists of one or more of these cells electrically connected in series and/or parallel, depending on the desired output voltage and current levels, and, sometimes, including ancillary components. As a rule, in this thesis, the term *cell* will be used when describing the components and chemistry of the battery, or experimental results performance over a single "battery", while the term *battery* will be more related to performance characteristics and general comments [32].

2.2.1 Electrochemical fundamentals

Fig. 2.3 shows a simple battery scheme. There is a positive and a negative electrode immersed in an electrolyte solution. Electrodes can be solid or porous, so the electrolyte can infiltrate through. The electrolyte is an ionic conductor that allows the transfer of charge, as ions, inside the cell between the anode and the cathode. It can be liquid (water or solvent) with dissolved salts, acids, or alkalis (basic, ionic salt of an alkali metal, which are the ones in the s-block of the periodic table) to improve ionic conductivity. The electrolyte can also be sometimes solid or made of gel-type polymers. Finally, there is a separator between electrodes that prevents both of them to react directly in the electrolyte, but allows positive and negative ions to migrate between them [32, 57, 68–70]. It guarantees the safe insulation of the electrodes, even under abusive conditions. Its resistance to ion transport depends on its thickness, porosity and its number of turns [57].

Electrons flow through and external circuit through the positive and negative current collectors, during either charge or discharge. During the discharge process (Fig. 2.4a), the negative electrode becomes the anode, while the positive electrode becomes the cathode. In this situation, positive ions travel from the anode to the cathode through the electrolyte and separator, while negative ions travel in the opposite direction. This way, the anode builds up negative charge and the cathode positive charge, which creates the cell voltage. Negatively charged electrons move from the anode to the cathode through an external load, thus creating current in the opposite direction. Positive current is consider in opposite direction to the electron flow [35, 70].

During charge (Fig. 2.4b), the process is reversed and the positive electrode becomes the anode, while the negative electrode becomes the cathode. In this

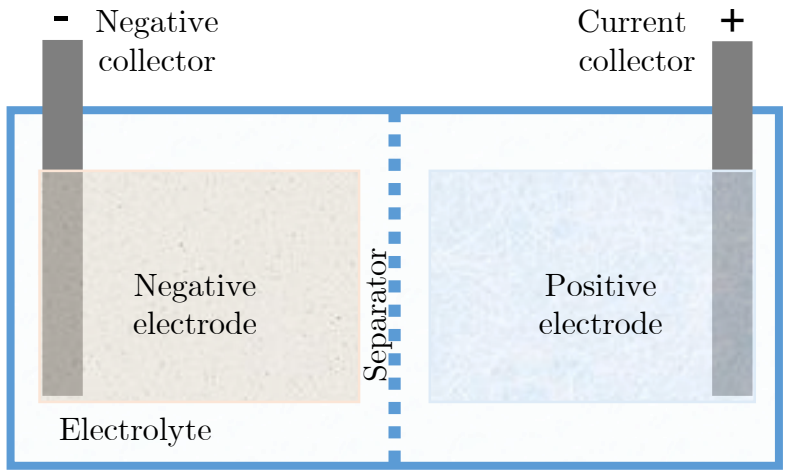

Figure 2.3: Battery scheme (adapted from [70]).

situation, the negative electrode dissolves in the electrolyte solution and forms a positive ion and electron. This process is called oxidation reaction. In parallel, the positive electrode consumes electrons by depositing positive ions from the electrolyte. This process is called reduction reaction [70].

This charge process is only possible in the secondary batteries, which are the rechargeable ones, as seen in Section 2.1.5.

There are two processes that result in the ions moving through the electrolyte [70]:

- **Diffusion:** due to the existence of a concentration gradient in the electrolyte. If enough time is allowed and there is no ion production, the ions in the electrolyte end up diffusing evenly throughout the cell.
- **Migration:** due to the presence of the electric field generated by the positive and negative electrodes. Positive ions migrate towards the negative electrode while the negative ions migrate toward the positive electrode. This movement of ions through the electrolyte together with the movement of electrons through the external circuit are the mechanisms that allow the storage and release of energy.

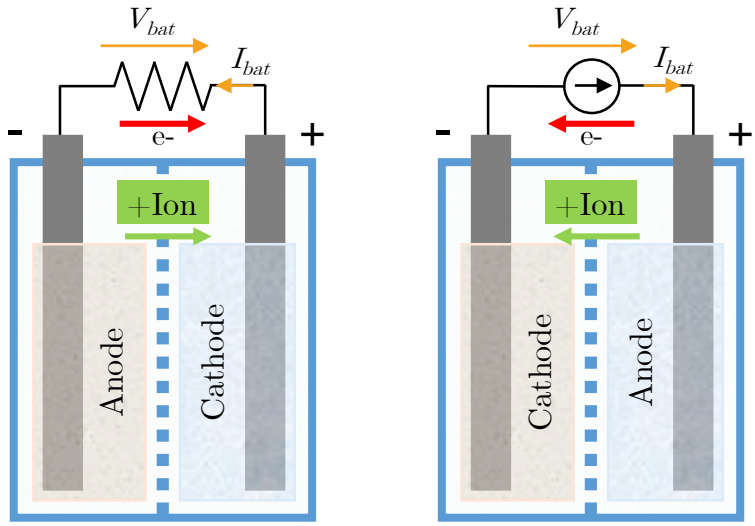

(a) Discharge process.

(b) Charge process.

Figure 2.4: Discharge and charge process of a battery (adapted from [70]).

2.2.1.1 Terminology

These are the most important parameters in a battery:

- **State Of Charge (SOC):** Indicates the available charge stored in the battery compared to the charge available when it is fully charged, expressed as a percentage or as an absolute capacity (in Ah). It cannot be directly measured from battery terminals, thus it must be estimated based on different indicators. SOC is directly proportional to the Open Circuit Voltage (OCV) and varies in a non-linear way depending on the chemistry of the battery. Fig. 2.5 shows a SOC-capacity discharge curve, similar to the one of a $LiFePO_4$ battery [38]. In this curve there are three main regions: in yellow there is the exponential zone, which occurs at the beginning of the discharge. Then it comes the nominal region. Finally, the end-of-discharge region, in green, represents the final discharge, where a small variation of capacity results in a great difference in OCV.

  The knowledge of the SOC is useful for the optimal management of the energy in the building [38, 71]. The most typical estimation method due to its simplicity is the coulomb counting, based on integrating the battery current over time to get the energy absorbed or released by the battery. Another

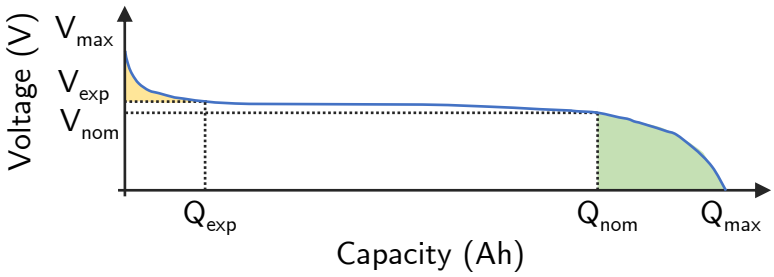

Figure 2.5: SOC vs discharged capacity in a battery.

method could be measuring the OCV, although it requires the battery to stay at rest for some time before performing the measurement. Observers and recursive technique based on offline/online parameters identification can also be employed [38, 70].

- **State Of Health (SOH):** Indicates the charge lost from a battery respect to its first charge, i.e. the difference between the maximum capacity when it was new and the actual charge, and is related with the aging of the battery (see Section 2.2.3). It predicts its cycle lifetime, the number of times that a battery can be charged or discharged before it arrives to a certain capacity fade. This definition has to be linked to the battery application: for some application, a given SOH may be unacceptable, while for others it can still be used. As in the case of the SOC, this cannot be measured, thus it has to be estimated [38, 72].

- **Energy density / specific energy:** Energy stored in the BESS respect to its mass or volume. If it respect to its mass is called gravimetric energy density and expressed in Wh/kg. A battery with a higher gravimetric energy density will store the same energy with less weight. If the energy density is given with respect to the volume it is called volumetric energy density, expressed as Wh/L and referring to the volume that the battery occupies. Both identifiers are normally referred to as simply energy density, distinguishing the type thanks to their units [73].

- **Power density:** Power that the battery can supply respect to its mass in W/kg. A battery with a higher power density will need less weight to achieve a given current capability.

- **Charge and discharge rate:** It refers to the current being drained or provided to the battery. It is normally expressed as a fraction of the battery's nominal current followed by the letter C (C-rate). In this way, a battery providing 1C current is supplying its nominal current.

2.2.2 Batteries for ESS

Batteries differ between them based on the material the electrodes are made of and the type of electrolyte in which the electrodes are immersed [25,32]. Electrode combinations are selected to be light and give a high cell voltage and capacity. This statement is, however, limited by certain factors, as reactivity with other cell components, polarization, difficulty in handling or high cost, among others [32]. There are a lot of factors that influence the selection of a battery [20, 25], as:

- Power
- Power dependent costs
- Efficiency
- Self discharge
- Cycles
- Maximum Depth Of Discharge (DOD)
- System lifetime
- Capital cost
- Maintenance and services
- Energy density
- Energy cost
- Capacity
- Cycle lyfetime at DOD
- Charging time
- Internal resistance
- Temperature dependency

All these parameters impact the final cost of the BESS. In the next sections a study of different chemistries that could be used for the BESS needed in an autonomous building will be included. Fuel cells are also briefly explained.

2.2.2.1 Lead-acid batteries

Lead-acid (Pb–acid) batteries were the first (1859) rechargeable batteries for commercial use and are still widely used, for example as the electrical source in conventional petrol cars and trucks [56, 70]. They were also the choice for the first-generation EVs [35]. The "Valve-Regulated Lead Acid battery" or VRLA, includes a one-way, pressure-relief valve designed to seal the cell unless its internal pressure exceeds a maximum. It was an important development in lead-acid battery technology, since they reduce gas emission by over 95 % [32].

When charged, lead-acid batteries consist of a positive electrode with lead dioxide (PbO_2) and a negative electrode with lead (Pb) as the active material. The electrolyte is sulfuric acid (H_2SO_4) [25].

With 2 V as the nominal voltage and an efficiency of around 75-85 % [20, 70], these batteries are safe, cheap and reliable. They are also simple to manufacture, with low self-discharge and high specific power ($\approx$ 150 - 180 W/kg). However, they are big and heavy because they have low energy density (30-50 Wh/kg) [35, 56] and cannot be fast-charged [56]. Moreover, some of its components are toxic [56]. In addition, they are less durable than nickel- and lithium-based systems when deep cycled, and do not behave as good with temperature [56].

The primary reasons for its relatively short cycle life are corrosion (increases the resistance in the positive electrode), gas generation due to overcharges, sulfatation (reduces battery capacity), active material degradation and separator metallization (can cause a short circuit through the separator) [56, 70]. Sulfatation is produced at low SOC, thus the battery must always be stored at full SOC [56].

2.2.2.2 Nickel batteries

Nickel-cadmium (NiCd) batteries were very popular for several decades until the 1990s, but their high toxicity due to cadmium lead to substitute them by nickel-metal-hydride (NiMH) batteries. Other batteries containing nickel could be the Nickel-iron (NiFe), Nickel-zinc (NiZn) or Nickel-hydrogen (NiH), but are not as popular as the other two [56, 57].

2.2.2.2.1 Nickel-cadmium

NiCd batteries have been in production for more than a century (1899). Their electrolyte is liquid potassium hydroxide (KOH), an alkaline electrolyte, thus they are all sealed [25].

Compared with lead-acid, the influence of the temperature on the battery capacity is rather small up to 40°C. Their nominal voltage is 1.2 V. Their lifetime and number of cycles (≈1000) are higher (with proper maintenance), with 30-80 Wh/kg specific energy, high discharge current and specific power (150-500 W/Kg), fast-charging and low internal resistance. In addition, they can be stored completely discharged. However, they are more expensive (≈3 times more) with a lower nominal voltage (1.2 V). Moreover, they have "memory effect" [25,56]. This effect causes a loss of capacity if the battery is not periodically fully discharge. In this situation, the battery gets used to a certain shallow DOD and is not capable of going further if needed after a certain number of cycles [25, 56, 74]. They also have a high self-discharge, losing approximately 40 % of their stored energy in three months, same percentage that a lead acid losses in a year. Moreover, their efficiency is lower (60-70 %) [25, 56].

Since cadmium is a toxic metal and due to environmental regulations, NiCd is nowadays limited to special applications [56].

2.2.2.2.2 Nickel metal hydride

NiMH batteries were developed as a substitute for NiCd due to their lower toxicity. The positive electrode contains nickel hydroxide, while the negative electrode is mainly composed of hydrogen-absorbing nickel alloys. As in NiCd batteries, the electrolyte is KOH [70].

NiMH batteries inherit some of the characteristics of the NICd, as the simplicity of storage, the same nominal voltage (1.2 V) or a wide temperature range of operation [56]. With more energy density (40-120 Wh/kg) and efficiency (80-90 %) than lead-acid and standard NiCd batteries, they are more delicate and can be permanently damaged if allowed to discharge too much [25, 35, 56]. Their specific power (≈ 200-300 W/kg) and number of cycles (300-500) are lower than NiCd. As NiCd, their self-discharge is high and can loose a 10 % capacity during the first 24 hours after a charge, reduced to a 10 % each month after that. Although some modifications can be carried out in the chemistry to reduce this

discharge (and also reduce corrosion), this also reduces the specific energy. They also suffer from memory effect, but less severely than NiCd, and require complex algorithms to correctly charge [56, 57, 70]. This was the battery used in the Toyota Prius up to 2015, when they changed them for Li-ion batteries [57].

2.2.2.3 Lithium-ion batteries

Lithium-Ion Batteries (LIBs) are the most common choice in high capacity ESS. Graphite is the most common negative electrode choice in LIBs, while positive active materials are usually oxides, as lithium-cobalt oxide ($LiCoO_2$) or lithium iron phosphate ($LiFePO_4$). In addition, the separator between cathode and anode prevents both of them to react directly in the electrolyte. The negative current collector is made of copper and the positive current collector is made of aluminum [68].

LIBs advantages include high specific energy (60–260 Wh/kg) and high specific power ($\approx$ 250-350 W/kg), which makes them attractive for applications where weight or volume are important. Other advantages are a long number of cycles (>500 cycles), being environmentally friendly, low self-discharge rate (<10 % per month), high efficiency (90-95 %) and no memory effect. Depending on the chemistry, their nominal voltage range from 3.2 to 3.7 V. As drawbacks, they are expensive and thermal runaways can occur in this type of batteries if they are not properly handled, so they need a BMS. In addition, power capacity fade with cycling, due to the internal resistance rise, which increases losses, heat production and accelerates aging. Energy capacity also fades with cycling, due to the degradation of the electrodes and electrolyte [56, 68, 70, 75].

2.2.2.4 Lithium-polymer batteries

The lithium-polymer or LiPo batteries have solid polymer electrolyte. It does not conduct the electricity but allows ion exchange. This solid electrolyte replaces the traditional porous separator soaked with electrolyte [56], which is considered to be the most flammable component of LIBs, and it may affect the cycle life and its safety [76, 77]. Thus, this dry polymer in LiPO is advantageous from the fabrication, safety and size point of view and allows numerous batteries shapes and sizes [56, 77]. This could be seen as a drawback, since there is no standard sizes as in LIBs. However, it lacks conductivity below 60°C, so the internal resistance is higher than in LIBs. In order to solve this issue, some gelled electrolyte has been included in this kind of batteries. This results in a separator/ electrolyte

membrane made from the same porous material as the separator in traditional LIBs, which becomes gel when filled with the liquid electrolyte. This electrolyte does not require a metal shell for containing the liquid, thus reducing the weight of the overall system. In addition, LiPo batteries are more resistant to overcharge, since there is less chance for electrolyte leakage. Their nominal voltage (3.7 V), efficiency (90-95 %) and specific power (250-360 W/kg) are similar to LIBs. However, they have lower specific energy (90-120 Wh/kg) and less cycle life (300-500). They are also more expensive [56].

2.2.2.5 Sodium and Sodium-Ion batteries

Batteries using liquid sodium in oxide ceramic solid electrolytes like the NaS or the ZEBRA.

2.2.2.5.1 Sodium–sulfur battery

The sodium–sulfur battery (NaS) was developed for EV at the end of the 1960s, using βAl_2O_3 electrolyte, which is a solid ceramic. The electrodes are liquid, sodium in the negative electrode and sulfur at the positive electrode. The specific energy is around 150-240 Wh/kg and the specific power 150-230 W/kg. They also have long cycle life (≈4500 cycles) [22, 56, 78]. Their efficiency is slightly lower than lithium-based batteries, ≈86-90 %. The cell (2 V nominal voltage) operates at very high temperatures (270–350°C), needed to achieve high conductivity. Their main problem is the need to be heated to work (electrodes are solid at room temperature). This battery can be stored in solid-state for more than 50 years [56, 57, 79].

2.2.2.5.2 ZEBRA batteries

A derivative of this battery comes from using the same electrolyte but substituting the sulfur by $NiCl_2$ in NaS batteries ($NaNiCl_2$). These batteries are called ZEBRA. The cell voltage increases to 2.6 V in this case compared to NaS [79]. The acronym ZEBRA stands for Zero Emission Battery Research Activities, which is the name given to them by their original developers. These batteries are also know as Sodium/Nickel-Chloride [32]. They have less specific energy (90-125) and similar efficiency (90 %) of NaS batteries and slightly smaller specific power (150-180 W/kg) and cycle life (≈3000). ZEBRAs are safer than

NaS, if one cell forming the battery fails, it becomes low ohmic and can conduct the full current, so the string remains operational and it does not need a battery balancing system [20,22,32,56,57]. As the NaS, their performance is optimum at 300°C. Heating consumes 14 % of the battery's energy per day if not used, while reheating the battery from cool state takes around two days. [56].

2.2.2.6 Redox cells

Redoxflow cells continuously converts the chemical energy of the fuel and oxidant to electrical energy. It can be reversed by charging back the electrolyte [22, 25]. Redoxflow batteries are different from the other batteries: the active materials are not integrated with the battery, but fed into the fuel cell from an external source, been generally stored in tanks. It consists of a couple of electrochemical reduction and oxidation reactions occurring in two liquid electrolytes containing metal ions, where ions migrate from one electrode to the other through the electrolyte, while the electrons go through an external circuit providing electric energy exchange. The cell needs to operate at near room temperature (between 15°C and 35°C) in order to keep the solutions at liquid state [22,80,81].

Each cell produces between 1 or 1.8 V depending on the technology [22, 80]. Their performance does not decrease with cycling, as long as the electrodes do not fail, thus their cycle life is higher than in any other battery and can be in the range of 10,000 cycles. These electrodes are inert and are not consumed during the reaction [27, 56, 57]. They are also easily scalable and flexible, and allow independent sizing of power and energy and deep DODs. Moreover they are safer than any other battery, since the active materials are stored separately. Besides, their response is fast and are not toxic. However, the tight temperature range needed to avoid precipitation implies some means of temperature control [80,81], and they have a high cost [81].

Examples of these kinds of batteries are Iron-chromium redox, Vanadium redox, Zinc-bromine or polysulfide-bromine redox. From these, only the vanadium redox is available commercially [22, 57]. Vanadium redox can get to ≈40 Wh/kg energy density (similar to lead-acid batteries) but have low power density. Power density in these batteries are generally expressed as W/cm^2, and it is around 0.13-0.51 W/cm^2 [22,82,83]. Its efficiencies range between 70 % and 85 %. Zinc-bromine or polysulfide-bromine redox can get to higher energy densities, but are in an early development stage [22].

These batteries are a good option for wind-power applications [27] and for

general RES [80], where the size is not a tight constraint (due to the lower energy density) [57].

2.2.2.7 Conclusions

The most important characteristics of batteries analyzed in the previous sections are summarized in Table 2.2. In this table, the cycles are considered as a mean estimation, since for some of the chemistries this depends immensely on the DOD, as in lead-acid batteries (Section 2.2.2.1). Fig. 2.6 shows their energy density as a function of their power density.

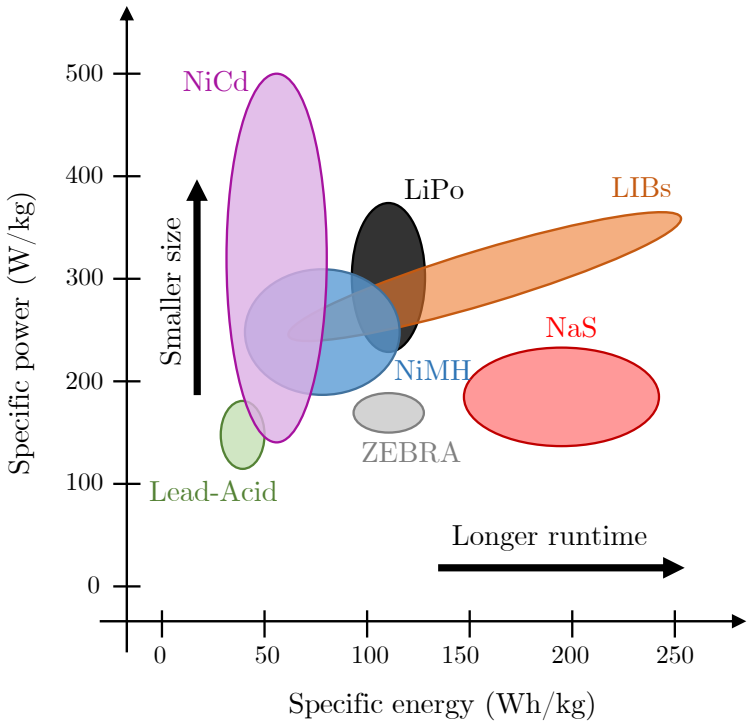

Figure 2.6: Specific density vs. power density of some rechargeable batteries based on the data from [22, 25, 57, 84].

Among these batteries, LIBs are the most attractive in terms of efficiency, nominal voltage and specific energy. NaS batteries also have high specific energy and cycle life, but the need for heating them makes them less practical, in addition

to its lower voltage levels. In terms of specific power, NiCd batteries are better, but NiCd is very toxic so they cannot be used.

2.2.3 Lithium-ion batteries

Lithium-Ion Batteries (LIBs) are the most common choice in high capacity ESS, with a market value that has increases almost steadily in the last 30 years (see Fig. 2.7) [68]. They are often used in microgrids [68], [86], electric vehicles (EV) [33,35,60,62] or satellites [67,87] applications due to their high energy density, good temperature operation range, low self-discharge and high cell voltage compared with NiCd, NiMH or Pb-acid [67].

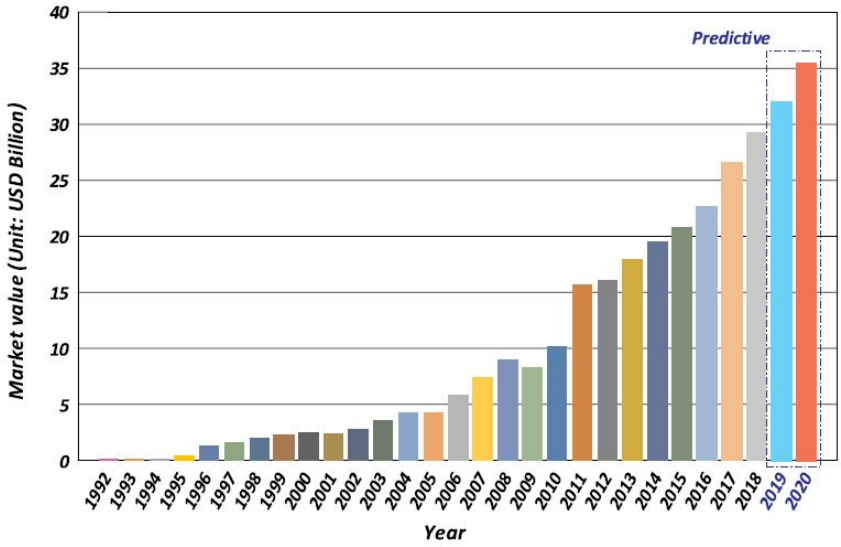

Figure 2.7: Evolution of Li-ion batteries world market from 1992 [68].

The main parts of these batteries are:

- **Electrodes:** Graphite (C_6) is the most common negative electrode choice in LIBs, which gives them a characteristic flat SOC curve [56]. LIB positive electrode active materials are usually oxides, as lithium-cobalt oxide ($LiCoO_2$ or LCO), lithium- manganese oxides ($LiMn_2O_4$ or LMO) or lithium iron phosphate ($LiFePO_4$ or LFP), which are transition metals and give name to the batteries [32,68,70,88,89].

Table 2.2: Comparison of Different Electrochemical Storage Technologies [19, 20, 22, 25, 56, 57, 70, 80, 82–85]

Technology	**Efficiency (%)**	**Nominal voltage (V)**	**Discharge temp. (°C)**	**Charge temp. (°C)**	**Specific energy (Wh/kg)**	**Specific Power (W/kg)**	**Cycles**
Lead Acid (2.2.2.1)	75 - 85	2	-20 - 50	-20 - 50	30 - 50	150 - 180	200 - 500
Nickel Cadmium (2.2.2.2.1)	60 - 70	1.2	-20 - 65	0 - 45	30 - 80	150 - 500	1000
Nickel metal hidride (2.2.2.2.2)	80 - 90	1.2	-20 - 65	0 - 45	40 - 120	200 - 300	300 - 500
Lithium-ion (2.2.2.3)	90 - 95	3.2 - 3.7	0 - 45	-20 - 60	60 – 260	250 - 350	500 - 3000
Lithium-polymer (2.2.2.4)	90 - 95	3.7	0 - 50	-20 - 60	90 - 120	250 - 360	300 - 500
Sodium Sulphur (2.2.2.5.1)	86 - 89	2	270 - 350	270 - 350	150 - 240	150 - 230	4500
ZEBRA (2.2.2.5.2)	90	2.6	270 - 350	270 - 350	90 - 125	150 - 180	3000
Redox flow (2.2.2.6)	70 - 85	1 - 1.8	15 - 35	15 - 35	40	-	10000

- **Separator:** The separator is either a microporous polymer separator film or gel-polymer. This last one allows lithium ions (Li+) to diffuse between the positive and negative electrodes [68, 70, 88].

- **Electrolyte:** For the electrolyte, materials with high ionic conductivity are used in such a way that lithium ions move easily. The electrolyte is considered to be the most flammable component of LIBs, and is normally a nonaqueous system made of carbonate solvent with low boiling point and lithium hexafluorophosphate ($LiPF_6$). It provides the best balance between performance, cost and toxicity, but it fails in terms of safety. This is because it produces a strong acid with high reactivity when decomposed. This material is exposed to large thermal risks when the battery is overcharged, short-circuited or exposed to high temperatures, among other things [76].

- **Collectors:** The active materials are attached to metal-foil current collectors at both ends of the cell. The negative current collector is made of copper and the positive current collector is made of aluminum [68, 70, 88].

- **Electrochemical double layer:** When a metal electrode is brought into contact with a solution of its positive ions, a reaction will occur until equilibrium is reached. In this reaction there is a separation between the electrolyte and the metal phase. The metal is partially dissolved and negative charges accumulate in the metal at the metal–solution interface. These charges are counterbalanced by positive ionic charges on the solution side of the interface. On the other hand, there is partial plating of the metal, and positive charges accumulate in the metal at the metal–solution interface. These charges are counterbalanced by negative ionic charges on the solution side of the interface. There is an interfacial region in which the excess charges on the electrode and the solution accumulate. This region is called the electrochemical double layer [73].

- **Solid Electrolyte Interface:** Another important part of LIBs is the Solid Electrolyte Interface (SEI), a film that is naturally formed when the graphite becomes intercalated with lithium and exposed to the electrolyte. This process occurs during the first few cycles (especially the first one) in the life of the battery because graphite operates at voltages that are outside of the electrochemical stability of the electrolyte, so the positive electrode (graphite) reacts with the electrolyte solution. In this reaction, the electrolyte is decomposed and there is also lithium ions consumption at the electrode/electrolyte. Due to this lithium ions consumption there is an

immediate and permanent capacity loss [69,88,90]. The resulting products from the decomposition cover the electrode's surface, thus forming the SEI. The SEI protects the electrolyte from further reduction and the electrode from corrosion [88]. SEI plays a major part when determining battery performance, as cycle life, calendar life, self-discharge, safety or efficiency. Below -30°C, the SEI has low ionic conductivity, while at high temperatures (over 50°C) it becomes unstable, thus resulting in poor behavior of the LIB [90]. SEI does not store charge itself, thus been largely unaffected by SOC [91]. This property is used by several authors (see Section 2.2.8.2) to estimate cell temperature.

The dominant aging mechanisms in LIBs take place at the negative electrode and cause capacity loss and impedance rise. Impedance increases due to the SEI layer growth, especially at higher temperatures or due to a contact loss due to the disconnection of the SEI from the negative electrode. Capacity fades due to the loss of mobile Li+ ions, caused by lithium corrosion or lithium plating. This last effect takes place at low temperatures, high charge rates or low cell voltages [70,88].

The specific energy depends on the type of positive electrode used and constituting anode materials, in addition to their nano and micro-structures. On the other hand, the maximum power depends on the voltage, density of lithium ions, SEI, diffusion coefficient of the electrodes and their conductivity [89].

In the next sections, the most popular LIBs are analyzed: Lithium Cobalt Oxide ($LiCoO_2$), Lithium Manganese Oxide ($LiMn_2O_4$), Lithium Nickel Manganese Cobalt Oxide ($LiNiMnCoO_2$), Lithium Iron Phosphate ($LiFePO_4$), Lithium Titanate (Li_2TiO_3) and Lithium Nickel Cobalt Aluminum Oxide ($LiNiCoAlO_2$) [92].

2.2.3.1 Lithium Cobalt Oxide

This is one of the most common LIBs and was the most used LIB by 2018 [92] due to its high presence in portable applications as mobile phones [89]. Its chemical symbol is $LiCoO_2$ and is usually abbreviated as LCO or Li-cobalt. Cobalt oxide is the main active material in the positive electrode [56,57].

With 3.6 V as nominal voltage, it has high energy density (150-200 Wh/kg) and good electrical and safety performance. In addition, it is a mature technology with almost 30 years in the market. It has an acceptable life span (500-1000

cycles) but low thermal stability (due to the cobalt-oxide) and limited specific power: it cannot be charged and discharged at a current higher than its C-rating. Forcing a higher power will cause overheating and stress. In addition, cobalt has a high prize and is toxic and harmful to the health and the environment [32, 56, 57, 73].

2.2.3.2 Lithium Manganese Oxide

Its chemical symbol is $LiMn_2O_4$ and is usually abbreviated as LMO or Li-manganese. Its nominal voltage is 3.7 V. This LIB was the fourth most used LIB by 2018 [92]. Its special structure (called spinel) improves ion flow on the electrode, which results in lower internal resistance and better current capability, thus it can be fast-charged and discharged with moderate heating. Besides, it provides a high thermal stability (due to the higher thermal stability of manganese oxide) and improves safety. Moreover, been cobalt-free makes it a less toxic battery than LCO. Its nominal voltage is 3.7 V. However, its cycle (300-700) life is limited and the energy density (100-150 Wh/kg) is lower than the one from cobalt, as well as its capacity (see Section 2.2.3.1) [56, 57, 89].

A combination of LMO with cobalt, nickel, manganese or aluminum in the positive electrode can improve the specific energy (capacity), specific power (load capability) or longevity, thus the most convenient blend can be used for each application. In addition, silicon can be added to the negative electrode to improve the capacity, at the expense of a shorter life cycle, since the addition of this element creates mechanical stresses [56, 57].

2.2.3.3 Lithium Nickel Manganese Cobalt Oxide

Its chemical symbol is $LiNiMnCoO_2$ and is usually abbreviated as NMC. It was the second most used LIB by 2018, after LCO [92]. Its nominal voltage is 3.7 V and specific energy around 150–220 Wh/kg. It can last for between 1000–2000 cycles if the DOD is not much and the temperature is kept at reasonable values. The positive electrode normally combines equal parts of nickel, manganese and cobalt, although other blends are possible. Nickel has a high specific energy but poor stability, while manganese has the benefit of forming a structure that achieves low internal resistance with low specific energy (see Section 2.2.3.1) [56].

This battery is one of the possible blends explained in Section 2.2.3.2 and can be prepared to have high energy or power density. Combining NMC with LMO

(see Section 2.2.3.2), specific energy and life span can be prolonged, making this resulting battery an option for a lot of EVs nowadays. The LMO corresponds to about a 30 % of the battery, providing high current capability, while the NMC part increases the capacity range [56].

2.2.3.4 Lithium Iron Phosphate

Among LIBs, Lithium Iron Phosphate, whose chemical symbol is $LiFePO_4$ and is normally abbreviated as Li-phosphate or LFP, is the third most used type and keep a similar market growth rate to their counterparts [92]. The reasons for its good market share are their advantages in terms of safety, low toxicity (in opposition to cathodes based on rare metal composites, as LCO [93]), long cycle life (>2000), high power capability, reliability, relatively low cost, wide temperature range (-20°C – 60°C), good thermal stability and flat voltage profile (considered as a drawback for SOC estimation [57, 93]). They can also be kept at full charge conditions with better results than other LIBs. As a drawback, compared to other LIBs, they have low-average cell voltage (3.2 V), higher self-discharge and lower specific energy (90–120Wh/kg). As other LIBs, cold temperature reduces performance and elevated storage temperature shortens the service life [33, 56, 69, 70, 92–94].

2.2.3.5 Lithium Titanate

Its chemical symbol is Li_2TiO_3 and is usually abbreviated as LTO or Li-titanate. It was the fifth most used LIB by 2018 [92]. Its nominal voltage is 2.4 V, around 1 V or more lower than the rest of the LIBs presented in this section. This is due to not using graphite at the negative electrode and instead using $Li_4Ti_5O_12$. The positive electrode is lithium manganese oxide or NMC. This battery can be fast-charged and has a high current capability, with high cycle life. They are also safer and behave well at low-temperatures. The absence of graphite results in no SEI formation and no lithium plating (see Section 2.2.3). However, they are more expensive than other LIBs and have lower specific energy (≈65 Wh/kg), in addition to the already mentioned lower nominal voltage due to the different negative electrode material [56, 57, 95].

2.2.3.6 Lithium Nickel Cobalt Aluminum Oxide

Its chemical symbol is $LiNiCoAlO_2$ and is usually abbreviated as NCA. It was the sixth most used LIB by 2018 [92]. The positive electrode is normally composed of 80 % nickel, 15 % cobalt and 5 % aluminum. This means that the cobalt percentage is quite low compared to LCO batteries (Section 2.2.3.1), thus been far less toxic. Its nominal voltage is 3.6 V. It shares aspects with the NCA (Section 2.2.3.3), with high specific energy (200-260 Wh/kg), good specific power and a long life span (typically 500 cycles, but can go up to 1500 full cycles). However, they are more expensive and entail more safety risks [56, 89]. These are the batteries employed by Tesla in their EVs, and there are projections to use them as backup in grid-connected applications [89].

2.2.3.7 Conclusions

Table 2.3 shows a summary of the LIBs analyzed in the previous sections. Among them, $LiFePO_4$ batteries are one of the most attractive due to a number of reasons (see Chapter 2.2.3.4) including safety, long cycle life and low toxicity. Its benefits surpass the drawbacks, as the lower nominal voltage or lower specific energy. Those LIBs that have a higher specific energy (all except from LTO) have in general a lower number of cycles. Since in this application the size is not as important as in other applications, as EV, they are discarded. LTO, on the other hand, although having more cycle life, has a lower energy density, but more importantly, it is much more expensive. Due to all of this, $LiFePO_4$ batteries were the batteries selected for the ESS in the building that was described in Section 1.2.

2.2.4 Batteries used in this work

Batteries can be found in a lot of shapes and sizes, been the most common ones prismatic (normally rectangular, also called pouch cells) or cylindrical [70]. Cylindrical LIBs are commonly found in EV and ESS technologies due to their safety and manufacturing simplicity [96].

The basic cell used in the BESS for the autonomous building is a cylindrical $LiFePO_4$, shown in Fig. 2.8. It is an 26650 type cell, which is 26 mm in diameter and 65 mm in length [32]. Its main characteristics are shown in Table 2.4.

In cylindrical cells, a layer of the positive electrode, separator, negative electrode, and then a second separator are rolled up to form a cylinder (see Fig. 2.9).

Table 2.3: Comparison of Different LIBs [56, 57]

Technology	Nominal voltage (V)	Cycles	Specific energy (Wh/kg)	Price
Lithium Cobalt Oxide - LCO (2.2.3.1)	3.6	500 - 1000	150 - 200	Medium-low
Lithium Manganese Oxide - LMO (2.2.3.2)	3.7	300 - 700	100 - 150	Medium-low
Lithium Nickel Manganese Cobalt Oxide - NMC (2.2.3.3)	3.6	1000 - 2000	150 - 220	Medium-low
Lithium Iron Phosphate - LFP (2.2.3.4)	3.2	>2000	90 - 120	Low
Lithium Titanate - LTO (2.2.3.5)	2.4	3000 - 7000	50 - 80	High
Lithium Nickel Cobalt Aluminum Oxide - NCA (2.2.3.6)	3.6	500	200 - 260	Medium-high

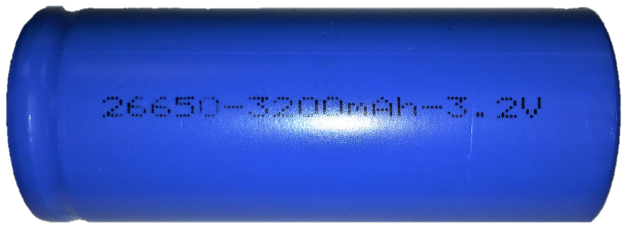

Figure 2.8: $LiFePO_4$ battery.

The second separator is needed to keep the positive electrode from the negative electrode in this configuration. Leads are used to connect the positive electrode

Table 2.4: $LiFePO_4$ Parameters Used in This Work

Nominal voltage	3.2 V
Nominal current	3.2 A
Maximum charge current	1C
Maximum discharge current	3C
Battery capacity	3200 mAh

to the top terminal and the negative electrode to the bottom terminal. The current capability of the cell depends on the electrode area, so bigger cells means higher maximum currents [70].

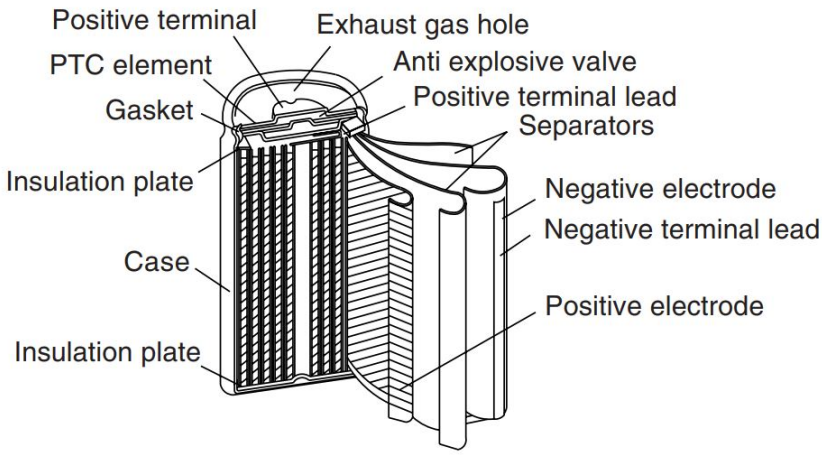

Figure 2.9: Structure of a cylindrical LIB [75].

2.2.5 Batteries and switching converters

Voltage in a battery varies with SOC, being the OCV vs. SOC curves dependent on the battery chemistry [38]. $LiFePO_4$ batteries have a flat characteristic for medium SOCs [38]. This is an advantage from the user point of view because the voltage variation will be rather small. Fig. 2.10 shows the OCV vs. SOC curve for the $LiFePO_4$ cell shown in Fig. 2.8. In this kind of batteries, a cell voltage measurement as accurate as 1-2 mV is normally required for good and

reliable SOC estimation [38].

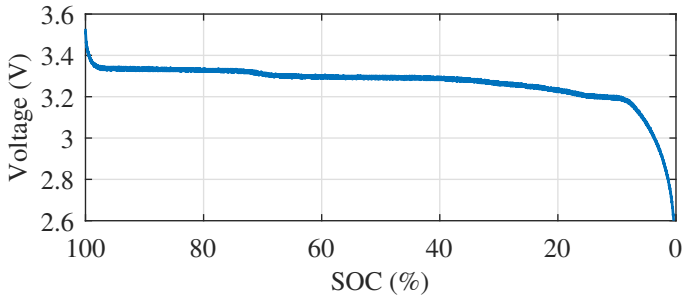

Figure 2.10: SOC curve of a $LiFePO_4$ cell (discharge).

In some systems, the admissible DC voltage variation limit is very small, or the required voltage is very high, making unpractical a high number of series-connected cells. In this case, a DC/DC converter between the batteries and the rest of the system to stabilize the DC voltage independently of the battery SOC is required [20,64], adding controllability to the system [29]. These converters can also provide galvanic isolation if needed. They can be found in microgrids or electric vehicles, among other applications [20, 64]. Examples of DC/DC converters used for battery integration are:

- **Non isolated converters:** direct coupling.
  - ◇ **Bidirectional boost / buck-boost converter:** classical power converters for battery connection to the rest of the system and charging. With two switches, an inductor and the DC-link capacitor (Fig. 2.11), it is simple to control and design [97, 98].
  - ◇ **Interleaved converters:** for high current applications. It replicates the number of switching branches in the converter (Fig. 2.12). This configuration reduces device stress, improves thermal management, allows for filters and switching frequency reduction, lowers the ripple and improves system reliability. These benefits increase with the number of interleaved branches. As a drawback, the control complexity and the number of devices increase [97, 99].
  - ◇ **Multilevel converters:** for medium-voltage systems where a 2-level converter cannot stand the required voltage. An example of this kind of converters could be the multilevel boost converter [100].

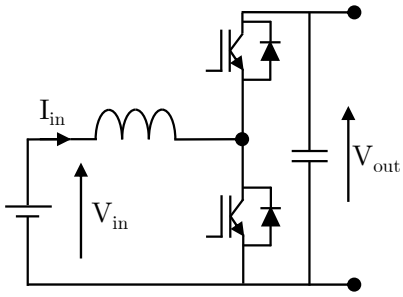

Figure 2.11: Boost converter.

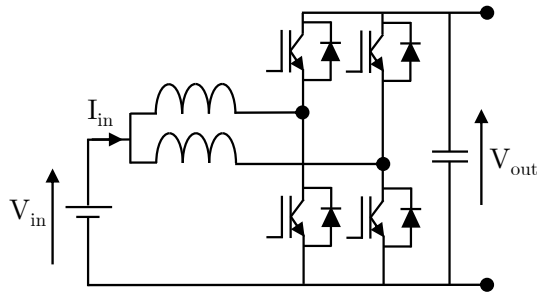

Figure 2.12: Interleaved boost converter.

- **Isolated converter:** required in some situations, it increases the complexity and number of components of the system.
  - ◇ **Flyback converter:** isolated version of the buck–boost converter (Fig. 2.13), mostly used for low power applications [101]. The efficiency decreases with respect to non-isolated converter due the losses in the leakage inductance of the transformer [102].

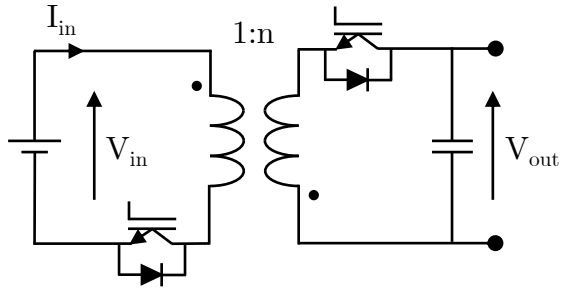

Figure 2.13: Bidirectional flyback.

  - ◇ **Dual Active Bridge (DAB):** the galvanic isolation is through a high-frequency transformer in between two H-bridges (Fig. 2.14). This converter can achieve high efficiencies despite the transformer by means of a careful design and low losses commutation when using zero voltage switching (ZVS) in the switches. Moreover, it is suitable for high power applications. However, it requires 8 switches per converter and the design to keep the efficiency high can become rather complex [103, 104].
  - ◇ **Multilevel converters:** same as in the case without isolation, these converters are used when the output voltage is too high to achieve with

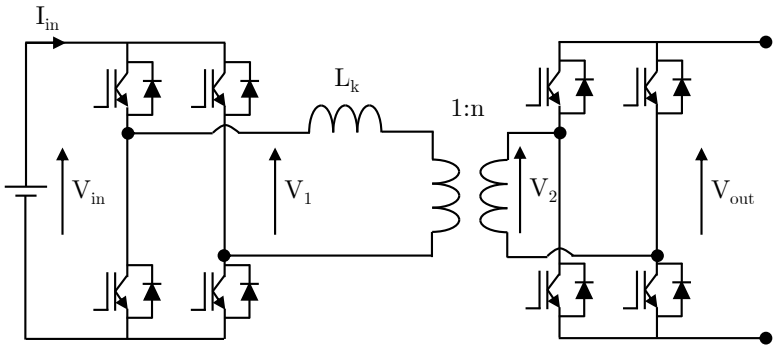

Figure 2.14: Dual Active Bridge.

a 2-level converter (Fig. 2.15). Several batteries are connected each to a DC/DC converter, which outputs are then parallelized to create a high voltage end [105]. A good option for the DC/DC converters that are used to create the different levels could be the DAB [20].

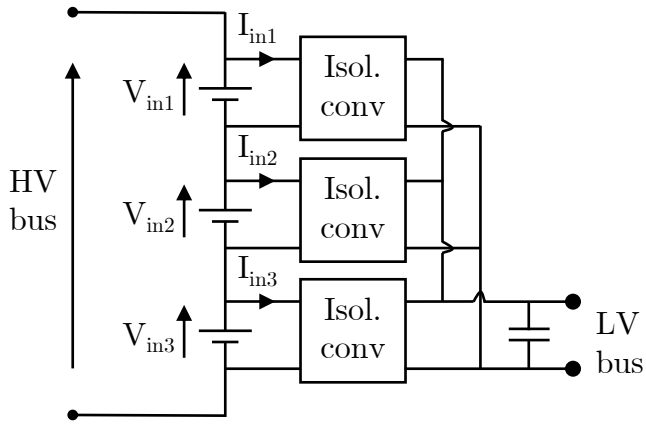

Figure 2.15: Multilevel converter.

2.2.6 Battery management systems

Development of battery monitoring methods aimed to guarantee safe operation and to improve their performance, reliability and lifetime have been the focus of significant research efforts in the last two decades. A Battery Man-

agement System (BMS) controls how a BESS is going to be used, ensuring a proper work while meeting all the technical and safety requirements of a given application [29, 38, 67, 106].

Since the cell voltage and/or current for any know battery chemistry is low (see Table 2.2) compared with typical industrial requirements, battery packs are built stacking cells in series and/or parallel configurations [29, 107]. Manufacturing tolerances, temperature differences, cell distribution inside the pack (which affects the battery temperature), among other reasons, result in voltage imbalances among cells during normal pack operation. These imbalances accelerate the aging of cells and increase the internal battery resistance and a decrease in its capacity. Mismatches in voltage among cells also increase the internal battery temperature, decreasing therefore safety operation [106, 108, 109]. These imbalances can also cause overvoltage or undervoltage in one or more of cells forming the pack. As it was explained in Section 2.2.3, active materials in the Li-ion Batteries (LIB) can be potentially damaged in this situation, causing safety issues, as temperatures rise [109–111]. The electrolyte is considered to be the most flammable component of LIBs, so high temperatures will also affect its stability [76].

For all these reasons, BMSs are needed to increase the overall safety of the system ensuring a correct performance. In general, a BMS can do one or more of the following things, depending on its complexity [29, 38, 62, 64, 65, 67, 106, 108, 110, 111]:

- **Supervision level:**
  - ◇ Monitor operational parameters:
    - ∗ Temperature: very important for LIBs safety (see Sections 2.2.3 and 2.2.8.1).
    - ∗ Voltage: needed for SOC estimation.
    - ∗ Current: it is normally the major input of any SOC algorithm (see Section 2.2.1.1), thus it must be measured accurately.
  - ◇ SOH estimation (see Section 2.2.1.1).
  - ◇ SOC estimation (see Section 2.2.1.1).
  - ◇ Controlling:
    - ∗ Overcharge.
    - ∗ Overdischarge.

    - Short-circuit.
    - Temperature range.

- **Control level:** performs the different tasks entrusted by the control algorithms, e.g. charging or equalizing.

    - Extend the life of the battery by ensuring a safe range of operation for all the cells forming the pack, acting if the battery is out of the safety range of operation for the different parameters mentioned before, as voltage or temperature.
    - Cell balancing (see Section 2.2.6.1).
    - Charge control.

2.2.6.1 Cell equalizers

An unbalance battery pack has a lower effective capacity [72]. Battery equalizers extract energy from the most charged cell of a series-connected battery pack and either dissipate it or transfer it to a less-charged cell, in such a way that all the cells are at the same SOC level and make the most out of the available capacity (see Fig. 2.16) [111].

Based on the energy destination (dissipate/transfer), equalizers can be classified as passive or active [111]:

- **Passive balancing:** dissipates the excessive energy difference in a bleeding resistor or transistor. It is relatively inexpensive, small and easy to implement, although inefficient, losing the excessive energy and thus reducing the efficiency of the system. In addition, it is a slow system limited by the maximum allowable dissipated power; if there is too much heat generation, thermal management can be compromised [38,109,111]. Due to this, recent research efforts are focused on active balancing methods.
- **Active balancing:** It transfers the energy in between cells with high efficiency. Methods for active balancing can be classified according to different criteria, as the connections between the cells which determines the energy flow (cell-to-cell, pack-to-cell, cell-to-pack...) or according to the circuit topology [38,106,108,110,111]:

    - **Shunting methods:** transfer the energy from one cell to another without any external energy storage device. Examples of this system are [106]:

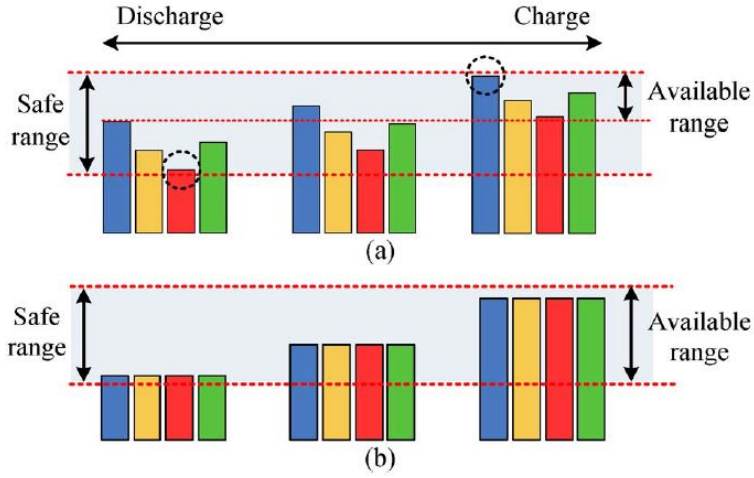

Figure 2.16: Available range according to SOC. (a) Unbalanced cells. (b) Equalized cells [111]

.

- ∗ **PWM Controlled Shunting:** with a pair of MOSFETs and an inductor for each N-1 cells, the current through each cell is controlled based on the voltage difference between cells. It needs accurate voltage measurement.
- ∗ **Resonant Converter:** Works similar to the previous case but it does not need to measure the voltage, although it needs a startup system to start the resonance. It uses one set of resonant circuits for every pair of neighboring cells.
- ∗ **Boost Shunting:** There is a boost converter for each cell. The system measures all the voltages and uses the boost converter to derive the energy from the most charged cell to the rest.
- ∗ **Complete shunting:** When a cell in the string is charged it is bypass so the charging of the rest of the cells can be completed. This method becomes complicated as the string increases in size because it may need a buck converter with a wide range of output voltages.

◇ **Shuttling methods:** use external energy storage devices to transfer the energy between cells, e.g. capacitors, inductors or other cells. The most popular one is the Switched Capacitor Equalizer (SCE). There

are a lot of proposals in the literature regarding this kind of equalizer, with one or more capacitors to balance the charge [111–116]. There are more complex systems based on the same principle that combine inductors and capacitors to improve the performance in terms of speed and losses, such as achieving zero current switching [117]. However, the increased difficulty in the design and number of components makes them impractical for low-cost applications.

- ◇ **Energy conversion methods:** this method uses isolated converters for equalizing the cells. Examples of this method are:
  - ∗ **Step-up Converter:** uses isolated boost converters to extract charge from the most charged cell and give it to the complete pack. It needs to measure the voltage to control the equalizer and is expensive, but easy to escalate. However, it needs special considerations when the pack is large, because a single cell voltage must be boosted up to the pack level.
  - ∗ **DAB converters:** Similar to the previous method, it uses DABs converters to transfer the energy among cells [118]. Although more complex and expensive, the zero-voltage switching nature of the converter increases the efficiency of the system.
  - ∗ **Transformer converters:** there can be one transformer per cell or a transformer with several secondary taps and a single core. This last system is cheaper, however, it is not modular, so the number of cells cannot be increased if needed.
  - ∗ **Switched Transformer:** the whole battery is connected to the lowest charged cell in the pack through a transformer by means of a series of switches using the information provided by the voltage sensors.

The methods explained in this Section are summarized in Table 2.5. It takes into consideration several parameters: price, speed of equalization, complexity of the design and/or control, efficiency, modularity of the design and if the method is more effective during charge or discharge of the pack. From the methods presented, the best option to balance the cells forming the $LiFePO_4$ battery in the building (see Section 1.2) are the shunting methods. These are the only methods that work effectively both in charge and discharge [106]. Shuttling methods, although not needing a storage system, are complex to design or need precise measurements. In addition, not having energy storage elements does not

Table 2.5: Equalizing Methods Comparative

Type	Price	Speed	Com-plexity	Effi-ciency	Modularity	Control	Charge & discharge operation
Passive balancing	✓	✗	✓	✗	✓	No	Charge
PWM controlled shunting	✗	✓	✗	✓	✓✗	Yes	Charge
Resonant converter	✗	✓	✗	✓	✓	No	Charge
Boost shunting	✓	✓✗	✓✗	✓	✓✗	Yes	Charge
Complete shunting	✓✗	✓	✓✗	✓✗	✓✗	Yes	Charge
Shuttling with capacitors	✓	✓ or ✓✗ [1]	✓	✓ or ✓✗ [1]	✓ or ✓✗ [1]	No	Both
Shuttling with capacitors and inductors	✓✗	✓✗	✓✗	✓	✓	No	Both
Step-up converter	✗	✓	✗	✓✗	✓✗	Yes	Both
DAB converter	✗	✓	✗	✓	✓	Yes	Both
Transformer converters	✗	✓	✗	✓✗	✓ or ✗ [2]	Yes	Charge
Switched transformer	✗	✓✗	✗	✓✗	✓✗	Yes	Charge

[1] Depending on the capacitor's arrangement.

[2] Easy modularity for the cases with one transformer per cell.

mean that the number of elements is lower. On the other hand, energy conversion methods are too complex and expensive to be used in the process of balancing single cells, so they are only suitable for balancing packs. Regarding shuttling active balancing methods, one of the most appealing methods to equalize single cells is the SCE [112], due to its low cost and simplicity. This system is the one selected for the building.

2.2.6.1.1 Switched-capacitor equalizers

This shuttling cell-to-cell equalizer balances N cells with N-1 capacitors and 2N switches, see Fig. 2.17.

The switches continuously work with a fixed duty cycle of 50 %, but the corresponding dead time to avoid shortcircuit, alternating ON/OFF states between switches "a" and "b". This results in a very easy system that can work without any control strategy: there will be energy transfer between the cells if there is a voltage difference among them. This can be seen in Fig. 2.18, where Ts is the switching period and dt the dead time. This way, each capacitor is connected half of the switching period in parallel with one cell and the second half with an adjacent cell, transferring energy from the one with the highest voltage to the one with the lowest voltage. This is schematically shown in Fig. 2.19 assuming $V_{B1} > V_{B2} > V_{B3}$. In state 1 (in red), B1 charges C_{12} and B2 charges C_{23}, i.e. they are connected in parallel, and in state 2 (blue), C_{12} discharges over B2 and C_{23} discharges over B3.

The main advantages of this equalizer are that it does not require control, it is fully scalable, cost-effective and easy to implement. In addition, and unlike other methods, it can work effectively both in charge and discharge [106]. As a drawback, cells transfer energy effectively only to their adjacent ones, so on certain occasions, e. g. the upper cell has the highest voltage and the lower one the lowest, the energy should flow through all the batteries to get to the less charged one, which increases the losses and the equalization time. The total resistance in the adjacent path includes the battery resistance, the capacitor resistance, two switches and the path itself. There is a path for the energy to flow through non-adjacent cells, however, it is a higher resistive path; to go from B1 to B3 in Fig. 2.19, there will be 2 capacitors, 3 batteries and the same number of switches, in addition to a longer path, increasing the total resistance. This means that the resistance increases with the distance between cells, therefore decreasing the amount of energy flowing through non-adjacent cells and increasing

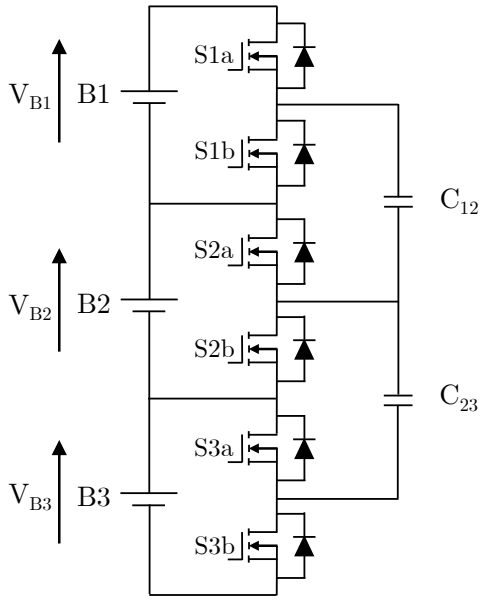

Figure 2.17: Schematic of the SCE ballancing 3 cells.

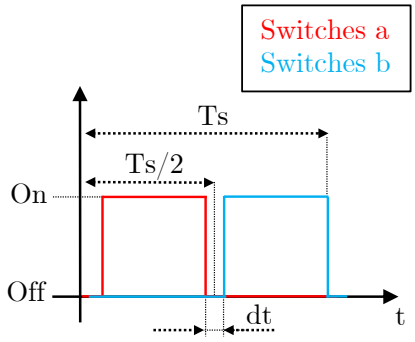

Figure 2.18: Switching function of the control of the SCE.

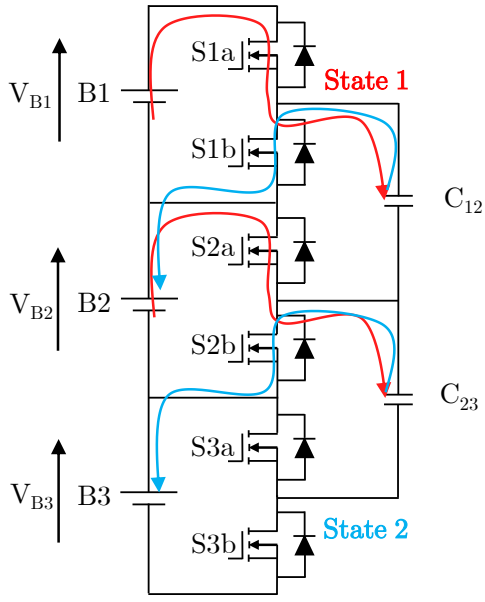

Figure 2.19: Switching paths of the SCE with with 3 cells.

the equalization time [111]. Note that this equalizer may induce losses if the switching is maintained once the cells reach an equilibrium. To avoid this, a threshold to start and stop the equalization may be selected to reduce these losses.

The SCE from Fig. 2.17 can have large equalization time, especially if the capacity of the cells is high or they are extremely unbalanced. However, it is expected that this time is reduced if the SCE is permanently connected, since it will not allow large unbalances among cells. To reduce this time, different SCE topologies have been proposed. These equalizers improve the equalization time at the price of increasing the number of components used or the loss of modularity. These alternative SCE topologies are are listed and analyzed below [111–116]:

- **Basic switched-capacitor equalizer [112]**: Explained earlier in this section.

- **Double-tiered switched-capacitor equalizer [111,113,114]:** Fig. 2.20. An extra capacitor bridges the capacitors in the first row, so batteries have two paths to exchange charge, reducing the equalization time. As a drawback, there is a need of adding an extra capacitor to the system, which must withstand the combined voltage of all the capacitors, compromising the scalability of the topology.

- **Chain structure using additional switches or capacitors [111]:** Fig. 2.21. Requires four additional switches compared to the double-tiered SCE, top and bottom cells become therefore adjacent, forcing them to exchange energy between them and their adjacent cells only, and not with all the cells in the pack as in the previous case. The scalability of this topology is compromised as in the previous case since the voltage that the new switches must withstand is the same as the whole battery pack.

- **Star-structured switched-capacitor equalizer [113]:** Fig. 4 left. It requires one additional capacitor respect to the classic proposal and connects the capacitors in a star-structure that allows the interconnection of all the cells at the same time, which decreases the equalization time (making it independent of the initial imbalance status of the string) and efficiency. As a drawback, the scalability is again compromised because the voltage that each capacitor must withstand is different. A variation of this equalizer with one less capacitor can be seen in Fig. 4 right, [113, 115].

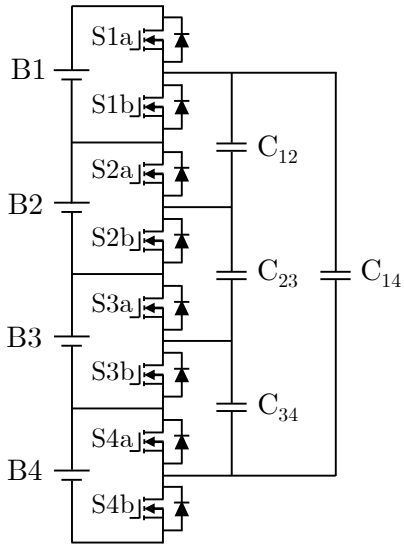

Figure 2.20: Double-tiered switched-capacitor equalizer.

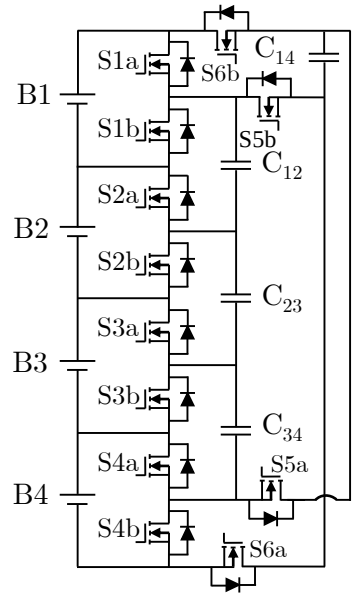

Figure 2.21: Chain structure using additional switches or capacitors.

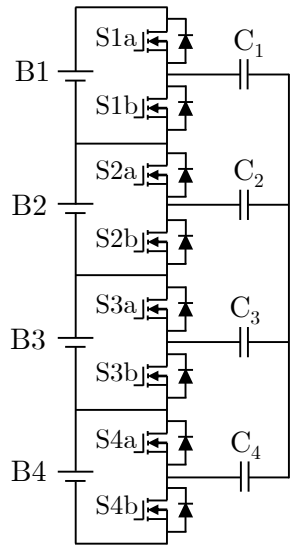

(a) Version with one extra capacitor.

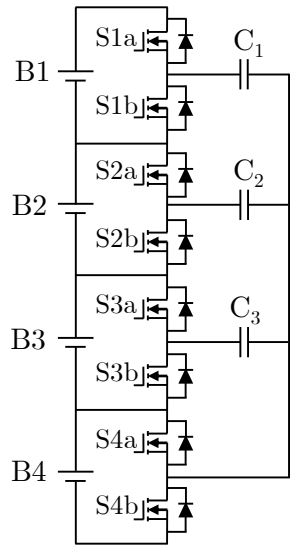

(b) Optimized version.

Figure 2.22: Star-structured SCE.

- **Delta structured switched-capacitor equalizer [116]:** Fig. 2.23. This equalizer adds capacitors in such a way that there is always one capacitor connecting any two cells, allowing interconnection of all the cells at the same time. As the double-tiered SCE, it maintains the number of switches but increases the number of capacitors (in a higher number) while reducing the equalization time. The voltage that each capacitor must hold is different and dependent on the cells they are bridging.

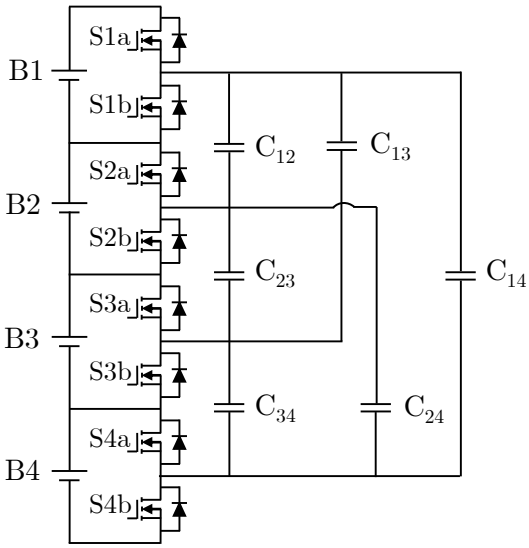

Figure 2.23: Delta-structured SCE.

A summary of the SCEs presented in this section is given in Table 2.6, which shows a comparison among SCEs based on the number of switches and capacitors depending on the number of series-connected cells (N), if the equalization time varies with a change in the position of the cells and if the capacitors can be all equal or not depending on the voltage that they should withstand.

The previous discussion has considered only balancing systems based on capacitors. They all have in common the same working principle, being cost-effective solutions easy to implement thanks to the absence of control. There are more complex systems based on the same principle that combine inductors and capacitors to improve the performance in terms of speed and losses, such as achieving zero-current switching [117]. However, the increased difficulty in the

Table 2.6: Comparative of Different Switched-Capacitor Methods

	Switches	**Capacitors**	**Variable equalization time**	**Equal capacitors**
SCE classical [112]	2N	$(N-1)$	Yes	Yes
Double-tiered [111, 113, 114]	2N	$(N-1)+1$	Yes	No
Chain structure [111]	2N+4	$(N-1)+1$	Yes	Yes
Star-structure [113, 115]	2N	N or $(N-1)$	No	No
Delta-structure [116]	2N	$\sum_{i=1}^{i=N-1}(N-1)$	No	No

design and number of components make them impractical for low-cost applications

2.2.7 Electric modeling of batteries

There are several ways of modeling the battery behavior [119]:

- **Electrochemically:** complex, and difficult to obtain, based on the chemical reactions described by partial differential equations which are slow to compute. They are accurate and oriented to design aspects and microscopic and macroscopic descriptions.
- **Mathematically:** abstract and application-focused, useful to predict system-level behaviors, such as efficiency or capacity. However, they do not offer

I-V information and can provide highly inaccurate results when working conditions change.

- **Electrically:** electrical equivalent models based on a combination of electrical passive element. This method is the most appealing due to its intuitiveness and computational burden. They are less accurate than electrochemical models, but more precise than the mathematical ones.

Several electric equivalent-circuits have been proposed in the literature to model the electrical behavior of batteries, including Thévenin [60,93,93,119–121], RC [60, 120, 122], and Randles (impedance-based) [61, 66, 91, 119, 120, 123–126] models. These models are simpler (i.e. with lower computational burden) alternatives to chemical and mathematical models often based on partial differential equations [124, 127, 128]. In general, the parameters in equivalent-circuit models may vary with aging or operating conditions, so impedance must be obtained for different setpoints (SOC, temperature...) to get a complete and good parametrization [124].

2.2.7.1 Thèvenin electric model

This model consists of a voltage source in series with a resistor and an RC branch in parallel. It models the charging and discharging behavior of a battery with simple electric elements as shown in Fig. 2.24a. In this figure, each element represents an electrochemical aspect of the battery [93, 119]:

- $\boldsymbol{C_{SOC}}$: Models the battery capacity. Its voltage represents the battery OCV. It can also be represented by a DC voltage source.
- $\mathbf{R_i}$**:** the cell IR. It accounts for the resistance of the contacts, terminals, collectors, electrodes and electrolyte.
- $\mathbf{R_d}$ **and** $\mathbf{C_d}$**:** they model the battery transient response, resulting from the effect of diffusion and charge transportation, in addition to the double-layer capacitance existing between the electrolyte and the active materials [60, 93].

The circuit parameters can be obtained from the voltage response of the battery to a current step [121] (see Fig. 2.24b).

The transfer function of this model is shown in (2.1).

$$G(s) = \frac{V_{bat}(s)}{I_{bat}(s)} = R_i + \frac{R_d}{1 + R_d C_d s} + \frac{1}{s} C_{SOC} \tag{2.1}$$

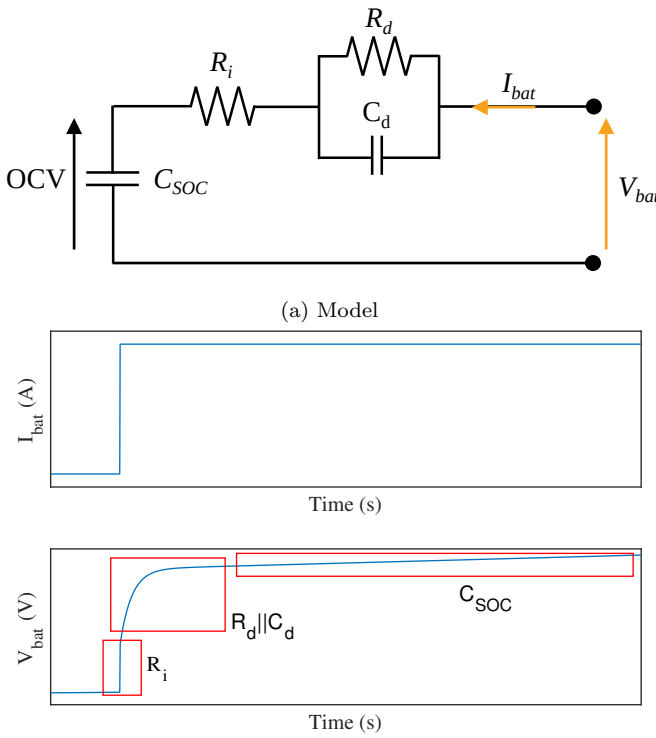

(a) Model

(b) Response of a battery to a current step.

Figure 2.24: Thèvenin equivalent model of a battery.

All the terms on the right hand side of the equation can be related to a region in Fig. 2.24b:

- **First term (R_i):** corresponds to the IR, R_i, and is obtained from the initial response to the current step.
- **Second term ($\frac{R_d}{1+R_dC_ds}$):** corresponds to the dynamic RC circuit, a first-order system corresponding to the exponential part of the voltage variation.
- **Third term ($\frac{1}{s}C_{SOC}$):** corresponds to C_{SOC}, a pole at the origin, which accounts for the continuously increasing slope in the voltage in Fig. 2.24b due to a constant current.

2.2.7.2 RC model

This model consists of a voltage source in series with a resistor and several RC branches in parallel, as shown in Fig. 2.25, where the voltage source is the OCV; Rs represents the internal resistance; and the parallel branches (i.e. R1||C1, R2||C2, R3||C3) model battery dynamics [120]. This model can be seen as an extension/improvement of the Thèvenin model. The number of parallel branches increases the accuracy but also the complexity of the model.

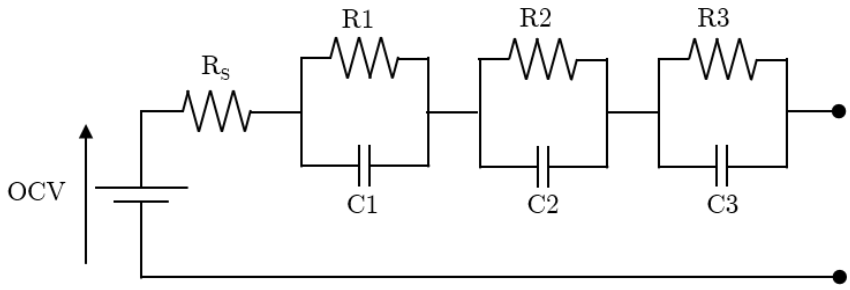

Figure 2.25: Battery model using a third-order RC circuit.

2.2.7.3 Randles model

A widely extended methodology for battery characterization is the Electrochemical Impedance Spectroscopy (EIS). EIS-meters apply a sinusoidal AC voltage to the battery; the impedance at different frequencies is obtained from the applied voltage and the resulting current, as seen in Fig. 2.26 [61, 125, 129, 130].

Fig. 2.27a shows the EIS results (polar plot) for one sample of the $LiFePO_4$ batteries used in this work (see Fig. 2.8 and Section 2.2.4). The real axis represents the resistance while the imaginary axis represents the reactance. Each point in the graph corresponds to the impedance at a different frequency; the frequency increases from right to left in the capacitive region, and opposite in the inductive region, as indicated in the figure.

The impedance values obtained by the EIS analysis are used to obtain the Randles model [66, 91, 123] equivalent circuit (Fig. 2.27b). Each range of frequencies is dominated by different phenomena in the battery [91, 131], i.e. each components in the equivalent circuit represent a physical phenomenon in the cell [126]:

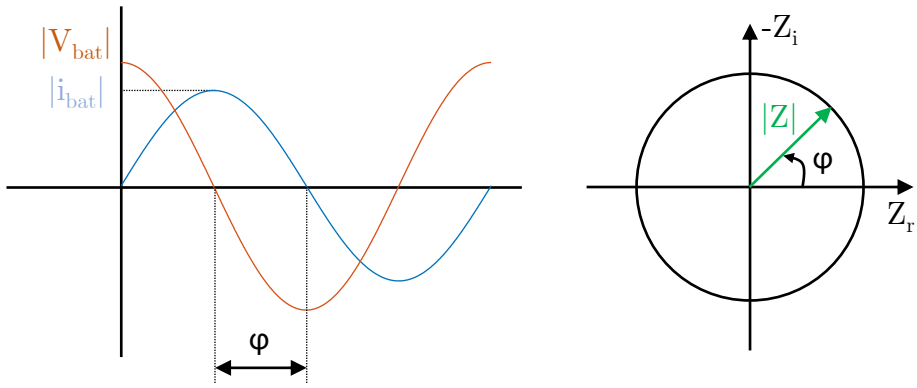

Figure 2.26: Principle of the EIS.

- **Low frequency range:** used to obtain $\mathbf{Z}_W$, which represents the Warburg impedance and accounts for the diffusion phenomena and cathode resistance.
- **Middle frequency range:** dominated by the parallel RC branch dynamics (in some cases, more than one parallel RC branch is used to accurately describe the battery behavior), which corresponds to the electrolyte and SEI resistance on the anode:
  - ◇ **C**: represents the double-layer capacitance at the cathode/electrolyte and lithium/electrolyte interface.
  - ◇ **R**: charge transfer resistance (transfer of Li+ ions between electrode and electrolyte)
  - ◇ $\boldsymbol{R_i}$: resistance of the electrolyte and collector when the battery impedance changes from capacitive to inductive, which corresponds to the intercept frequency [132].
- **High-frequency range:** inductive behavior, which represents the battery collectors and leads. It is sometimes represented by a pure inductor in the Randles model, but is normally neglected [66].

Although its use is normally restricted to static analysis [129], EIS analysis can also be used for transient impedance estimation during battery charging/discharging [60].

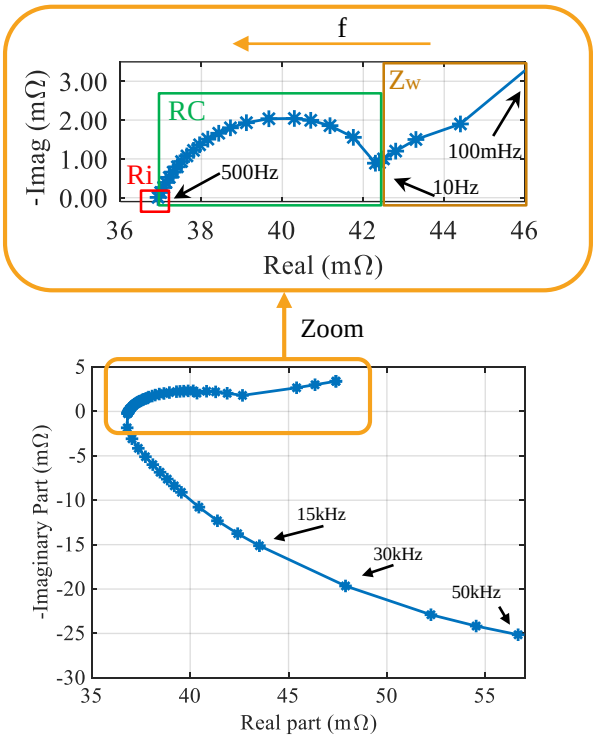

(a) EIS analysis with a closed detail from the capacitive part.

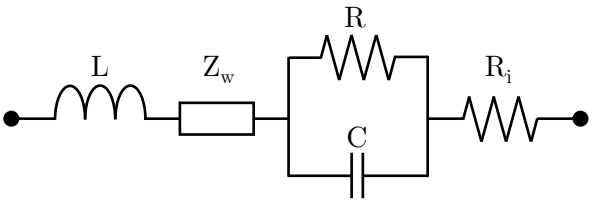

(b) Randles equivalent model derived from the EIS analysis.

Figure 2.27: EIS analysis with a closed detail from the capacitive part and Randles equivalent model derived from the EIS analysis.

2.2.8 Temperature and LIBs

As explained in Section 2.2.3, LIBs are very sensitive to temperature variations, due to the chemistry and the different elements forming the cell.

2.2.8.1 Temperature effects on LIBs

The OCV, capacity and internal resistance of a LIB have been reported to be affected by temperature variations [62, 107, 133, 134]. Furthermore, operating temperature limits can be different during charging and discharging processes [135]. While higher battery temperature may temporarily increase its capacity, it also increases the internal resistance in the long term, due to premature aging. This increases the losses and the risk of thermal runaways, fires, and explosions [37, 68, 91, 131, 136]. Over 80°C, thermal runaway can occur spontaneously due to the exothermic reactions taking place between electrolyte, anode, and cathode, which can cause the decomposition of the SEI, electrolyte and/or electrodes (see Section 2.2.3) [37, 91]. This temperature may vary depending on the battery constructive elements, as the electrolyte solvents [131]. On the other hand, lower temperatures result in a reduction of the power and energy capabilities as the diffusion of the lithium in the electrolyte is reduced [136,137]. A $LiFePO_4$ battery as the one in [135] can operate between -20°C and 60°C while discharging, but only from -10°C to 45°C while charging. These numbers are far more restrictive than other elements in the system. For example, a typical encapsulated power converter as the one shown in Appendix A, can correctly operate between -20 and 150°C [138]. It is concluded from the previous discussion that LIB temperature monitoring is of great importance, which explains the proliferation of temperature measurement [33, 62, 136] and estimation [91, 95, 129, 131, 132, 139–144] methods during the last decade.

LIB temperatures are often described following the Arrhenius Equation [70, 131]. This equation, considered as one of the greatest advancements in chemical kinetics, is capable of modeling most chemical reaction over large temperature ranges [145]

$$k_A(T) = Ae^{\frac{-E}{RT}} \tag{2.2}$$

where:

- $\boldsymbol{k_A}$: Specific reaction rate, independent of the concentrations of the species involved in the reaction. It is normally asummed to depend only on the temperature.
- **A**: pre-exponential factor or frequency factor.
- **E**: Activation energy, must be determined experimentally by measuring the reaction rate at several different temperatures.

- **R**: gas constant (8.314 J/molK).
- **T**: absolute temperature (K).

LIB temperature can be directly measured using temperature sensors [139], as RTD (Resistance Temperature Detector) [95], like a PT100 [33], or thermocouples [129, 136, 140]. While the sensors themselves can be cheap, their installation and the subsequent cabling, signal conditioning and acquisition, add cost and complexity and can compromise the system reliability as there are more elements susceptible to failure [91]. In addition, determining the number and location of the sensors to trade-off accuracy, cost, and complexity, is not straightforward. Moreover, sensors can suffer from heat transfer delays [95,132]. Alternatively, LIB temperature can be estimated. There are several methods to estimate battery temperature:

- **Thermal models:** these models [139] require a good knowledge of the cell, as heat generation and cell thermal properties, and they are normally used together with surface mounted temperature sensors. The dynamics of this kind of methods are slow and sometimes they cannot accurately track thermal runaways. This can be partly solved by inserting micro-temperature sensors into the cell, which increases complexity and cost and leads to the same problems that were explained before regarding temperature sensors.

- **Battery parameters:** they rely on the relationship between the battery impedance and its temperature [91, 95, 129, 131, 132, 139–144]. The battery impedance is typically estimated by injecting sinusoidal currents, which are preferably injected when the battery is at rest to improve the accuracy; however, this limits the applicability of the method; as an alternative, methods based on the impedance estimation while the battery is at use has been recently proposed [146].

The three different methods to get the cell temperature are compared in Table 2.7.

2.2.8.2 Temperature estimation of LIBs

This section reviews existing LIB temperature estimation methods based on impedance:

Table 2.7: Methods to Know the Cell Temperature

Method	Accuracy	Complexity	Sensors	Knowledge of the cell	Dynamics
Measure	✓	✓	Yes	No	✓✗
Thermal models	✓	✗	Yes	Yes	✗
Cell parameters	✓✗	✓	No [1]	Yes [2]	✓

[1] Added in some methods to complement the estimation.
[2] Some methods require a pre-commissioning process to tune some parameters.

- In [131] and [141] phase shift between applied sinusoidal current and the resulting voltage at 40 Hz was presented as a reliable metric of internal mean cell temperature for $LiFePO_4$ and $LiCoO_2$, which follows an Arrhenius fit (2.2). The frequency selected is chosen because that is the frequency of dominance of the SEI while not being affected by SOC (see Section 2.2.7.3). Lower frequencies would be affected by the charge transfer process, which is highly dependent on SOC. This method was further analyzed in [142] for a $LiCoO_2$ cell with temperature gradient. It concludes that SOC affects low-frequency impedance. Impedance measurement was performed at higher frequencies, i.e. 10.3 kHz, to further avoid SOC influence. Nevertheless, they included SOC correction to improve the estimation accuracy.

- In [139], a combination of impedance estimation based on voltage and current measurements and surface cell temperature measurements was presented to estimate the internal temperature in cylindrical $LiFePO_4$ batteries. The battery was excited with a current at 215 Hz to obtain the real part of the impedance, which shows an Arrhenius (2.2) dependency with temperature. The selected frequency was shown (see also [131, 141]) to be high enough to be SOC independent; but not so high that the relationship between impedance and temperature becomes too low (as stated also in [142]). This method improves the estimation when compared to methods that use sensors combined with thermal models, but still the need of mounting a sensor in each cell, which is not a desired feature for a low-cost BMS. Due to this, the method was improved in [144] by avoiding cell temperature measurements. Impedance estimation at 215 Hz and an extended Kalman filter (EKF) using a parameterized thermal model with a polyno-

mial approximation were combined instead. These combination solves the problem of low dynamics in methods using thermal models and allows a multi-point temperature estimation. However, a calibration measurement must be still carried out with the battery at rest.

- In [129] frequency selection to minimize the interference of SOC and SOH for LIBs was analyzed. The mean temperature of a lithium-ion battery is estimated by analyzing the impedance phase and magnitude change with temperature, which also follows an Arrhenius relationship, decreasing the impedance as the temperature increases, due to the increase in the electrochemical reaction rate. Depending on the temperature, the frequency range used to estimate the temperature without being influenced by the SOC changes. The lowest frequency that can be used is almost independent of temperature. The highest frequency significantly changes with temperature; especially challenging is the operation at low temperatures (-10°C). This study also concludes that SOH has almost no effect on the phase angle of the battery impedance, despite highly affecting the impedance magnitude. The conclusion regarding frequency range selection for temperature estimation (1-100 Hz) slightly differs from those in [139], a potential reason being the differences in LIB technologies used in each study. This study was further extended in [140] measuring phase shift at 10 Hz. They add a thermocouple to the battery to improve the temperature estimation in a similar way as in [142] and with the same drawbacks.

- In [132], the Zero-Intercept Frequency (ZIF), which is the frequency at which the impedance seen in the EIS plot crosses the real axis, was shown to be dependent solely on the cell temperature for a $LiNiCoAlO_2$ and a $LiFePO_4$ cell. ZIF is not being affected by SOC, aging or heat transfer delays, because it is far enough from the frequencies at which electrochemical reactions take place. For $LiNiCoAlO_2$, the ZIF is between 300 and 1700 Hz, while for $LiFePO_4$ is higher and is between 500 and 6000 Hz, depending on the temperature and decreasing as the temperature increases, following an Arrhenius-like behavior. This work was further developed in [143], where a so-called Non-Zero Intercept Frequency (NZIF), a frequency in which the imaginary part of the impedance is equal to a non-zero constant, is used to estimate battery temperature. The constant is selected depending on the application and allows the selection of a range of frequencies that is not affected by disturbing frequencies that can interfere with the injected frequencies. Resulting estimations are shown to be better than in [140]

because of its higher signal-to-noise ratio. The main drawback of these methods is the need to scan a given frequency range to find the frequency of interest.

- [95] also analyzes the ZIF for Li_2TiO_3 cells, been between 16.74 Hz and 264.62 Hz and decreasing as the temperature increases, but also affected but SOC in a non-linear way, contrary to what happened to $LiNiCoAlO_2$ and $LiFePO_4$ in [132]. Due to this, the phase shift between voltage and current for temperature estimation was used instead (as in [131, 131, 142]), because it is faster than searching for the ZIF. The method includes SOC correction for more precise estimation, since at the frequency of interest it is seen to decreases with decreasing phase shift. Injection of the signal is done at 1 kHz, above the ZIF. Contrary to the rest of the results presented in this review, the real part of the impedance increases almost linearly with temperature. This is related to the region of operation of the battery, as will be demonstrated in the following chapters.

- In [91], a frequency of 300 Hz is used. At this frequency, a strong temperature dependency was found in the battery impedance with a low dependence from the SOC (see also [131, 139, 141]) for $LiCoO_2$ cells. The Arrhenius model is reported to fail to correctly estimating temperatures above 68°C; additional models are, therefore, proposed for higher temperatures that are able to estimate temperature accurately up to 95°C.

The above-described methods estimate temperature based on impedance, using the EIS technique at a single frequency point. In general, they eliminate the requirements of using temperature sensors (although some of them include them to increase the accuracy) and the knowledge of cell thermal parameters. However, they need to inject the signal at the desired frequency and the majority works with the battery at rest. A summary of the methods is provided in table 2.8.

2.3 Conclusions

Batteries are one of the best options among ESS when combined with RES for medium power storage applications, as buildings or EVs. $LiFePO_4$ batteries are a good battery choice in terms of safety, low toxicity, life cycles, reliability and cost, even though they have lower cell voltage compared to other LIBs technologies and lower specific energy.

Table 2.8: Temperature Estimation Methods Based on Impedance

	Metric	Frequency	Cell Type (shape)	Temperature range
[131]	Phase shift	40 - 100 Hz	$LiCoO_2$ (unknown) and $LiFePO_4$ (cylindrical)	-20 - 60
[141]	Phase shift	40 - 100 Hz	$LiCoO_2$ (unknown)	-10 - 50
[142]	Phase shift	10.3 kHz	$LiCoO_2$ (pouch)	0 - 25
[139]	Real part + temperature sensor	215 Hz (>100 Hz)	$LiFePO_4$ (cylindrical)	0 - 40
[144]	Real part + thermal model	215 Hz (>100 Hz)	$LiFePO_4$ (cylindrical)	0 - 40
[129]	Phase shift or magnitude	Variable (1 - 100 Hz)	$LiFePO_4$ (pouch)	-20 - 50
[140]	Phase shift	10 Hz	$LiFePO_4$ (pouch)	-20 - 20
[132]	ZIF (phase shift related)	Variable (ZIF)	$LiFePO_4$ (cylindrical) and $LiNiCoAlO_2$ (cylindrical)	-20 - 50
[143]	NZIF (phase shift related)	Variable (NZIF)	$LiFePO_4$	-20 - 50
[95]	Phase shift	1 kHz	Li_2TiO_3 (unknown)	0 - 40
[91]	Imaginary impedance	300 Hz	$LiCoO_2$ (cylindrical)	-20 - 95

There are two types of power converters that batteries are generally connected to, DC/DC converters and equalizers. DC/DC converters are needed to meet required DC voltage levels and enhance controllability. Equalizers are important to keep the voltage of each cell in the recommended range while maximizing the energy utilization. From the different existing equalizers, SCEs are a good choice for batteries equalization due to their easy controllability and low prices. In the following two chapters, two different methods to estimate cell temperature are proposed using each of one of these power converters. Both methods use the signals naturally present in the converters to estimate internal resistance, which is then used to estimate temperature. These two methods are not mutually exclusive, and could be used in combination (see Fig. 2.28) to improve the accuracy or when both of the converters cannot work at the same time, e.g. if the cells are equalized and the SCE is not working or when the DC/DC converter is working and the cells are equalized.

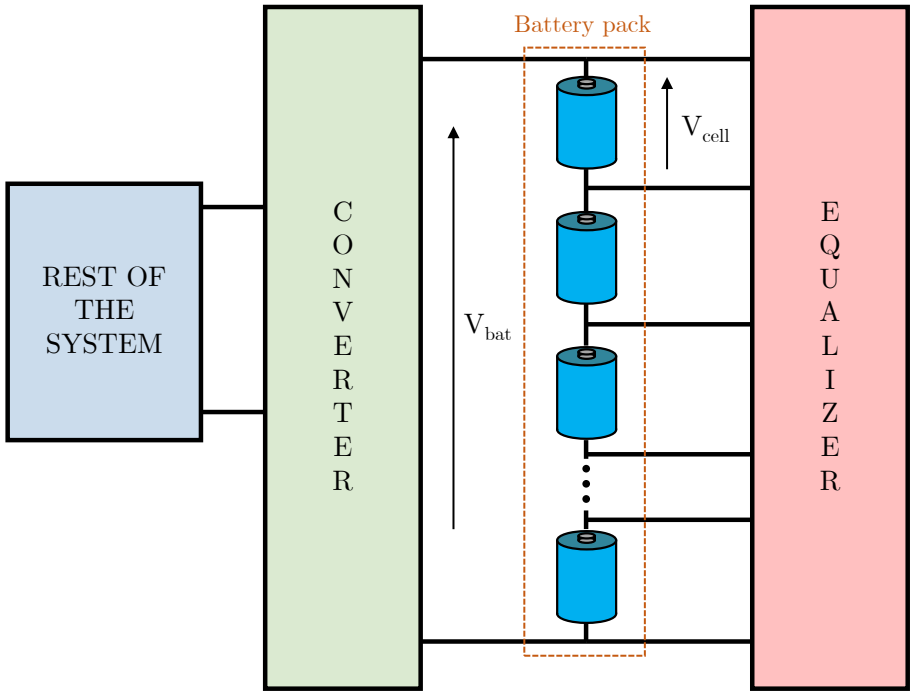

Figure 2.28: Battery pack connected to an equalizer and through a converter to the rest of the system.

LIBs in general are sensitive to temperature, and there should always be a BMS monitoring its temperature to avoid undesired behaviors, as low performance or explosions. Due to this, in Chapters 3 and 4 thermal monitoring of batteries is studied. Single $LiFePO_4$ cells are connected to a switching power converter and SCE, and methods to estimate its temperature are proposed.

Chapter 3

Thermal monitoring using switching harmonics

3.1 Introduction

Thermal monitoring is of high relevance for safe operation and degradation management of batteries. Direct measurement of battery temperature has drawbacks due to both cost and reliability issues (see Section 2.2.8.1). To overcome these limitations, the development of temperature estimation methods has received significant research attention. Most of the existing estimation methods are based on the injection of an additional signal, which can produce additional losses.

This chapter proposes a temperature estimation method for $LiFePO_4$ batteries using the switching harmonics naturally produced by the the power converter feeding the battery [147]. The inherent switching harmonics of the power converter will allow the estimation of the battery impedance, see Fig. 2.27a, the battery temperature will be estimated from the variation of the estimated battery impedance. The method operates online and without interfering with the normal operation of battery and power converter, and does not introduce therefore additional losses or any other adverse effect in the batteries.

The chapter is organized as follows: the variation of battery voltage with SOC and the consequent need for a converter is studied in Section 3.2; the proposed

battery temperature estimation method using switching harmonics is presented in Section 3.3; implementation issues are discussed in Section 3.4; experimental results are shown in Section 3.5; conclusions are finally presented in Section 3.6.

3.2 Battery control using electronic power converters

It was already explained in Section 2.2.5 that a lot of battery systems include a switching power converter. In any of the cases presented, the converter will generate switching harmonics, which will affect the voltage and current waveform in the battery. The effect of switching harmonics in the batteries is still an open topic for intense research efforts, and limited information is available [148, 149]. In this thesis, the bidirectional boost converter shown in Fig. 3.1 is used. It is intended to be an scaled version without interleaving of the real DC/DC converter that is a part of the power converter in the smart building, which is explained is Section 7.2. Table 3.1 shows the test setup parameters. Battery parameters can be found in table 2.4.

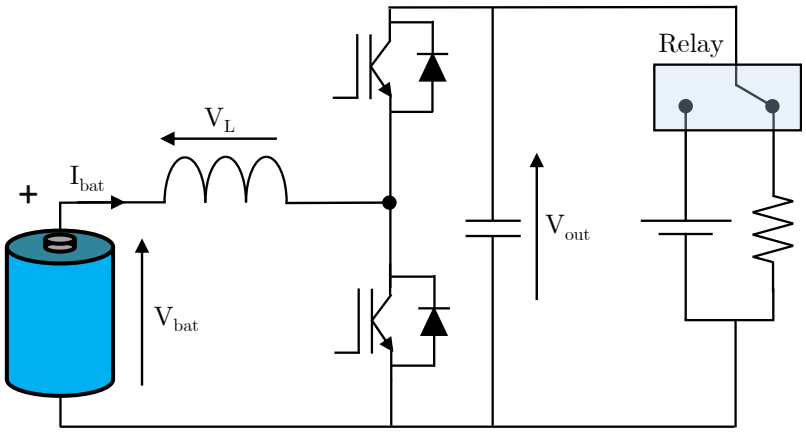

Figure 3.1: Boost converter scheme used to charge and discharge the battery.

The current control loop block diagram of the bidirectional boost converter is shown in Fig. 3.2, where:

- $\boldsymbol{I}^{*}_{\mathbf{bat}}$: current command
- $\boldsymbol{I}_{\mathbf{bat}}$: battery current

Table 3.1: Bidirectional Boost Converter Characteristic Parameters

Switching frequency	15 kHz
Converter inductor	478 µH
MOSFETs nominal voltage	75V
MOSFETs nominal current	56A

- ε_i: current error signal
- V_{bat}: battery voltage
- V_{out}: power converter output voltage
- V_L: voltage across the inductor
- **d**: top switch duty cycle
- **G(s)**: plant model, i.e. the battery and converter filter

A Proportional-Integral (PI) controller is used to track the battery current command.

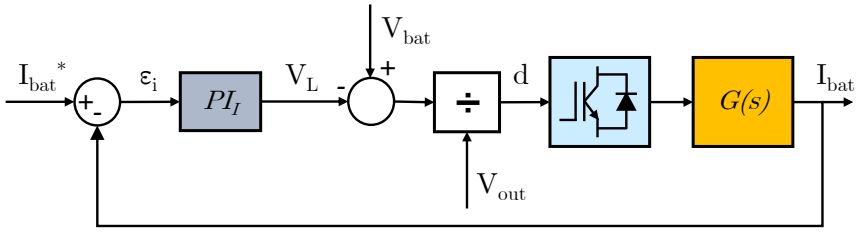

Figure 3.2: Battery current controller.

3.3 Battery temperature estimation using switching harmonics

This section will present the proposed battery temperature estimation method using switching harmonics. The switching frequency is set depending on the application and power switch technology, e.g. MOSFET/IGBT, Silicon/Silicon Carbide/Gallium Nitride... Fig. 3.3 and Fig. 3.4 show discharging waveforms of the battery current and voltage, respectively, as seen in Fig. 3.1, and the

corresponding frequency spectrum when the battery current command is 2.6 A (discharging current). In addition to the DC component, harmonics at integer multiples of the switching frequency are readily visible in the frequency spectrum.

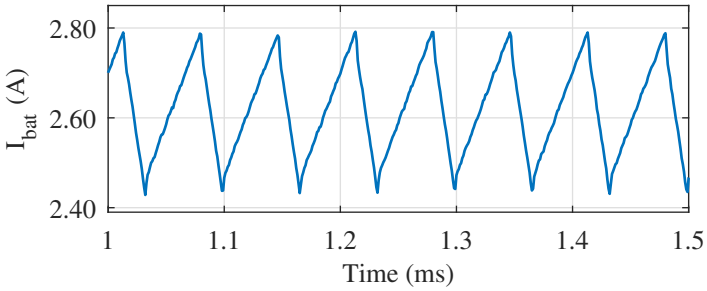

(a) Battery current, I_{bat}.

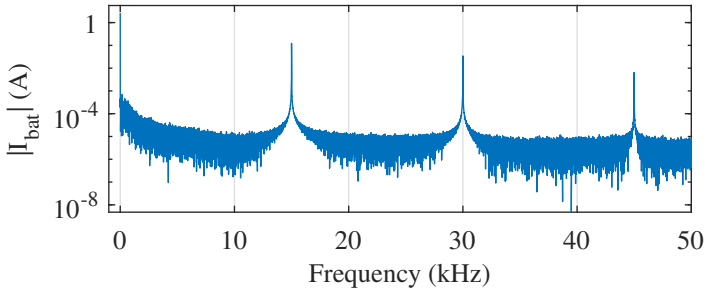

(b) FFT of I_{bat}.

Figure 3.3: Battery current. Battery discharging @ 20°C.

Battery current and voltage can be expressed as:

$$I_{\text{bat}} = I_{\text{DC}} + \sum_{h=1}^{h=\infty} I_h sin(h \cdot 2\pi f_{\text{sw}} t + \varphi_{I_h}) \tag{3.1}$$

$$V_{\text{bat}} = V_{\text{DC}} + \sum_{h=1}^{h=\infty} V_h sin(h \cdot 2\pi f_{\text{sw}} t + \varphi_{V_h}) \tag{3.2}$$

where:

- $\boldsymbol{I_{DC}}$: battery DC current.
- $\boldsymbol{V_{DC}}$: battery DC voltage.
- $\boldsymbol{I_h}$: magnitude of the hth switching harmonic of the current.
- $\boldsymbol{V_h}$: magnitude of the hth switching harmonic of the voltage.

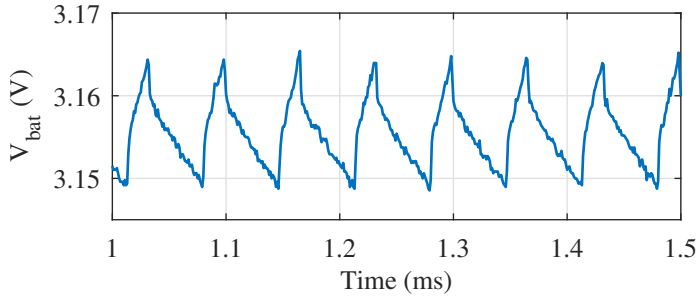

(a) Battery voltage, V_{bat}.

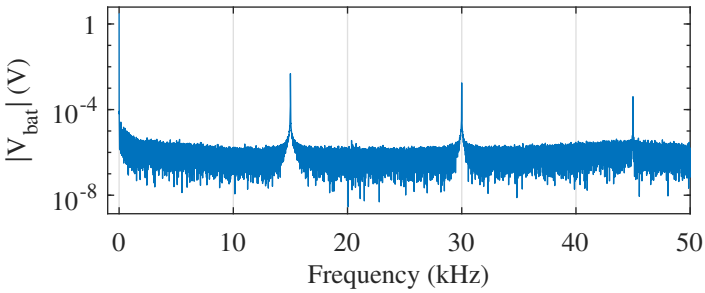

(b) FFT of V_{bat}.

Figure 3.4: Battery voltage. Battery discharging @ 20°C.

- $\boldsymbol{\varphi_{V_h}}$: phase angle of the voltage hth harmonic.
- $\boldsymbol{\varphi_{I_h}}$: phase angle of the current hth harmonic.

The battery impedance at each frequency can be obtained from any of the harmonic components of the voltage and current:

$$Z_{\text{bath}} = \frac{V_h \lfloor \varphi_{V_h}}{I_h \lfloor \varphi_{I_h}} = R_{\text{bath}} + jX_{\text{bath}} \tag{3.3}$$

where R_{bath} and X_{bath} are the battery resistance and reactance at the frequency of the hth harmonic component.

Resistance value at any frequency can be modeled to be a linear function of the battery temperature:

$$R_{\text{bat}} = R_{\text{bath0}} \left(1 + \alpha_{\text{bat}} \left(T_{\text{bat}} - T_0\right)\right) \tag{3.4}$$

where:

- $\boldsymbol{T_0}$: room temperature.

- $\boldsymbol{R_{bath0}}$: battery resistance at the frequency of the hth harmonic component at T_0.
- $\boldsymbol{T_{bat}}$: current battery temperature.
- $\boldsymbol{\alpha_{bat}}$: temperature coefficient.

R_{bath0} and α_{bat} can be measured during a commissioning process. The battery temperature is finally estimated as:

$$T_{bat} = \frac{R_{bath} - R_{bath0}}{R_{bath0} \cdot \alpha_{bat}} + T_0 \tag{3.5}$$

In this thesis, the fundamental component is used to estimate temperature, but other harmonics could be potentially used if necessary, e.g. in case the fundamental switching frequency is not in the inductive region of the battery. The only limitation is the resolution of the Analog-to-Digital Converter (ADC), as will be seen in Section 3.4. The signal processing block diagram for temperature estimation is shown in Fig. 3.5. The inputs are the battery current and voltage, both containing the DC fundamental component and the switching harmonics. Two bandpass filters (BPF) are used to isolate the harmonic component at the switching frequency of each signal. These BPFs are adjusted to the frequency of interest, in this case the fundamental component. The battery high-frequency impedance (Z_{bath}) is obtained from eq. 3.3. The battery high-frequency resistance (R_{bath}) is obtained as the real part of the resulting impedance, and the estimated battery temperature ($\widehat{T_{bat}}$) is finally obtained using eq. 3.5.

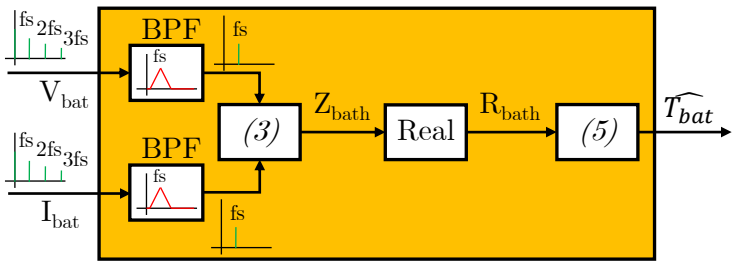

Figure 3.5: Signal processing for battery temperature estimation.

Generally speaking, all methods reviewed in Section 2.2.8.2 ([91,129,131,132, 139–144]) show that resistance of the battery decreases as temperature increases. This is explained since the frequencies used to excite the battery in [91, 95, 129, 131, 132, 139–144] are low frequencies in which the effect of the solid electrolyte

interface (SEI) [70] and the diffusion processes dominate the battery dynamics in the capacitive region [123]. On the contrary, the switching frequency of power converters are typically in the range of tens/hundreds of kHz; 15 kHz will be used in this case, meaning that the battery is in the inductive region as seen in the EIS in Fig. 2.27a. This means that the high-frequency battery impedance is not expected to follow an Arrhenius-like behavior [70] but linear due to the higher impact of the battery collectors and leads on the overall battery impedance in this frequency range [131]. This effect can be seen in Fig. 3.6, which shows the variation of the internal resistance of the test battery with temperature for two different frequencies: 8 Hz (Fig. 3.6a) and 15 kHz (Fig. 3.6b). At 8 Hz, the internal resistance decreases with temperature, as expected [136, 142], but at 15 kHz increases.

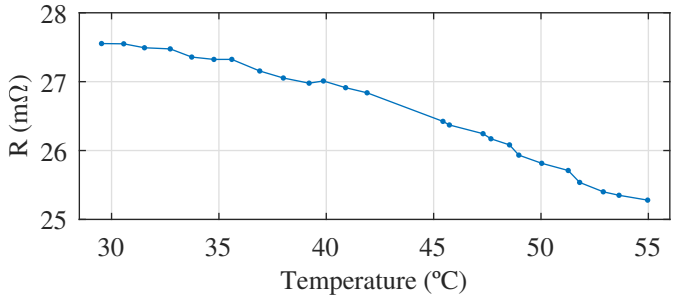

(a) 8 Hz frequency.

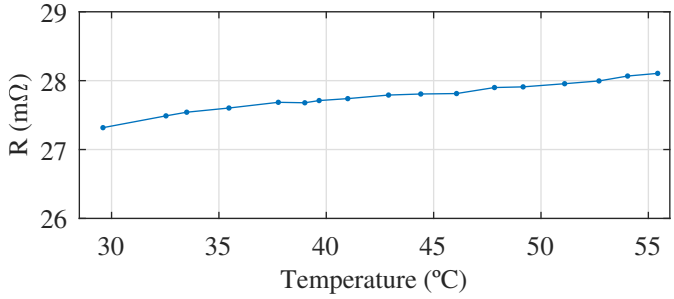

(b) 15 kHz frequency.

Figure 3.6: Evolution of the battery resistance with temperature applying sinusoidal waveforms (EIS) to the battery at no load.

It is noted that the proposed method can be used with any switching frequency, as long as the battery is in the inductive region. In addition, enough spectral separation between the fundamental and the switching components must

exist in order to properly filter the desired component (see Fig. 3.5). The range in which the method is valid may vary with the battery type and physical construction. As examples, the batteries used in this work show an inductive behavior from 500 Hz (see Fig. 2.27), while 1.1 kHz is reported in [124].

3.4 Implementation issues: ADC resolution

Voltage switching harmonic components are significantly smaller than the fundamental component; bit resolution of the data acquisition system is, therefore, a critical implementation issue for the battery characterization. Experimental results shown in Fig. 3.3 and Fig. 3.4 were obtained using a 16-bit resolution data acquisition system. Fig. 3.7 and Fig. 3.8 show the same results using both 16-bit (1 MHz sampling frequency) and 8-bit (4 MHz sampling frequency) resolution. These two resolution levels were selected to show the differences between a low- and a high-resolution data acquisition system. It can be observed in Fig. 3.8 that there is a remarkable difference in the voltage waveform between both cases. It is clearly observed that 8-bit resolution does not provide accurate voltage measurement. The experiments in these figures were carried out at 2.6 A of DC discharging current. As it will be demonstrated in Section 3.5.1, there is almost no change in the amplitude of the peak to peak variation of the current with DC current level, so these results are representative for all DC current levels.

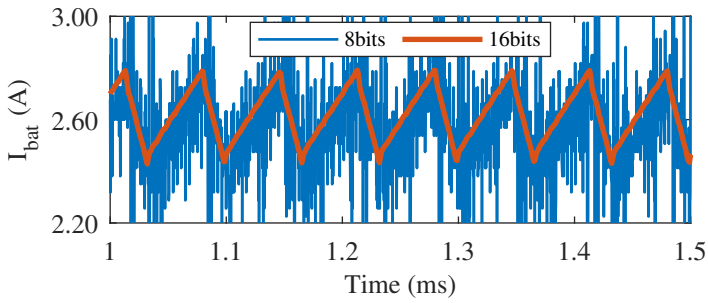

Figure 3.7: Battery current I_{bat}, when measured with an 8 and a 16 bits data acquisition system.

Fig. 3.9 shows the ideal transfer function of an analog to digital converter (solid black).

The Least Significant Bit (LSB) is the result of dividing the Full-Scale Range

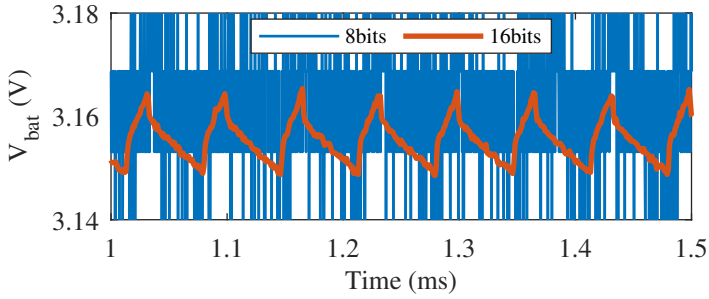

Figure 3.8: Battery voltage, V_{bat}, when measured with an 8 and a 16 bits data acquisition system.

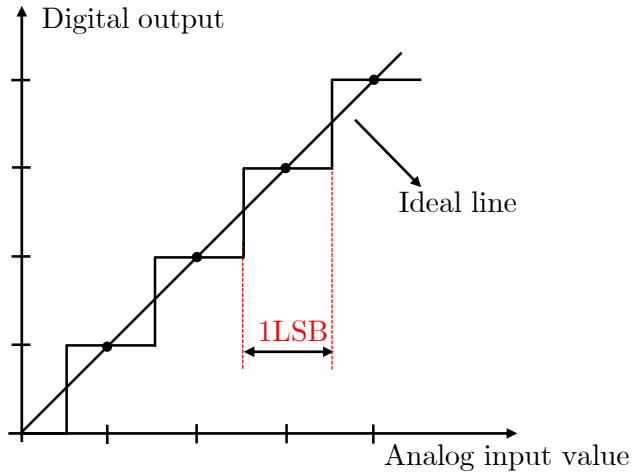

Figure 3.9: Ideal transfer function of an ADC.

(FSR) of the acquisition system by the number of discrete values obtained with N bits:

$$LSB = \frac{FSR}{2^N} \tag{3.6}$$

From Fig. 3.8 it is clear that the maximum quantization error (ε_{aa}) is half the LSB (3.7) [150]; the relative error (ε_{ar}) being, therefore, the quantization error

divided by the amplitude of the signal (M) being measured according to (3.8).

$$\varepsilon_{aa} = \frac{LSB}{2} \tag{3.7}$$

$$\varepsilon_{ar} = \frac{\varepsilon_{aa}}{M} \cdot 100 = \frac{LSB}{2M} \tag{3.8}$$

Experimental results in Fig. 3.8 are captured with 5 V FSR, so applying (3.6) the LSB for the 8-bit case corresponds to 19.53 mV, which is larger than the peak-to-peak amplitude of the triangular waveform in Fig. 3.4a (14.6 mV); for the 16-bit case, the LSB corresponds to 0.076 mV. This means it will be difficult to measure the voltage with the 8-bit ADC.

Fig. 3.10a shows the battery voltage for both the 8-bit and 16-bit case after it has been filtered with a 15 kHz first-order bandpass filter (as a part of the signal processing shown in Fig. 3.5). As it can be seen, the high value of the LSB in the 8-bit case results in an inaccurate and oscillating measurement, while with 16 bits the peak value of the sinusoidal is steady. For clarification, Fig. 3.10b shows a shorter interval from Fig. 3.10a, where the peak oscillation in case of 8 bits is clearly noticed.

Fig. 3.11a shows the relative measurement error [eq. (3.8)] in the battery current and voltage for different bit resolutions of the data acquisition system, assuming a voltage level as in Fig. 3.4a. It is observed that for an 8-bit resolution, the voltage error is ≈ 67 %, while for 16-bit resolution is ≈ 0.02 %. For the case of the current, the peak-to-peak value at the switching frequency, Fig. 3.3a, is higher compared to the DC component, so it is not as critical as the voltage, resulting therefore in a smaller error for the same bit resolution (e.g. error with 8-bit resolution for the current is ≈ 5.5 %, while for the voltage is ≈ 66 %). Fig.3.11b shows the relative temperature estimation error vs. the bit resolution of the data acquisition system. It can be observed that a bit resolution greater than 8 bit results in a small relative error, <3 %. This is the maximum propagation error of the real part in eq. (3.3), provided that there is no phase estimation error. Therefore, ADC resolutions commonly found in cost-effective microcontrollers can be employed for this application.

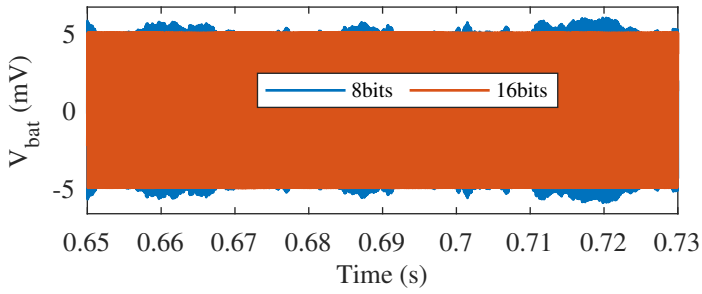

(a) Filtered voltage in the battery with a BPF at 15 kHz.

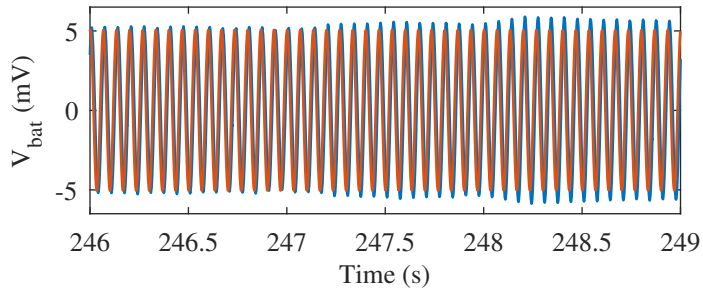

(b) Short interval from (a).

Figure 3.10: Filtered voltage in the battery with a BPF at 15 kHz.

3.5 Experimental results

Fig. 3.12 shows a picture of the power converter in Fig. 3.1. The battery terminal voltage and current are measured using a 16-bit data acquisition system. According to Section 3.4, any acquisition system with resolutions higher than 8-bit could be used. $LiFePO_4$ battery and IRFU3607 MOSFETs [151] rated parameters are shown in Table 3.1. Actual battery temperature is measured with an LM35 temperature sensor [152], placed in direct contact with the middle of the battery's surface.

Some geometries of batteries, as pouch cells, have a temperature gradient during normal battery operation [153], which results in higher temperatures in the collectors. However, this is not the case of the batteries under test (i.e. cylindrical batteries), see Fig. 3.13, which is also in good agreement with [96]. Fig. 3.14 is also included to show the battery at a different temperature. This is explained by the construction of the cell, in which the anode and the cathode are rolled up together with a separator on the middle [154]. In batteries where a temperature gradient exists during normal battery operation, the method still can

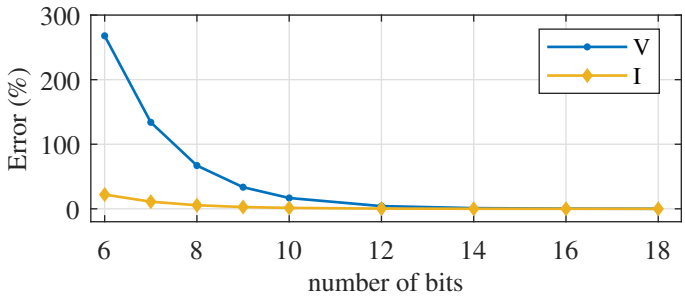

(a) Battery current and voltage magnitude.

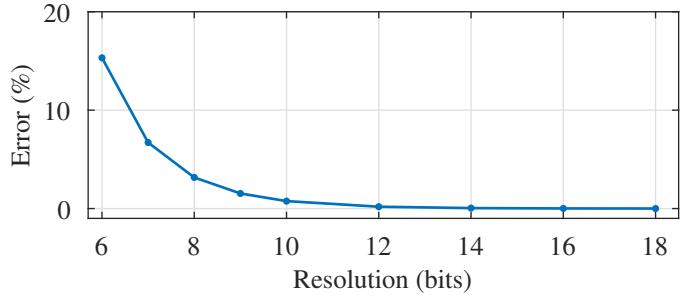

(b) Battery temperature estimation.

Figure 3.11: Relative measurement error at the switching frequency as a function of the bit resolution of the data acquisition system.

be applied provided that during the commissioning process to estimate α_{bat}, the sensor is in contact with the collector (hottest point), meaning that the estimated temperature will be always the highest one.

3.5.1 Resistance variation with SOC

Fig. 3.15 shows the estimated battery resistance at 15 kHz (switching frequency) vs. discharging DC current for different SOCs and for two $LiFePO_4$ battery samples, B1 and B2, respectively. The battery temperature is kept constant during these experiments. Battery internal resistance at 15 kHz is shown to vary less than 1.7 % when the discharging current changes from 0.6 A (0.15C) to 5.6 A (1.75C). The variation rate of the battery internal resistance with the discharging current is approximately 0.08 mΩ/A, and almost independent of the SOC. Fig. 3.16 shows the variation of the battery internal resistance with the SOC at 1C discharging rate. It is observed that the battery internal resistance is

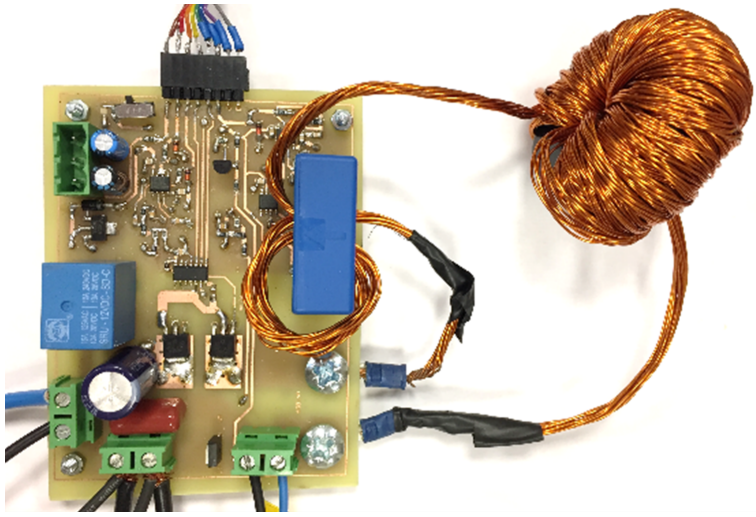

Figure 3.12: Power converter prototype.

almost independent of the SOC at the switching frequency (15 kHz).

3.5.2 Resistance and reactance variation with temperature

Fig. 3.17 shows the battery resistance and reactance at the switching frequency vs. the battery temperature for cell B1 in Fig. 3.15a. The battery temperature was initially heated up to 70°C; the battery impedance is measured while the battery cools down at room temperature. The converter is only operated for measurement in short periods to avoid battery discharge before the room temperature has been achieved. Resistance is seen to increase almost linearly with temperature, while the reactance variation does not show a clear trend.

As expected from Fig. 3.6, the resistance increases with temperature, since the switching frequency (15 kHz) is high enough for the battery to be in the inductive region (see Fig. 2.27a), the battery resistance is dominated by the collector resistance in this region [91]. It is also observed from Fig.3.15 and Fig. 3.17 that resistance variations with SOC are negligible compared to variations due to temperature [129, 139, 142]. In the other hand, DC current levels can be easily compensated, since they follow a linear trend (see Fig. 3.15). This means that SOC and DC fundamental current are not expected to influence the reliability of the proposed method significantly. These results confirm the validity of the

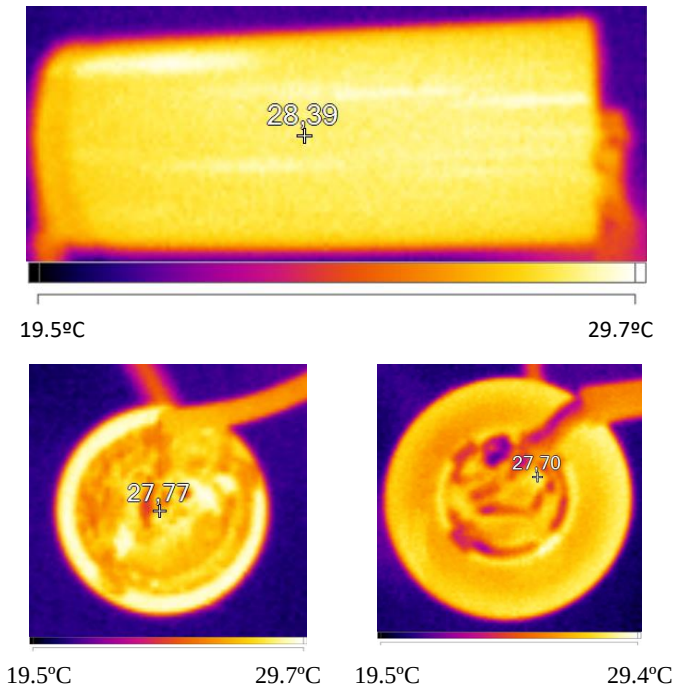

Figure 3.13: Thermal map of the cell during a discharging process; the cell is connected to the converter shown in Fig. 3.12. Top: cell. Bottom left: negative collector. Bottom right: positive collector. The thermal image is obtained with a Fluke Thermal Imager Ti110.

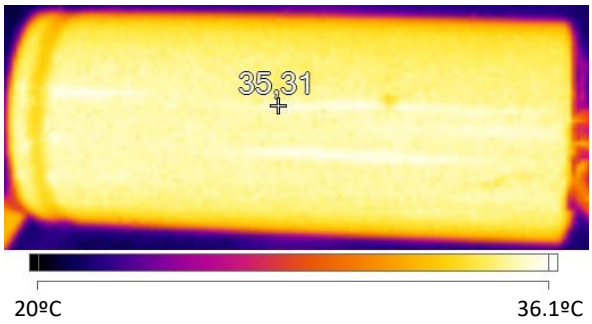

Figure 3.14: Thermal map of the cell during a discharging process at 35°C.

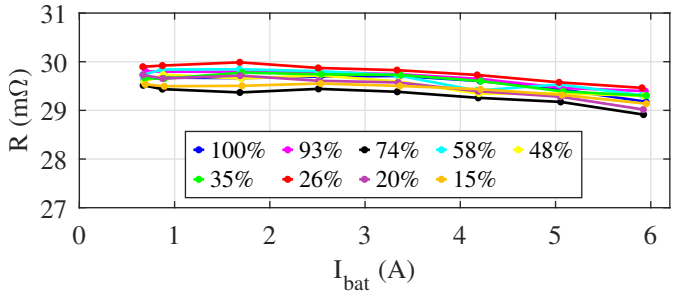

(a) Cell B1.

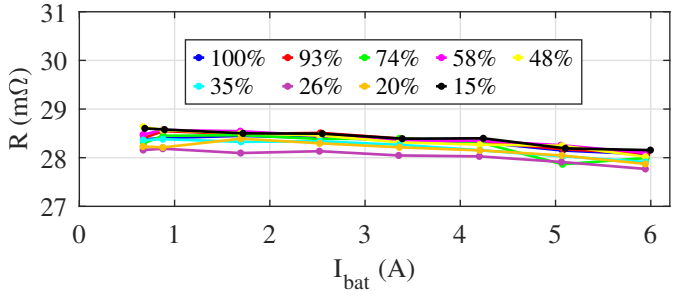

(b) Cell B2.

Figure 3.15: Battery resistance (@ 15 kHz) vs. discharging DC current for different SOCs for two different batteries. T=22°C.

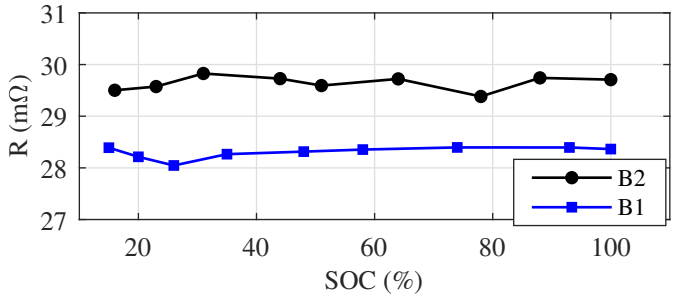

Figure 3.16: Variation of R@15kHz at 3.2 A discharge current with SOC for the two batteries in Fig. 3.15. T=22°C.

proposed method for battery temperature estimation.

The experimental results shown in Fig. 3.17a have been performed in two additional $LiFePO_4$ units (B2 and B3); the results are shown in Fig. 3.18. These

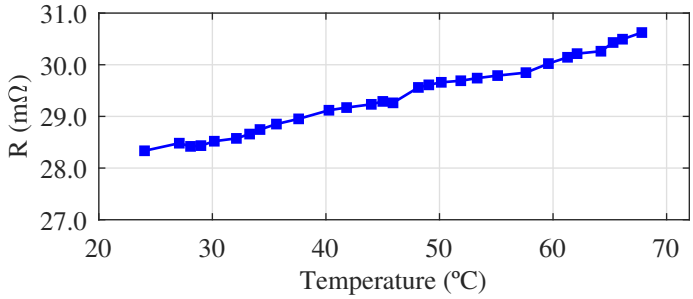

(a) Battery resistance.

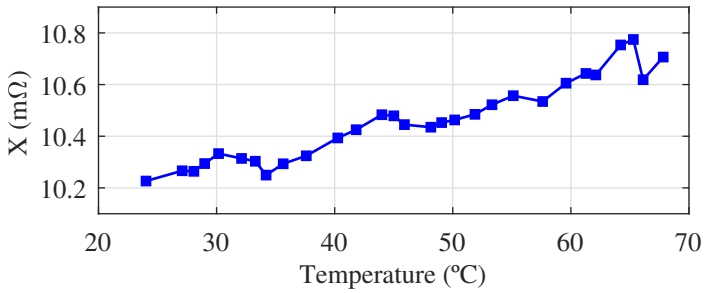

(b) Battery reactance.

Figure 3.17: Battery resistance and reactance at the switching frequency (15 kHz) vs. the battery temperature. IDC=3.2A

results were obtained following the same procedure as in Fig. 3.17. It is observed that there is an offset in the internal resistance among cells, however, the rate of variation of the internal battery resistance is almost the same for all batteries. Since the battery temperature will be estimated from the variation of the resistance with temperature respect to the room temperature resistance (R_{bath0}), see eq. (3.5), offsets among cells are not expected to affect the accuracy of the method.

Fig. 3.19 shows the measured and estimated temperature using eq. (3.5); α_{avg} ($\approx$0.0632 1/°C) being obtained as the average of α_{bat} for the three cells that have been analyzed (see Fig. 3.18). α_{bat} for each battery can be seen in Table 3.2. This coefficient is obtained from the slope of the linear regression approximating the temperature variation in each battery, which is obtained during a commissioning process.

Fig. 3.20 shows the temperature estimation error for all batteries analyzed in Fig. 3.19; the temperature estimation error is seen to be less than $\approx$ 10°C. This

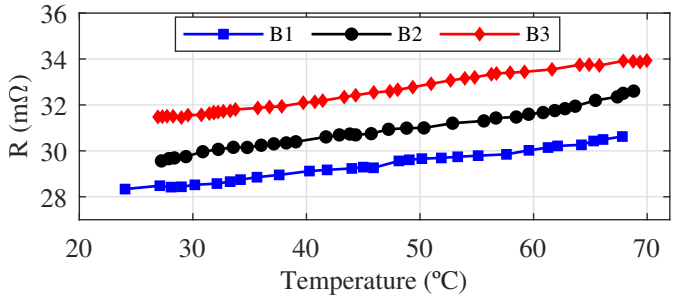

Figure 3.18: Battery resistance (@15 kHz) vs. battery temperature for different batteries. IDC=3.2A.

Table 3.2: Thermal Coefficients for the Different Cells Evaluated with the Switching Converter

Cell	**Thermal coefficient α_{bat} (1/°C)**
1 (Fig. 3.19a)	0.0526
2 (Fig. 3.19b)	0.0743
3 (Fig. 3.19c)	0.0626
Average	0.0632

error can be reduced if the calibration is considered for individual batteries but would not be considered practical in most cases.

Fig. 3.21 shows the temperature estimation error of the proposed method for cells B1 and B2 for different discharging current and SOC levels; cell temperatures were kept constant during all experiments. The variation of resistance with different current levels is compensated by means of a look-up Table (LUT), experimentally obtained like Fig. 3.15, since the resistance decreases evenly with current for every SOC. The reference value for the resistance is taken at 1C current (same level used to obtain all the experimental results in this section). It can be observed that the estimation errors in both cases is less than 5°C, except for one of the SOC levels in cell 2 (Fig. 3.21b).

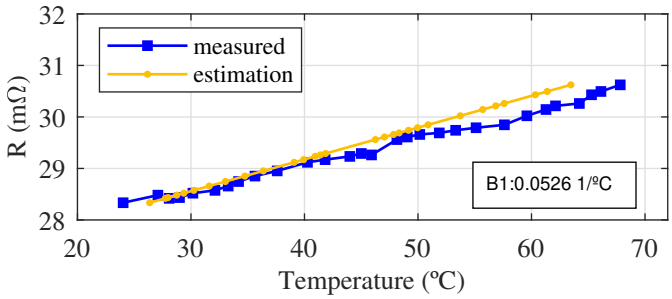

(a) Cell B1.

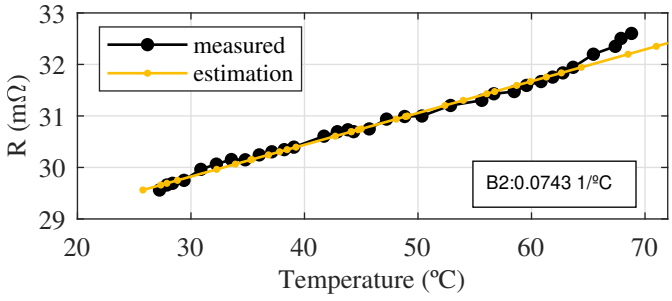

(b) Cell B2.

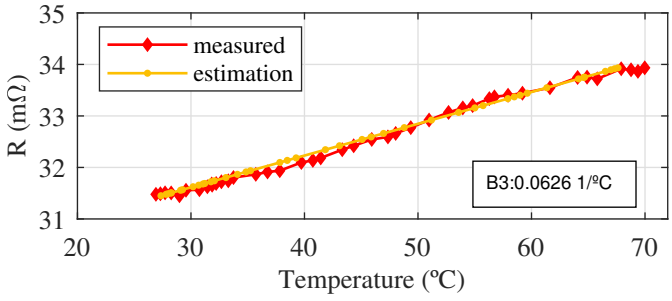

(c) Cell B3.

Figure 3.19: Measured and estimated temperatures for three different batteries. fsw=15kHz. IDC=3.2A.

3.6 Conclusions

This chapter proposes a temperature estimation method for $LiFePO_4$ batteries using switching harmonics produced by the power converter used to feed the battery. Temperature is estimated from the measured battery resistance at the switching frequency. The method allows online temperature monitoring without

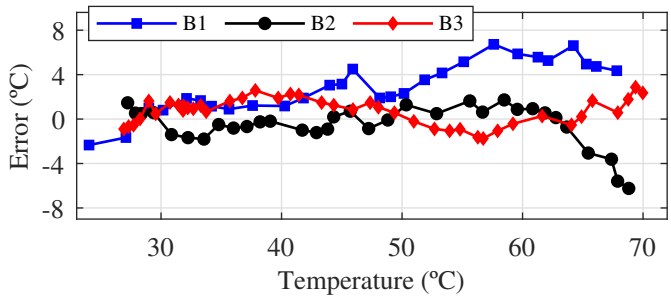

Figure 3.20: Error between measured and estimated temperature. fsw =15kHz, IDC=3.2A.

injecting additional signals and without interfering with the normal operation of the system. It has been shown that the SOC and the discharging DC current do not affect significantly the method reliability and can be easily compensated. Experimental results have been provided to demonstrate the viability of the proposed method.

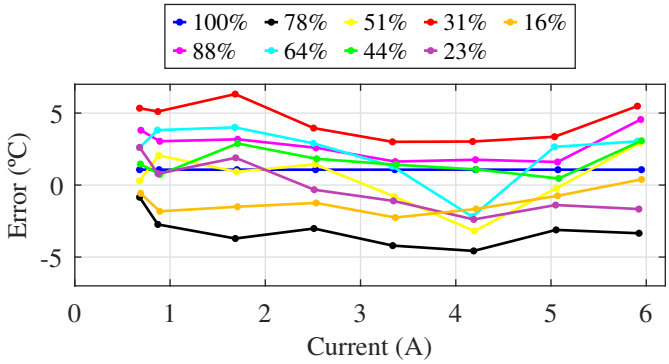

(a) Cell B1.

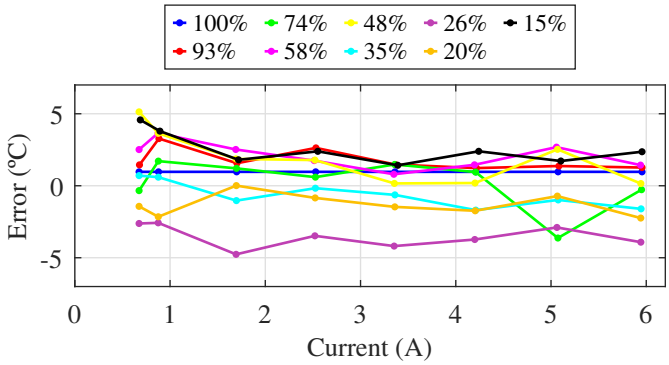

(b) Cell B2.

Figure 3.21: Estimation error at 22°C for batteries in Fig. 3.15 for different SOCs and current levels. T= 22°C.

Chapter 4

Battery internal resistance estimation using a battery balancing system based on switched capacitors

4.1 Introduction

As already shown in Section 2.2.6, BMS are key components in battery storage systems. BMS monitor critical parameters in the battery as SOC, SOH or temperature. Direct measure of SOC or SOH is not possible, so it must be estimated, while temperature, on the other hand, can be measure with different types of sensors. These sensors, although cost-effective, raise concerns regarding cabling, signal conditioning and acquisition systems, increasing cost, complexity and decreasing reliability (see Section 2.2.8.1). BMS can also include the function of balancing (equalizing) cells of a battery pack. Among all available equalizing systems, those based on switched capacitors are interesting due to their simplicity and easy scalability. This chapter [155] proposes an internal resistance (IR) estimation method for $LiFePO_4$ batteries using signals naturally produced by a SCE during cell balancing. The IR will be used to estimate the battery temperature. It will be shown that the method can operate online and without interfering with the regular operation of the SCE.

This method cannot be directly compared to those methods presented in Section 2.2.8.2. Those kind of methods estimate the battery impedance from the battery terminal voltages and currents when the battery is being connected to a power converter which has the capability of injecting some high frequency signal superimposed on top of the fundamental DC current component; i.e. these methods work in an analogous way to the EIS analysis (see Section 2.2.7.3) but only for a single frequency. Nevertheless, and since battery packs can be connected to the rest of the system using a power converter (see Section 2.2.5 and Chapter 3), both estimation methods could be employed simultaneously, thus increasing the reliability of the temperature estimation.

This chapter is organized as follows: the proposed method for battery IR estimation is presented in Section 4.2; simulations and experimental results are shown in Sections 4.3 and 4.4 respectively and conclusions are finally presented in Section 4.5.

4.2 Battery parameter identification based on SCE

This section presents the proposed method for battery IR estimation using signals produced by the SCE operation.

Among the models shown in Section 2.2.7, the Thèvenin one is the most appropriate for battery parameter identification using a SCE, since the process for extracting the parameters involved in (2.1) (i.e. step response) are similar to the steps produced in the battery as a result of the SC switching.

A simplified scheme of an SCE is presented in Fig. 4.1a, where the battery and SCE parameters are shown in table 4.1. The circuit is connected at the instant t_i, and the waveforms resulting from this connection are shown in Fig. 4.1b, which resemble SCE waveforms. Note that applying step voltages is analogous to applying step currents from the point of view of battery parameter estimation [121].

Before the switch connection there is no current circulation, so the voltage measured (V_{bat} in Fig. 4.1a) is the OCV (the voltage in the capacitor C_{SOC}). After the switch connection, there is current flowing from/to the battery and consequently a voltage drop in the battery IR, R_i, exists. Therefore, R_i can be

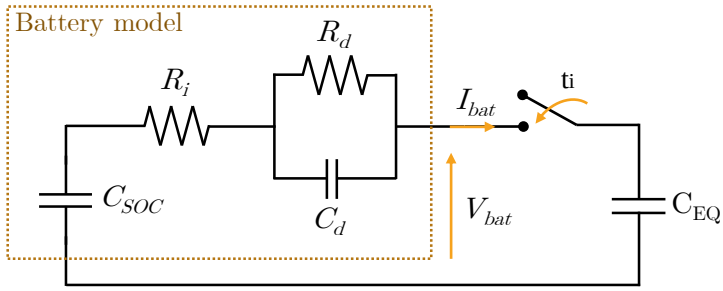

(a) Simplification of the SCE, modeling the battery as a first order Thèvenin model.

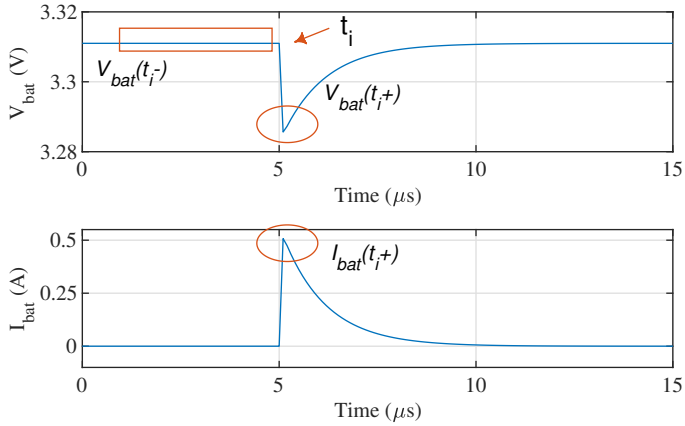

(b) Resulting voltage and current waveforms of the simplified SCE.

Figure 4.1: Simplification of the SCE with its voltage and current waveforms.

obtained from (4.1).

$$R_i = \frac{|V_{\text{bat}}(t_i-) - V_{\text{bat}}(t_i+)|}{|I_{\text{bat}}(t_i+)|} \tag{4.1}$$

Where the variables are related to Fig. 4.1b:

- $\boldsymbol{V_{\text{bat}}(t_i+)}$: Voltage right after the connection instant (t_i).
- $\boldsymbol{I_{\text{bat}}(t_i+)}$: Current right after the connection instant (t_i).
- $\boldsymbol{V_{\text{bat}}(t_i-)}$: OCV.

When using this SCE, two different currents may be superimposed, the current through the series-connected cells due to the charge/discharge of the battery, and the transient current due to the switching of the SCE. The first current,

Table 4.1: Battery Model Parameters

R_i	50 mΩ
R_d	6.7 mΩ
C_d	48 F
C_{SOC}	19 kF
C_{EQ}	22 μF

which will be DC, can be controlled provided that the battery is connected to a power converter. The second current cannot be controlled since it depends on the voltage difference between the cells been equalized. As seen in Section 3.5.1, the current level may affect slightly the IR estimation. This effect can be compensated using an analogous procedure as shown in Section 3.5.2.

In case the battery is being charged or discharged, the method is similarly applied with the exception the current in Fig. 4.1b will include this charging / discharging current. In this case, a more general equation, (4.2) should be used. $I_{\text{bat}}(t_i-)$ is the current before the commutation, in this case the current been charging/discharging the battery. The absolute value allows, as in (4.1), the equation to be used for both charging and discharging. The results remain unchanged.

$$R_i = \frac{|V_{\text{bat}}(t_i-) - V_{\text{bat}}(t_i+)|}{|I_{\text{bat}}(t_i+) - I_{\text{bat}}(t_i-)|} \tag{4.2}$$

The limitations of the method can be extracted directly from (4.2): once the batteries are equalized, there is no voltage difference among them, nor equalization current, meaning that R_i cannot be estimated this way. The SCE used in this work (Fig. 2.17) equalizes based on voltage differences among cells, however, $LiFePO_4$ cells can have a rather flat OCV-SOC curve [38], so it may not achieve a perfect balance in terms of SOC. This is a limitation of the SCE employed in this work. Nevertheless, this SCE can be used with any LIB technology with less flatness OCV-SOC [38]. Besides, and as stated in the introduction of this chapter, this method can be combined with signal-injection based battery resistance estimation methods to estimate temperature. This would increase the reliability of the estimation, allowing to estimate the desired parameters even when the method proposed in this paper cannot be employed.

4.2.1 Effect of inductive parasitic components

As it will be seen in Section 4.3, the circuitry has some unavoidable parasitic inductances due to e.g. cabling that affect the waveforms shown in Fig. 4.1b. This effect can be simulated by adding a small inductor L_p in series with C_{EQ} (see Fig. 4.2a). An inductor of 0.1 nH has been used to emulate this effect.The resulting waveforms are shown in Fig. 4.2b. The orange waveform represents the response of the battery's voltage and current when L_p is added to the circuit, in comparison with the blue waveforms that show the ideal case.

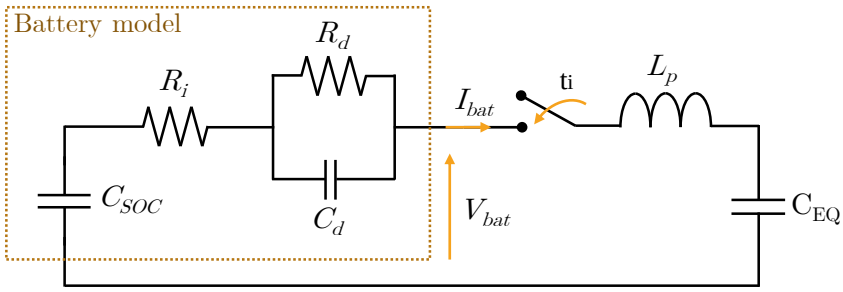

(a) Simplification of the SCE with a parasitic inductor in series with the equalization capacitor

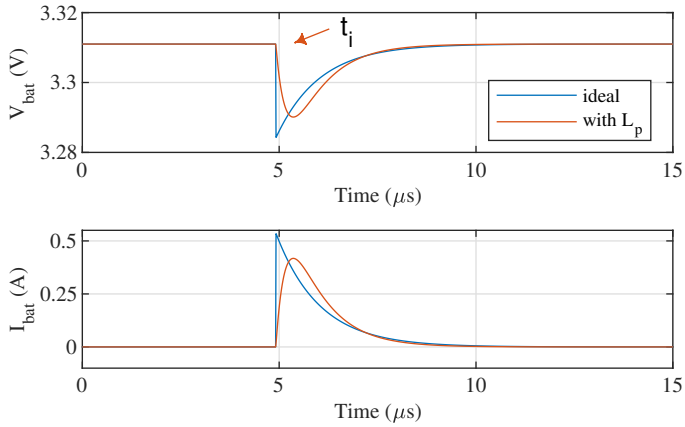

(b) Resulting voltage and current waveforms of the simplified SCE with a parasitic inductor.

Figure 4.2: Simplification of the SCE with a parasitic inductor with its resulting voltage and current waveforms.

Since V_{bat} is measured at the battery terminals, the existence of this parasitic inductor does not affect the estimation of the IR. Any combination of voltage and current from the graph would result in the IR estimation. However, peak values

are preferred since they provide a high signal-to-noise ratio. Equation (4.2) can be rewritten as (4.3), where $V_{batpeak}$ and $I_{batpeak}$ correspond to the peak values for current and voltage, respectively, right after t_i.

V_{batpeak} and I_{batpeak} can be obtained from the derivatives of V_{bat} and I_{bat} respectively, which can be approximated by (4.4) using the Euler approximation, where X_{bat} represents either the current or the voltage, X'_{bat} represents either the discrete-time derivative of the current or the voltage, k represents the current time instant and T_s is the sampling time. V_{batpeak} and I_{batpeak} are theoretically acquired when X'_{bat} is zero; in practice when there is a change in the sign of X'_{bat}.

$$R_i = \frac{|V_{\text{bat}}(t_i-) - V_{\text{batpeak}}|}{|I_{\text{batpeak}} - I_{\text{bat}}(t_i-)|} \tag{4.3}$$

$$X'_{\text{bat}} = \frac{X_{\text{bat}}(k) - X_{\text{bat}}(k-1)}{T_s} \tag{4.4}$$

4.2.2 Battery temperature estimation

As it was already covered in Chapter 3, it is generally expected [62,91,142] for the battery resistance to decrease as temperature increases at low frequencies. In this region, the electrolyte and SEI dominate the behavior of the battery and follows the Arrhenius law [91]. However, it must be noted that the proposed method estimates the IR, R_i in Fig. 4.1, which is dominated by the metal collectors and leads [93], which resistances increase as temperature does [62,142]. Hence, IR can be modeled as a linear function of the battery temperature (3.4), provided that the metallic part of the battery dominates the response. The battery temperature is finally estimated as in Chapter 3, using (3.5).

4.3 Simulations

A SCE with two cells was implemented in Matlab/Simulink, see Fig. 4.3.

The equalizer main parameters and settings are shown in Table 4.2. Cells are implemented using the battery model from Simscape Electrical toolbox, with $LiFePO_4$ battery equivalent parameters. Battery parameters can be found in table 2.4.

Fig. 4.4 shows the voltage and current of the most charged cell (B1 in Fig. 4.3) when it is connected in parallel to the balancing capacitor at t=5 μs. Voltage and

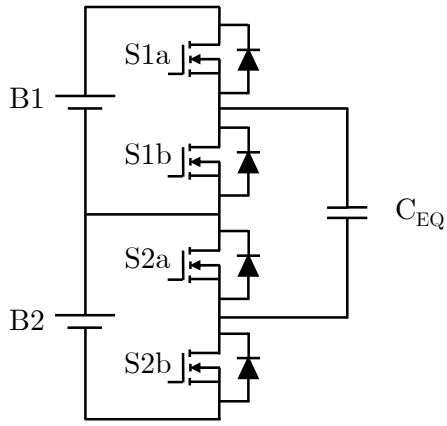

Figure 4.3: SCE with two batteries and one capacitor.

Table 4.2: Equalizer Parameters

Equalizer capacitor	C_{EQ}	22 μF
IR	R_i	50 mΩ
Initial SOC difference	-	30 %
Voltage B1	V_{B1}	3.312 V
Voltage B2	V_{B2}	3.284 V

current waveforms are seen to be in good agreement with the ones obtained with the Thèvenin model, see Fig. 4.1b. The estimated IR (4.1) is $\approx$ 50 mΩ, which matches R_i defined in Table 4.2 and included in the cell model for the simulation.

The same results are obtained if the parasitic inductor is added in series with C_{EQ} (Fig 4.5), as it was explained in Section 4.2.1.

Simulation results with more than two cells have also been carried out. A simulation scenario with three cells, see Fig. 2.17, has been used, voltage and current are measured for B2, since this cell will share energy with both the upper (B1) and lower (B3) cells. SOCs of B1, B2 and B3 are 80 %, 50 % and 20 % respectively. The resulting waveforms for a switching cycle (voltage ad current) can be seen in Fig. 12.

As expected, in the first half of the switching cycle B2 charges the bottom capacitor (C_{23}) since its voltage is higher than the one from B3. In the second half

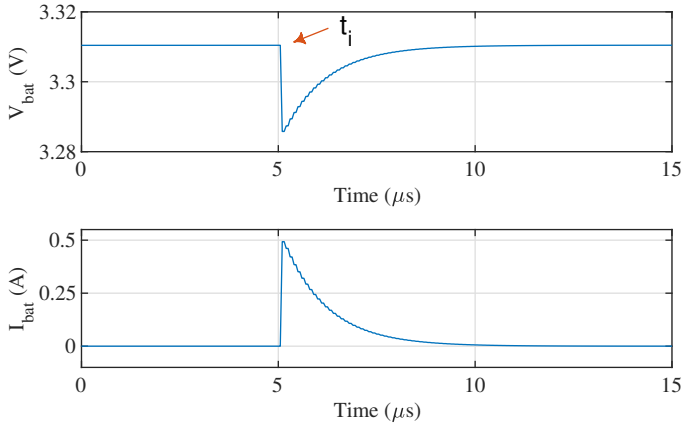

Figure 4.4: Resulting waveform from the SCE configuration in Fig. 4.3 simulated with Simulink, ideal case.

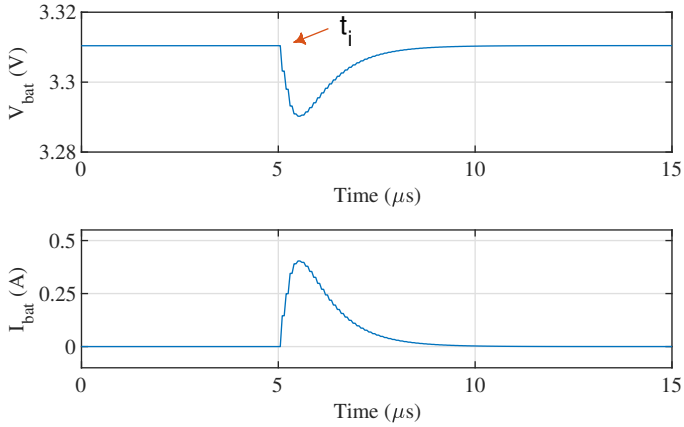

Figure 4.5: Resulting waveform from the SCE configuration in Fig. 4.3 simulated with Simulink, case with a parasitic inductance.

of the switching cycle, B2 receives energy from the upper capacitor (C_{12}), since B1 has a higher voltage than B2. The cell IR can be calculated from any of these two transient responses with identical results. Different SOCs and arrangement of the cells would not interfere with the method either.

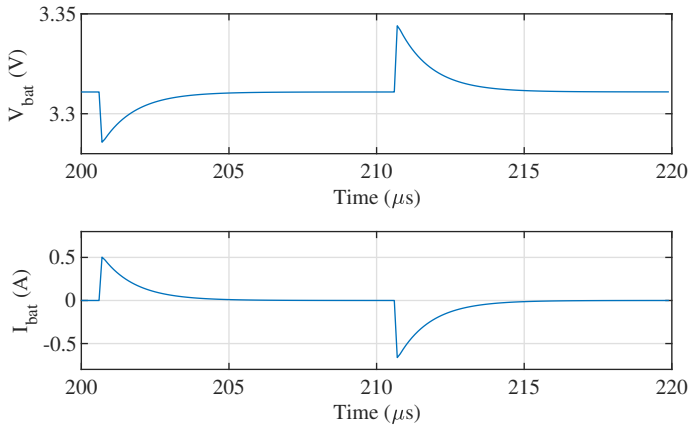

Figure 4.6: Voltage and current in one cycle for B2 cell in an SCE with 3 series-connected cells (see Fig. 2.17).

4.4 Experimental results

A prototype for a SCE to balance four cells is shown in Fig. 4.7, this prototype was used for the experimental verification of the proposed battery IR estimation method.

Figure 4.7: SCE prototype for balancing up to 4 cells.

A two-cell arrangement has been used to be consistent with the simulation results shown in Section 4.3. Current and voltage waveforms were measured with a Yokogawa 701932 current probe and with a Yokogawa 701938 voltage probe, respectively. Signals were captured with a Yokogawa 720250 12-bit 2-channel module plugged into a Yokogawa DL850 ScopeCoder. Parameters of the cell (Table 2.4) and SCE (Table 4.2) are the same than in Section 4.3.

In addition to the parameters shown in Table 4.2, the Equivalent Series Resistance (ESR) of the equalization capacitor is 0.7 Ω [156]. This resistance will affect several aspects of the system:

- It affects the equalization time and the efficiency of the equalization [111].
- It will affect the sensitivity of the method, i.e. the bigger this resistance, the smaller will be the current peak and the highest the accuracy needed in the measurement system.

It is also noted that the ON resistance of the MOSFETs will affect in a similar way; the ON resistance of the selected MOSFET is 2.4 mΩ [157]. In general, when designing an SCE, and since they are intended for low-cost applications, a good compromise among parasitic resistances, overall performance of the components and cost must be achieved.

Voltage measurement is performed at cell terminals. Cell voltage and current in one switching cycle are shown in Fig. 4.8. It can be seen that the current has a smoother response than in the ideal simulation in Fig. 4.4, and similar to Fig. 4.5, due to inductive parasitic components present in the actual system, as it was previously explained in Section 4.2.1, hence (4.3) is used to estimate the IR.

The OCV-SOC curve of LFP batteries is rather flat (see Fig. 2.10) [38], meaning that the accuracy of the measurement system should be carefully analyzed. As stated in [38], a good target for SOC and IR estimation in these batteries would be in the range of 1-2 mV. The LSB, as explained in Section 3.4, indicates the resolution of an acquisition system and is the result of dividing the FSR of the acquisition system by the number of discrete values obtained with N bits (3.6) [150]. With a 12 bits resolution acquisition system, which is a common resolution in digital processors nowadays (e.g. DSPs), the LSB would be < 1 mV, which is in the recommended range in [38].

In addition, the method does not work when the cells are equalized within the LSB limit, see Section 4.2. This methodology could be used with any LIB

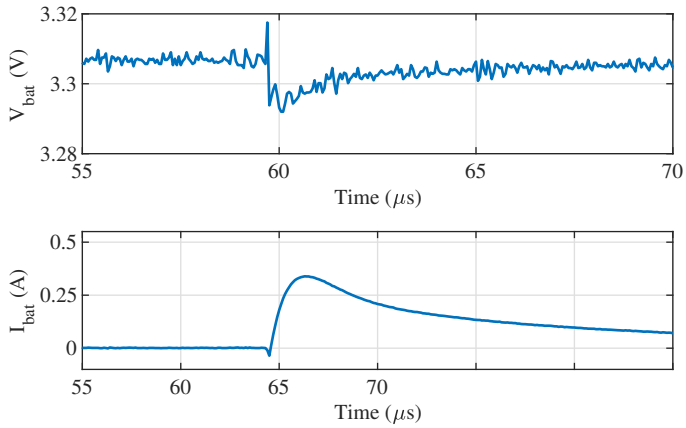

Figure 4.8: Resulting waveform from the SCE configuration in Fig. 4.3, experimental results (f_s = 20 kHz, T=20°C, SOC differences = 30 %).

chemistries (not only in $LiFePO_4$ batteries which have the flattest profile among LIBs). It is finally noted that the voltage variation is expected to be always smaller than the current variation, so the current variation will not be a problem before the voltage variation is.

4.4.1 Resistance Variation With Switching Frequency

Switching frequency in an SCE can be optimized for a given capacity of the equalizing capacitors [158], in such a way that the capacitor can be fully charged/discharged during its switching cycle without staying charged/discharged for long before the next commutation. The maximum equalization frequency is related to the driver (driving the MOSFETs). In addition, increasing the switching frequency allows for a capacitor size reduction, but it also increases the switching losses in the MOSFETs, thus reducing the efficiency. In the case of the setup used in this paper (see Fig. 4.7) the maximum switching frequency is $\approx$ 50 kHz.

Fig. 4.9 shows the estimated cell resistance for a set of experimental data captured with the SCE working at 10 kHz (Fig. 4.9a), 20 kHz (Fig. 4.9b) and 30 kHz (Fig. 4.9c); the mean value of the estimated cell resistance is shown in red.

The mean value at all the frequencies of the estimated resistances shown in Fig. 4.9 is similar at all the frequencies, since the resistance being estimated

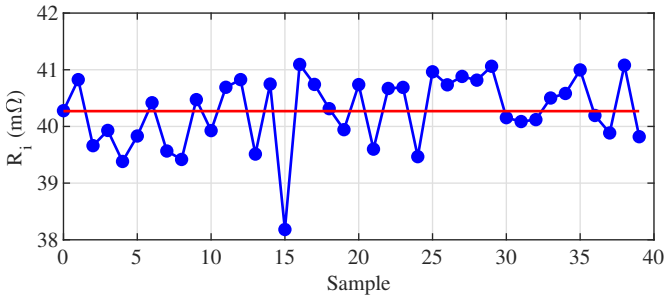

(a) 10 kHz.

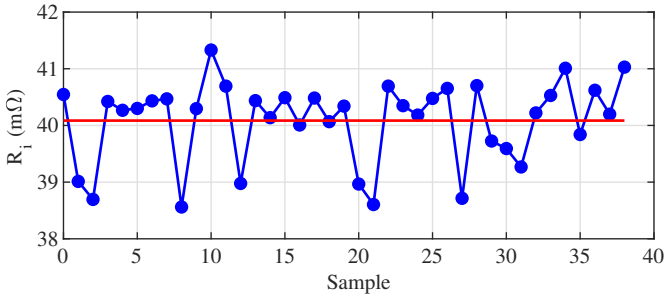

(b) 20 kHz.

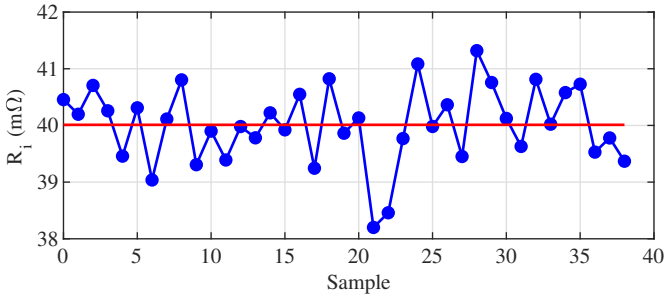

(c) 30 kHz.

Figure 4.9: Cell 1 IR estimation using the experimental data collected from the equalizer (blue) and mean value of the estimated resistance (red).

is R_i, which depends on the voltage/current at the switching instant, which is independent of the SCE switching frequency. It is also noted that SOC, SOH or temperature time constants are significantly larger than battery resistance estimation time [159], meaning that averaging the measurements for a certain period could be an acceptable and easy solution to reject measurement noise. Experimental results are repeated with another cell (see Fig. 4.10) with the same

characteristics, to show the replicability of the methodology. It is shown that R_i mean value is independent of the switching frequency. However, absolute value of R_i is different: for the first cell the mean value of R_i is ≈ 40 mΩ, while for the second one is ≈ 30 mΩ. This was expected due to differences among cells existing in practice [106, 108].

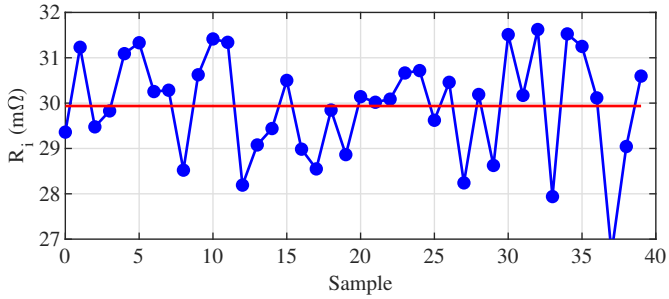

(a) 10 kHz.

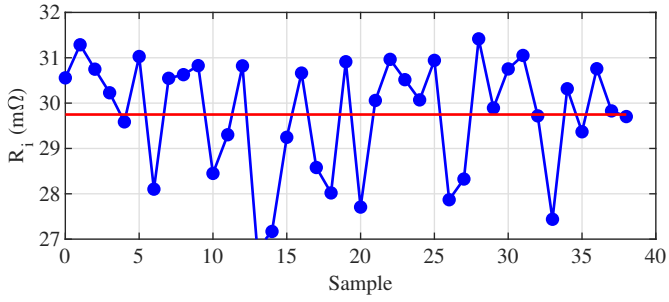

(b) 20 kHz.

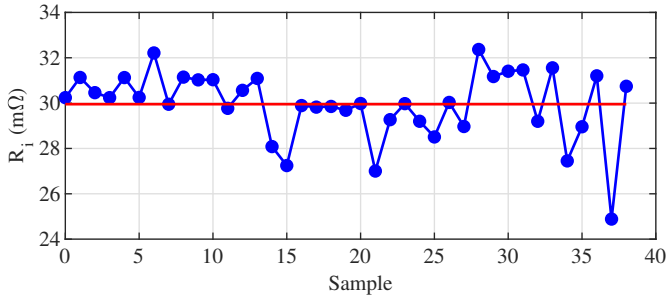

(c) 30 kHz.

Figure 4.10: Cell 2 IR estimation using the experimental data collected from the equalizer (blue) and mean value of the estimated resistance (red).

4.4.2 Resistance Variation With Temperature

Fig. 4.11 shows the estimated IR for three different cells as the temperature increases. The cells are slowly heated (for around 45 minutes, see Fig. 4.12) up to 65°C while capturing current, voltage and temperature. Temperature of the cells are monitored using LM35 temperature sensors [152], placed on the surface of the cell. It can be observed from Fig. 4.11 how the cell resistance increases almost linearly with temperature for all tested cells.

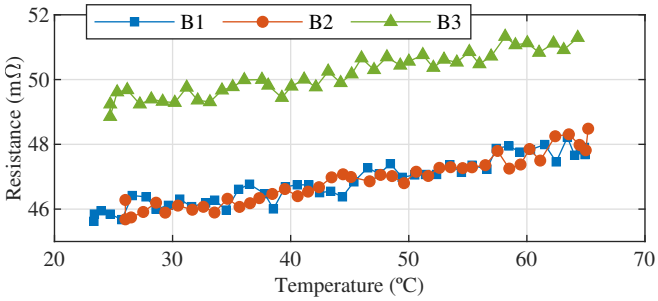

Figure 4.11: Cell resistance vs. cell temperature for different cells.

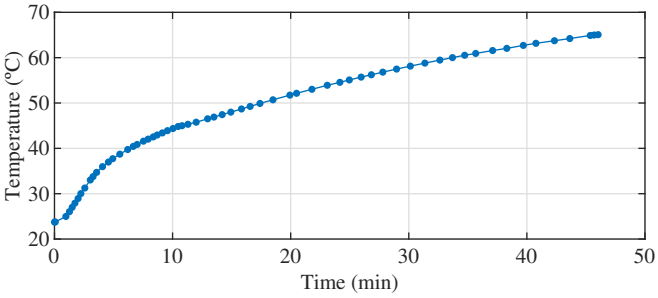

Figure 4.12: Temperature evolution of the cell with time.

It can be observed from Fig. 4.11 that, although there is an offset among IRs, the rate of variation of IR with temperature is similar for all cells under test. Offsets present among cells will not affect the accuracy of the proposed method because the cell temperature will be estimated from variations of the resistance with temperature respect to the room temperature resistance (R_{bat0}) as seen in (3.5).

Fig. 4.13 shows the measured and estimated temperature using (3.5). First, the slope that best fits the temperature variation for each of the three cells was obtained (see table 4.3), then, the average value of this slope ($\alpha_{\text{bat}} = 0.0598$ 1/°C) is used to estimate the temperature for all cells under test.

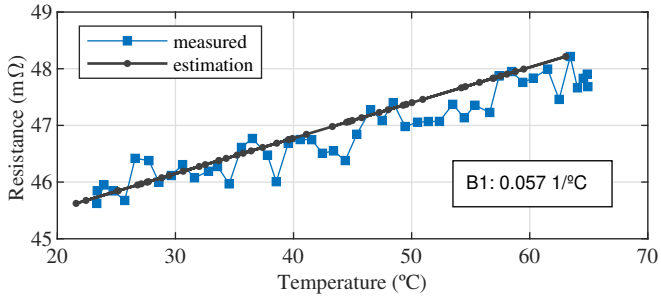

(a) Cell B1.

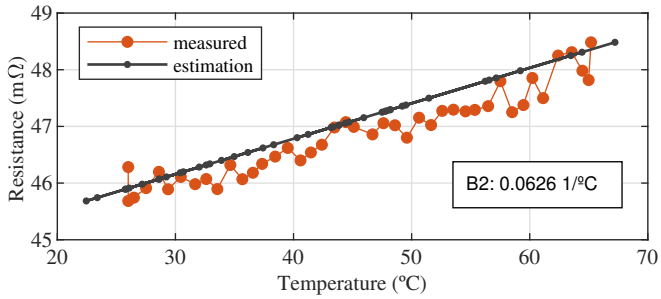

(b) Cell B2.

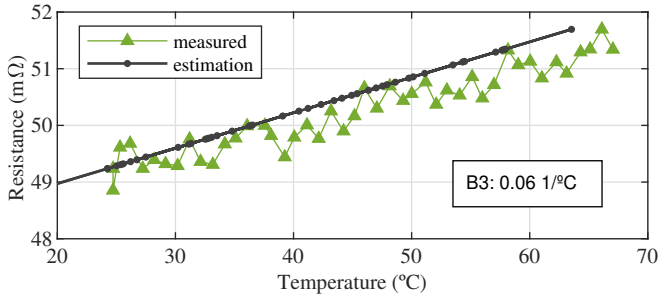

(c) Cell B3.

Figure 4.13: Measured and estimated temperatures for three different cells.

The temperature estimation error for the three cells analyzed is shown in Fig. 4.14; the temperature estimation error is seen to be less than ≈ 12°C for any point, with a mean value of 4°C and a standard deviation of 4.11°C. Due to this

Table 4.3: Thermal Coefficients for the Different Cells Evaluated with the Equalizer

Cell	Thermal coefficient α_{bat} (1/°C)
1 (Fig. 4.13a)	0.057
2 (Fig. 4.13b)	0.0626
3 (Fig. 4.13c)	0.0601
Average	0.0598

difference, it is important to analyze more than one point every time, as seen in Fig. 4.9 and Fig. 4.10, so the conclusions in terms of temperature are valid.

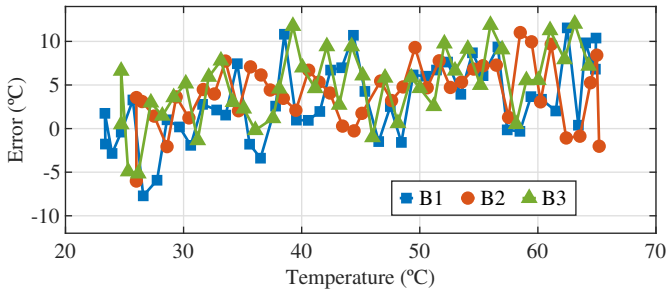

Figure 4.14: Error between measured and estimated temperature.

4.5 Conclusions

This chapter proposed the use of signals naturally produced by SCEs to estimate the battery IR. The method operates without interfering with the regular operation of both the equalizer and the DC/DC converter that can be connecting the battery to the rest of the system. Experimental results have been provided to demonstrate the viability of the proposed method. The method is valid for a wide range of switching frequencies. IR estimated can be used to estimate battery's temperature.

Part III

Control techniques for power converters

Chapter 5

Introduction to power converters for hybrid systems

5.1 Introduction

A microgrid was originally defined as a portion of an electric power distribution system located downstream of the distribution substation [160]. It is connected at the low-voltage side of the substation transformer in a connection point known as Point of Common Coupling (PCC). DERs can be renewable (e.g. wind turbines, PV) or non-renewable (e.g. diesel generation) and can include different ESS, as BESS or TES. A microgrid is seen as a single producer or load from the grid's perspective, despite is multiple and different forming blocks [161]. A microgrid can operate connected to the grid through the substation transformer, but it can also operate after being disconnected from the distribution system at the PCC. This autonomous operating mode is often referred to as islanding mode [162]. Nowadays, microgrid definition also extends to grids completely isolated from the grid and autonomously working, without even being located near an electrified area.

There is not a standardized consensus regarding the sizes of microgrids or technologies that must be part of the design [163]. However, the terminology is

continuously varying and different researches give different definitions. One of these classifications distinguishes between microgrid, nanogrid and picogrid. A single building can be termed as a nanogrid [164,165]. The term picogrid can be employed when referring to a household, smaller in general than the building in the nanogrid. While the microgrid and the nanogrid can include generation and consumption, a picogrid is generally considered to lack in generation systems; its main objective is the energy management of its loads and some small energy storage units, as Uninterruptable Power Systems (UPS) [165]. Several nanogrids can be connected to form a microgrid.

Based on the previous description, the building grid studied in this thesis can be considered as a nanogrid, as shown in Fig. 1.3 [164,165]. A definition of nanogrid could then be [164]:

"... a power distribution system for a single house/small building, with the ability to connect or disconnect from other power entities via a gateway. It consists of local power production powering local loads, with the option of utilizing energy storage and/or a control system."

As in the general microgrid, the nanogrid can have two main modes of operation:

- **Grid forming:** Generates the grid, working in voltage control mode (controls frequency and phase). This corresponds to the islanding mode.
- **Grid feeding:** Injects or absorbs energy from an established grid. The current must be injected according to the phase and frequency of the grid.

Regardless of their size, microgrids can be either DC, AC or hybrid power structures [164]. This thesis focus on AC distribution systems since the distribution in the building of Fig. 1.3 is AC, despite a DC-bus existing to connect the BESS and RES.

5.2 Power converters in DPGSs

The majority of the DPGSs, in either a grid or a microgrid, are connected to the PCC by means of an electronic power converter [42], which can be:

- **DC/DC converters:** Section 2.2.5 describes the types of DC/DC converters normally employed for connection batteries to the rest of the system via

the DC-link. The same type of converters can be employed for other types of DC sources, as PV panels. These converters can only be employed to connect the DPGS to the grid in case of DC grids.

- **DC/AC converters:** A DC/AC converter can be employed in different situations. For example, they can be used for direct connection between DC sources and the grid, as batteries or PV panels. In addition, they are typically employed in the AC/DC/AC and DC/DC/AC configurations, decoupling the input and the output generation using a DC-link [166]. An example of the first case could be a variable speed drive fed from the grid, while for the second case it can be a low voltage battery which voltage is boosted to a certain DC-link voltage level and finally inverted to get a 3-phase grid. This case would be the premise of this thesis.

- **AC/AC converters:** allows direct coupling from an AC source (as wind turbines) to the grid. They avoid the DC-link capacitor, which is bulky and can become a source of failure due to its limited life span compared to other components in the system. An example of these kinds of systems is the matrix converters [166].

Section 5.3 focus on DC/AC converters, since the building's power converter will necessarily include a DC-link, due to the presence of the batteries. DC/DC converters, which are also needed to connect the battery pack to the DC-link, were already explained in Section 2.2.5.

5.3 DC/AC voltage source inverters for low voltage grid application

Voltage Source Inverters (VSI) are DC/AC converters. They are normally single-phase converters or 3-phase converters when connected to the classical 3-phase grid. If there is a need of a neutral connection a 4^{th} terminal is provided, either employing a split DC-link or a 4^{th} leg in the VSI.

A three-phase two-level VSI is shown in Fig. 5.1. It consists of three half-bridge legs, one per phase, with two switches (IGBTs in this case) per leg. The DC voltage source represents the DC-link. As the neutral connection is not distributed, it is not possible to control the zero-sequence component in the voltage.

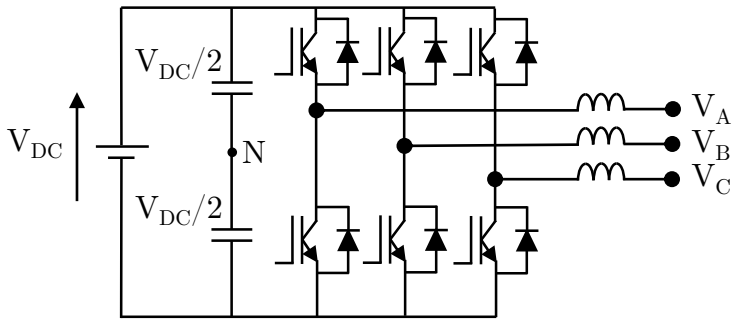

Figure 5.1: 3-phase converter.

There are other DC/AC converter options for grid applications, as multilevel converters, from the Neutral Point Clamped (NPC) to the Cascaded H-bridge (CHB) [167]. As explained in section 2.2.5, these converters are intended for medium/high power ranges where the ratings of a single switch from a 2-levels converter is not enough. They increase the number of components, cost and size of the converter, their design and control are more complex and would not be practical for low voltage applications, as the one in this thesis for the autonomous building. As a conclusion, 2-level converters are employed for their simplicity and cost.

5.3.1 Neutral distribution

Zero-sequence components appear in case of an unbalance caused by a single-phase element connection, either power systems or loads. These power systems can be small local subsystems, as RES like PVs or wind, or ESS [168]. In a more reduced scale, as in a building, they can be home appliances or lighting devices, all connected just to one phase of the grid. It is not possible to mitigate these voltage unbalances using the previously described 3-phase VSI since the neutral wire is not distributed [169]. However, if the neutral wire is distributed the zero-sequence component in the voltage is also seen in the current, and this unbalance can be as high as three times the phase current [168].

The neutral connection can be made through an LFT in delta/star configuration that blocks the homopolar component from flowing to the loads. Alternatively, the neutral can be distributed using a split DC-link capacitor configuration or adding a 4^{th} leg to the system. In these last options, there must be a con-

trol of the undesired current/voltage homopolar components [168, 170]. These configurations are explained in the following sections.

5.3.1.1 Delta/star transformer

The classical solution to prevent the propagation of the homopolar component is using an LFT in delta-star configuration, so the neutral connection of the secondary is used for the distribution (see Fig. 5.2). As mentioned in Section 1.1, these transformers are bulky and heavy, with low power to weight and power to volume ratios [44, 171, 172], in addition to a lack of controllability [171]. If galvanic isolation was still required, for safety issues or to comply with the regulations, a star-star LFT at the output of the VSI could be used [171]. In this way, the controllability would still be maintained. However, since this would potentially have the same drawbacks as the delta-star LTF mentioned before, a high frequency transformer could be used instead in another part of the system (e.g. as part of the DC/DC converter as seen in Section 2.2.5) [44].

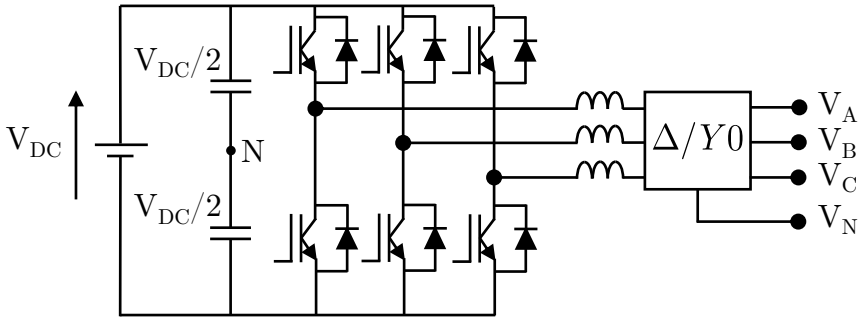

Figure 5.2: 3-phase 4-wire converter with delta/star transformer.

5.3.1.2 Split-capacitor inverter

One option to distribute the neutral wire is using the scheme in Fig. 5.3, known as the Split-Capacitor Inverter (SCI) [170], also referred to sometimes as the 3-Phase 4-Wire (3P4W) scheme. First proposals regarding this configuration did not include the extra neutral inductor than can be seen in the neutral wire in Fig. 5.3 [170, 173].

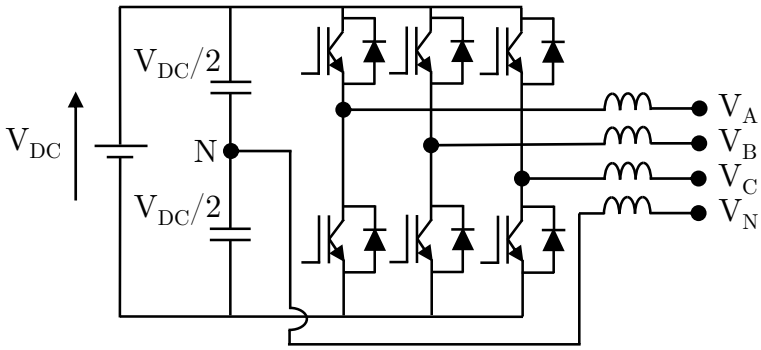

Figure 5.3: 3-phase 4-wire converter.

In this simple configuration, the neutral point is clamped at half of the DC-link voltage, with the inverter operating as three independent single-phase half-bridge inverters [174, 175]. The maximum output voltage is limited to half the DC-link voltage, which is the amplitude that can be achieved by each phase [176]. Due to the system configuration, zero-sequence harmonics are generated. If the expected unbalance is severe, the capacitance value must be highly increased due to the neutral current flowing directly through the capacitors and producing high voltage ripples in the midpoint [170, 175, 176]. Moreover, if there is a DC component in this neutral current, the neutral point shifts, so both capacitor's voltages must be controlled to precisely share the input voltage [175].

An inductor can be added to the neutral wire to improve the system performance [172, 175] by:

1. Reducing the zero-sequence switching harmonics in the voltages between the phase-leg midpoints and the output neutral point.
2. Reducing the current ripple in the filter inductors and the neutral line.
3. Decreasing ripple current of filter capacitors.
4. Partly suppressing unbalance voltages.

5.3.1.3 3-phase 4-leg

The addition of a 4^{th} leg to the converter in Fig. 5.1, as seen in Fig. 5.4, is a better solution to provide the neutral wire distribution. This configuration can provide better utilization of the DC-link, increasing it by about a 15 % compared with the previous solution with proper modulation [170, 171, 176]. Besides, the

harmonics in the neutral currents are reduced because the neutral wire is not connected to the split DC-link capacitor [176]. The neutral inductor is added to the system to suppress the neutral point voltage ripple caused by the high-frequency operation of the fourth leg [175].

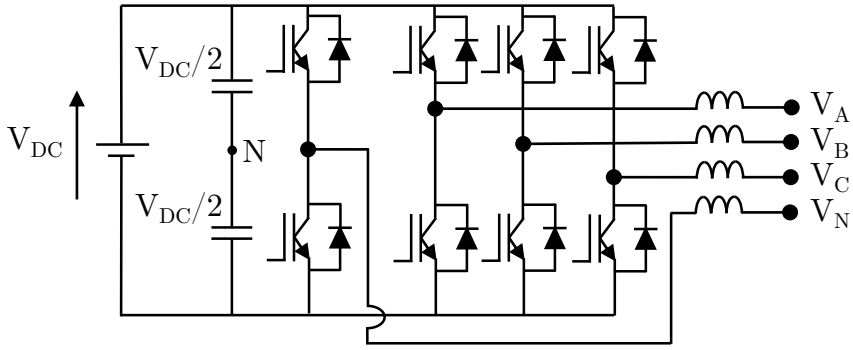

Figure 5.4: 3-phase 4-leg converter.

This topology can be used in several applications, as collaborative power-sharing control of the active and reactive power of the loads connected to a microgrid, fault ride-through control, fault current limitation, active power filtering or interfacing energy storage systems to the microgrids [171].

In [170], a modification is proposed in which the middle point of the two extra switches is connected to the middle point of the split capacitor (N), as seen in Fig. 5.5. It is claimed that this solution enables independent control of the 3-phase system from the extra leg. However, as it will be shown in Chapter 7, this can also be achieved with the configuration in Fig. 5.4, while the proposal in [170] can become highly unstable without the appropriate control.

5.3.1.4 Other topologies

In addition to the topologies presented in the previous sections with neutral distribution there are other alternatives in the literature.

For example, an H-bridge three-phase four-wire inverter is analyzed in [168]. In this solution there is an H-bridge per phase. The output of each bridge is then connected to a transformer, with all the negative outputs connected forming the neutral wire. Although claiming the need for a lower DC-link voltage, lower output harmonic content and smaller output filters, the higher number of devices

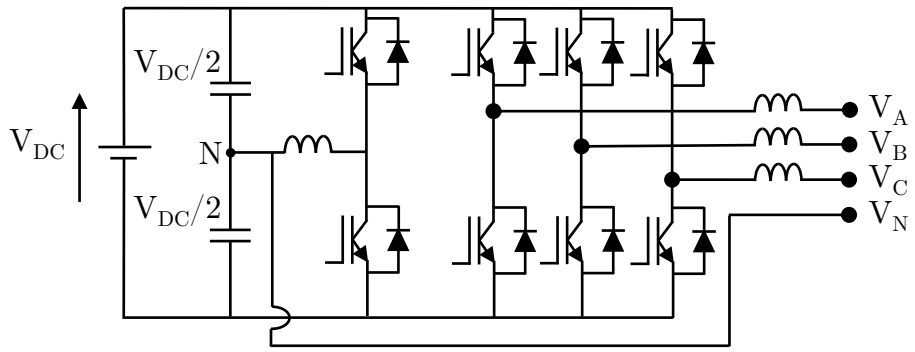

Figure 5.5: 3-phase 4-leg converter connecting the middle point of the DC-link voltage to the middle point of the 4^{th} leg by means of the neutral inductor.

and the need of three isolation transformers make them impractical for general-purpose applications. However, it could be an attractive solution in case of requiring isolation to meet the regulations.

Another option could be the use of the Neutral Point Forming Transformer (NFTI) [172]. In this topology, three inductors are star-connected after the filter, working as an autotransformer, with the neutral point of this connection becoming the neutral of the system. However, these extra inductors increase the size, cost and weight of the system similarly as a transformer does.

As a final remark, the previous topologies could all be used in a similar ways in multilevel topologies.

5.3.1.5 Conclusion

The 3P4L converter can become a great alternative to bulky and heavy delta-star transformers in those cases where the voltage is expected to get unbalance due to the connection of single-phase loads. Their controllability and voltage utilization is better than in the case of the split-capacitor solution with the addition of two extra switches. Due to all of these, a 3P4L converter was selected for the converter of the autonomous building designed in this thesis.

5.4 Modulation

The process of switching the electronic devices in a power electronic converter from one state to another to produce a waveform with discrete states is known as modulation. In this section, the basis of Pulse-Width Modulation (PWM) is explained. Sinusoidal Pulse-Width Modulation (SPWM) and Space Vector Modulation (SVM) are analyzed. They will be both used along this thesis, SVM in Chapter 6 and SPWM in Chapter 7.

5.4.1 Pulse-width modulation

PWM consists of recreating a commanded signal (modulation signal, in orange in the upper plot from Fig. 5.6) using the points of intersection of said signal when compared to a carrier to define the switching instants, as seen in Fig. 5.7, where v_x^* represents the commanded signal and S_x^+ represents the resulting square waveform, with x = a, b or c. This carrier can have different shapes, being the most typical ones the saw-tooth and the triangular carrier [177]. A triangular carrier is shown in blue in the top plot from Fig. 5.6. The resulting signal from the comparison can be seen in the middle plot in Fig. 5.6.

The triangular carrier must have a switching frequency (f_{sw}) sufficiently high when compared to the frequency of the modulation signal (f_f), so it can be properly filtered (see next section, 5.6) to finally get the desired signal. If the commanded signal is a constant value, the mean of the resulting square waveform is the value commanded. If the commanded signal is sinusoidal, the resulting square waveform varies with time and the modulation process is called Sinusoidal Pulse-Width Modulation (SPWM). In a 3-phase, 2-levels system (with or without neutral distribution) there will be 3 sinusoidal references that will be compared with the same triangular carrier [177–179].

The voltage utilization can be defined in different ways, related to different maximum voltages. In PWM it can be the maximum from the linear range, $\frac{1}{2}V_{\mathrm{DC}}$, or the maximum total achievable voltage, $\frac{V_{\mathrm{DC}}}{\sqrt{3}}$ [180]. Here it is defined as the relationship between the output waveform voltage (line to neutral) and the maximum reachable fundamental output voltage in six-step modulation with SVM, $\frac{2V_{\mathrm{DC}}}{\pi}$ (see next section 5.4.2), for consistency. This relationship is known as Modulation Index (MI):

$$MI = \frac{u_{in}}{\frac{2V_{\mathrm{DC}}}{\pi}} \tag{5.1}$$

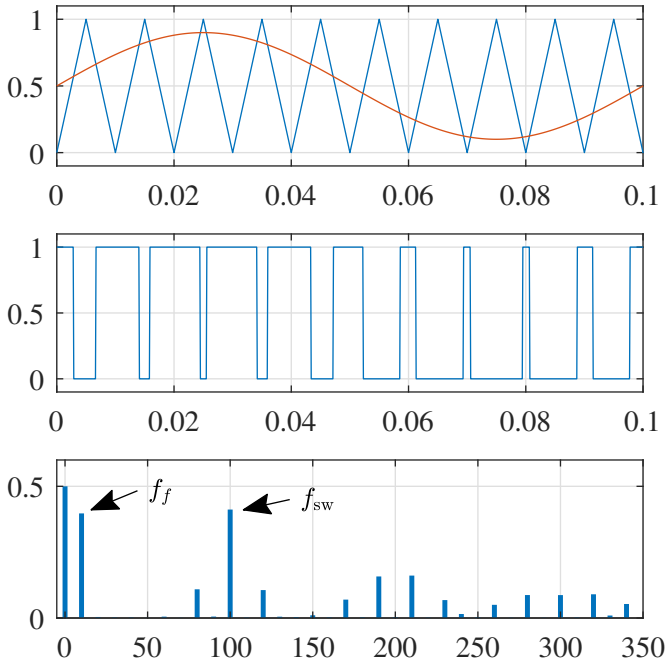

Figure 5.6: SPWM waveforms. Top plot: triangular carrier and commanded signal. Middle plot: resulting waveform from the comparison. Bottom plot: FFT of the PWM signal.

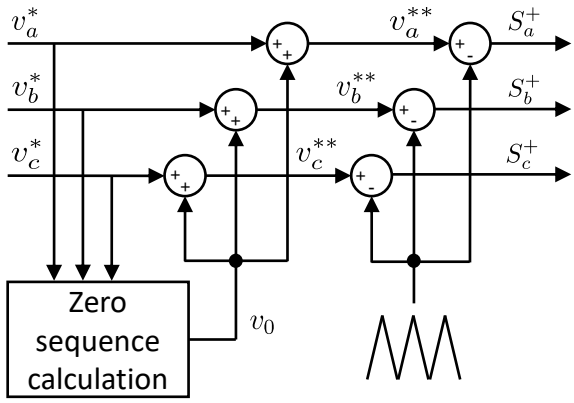

Figure 5.7: PWM generation including zero sequence injection.

If the peak of the modulation signal is less than or equal to the peak of the carrier signal, the system operates in the linear region, and MI≤0.79. This method uses 86.6 % of the available voltage. Homopolar harmonic injection (triplen-harmonic injection in 3-phase systems) can be added to the commanded signal to increase the linear region. This is shown in Fig. 5.7, in the "zero-sequence calculation" block, where u_0 is added to the three voltage commands, obtaining v_x^{**}. In this situation, the maximum peak value of the phase to neutral output voltage can reach a value of $\frac{V_{DC}}{\sqrt{3}}$, with a MI≈0.91.

Homopolar harmonic injection increases the Total Harmonic Distortion (THD) (see Section 5.7.1) but reduces the switching losses (due to a reduction in switching states as one of the legs is tied to the positive or negative rail). This zero-sequence signal will not appear in the line-to-line voltages, but will show in the phase-to-neutral ones, so it is not suitable for 3P4L converters [179, 181, 182].

5.4.2 Space vector modulation

In a VSI as the one in Fig. 5.1, there are six active voltage states and two zero-voltage states. They can be represented by the hexagon in Fig. 5.8. Each vertex represents one of the six possible active states (from V_1 to V_6), with the middle point representing the zero-voltage states (V_0 and V_7). SVM calculates the vectors and their time lengths needed to produce the average voltage vector over the switching period (T_s) equal to the command (V^* with a given angle θ) [181, 183].

Vector combinations to achieve the desired output are infinite. In the simplest solution, shown in Fig. 5.8, each commanded signal can be realized with two adjacent vectors plus some zero voltage vector. The time of each state (t_1, t_2) into the switching period will be given by the projection of said commanded signal into the adjacent active vectors. The remaining time to complete the switching period will be occupied by a zero voltage vector. In standard SVM, there are six branch commutations per switching period and a balanced use of zero voltage vectors, which minimizes the THD (see Section 5.7.1) [179, 183]. In this case, the resulting commutation pattern is similar as in the case of SPWM with triplen-harmonic injection.

The circle in Fig. 5.8 limits the end of the linear region ($\frac{V_{DC}}{\sqrt{3}}$). Over that, the region corresponds to overmodulation, with zero-sequence injection [184], meaning one of the switches does not change its state during the whole period. When MI reaches 1, at an output fundamental voltage of $\frac{2V_{DC}}{\pi}$, the system works

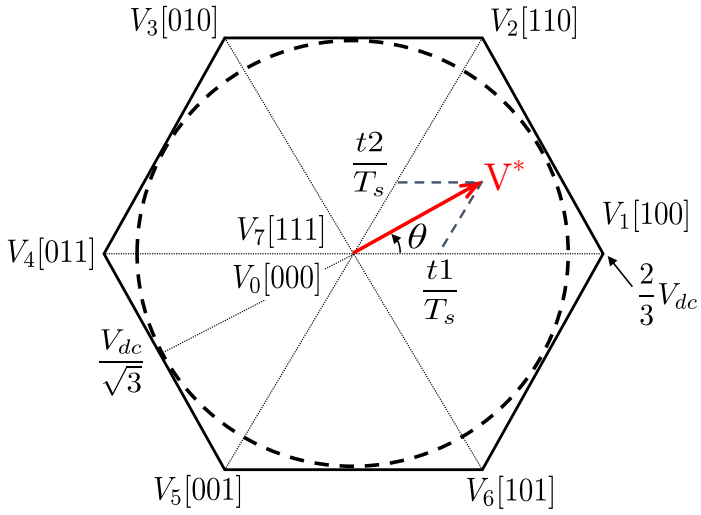

Figure 5.8: Space Vector Modulation.

in 6-step operation and jumps between the 6 possible vectors. PWM is replaced by a square-wave at the fundamental frequency.

In 3P4L converters (Section 5.3.1.3), the hexagon is extended from 2D to 3D, with 16 possible different states [174].

5.5 Sampling

In general control system, one sample per period is often taken from the different signals measured by the sensors. In the case of current control, the sampling instant can be synchronized with the peak of the PWM triangular carrier (see Section 5.4.1), which is known as synchronous sampling [185]. The benefits of doing so is that the carrier frequency and harmonics become hidden oscillations for the digital system. This is shown in Fig. 5.9, which represents the triangular carrier and the current through a boost converter as the one in Fig. 2.11. Sampling this way, the ripple is canceled, avoiding the use of low-pass analog anti-aliasing filters, which delay the signal. The drawback of this method is that it has a high noise sensitivity because because no filters are avoiding high-frequency components to get into the digital system. However, filters for spurious

noise at higher frequencies can still be used.

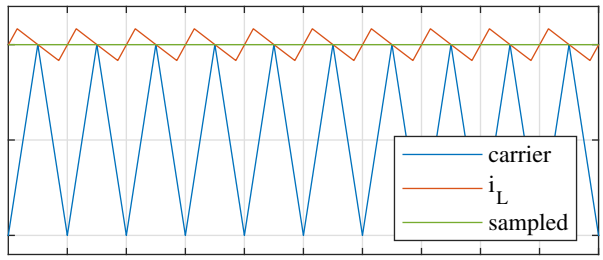

Figure 5.9: Comparison of the carrier and the current through the inductor in a simple boost converter.

5.6 Grid-side filters

Both SPWM and SVM generate a square waveform, as seen from the middle plot in Fig. 5.6. It contains the fundamental voltage plus high-frequency components at the carrier frequency and multiples, as seen in the bottom plot in Fig.5.6. Since high-order harmonics caused by the switching of power converter can disturb sensitive loads and produce extra losses they must be canceled out [186].

To eliminate these high-frequency harmonics, different passive filters can be used at the output of the VSI. Fig. 5.1 shows an L filter (Fig. 5.10a), but LC filter (Fig. 5.10b) and the LCL filter (Fig. 5.10c) are also often used low-pass filters. In all the cases, v_i represents the VSI output voltage and v_g the grid voltage. Not only they mitigate the unwanted frequencies, but also they simplify current and/or voltage control; the capacitor is used for voltage control and the inductor for current control.

5.6.1 L-filter

The L-filter (Fig. 5.10a) is the simplest filter and it has an attenuation of -20 dB/dec. It enables output current control, so it can be used in grid-feeding applications, but not in grid-forming applications which require voltage control. As it is composed of only one passive element there are no possibilities of system resonances. Due to all of this, systems with an L-filter are the easiest to control.

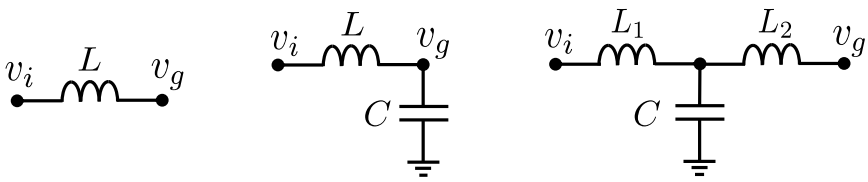

(a) L filter. (b) LC filter. (c) LCL filter.

Figure 5.10: Common output filters in VSI.

Nevertheless, this filter is also the bulkiest when aiming for low output ripples that comply with the regulations [40]. To reduce the size, higher switching frequencies must be used. This increases the losses and reduces the system's efficiency [187]. The block diagram of this filter, considering that the inductor has a parasitic resistance in series, is shown in Fig. 5.11.

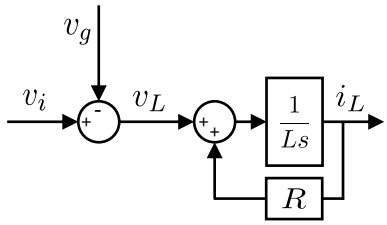

Figure 5.11: Per-phase block diagram of a VSI with an L filter.

From Fig. 5.11:

- v_i is the voltage generated by the VSI.
- v_g is the grid voltage.
- v_L is the inductor voltage drop.
- i_L is the current through the filter inductor.

5.6.2 LC-filter

If there is a requirement for voltage control, a capacitor is added after the inductance in parallel with the inverter output (Fig. 5.10b) [188]. In addition, the attenuation increases to -40 dB/dec. The system has a resonant frequency (f_r) at (5.2), which must be carefully designed to be above the desired closed-loop control

bandwidth. Otherwise, the system relative stability will be low. This means that if the fundamental frequency is, for example, 50 Hz, the resonant frequency of the filter must not be in the range of the main fundamental component or its harmonics, this last case to avoid resonances [189]. The block diagram of this filter is shown in Fig. 5.12.

$$f_r = \frac{1}{2\pi\sqrt{LC}} \tag{5.2}$$

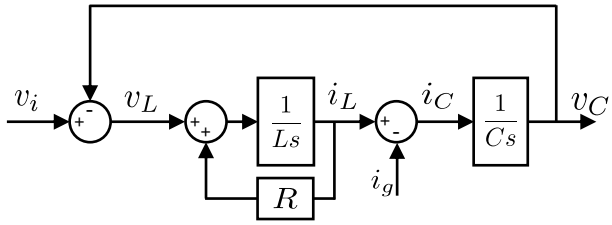

Figure 5.12: Per-phase block diagram of a VSI with an LC filter.

From Fig. 5.12:

- i_g is the current injected or absorbed from the grid.
- i_c is the current through the filter capacitor.
- v_c is the voltage in the filter capacitor, also the grid voltage.

Damping techniques of the LC resonance can be applied to ensure the stability of the system [187]:

- **Passive damping:** the most typical solution is adding a resistor in series with the capacitor. It reduces the peak magnitude of the resonance frequency but introduces extra losses in the system and reduces the ability of attenuation of harmonics by the filter.
- **Active damping:** emulates the effect of passive damping with control techniques. This increases the complexity of the control system but avoids the extra losses from the passive damping.

5.6.3 LCL-filter

The LCL filter (Fig. 5.10c) is a good alternative to L filters, especially for high power VSI, at which the L-filter inductor would become high, and thus quite

expensive with a poorer dynamic response [186]. With an LCL-filter, lower ripple and THD can be achieved with relatively small size filters and lower frequencies compared to L filters. The LCL attenuation is -60 dB/dec. As in the previous case, there is a resonant frequency (5.3), and damping techniques can be applied to reduce the effect of the resonance [187, 190, 191]. The block diagram of this filter is shown in Fig. 5.13.

$$f_r = \frac{1}{2\pi}\sqrt{\frac{L_1 + L_2}{L_1 L_2 C}} \tag{5.3}$$

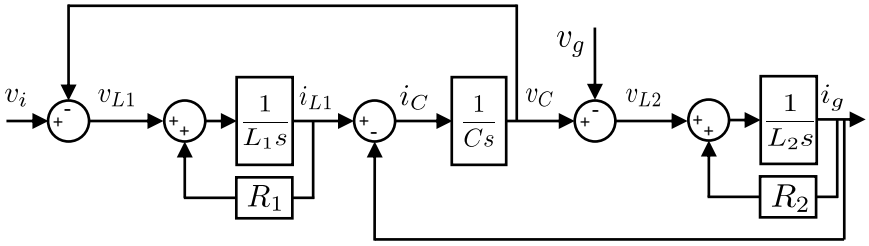

Figure 5.13: Per-phase block diagram of a VSI with an LCL filter.

5.6.4 Conclusions

A summary of the filters explained in these sections is shown in Table 5.1.

Table 5.1: Comparative Between Different Passive Filters

Type	Attenuation	Resonance	Allows voltage control
L-filter	-20 dB/dec	No	No
LC-filter	-40 dB/dec	Yes	Yes
LCL-filter	-60 dB/dec	Yes	Yes

An L-filter is best suited for low to medium power applications, in which the size will not be excessively high. This avoids complications with resonances and more complex control systems. However, an L-filter is only suited for grid-feeding applications, so in the case of grid-forming systems there is a need of adding a capacitor to enable voltage control. An LC-filter has also higher attenuation, but there is a resonance that must be taken into account in the designing process. In

high power applications (above several kilowatts), the design of the filter inductor in the previous case would become excessively bulky and expensive. Due to this, an LCL-filter is preferred. This filter improves the attenuation, but it also creates a resonance that must be correctly handled. In addition, the voltage is controlled at the filter capacitor, not at the output of the filter.

From the filters shown in this section, the one finally used for the autonomous building (see Fig. 1.5) is the LC filter (Fig. 5.10b) because the power requirements are not too high and it allows for simpler voltage and current control of the grid voltage.

5.7 Control of VSI

The control goal of the VSI can be different depending on the intended application. In grid-feeding applications, only the current needs to be controlled. If the VSI is used to generate the grid, voltage control will be also required. In the latter, a cascade control is often implemented, with an inner loop controlling the current and an outer loop controlling the output voltage. A general scheme for the cascade control can be seen in Fig. 5.14.

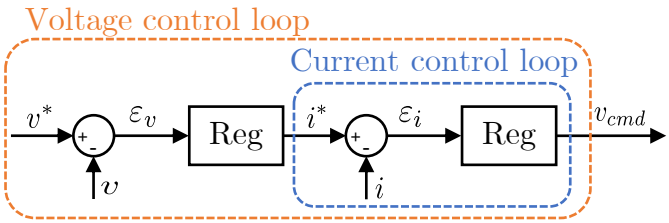

Figure 5.14: Generic cascade loop.

Here, voltage reference (v^*) is compared to the measured voltage (v) to obtain an error (ε_v) which is introduced to a regulator that will give as the output the current reference command (i^*). In the same way as in the outer voltage loop, this reference is compared to the measured current (i) and the resulting error (ε_i) introduced as the input of the current regulator, which will finally output the necessary voltage command (u_{cmd}) for the VSI.

The most used controllers (Reg in Fig. 5.14) are those based on Proportional-Resonant (PR) controllers [192], also known as Second-Order Generalized Integrators (SOGI); and those based on synchronous proportional-integral (PI)

controllers, implemented both in the synchronous or stationary reference frames [127, 193, 194], also known as Reduced-Order Generalized Integrators (ROGI). Repetitive Controllers (RCs) are also popular when there are multiple harmonics to be controlled (see section 5.7.1). These controllers will all be explained in Section 5.7.3.

Different frequency components need to be controlled. The main controller is for the fundamental frequency (50 Hz in European grids). There is also a need for controlling the negative sequence component (-50 Hz in European grids), since it will arise with 3-phase unbalances in the grid. Finally, harmonic controllers are also needed to increase the quality of the grid and comply with the grid-codes, when there are non-linear load in the system [40, 195]. An example of these components can be seen in Fig. 5.15, where the green component represents the fundamental frequency (f_f), the orange one the negative sequence component ($-f_f$) and in blue different harmonics (see Section 5.7.1 for more details on harmonic distribution).

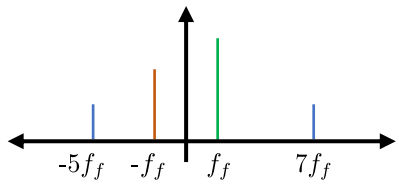

Figure 5.15: Different components to be controlled in a VSI.

5.7.1 Harmonic distortion compensation

5.7.1.1 Harmonic distortion

In the grid or a microgrid, there can be a high percentage of non-linear loads injecting a significant amount of current harmonic content that eventually can distort the grid voltage [196]. Not only they may increase the peak voltage value, but they can also cause heating, noise and life decreasing of capacitors and other components in the system. They can also excite system resonances, producing failures and reducing the overall system efficiency [184]. Due to all of this, requirements for the admissible harmonic distortion in the grid have been toughened up to improve general power quality [40].

Different loads produce different harmonics. Harmonics produced by a semiconductor converter equipment in steady state are known as characteristic harmonics of the converter. They can be expressed as:

$$h = np \pm 1 \tag{5.4}$$

where h is the order of the harmonic, n an integer number and p the number of pulses per cycle [197].

For example, a load supplied through a three-phase diode or thyristor front-end rectifiers (p=6), which is a very typical configuration, will have harmonics of the fundamental frequency in the order of 6n±1. Those harmonics that are obtained from 6n+1 are positive sequence harmonics (rotating in the same direction as the fundamental component), while the ones obtained from 6n-1 are negative sequence harmonics (rotating in the opposite direction to the fundamental component): -5, 7, -11, 13... [195].

Among the different metrics to measure the distortion of a grid in terms of harmonics, the THD is one of the most recommended to measure the quality of the grid in terms of harmonics (5.5) [40]:

"The ratio of the root mean square of the harmonic content, considering harmonic components up to the 50^{th} order and specifically excluding interharmonics, expressed as a percent of the fundamental. Harmonic components of order greater than 50 may be included when necessary."

$$THD_{V_{\text{pcc}}}(\%) = \frac{\sqrt{\sum_{h=2}^{h=50} V_{\text{pcch}}^2}}{V_{\text{pcc1}}} \cdot 100 \tag{5.5}$$

where V_{pcc1} is the amplitude of the fundamental component (h=1) and V_{pcch} the amplitude of the h^{th} harmonic component. According to [40], for low voltage grids ($v_g \leq 1.0$ kV), which would be the case of the building under study, the maximum recommended THD is an 8 % and the individual harmonics cannot exceed 5 % each.

5.7.1.2 Harmonic compensation

Harmonic compensation can be implemented using dedicated units, as passive filters or centralized active filters [42, 198] increasing the system cost. However,

since the interface of DPGSs is generally based on power converters, this opens opportunities for harmonic compensation [42]. The filter at the output of the converter (see Section 5.6) filters the high frequencies, but some of the lower frequency harmonics remain. The filter cut-off frequency could be decreased, but this would lead to an increase in the size and cost. In addition, there is a point up from where the filtering would start affecting the fundamental component as well. Alternatively, the bandwidth of the controllers could be increased. However, due to switching frequency and noise limitations, the bandwidth of the fundamental controllers cannot be increased enough to compensate for the higher harmonic frequencies [169]. Due to all of this, a better solution is adding additional harmonics controllers along with the fundamental positive and negative sequence controllers [199].

Harmonic compensation increases the voltage and current controllers complexity, requiring parallel structures [39], and sharing the DC voltage margin with the fundamental controls. This increases the chances of saturation (see Section 6.2 below). The selection of harmonics to be controlled is based on the control objective, which can be reducing the current THD (in grid feeding converters) or the voltage THD at the PCC (in grid forming converters), among others [199].

5.7.2 Reference frames

There are different approaches to multifrequency controllers needed for harmonic compensation. In these structures, the error signal can be treated in two different ways:

- **Common error:** a common reference can be selected. The error signal is unique, and it is transformed to the different reference frames [169, 200]. Since all the controllers use the same reference, they can contribute to control different frequency components within their bandwidth.

- **Individualized error:** using a different error signal for every component to be controlled. Filters are needed to isolate the different frequency components in Fig. 5.15. Without the filters, the controllers may overlap. If this happens and the control objective is different for each controller, they might interfere with each other, reducing the stability of the system. The implementation of multiple filters increases the computational cost.

The harmonic compensation can be realized in multiple reference frames or in a single reference frame. They are explained in the following sections.

5.7.2.1 Multiple reference frame

One approach consists of regulating each frequency component in its own reference frame, also known as controllers in Multiple Reference Frames (MRF). In order to do this, multiple Park's transformations (see Appendix B) must be applied [194]. This is shown in Fig. 5.16.

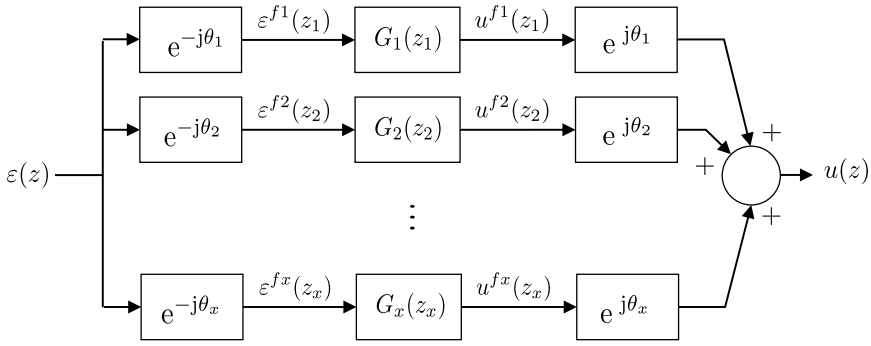

Figure 5.16: Block diagram of a multiple reference frame parallel controllers' structure.

In Fig. 5.16, u is the controller output (e.g. inverter output voltage in a current controller) and ε is the error signal (e.g. current error in a current controller). The error signal (which is common for all the components, as explained earlier in this section) is first transformed into the different reference frames. Each controller produces an output in its own reference frame; and finally, the outputs are transformed into a common reference frame (i.e. stationary) and added up. Superscript fl $(l = 1, 2, ..., x)$ is used to specify the different reference frames for the parallel controllers.

The main benefit from this is that each component is seen as a stationary space vector in its corresponding reference frame and thus it can be regulated with a simple PI controller (see Section 5.7.3.1), since the components become DC. However, performing a number of Park's transformation can become computationally expensive [194, 200–202].

Fig. 5.17 shows the usual harmonic content for a three-phase diode or thyristor rectifier in the stationary reference frame (left). In this case, the 5^{th} harmonic

has only negative-sequence components and the 7^{th} harmonic has only positive components [169]. The right figure shows the resulting spectra when the Park transformation is applied in such a way that the fundamental component becomes DC. In this case, all the harmonics are displaced to the left. The same procedure would be needed for the rest of the components.

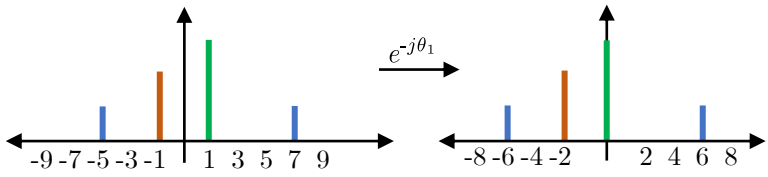

Figure 5.17: Harmonics in a stationary reference frame (left) and in a synchronous reference frame with the fundamental component (right). The x-axis represents the harmonic order and the y-axis the harmonic amplitude.

5.7.2.2 Single reference frame

Alternatively to an MRF control, there is the control in a Single Reference Frame (SRF), performed in a stationary reference frame. In this case, the different harmonics are controlled avoiding all the rotations needed in the previous case. In this case, the different components are sinusoidal rotating vectors in steady state [200]. An example of this reference frame is shown in Fig. 5.18.

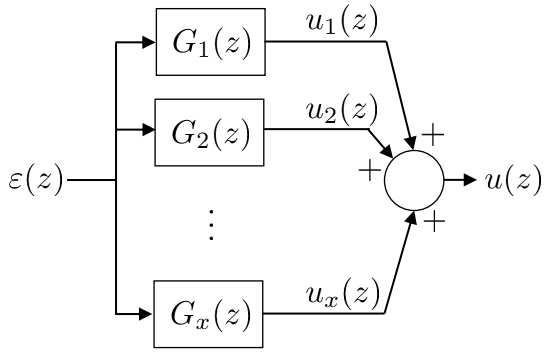

Figure 5.18: Block diagram of a stationary reference frame parallel controllers' structure.

There are different controllers that could be used in this reference frame, as the PI conntroller in the stationary reference frame (see Section 5.7.3.1), the PR controller (see Section 5.7.3.2) or the RC (see Section 5.7.3.3).

5.7.3 Current and voltage controllers

There are different controllers proposed in the literature for current and voltage control [200]:

- **Hysteresis control:** Although simple and robust, it does not guarantee zero steady-state error and different techniques must be applied in order to overcome problems derived from a variable switching frequency and interference among phases.
- **Dead-beat controller:** needs a good plant model.
- **Repetitive controllers:** based on a delay, allow control of multiple frequency components with a single transfer function.
- **Integrator-based regulators:** They are robust and guarantee zero steady-state error. Their most common forms are:
  - ◇ Multisynchronous PI: requires a particular frame for each harmonic and sequence to be controlled.
  - ◇ Stationary frame multiresonant: operates in stationary reference frame
  - ◇ A mix of the previous two.

Integrator-based regulators and repetitive controllers are explained in the following sections.

5.7.3.1 PI controllers

In the transfer function of a PI (5.6), K_p is the proportional gain and K_i the integral gain. The integral gain is proportional to the integral of the control error, so it is related to the past values of the control error and can achieve zero steady-state error [203]. In a PI controller (5.6), parameters are relatively easy to design and implement [201].

$$PI(s) = K_p + \frac{K_i}{s} \tag{5.6}$$

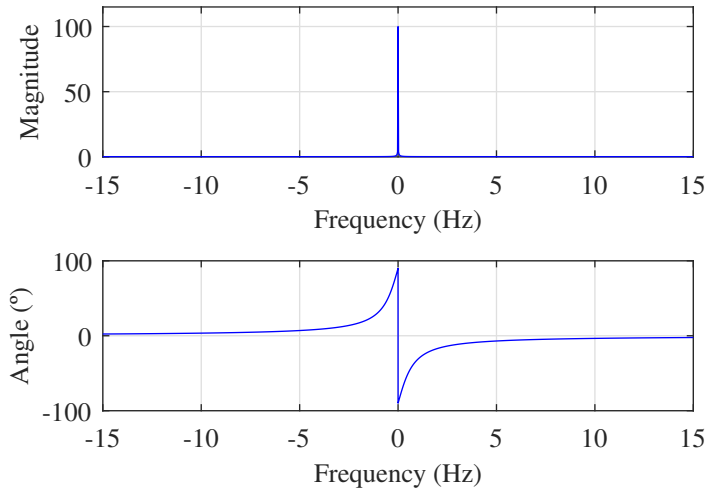

Figure 5.19: Frequency response of a PI controller.

The frequency response of a PI is shown in Fig. 5.19.

PI controllers can also be implemented in a synchronous reference frame (see Fig. 5.20), also known as ROGI controllers. In this case, there is no need to perform all the reference frame transformations needed in Section 5.7.2.1 for the control of the different harmonics, while still having the benefits of using a PI controller.

These regulators can be discretized using different approximations; bilinear (or Tustin) approximation is often used [204].

5.7.3.2 PR controllers

A PR-controller (also known as SOGI controllers) is equivalent to the addition of two PIs rotating in different directions at a given frequency ω_0 [192, 200, 205]:

$$PR(s) = PI^{+} + PI^{-} = K_p + \frac{K_i}{s + j\omega_0} + K_p + \frac{K_i}{s - j\omega_0} \tag{5.7}$$

with the resulting transfer function:

$$PR(s) = K_{p1} + \frac{K_{i1}}{s^2 + \omega_0^2} \tag{5.8}$$

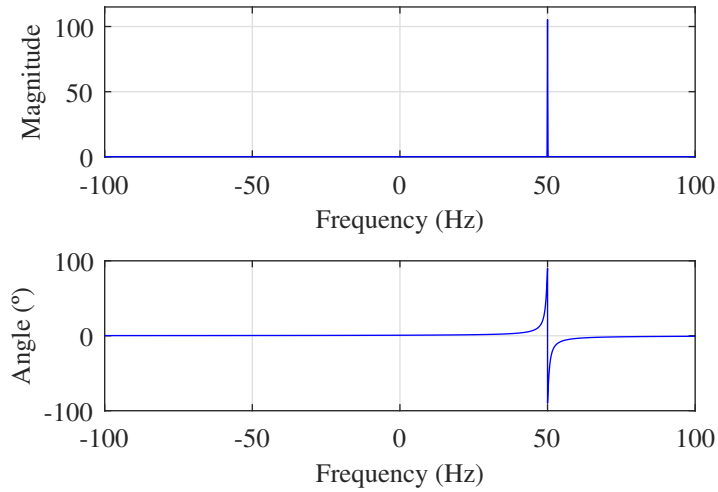

Figure 5.20: Frequency response of a PI controller in the stationary reference frame.

where $K_{p1} = 2K_p$ and $K_{i1} = 2K_i$.

These controllers are more complex than PIs because they are a second-order transfer function, but they can track a sinusoidal reference at a given frequency with zero steady-state error due to their theoretical infinite gain at that resonance frequency (ω_0). They are normally implemented in stationary reference frame, so they avoid coordinate transformations. In addition, they can track both positive and negative sequences due to their symmetric frequency response, as seen in Fig. 5.21, compared with Fig. 5.20. This means that in Fig. 5.17, once the rotation is made, one controller is enough to control both the 6^{th} and the -6^{th} components (which were the 7^{th} and -5^{th}, respectively, in the stationary reference frame). This is the same for other higher-order harmonics, as the 13^{th} and the -11^{th} and so on, reducing the total number of controllers needed and simplifying the whole control structure [184, 190, 200, 206]. As a drawback, they cannot be saturated independently, which may limit the voltage-utilization.

These regulators can be discretized using different approximations, as forward Euler, backward Euler, zero-order hold, first-order hold, zero-pole matching or Tustin [205, 206]. The selection of the method is crucial and more critical than in the PI. According to [206], some of these methods are more suitable than others to obtain zero steady state error at high frequencies and reduced sampling rates, as the impulse invariant or Tustin with prewarping. Tustin without prewarping

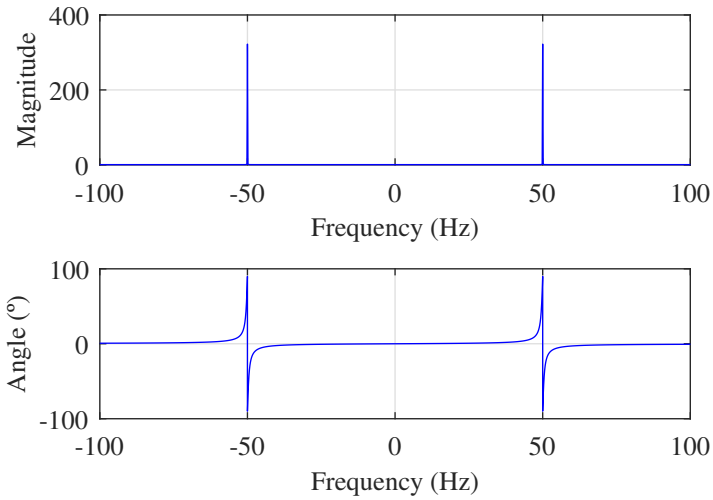

Figure 5.21: Frequency response of a PR controller.

can produce significant steady-state error due to resonant poles displacement, which increases with the sampling period and the harmonic order, but can be used with relatively good results for fundamental components and low order harmonics. The impulse invariant and the first-order hold methods are also good alternatives.

5.7.3.3 Repetitive control

The RC is able to control all the harmonics of the fundamental frequency (ω_1, e.g. $2\pi 50$ rad/s in the European grid) having poles at $s = \pm jh\omega_1$, being h = 0, 1, 2,..., of a periodic signal with a period of $T_p = \frac{2\pi}{\omega_1}$ [207]. Its transfer function can be expressed as:

$$RC(s) = \frac{\mathrm{e}^{-T_p s}}{1 - \mathrm{e}^{-T_p s}} \tag{5.9}$$

The frequency response of this transfer function is shown in Fig. 5.22. The sampling period (T_s) in this case must be selected in such a way that $N_{\mathrm{RC}} = \frac{T_p}{T_s}$ is an integer number, so the discretization of (5.9) can be performed by replacing $\mathrm{e}^{-T_p s}$ by $\mathrm{z}^{-N_{\mathrm{RC}}}$ [207].

As PR controllers, they provide infinite open-loop gain at the harmonic frequencies. Their main benefit is the low computational space required for their

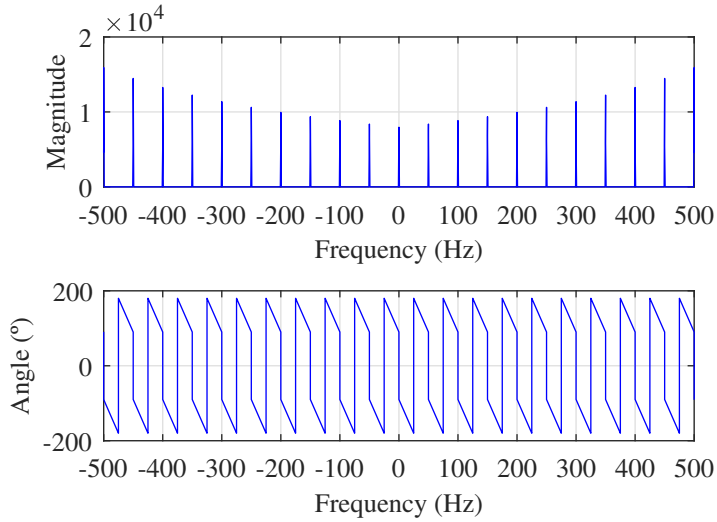

Figure 5.22: Frequency response of a RC.

implementation. While PR controllers have to be manually tuned for each component under control, the RC can deal with all the harmonics within its bandwidth. However, they cannot be independently tuned [208, 209]. In addition, although theoretically very interesting, the implementation of RCs have drawbacks that increase their complexity. For example, these controllers are very sensitive to grid frequency variations, which is easier to happen in microgrids, since they are weaker than the classical grid. When this happens, N_{RC} is not an integer number anymore and the performance starts to deteriorate [208]. Another issue is that their gain needs to be limited at high frequencies to ensure stability, due to delays introduced by filters and sampling at those frequencies [209].

5.7.3.4 Conclusions

Among all the existing regulators, the most interesting ones due to their performance and implementation are the PI, PR and RC controllers. Among them, the easiest to implement and tune are the PI controllers. On one hand, if they are to be implemented in synchronous reference frame there is a need of performing a rotation in their basic structure. On the other hand, they can be implemented in the stationary reference frame and perform Park transformations in the complex vector under controlled. The PR controllers work similarly as the

PI controllers, but they can control two components at the same time, due to an increased order in the transfer function. Since they are implemented in the synchronous reference frame, there is no need to perform Park transformations in the control signal. Finally, RCs are a very interesting alternative due to their low computational requirements while controlling a great number of harmonics in the system. However, several drawbacks related to their implementation complicate its use outside the simulation environment.

5.8 Conclusions

Microgrids connected or not to the main grid have increased their number and size in recent years. An autonomous building, considered as a nanogrid, can include power generation and consumption. The main converter in the building must be able to control the fundamental component (either of the current or the voltage, depending on whether it is working in grid feeding or grid forming configuration, respectively). In addition, it must be able to control those harmonics that the output filter is not able to filter/mitigate to maintain the power quality in the grid. Due to single-phase loads there is also going to be a homopolar/zero-sequence component. To control this component, a neutral wire must be distributed. The best way to do this is by using an extra 4^{th} leg in the converter.

Several controllers can be used for this matter. Among the existing ones, the most attractive due to their simplicity are the PI and the PR controllers. The first ones will be used in Chapter 6, while PR controllers will be used together with PI controllers in Chapter 7. Independently of their structure, converters will suffer from saturation problems under heavy load conditions, supply voltage drop or sudden change of power demand, among other reasons. This saturation must be correctly handled so there are no instabilities in the converter, both during saturation but also when returning to a normal operation state. This problem worsens in the case of several controllers in parallel, which is the case when having fundamental and harmonics control.

In Chapter 6, a realizable references methodology for multifrequency controllers is presented for 3-phase systems. Finally, in Chapter 7, basic control of the 3P4L converter for the smart building in Section 1.2 is developed, including experimental validation.

Chapter 6

Realizable reference anti-windup implementation for parallel controllers in multiple reference frames

6.1 Introduction

As seen in Chapter 5, parallel controller structures are often used for the control of harmonic components in those power converters including harmonic compensation functions. The harmonic compensation can be distorted during voltage saturation of the power converter output. This chapter proposes an implementation of the realizable reference anti-windup technique suitable for parallel controllers in multiple reference frames. The proposed implementation does not require a particular type of controllers nor special formulations.

The chapter is organized as follows: saturation problems and the state of the art are introduced in Section 6.2, the realizable reference anti-windup implementation for parallel controllers is explained in Section 6.3; different saturated voltage vector selection strategies are described in Section 6.4; the comparison of the proposed strategies is analyzed in Section 6.5, where simulation results in

open and closed-loop are provided with a special focus in grid-forming applications; experimental results are presented in Section 6.6; finally, a summary of proposed ideas can be found in Section 6.7.

6.2 Saturation problems

Despite the controller type or design, there is always a maximum voltage available for compensation. Due to this, the current controller voltage demand can exceed the maximum available voltage under heavy load conditions, supply voltage drop, or if there is a sudden change of power demand.

There are different anti-windup methods for parallel controllers in the literature [169, 201, 210–213]. Saturation can be partially avoided if the voltage maximum is increased. However, this is not easy to performance. Firstly, at a certain voltage level the switches reach their nominal voltage. To further increase the voltage, there is a need of substituting them for higher voltage rating components, normally more expensive and with higher switching losses, or completely changing the topology to multilevel converters. Moreover, in those applications where the input voltage is variable (PV panels, batteries...), increasing the voltage would require more components, increasing the complexity and cost of the overall system. Finally, higher voltages increase electromagnetic noise and reduce safety [199]. As a conclusion, DC-link voltage cannot be increased indefinitely, so finally entering into saturation sometimes will be unavoidable.

During saturated state, two problems may arise: controller wind-up and harmonic distortion. The controller wind-up can be avoided by individually saturating the parallel controllers to different preset values [169]. However, this solution does not ensure an efficient voltage utilization and correct transition from saturated to non-saturated state, since it just clamps the output of the regulators. This means that if one of the regulators needs to provide more voltage than the one assigned to it during the design stage, it will be saturated, whether or not there is enough voltage left by the rest of the regulators.

A back-tracking algorithm with proportionally assigned gains for each controller has been proposed [210] to overcome this issue. Again, the need for gain tuning makes the solution inefficient in a general case. A state feedback anti-windup algorithm is proposed in [211]. This solution is essentially the same as [169, 210] with a state-space formulation. A conditional cancellation of the multiple reference frame parallel controllers is proposed in [201]. It requires tun-

ing of a voltage threshold to disable the controller integrators as well as the calculation of the control signal derivative to enable and disable the cancellation of the different controllers. The slow dynamic response of this solution makes it inefficient for continuously varying conditions. In addition, it requires a particular controller structure.

An effective realizable reference (RR) anti-windup technique has been recently presented for stationary reference frame parallel controllers [212, 213]. The implementation requires a special formulation for the controller since it is efficiently implemented as a single transfer function. Unfortunately, this prevents manipulation of the individual parallel controllers outputs, which can be used to minimize harmonic distortion as will be discussed next. Moreover, the solution cannot be used when different types of controllers are used, or in different reference frames.

Along with the windup problem, saturation also produces waveform distortion in the controlled signals and there have been different proposals to mitigate its effect [184, 199, 202, 214–219]. A trajectory analyzer is proposed in [184, 214] to limit the controller output in case of saturation and avoid harmonic injection. This analyzer is used to adapt the output voltage in stationary reference frame. The main drawback is that due to its complexity it is limited to fundamental and negative sequence harmonic controllers. In addition, the saturation is considered with respect to the hexagon inner circle, limiting the DC-link usage.

A back-tracking scheme is proposed in [215] for a parallel structure based on ROGI in multiple reference frames. When output saturation is produced, the different voltage components are adjusted in such a way that lesser priority harmonics are removed from compensation. Although simpler, this method does not eliminate distortion entirely and requires a particular controller structure.

[216] proposes also a saturation scheme for a parallel structure based on ROGI. When output saturation is produced, the different voltage components are adjusted following an equal and pre-commissioned gain adjustment. The dynamic behavior of this method is improved in [217], while it is extended to multi-phase machines in [218]. The main drawbacks of this method are the required tuning process and the dynamic performance, since the gain adjustment is driven by integral controllers. controllers.

In [202], a partial current harmonic compensation for dual three-phase permanent magnet synchronous machines (PMSM) is proposed, based on manipulating the reference signals for the current harmonics. Since this scheme is presented for an electric machine, torque production (fundamental component) is favored over the current harmonics, whose control is completely disabled if necessary. In

this paper, only 5^{th} and 7^{th} harmonics are taken into consideration; the partial compensation is based on finding the optimal compensation level for each current harmonic (λ_h) based on a previous commissioning process, which makes it impractical for general application.

[199] proposes an instantaneous method that calculates a trajectory that avoids overmodulation at every time step with the aim of reducing the total harmonic distortion (THD) maximizing the power injected to the grid. However, this method is based on analytically solving non-linear equations any time that a trajectory reduction is predicted, which also increases the complexity as the number of harmonics to compensate increases. As in [202], only the 5^{th} and 7^{th} harmonics (in addition to the positive and negative components) are considered due to the nonlinearity of the equations and the consequent time needed to carry out all the calculations. In practice, the method maintains a low THD of the injected current by decreasing the reactive power. The computational burden of this method is reduced in [219].

This chapter generalizes the instantaneous realizable reference algorithm for application in parallel controller structures which was initially drafted in conference paper [220]. The proposed anti-windup implementation allows saturation of controllers in multiple reference frames and it does not require gain tuning. In addition, it is not restricted to any special type of controllers, allowing to develop new controller types and combine different controllers in different reference frames.

The proposed implementation is independent of the strategy followed to reduce harmonic distortion during saturation. Cancellation or minimization of the compensation of lower priority harmonics during saturation is easily achieved. If required, any controller in the parallel structure can be easily disabled by just setting its output to zero. It can also be used in combination with trajectory-based methods proposed in the literature.

The saturation method is tested in a grid forming application, although it is suitable for any application (e.g. grid support, electric drives, etc.). In this regard, the chapter analyzes different options for the selection of the saturated voltage vector to minimize current waveform distortion, recommending one especially suited for grid-forming applications. In general, researchers have focused in the concept of so-called "distortion-free" saturation methods [184,199,215–218]. The main goal is preserving the sinusoidal waveform shape of the currents injected to the grid or to electrical machines, rejecting harmonic distortion to comply with grid codes or to minimize the torque ripple. However, this always implies the

reduction of the fundamental component magnitude which translates into fundamental component magnitude distortion. This will reduce the injected power to the grid or the fundamental torque component in electrical machines. In the case of electrical machines, that strategy is questionable but can still be useful for certain applications. However, it will be shown that for grid-forming applications in the presence of non-linear loads, the saturation strategy goal might be different since the preservation of the fundamental component magnitude is a main requirement. This chapter analyzes this extent.

6.3 Realizable reference for parallel controllers

6.3.1 Basic concept

The transfer function of a discrete-time controller can be expressed as

$$D(z) = \frac{u(z)}{\varepsilon(z)} = \frac{b_0 + b_1 z^{-1} + \cdots + b_n z^{-n}}{1 + a_1 z^{-1} + \cdots + a_n z^{-n}} \tag{6.1}$$

assuming it has the same number n of poles as zeroes, where u is the controller output (i.e. inverter output voltage in a current controller); ε is the error signal (i.e. current error in a current controller); and b_i and a_i ($i = 1, 2, ...n$) are the polynomial coefficients. Please, note that u and ε can be either scalar or complex vector quantities, as well as the polynomial coefficients..

The assumption of having the same number of poles as zeroes is not very restrictive since all continuous-time controllers discretized using the bilinear (Tustin), matched pole-zero, first-order hold, or backward Euler approximations will meet this condition. For the zero-hold, forward Euler, or modified matched pole-zero approximations this condition is not necessarily met, resulting in discrete-time transfer functions that may have one more pole than zeroes. This can be circumvented by adding $\frac{T}{2}(z+1)$ to the numerator controller, where T is the sampling period; the new controller exhibiting a very similar response. Nevertheless, the discussion will be later extended to the case the controller transfer function might have a different number of poles than zeroes.

The difference equation needed for computer (e.g. microcontroller) implementation can be easily obtained as

$$u[k] = \sum_{i=0}^{n} b_i \varepsilon[k-i] - \sum_{i=1}^{n} a_i u[k-i] \tag{6.2}$$

The controller output must be limited to the actuator operating range to avoid controller windup. In case of scalar output (i.e. using DC power source), a maximum and minimum voltage will be easily set

$$u[k] = u_{\text{sat}} = \begin{cases} u_{\max}, \text{if } u[k] > u_{\max} \\ u_{\min}, \text{if } u[k] < u_{\min} \end{cases} \tag{6.3}$$

In case of a complex vector output (i.e. using a three-phase inverter), more complicated expressions apply. Fig. 6.1(a) shows the maximum allowable voltage range using a three-phase inverter. It is given by a hexagon with radius $\frac{2}{3}V_{\text{DC}}$ and apothem $\frac{V_{\text{DC}}}{\sqrt{3}}$, being V_{DC} the DC-link voltage, as seen in Section 5.4.2. When the amplitude of a voltage command u surpasses the voltage hexagon limits, its amplitude must be limited or its phase distorted. In this case, multiple options exist. Commonly used options are shown in Fig. 6.1(a): u_{sat} keeps the original vector angle; u_{sat1} maximizes $q-$axis component; u_{sat2} maximizes the $d-$axis component. The hexagon limitation maximizes the inverter voltage utilization but brings implementation complexity, reference frame dependence, and the injection of additional harmonics when the voltage moves along the hexagon sides. To avoid this, the hexagon inscribed circle seen in Fig. 6.1(b) is often selected as voltage limit.

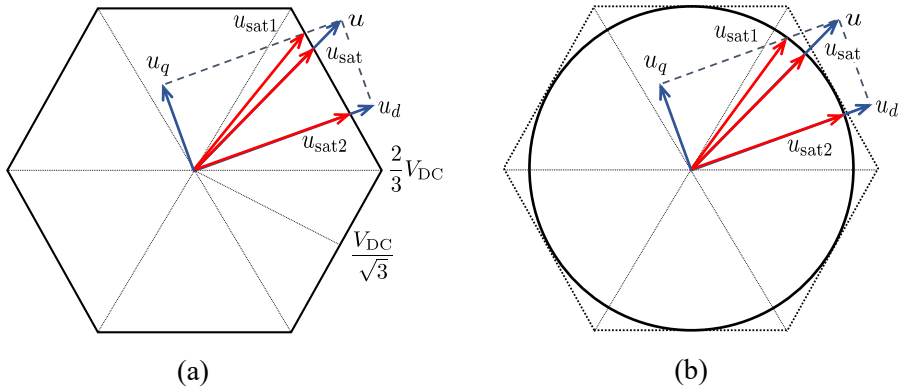

Figure 6.1: Complex vector voltage limits. (a) Hexagon saturation. (b) Circle saturation.

Limitation of the digital controller output to the actuator limits prevents from windup, but does not ensure a correct controller operation during the saturation

state and a fast transition to normal operation when the saturation cause ceases. There exist different anti-windup mechanisms, as described in Section 6.2; the back-calculation or realizable reference method [221,222] being the most effective and straightforward for digital implementation. It consists of calculating the error signal that would have made the controller to exactly produce the saturated output

$$\varepsilon_{\text{sat}} = \frac{1}{b_0}\left(u_{\text{sat}} - \sum_{i=1}^{n} b_i \varepsilon[k-i] + \sum_{i=1}^{n} a_i u[k-i]\right) \tag{6.4}$$

This value will be used as the previous step error signal in the next control period. This makes the controller always operate in the linear region, even under output saturation. Calculation of ε_{sat} requires recalculating the last two terms on the right side of (6.4) or storing those values during the controller computation. A simpler implementation is proposed next for later extension to parallel controllers.

6.3.2 Efficient implementation

The controller difference equation seen in (6.2) can be rewritten by extracting the first polynomial coefficient out of the summation

$$u[k] = b_0 \varepsilon[k] + \sum_{i=1}^{n} b_i \varepsilon[k-i] - \sum_{i=1}^{n} a_i u[k-i] \tag{6.5}$$

In case of saturation, the saturated controller output as a function of the realizable error (i.e. realizable reference minus actual output) can be calculated as

$$u_{\text{sat}} = b_0 \varepsilon_{\text{sat}} + \sum_{i=1}^{n} b_i \varepsilon[k-i] - \sum_{i=1}^{n} a_i u[k-i] \tag{6.6}$$

By subtracting (6.5) from (6.6) a simpler expression only dependent on the last terms can be obtained

$$u_{\text{sat}} - u[k] = b_0 \left(\varepsilon_{\text{sat}} - \varepsilon[k]\right) \tag{6.7}$$

Therefore, the realizable error can be easily calculated by only using the actual period input and output of the controller

$$\varepsilon_{\text{sat}} = \varepsilon[k] + \frac{1}{b_0}\left(u_{\text{sat}} - u[k]\right) \tag{6.8}$$

6.3.3 Parallel controllers in stationary reference frame

In grid-forming, grid-connected, or active filter inverters, parallel controllers are often used for the control of the fundamental current (or voltage) and its harmonics (see Section 5.7.1). A structure using stationary reference frame parallel controllers can be seen in Fig. 5.18.

A back-calculation or realizable reference anti-windup implementation has been proposed for a parallel structure composed of one proportional plus resonant harmonic controllers [212, 213]. The implementation in [212, 213] allows independent design of the fundamental and harmonic controllers and a straightforward anti-windup computation. The drawbacks are:

1. It requires a special arrangement of the controllers.
2. The structure is limited to proportional plus resonant controllers.
3. Individual controller outputs cannot be analyzed or limited.
4. It is only intended for controllers implemented in stationary reference frame.

The anti-windup implementation proposed in this paper overcomes those limitations.

The difference equation for the individual controllers are:

$$u_1[k] = b_{1,0}\,\varepsilon[k] + \sum_{i=1}^{n_1} b_{1,i}\,\varepsilon[k-i] - \sum_{i=1}^{n_1} a_{1,i}\,u_1[k-i] \tag{6.9a}$$

$$u_2[k] = b_{2,0}\,\varepsilon[k] + \sum_{i=1}^{n_2} b_{2,i}\,\varepsilon[k-i] - \sum_{i=1}^{n_2} a_{2,i}\,u_2[k-i] \tag{6.9b}$$

$$\vdots$$

$$u_x[k] = b_{x,0}\,\varepsilon[k] + \sum_{i=1}^{n_x} b_{x,i}\,\varepsilon[k-i] - \sum_{i=1}^{n_x} a_{x,i}\,u_x[k-i] \tag{6.9c}$$

They are computed as x independent controllers, where $u_j (j = 1, 2, \cdots, x)$ are the controller outputs, and $b_{j,i}$ and $a_{j,i} (i = 1, 2, \cdots, n)$, are the discrete-time

controllers' coefficients. Please, note the error signal is common for all of them (see Section 5.7.2). The total controller output is the sum of the individual controller outputs

$$u_T[k] = \sum_{i=1}^{x} u_i[k] \tag{6.10}$$

An identical result is obtained by summing the controllers' difference equations in (6.9), resulting in

$$u_T[k] = \sum_{l=1}^{x} b_{l,0}\ \varepsilon[k] + \sum_{l=1}^{x}\sum_{i=1}^{n_l} b_{l,i}\ \varepsilon[k-i] - \sum_{l=1}^{x}\sum_{i=1}^{n_l} a_{l,i}\ u_l[k-i] \tag{6.11}$$

Similarly to the single controller case, replacing the actual output and error signal by their saturated counterparts, gives

$$u_{\text{sat}} = \sum_{l=1}^{x} b_{l,0}\ \varepsilon_{\text{sat}} + \sum_{l=1}^{x}\sum_{i=1}^{n_l} b_{l,i}\ \varepsilon[k-i] - \sum_{l=1}^{x}\sum_{i=1}^{n_l} a_{l,i}\ u_l[k-i] \tag{6.12}$$

Finally, subtracting (6.11) from (6.12), and after clearing ε_{sat}, yields to

$$\varepsilon_{\text{sat}} = \varepsilon[k] + \frac{1}{\sum_{l=1}^{x} b_{l,0}} \left(u_{\text{sat}} - u_T[k]\right) \tag{6.13}$$

The obtained result shows the error back-calculation process is as simple as for the single controller. It must be remarked that (6.11) does not need to be computed; the parallel implementation, (6.9) and (6.10), are used instead. Finally, the fraction of saturation voltage corresponding to each parallel controller must be calculated

$$u_{l\_\text{sat}} = u_l[k] + b_{l,0}\left(\varepsilon_{\text{sat}} - \varepsilon[k]\right) \ \text{ for } l = 1, 2, ..., x \tag{6.14}$$

It is noted that only (6.13) and (6.14) must be computed for the anti-windup implementation once the saturated voltage (u_{sat}) is obtained. This implementation is advantageous since it allows disabling some harmonic controllers in case of saturation as it will be discussed in Section 6.4. Moreover, it mitigates rounding errors when combining large and small coefficients of the parallel controllers in

a single controller implementation due to the numerical precision of the digital system [223].

In a general case, the parallel controllers can be designed and implemented in different reference frames (see Section 5.7.2). Therefore, a realizable reference anti-windup implementation for multiple reference frames will be described next.

6.3.4 Parallel controllers in multiple reference frames

Different reference frames can be used for the design and implementation of the different controllers in the parallel structure (see Section 5.7.2) as can be seen in Fig. 5.16.

The difference equations for the parallel controllers can be expressed as

$$u_1^{f1}[k] = b_{1,0}\ \varepsilon^{f1}[k] + \sum_{i=1}^{n_1} b_{1,i}\ \varepsilon^{f1}[k-i] - \sum_{i=1}^{n_1} a_{1,i}\ u_1^{f1}[k-i] \tag{6.15a}$$

$$u_2^{f2}[k] = b_{2,0}\ \varepsilon^{f2}[k] + \sum_{i=1}^{n_2} b_{2,i}\ \varepsilon^{f2}[k-i] - \sum_{i=1}^{n_2} a_{2,i}\ u_2^{f2}[k-i] \tag{6.15b}$$

$$\vdots$$

$$u_x^{fx}[k] = b_{x,0}\ \varepsilon^{fx}[k] + \sum_{i=1}^{n_x} b_{x,i}\ \varepsilon^{fx}[k-i] - \sum_{i=1}^{n_x} a_{x,i}\ u_x^{fx}[k-i] \tag{6.15c}$$

After computation of the parallel controllers, the total output can be easily obtained

$$u_T[k] = \sum_{l=1}^{x} u_l[k] = \sum_{l=1}^{x} u_l^{fl}[k]\ \mathrm{e}^{\,\mathrm{j}\theta_l[k]} \tag{6.16}$$

where $\theta_l[k]$ is the angular position of the fl reference frame in the actual sampling period and 'e' the Euler number.

Summing the difference equations in (6.15) after transforming them to a sta-

tionary reference frame, gives

$$\begin{aligned} u_T[k] = &\sum_{l=1}^{x} b_{l,0}\ \varepsilon^{fl}[k] \mathrm{e}^{\ \mathrm{j}\theta_l[k]} + \sum_{l=1}^{x} \left(\sum_{i=1}^{n_l} b_{l,i}\ \varepsilon^{fl}[k-i] \right) \mathrm{e}^{\ \mathrm{j}\theta_l[k]} \\ &- \sum_{l=1}^{x} \left(\sum_{i=1}^{n_l} a_{l,i}\ u_l^{fl}[k-i] \right) \mathrm{e}^{\ \mathrm{j}\theta_l[k]} \end{aligned} \tag{6.17}$$

Writing the synchronous reference frame error signal in (6.17) in terms of the stationary reference frame error signal

$$\varepsilon^{fl}[k] = \varepsilon[k] \mathrm{e}^{-\ \mathrm{j}\theta_l[k]} \tag{6.18}$$

results in

$$\begin{aligned} u_T[k] = &\sum_{l=1}^{x} b_{l,0}\ \varepsilon[k] + \sum_{l=1}^{x} \left(\sum_{i=1}^{n_l} b_{l,i}\ \varepsilon^{fl}[k-i] \right) \mathrm{e}^{\ \mathrm{j}\theta_l[k]} \\ &- \sum_{l=1}^{x} \left(\sum_{i=1}^{n_l} a_{l,i}\ u_l^{fl}[k-i] \right) \mathrm{e}^{\ \mathrm{j}\theta_l[k]} \end{aligned} \tag{6.19}$$

This expression contains both the total controller output and the actual sample error signal in stationary reference frame.

Following the same thought process as in stationary reference frame, both the actual voltage and error signal can be replaced by the saturated versions

$$\begin{aligned} u_{\mathrm{sat}} = &\sum_{l=1}^{x} b_{l,0}\ \varepsilon_{\mathrm{sat}} + \sum_{l=1}^{x} \left(\sum_{i=1}^{n_l} b_{l,i}\ \varepsilon^{fl}[k-i] \right) \mathrm{e}^{\ \mathrm{j}\theta_l[k]} \\ &- \sum_{l=1}^{x} \left(\sum_{i=1}^{n_l} a_{l,i}\ u_l^{fl}[k-i] \right) \mathrm{e}^{\ \mathrm{j}\theta_l[k]} \end{aligned} \tag{6.20}$$

By subtracting (6.19) from (6.20), and after clearing $\varepsilon_{\mathrm{sat}}$, equation (6.13) is again obtained. Therefore, there is no difference in the calculation of the realizable error signal between the implementation in stationary or multiple reference

frames. However, a final step is required in this case to provide the realizable error signal in each of the multiple reference frames

$$\varepsilon_{\text{sat}}^{fl} = \varepsilon_{\text{sat}}\ \mathrm{e}^{-\ \mathrm{j}\theta_l[k]}\ \text{for}\ l = 1, 2, ..., x \tag{6.21}$$

The saturation voltage corresponding to each controller in the parallel structure can be then calculated similarly to the stationary reference frame case

$$u_{l\_\text{sat}}^{fl} = u_l^{fl}[k] + b_{l,0}\left(\varepsilon_{\text{sat}}^{fl} - \varepsilon^{fl}[k]\right)\ \text{for}\ l = 1, 2, ..., x \tag{6.22}$$

6.3.5 Controllers with different number of poles and zeroes

As stated, the former expressions assume each controller discrete-time transfer function has the same number of poles as number of zeroes. Note this does not mean all the controllers in the parallel structure must have the same number of poles, it means that all the controller outputs are updated with the error value at the present instant. However, similar results can be obtained if the controllers have a different number of poles than zeroes while all of them have the same pole/zero difference:

$$n_1 - m_1 = n_2 - m_2 = \cdots = n_x - m_x \tag{6.23}$$

where m_l are the number of zeroes of controllers $l = 1, 2, ..., x$.

where m_l are the number of zeroes of controllers $l = 1, 2, ..., x$. This means that all the controllers are updated with the same previous instant error value. Otherwise, a more complex and unpractical saturation scheme should be derived, in case the different controllers were updated with the error at different time instants. Although mathematically possible, this situation will not occur in practice.

6.4 Saturation strategies

The previous section has demonstrated the realizable reference anti-windup technique can be easily implemented in the case of parallel controllers independently of the reference frame. This technique ensures a fast transition from saturated to non-saturated state. However, this does not imply correct harmonic compensation or fundamental component realization during the saturated state. As it was described in the introduction, several researchers [184, 199, 201, 202, 214–217]

have dealt with the problem of the voltage command adaptation during saturation. The use of the realizable reference technique will further simplify the introduction of compensation mechanisms but the fundamental component production and the harmonic distortion will depend on the selection of the saturated complex vector. As it was seen in Fig. 6.1, multiple saturation options exist when the controller output magnitude exceeds the hexagon limits. In the case of parallel controllers, an increased number of options exist. Fig. 6.2 shows the options analyzed in this paper. It is considered that four parallel controllers would provide four voltage commands to exemplify the different analyzed options. The controllers are sorted (and numbered) in order of importance regarding fundamental component production and harmonic compensation, being u_1 the fundamental component.

Fig. 6.2(a) shows the first option that will be termed "Global" in this discussion. In this case, the resulting vector addition of the parallel controllers is compared with the hexagon limits. Since the magnitude exceeds the limits, the output voltage will be limited to the hexagon but keeping the original angle. This can be also applied using the inscribed circle limits for simpler implementation and lower harmonic distortion, but worst voltage utilization.

Fig. 6.2(b) shows another option, termed "Incremental 1", in which the saturated voltage is calculated from the first component crossing the hexagon (or circle) limit. The remaining voltage components are disregarded. A modified version is shown in Fig. 6.2(c), termed "Incremental 2". The same idea applies, but the saturated vector is calculated also rejecting the component crossing the hexagon (or circle) limit.

A fourth approach can be seen in Fig. 6.2(d), called "Group". This is the proposed method in this paper. The different components are grouped in two: the fundamental u_1 and the addition of the remaining voltage vectors u_h. A similar saturation technique to that described for Fig. 6.2(b) is then applied. An optimal version of this method is proposed in [202] where an algorithm decides each instant the weighting for the harmonic reduction. However, its complexity makes it difficult for grid-forming applications where several harmonics are compensated and the load type is subject to change.

Once the saturated vector is calculated following one of the described methods, no special treatment must be done to the controllers which outputs are disregarded, since the back-calculation method described in the previous section will automatically disable them in practice. It is also noted that the voltage vector is checked at every control step and no action is taken if the voltage is within

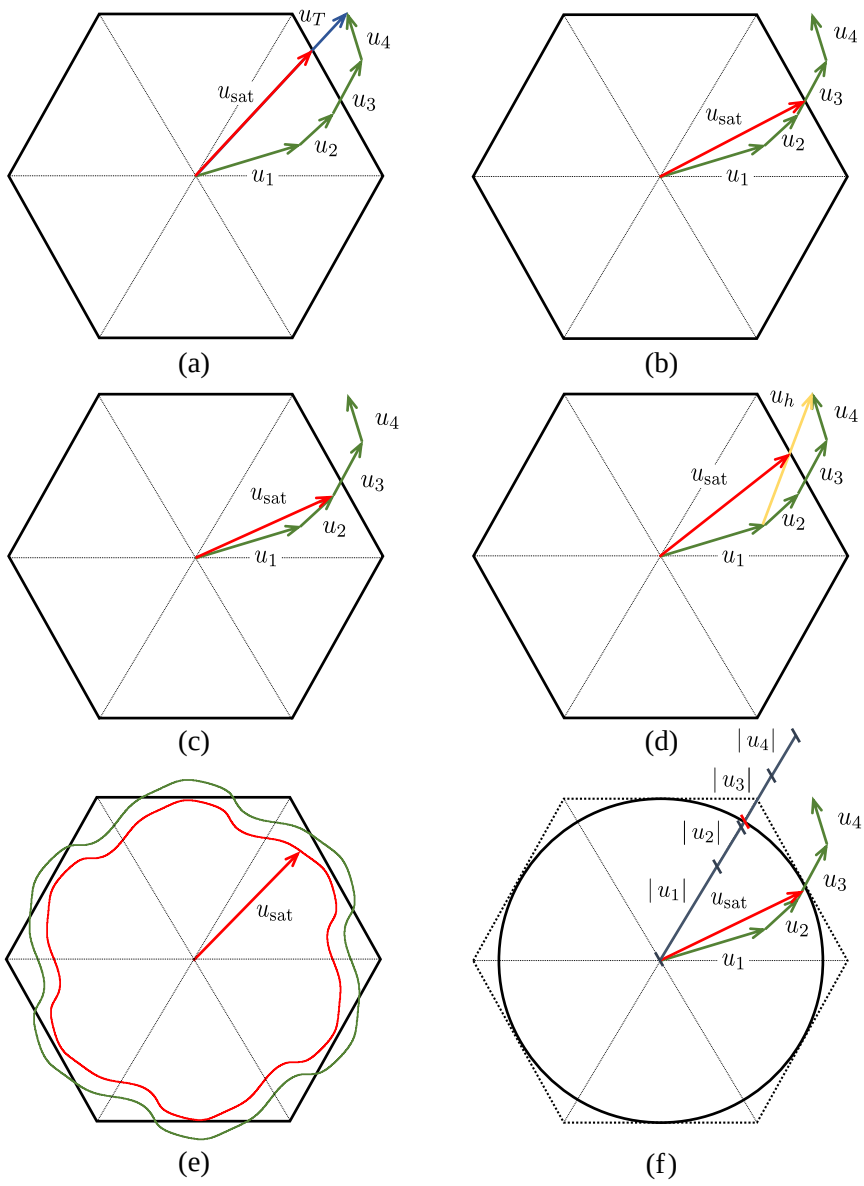

Figure 6.2: Saturation options analyzed: (a) Global. (b) Incremental 1. (c) Incremental 2. (d) Group (proposed method). (e) Trajectory. (f) Magnitude-based.

limits.

The above-described methods provide an instantaneous voltage command at each modulation step, but can increase the harmonic distortion due to the clipping of the voltage trajectory to the hexagon or voltage limits during saturation. Trajectory-based methods adapt the current commands to force the current controllers to produce voltage command outputs within the voltage limits in the whole fundamental voltage trajectory. In [201, 215] the harmonic controllers are progressively disabled when saturation is detected to make the voltage trajectory fit in the limits. Researchers have also proposed "distortion-free" saturators where the voltage trajectory is adapted to be contained within the voltage limits with no harmonic distortion. An example can be seen in Fig. 6.2(e) where all the components have been proportionally reduced to fit in the hexagon limits. This solution has been proposed in [184, 214] for the inscribed circle limit and in [199, 216–218] using the hexagon. The disadvantage of these methods is the increased complexity and lesser voltage utilization compared with the above-described methods. They are well suited for low-harmonic distortion current injection in grid supporting applications but could not be advisable in grid forming applications, where the magnitude of the fundamental voltage component is key. In addition, they still need a proper controller anti-windup method during the trajectory adaption. Therefore, they can be also benefited from the anti-windup implementation proposed in Section 6.3.

The last approach, seen in Fig. 6.2(f), can be seen as a simpler but less voltage-efficient implementation of trajectory-based methods. In this case, the magnitudes of the voltage vector components coming from the current controllers are added and compared with the circle voltage limit. The magnitude of the first voltage component crossing the inner circle will be limited, and the higher-order or less important components disregarded. Another option is to proportionally reduce all components to resemble "distortion-free" methods. Both solutions theoretically eliminate voltage clipping during steady saturation. The first case will favor the fundamental component magnitude while the second a low THD. Due to both the relative angular position of the harmonic voltage components is not considered, and the circle is used as voltage limit to make it simple, the voltage utilization will be poor. It is also noted that this solution might modify the voltage vector trajectory in cases it would fit within the voltage limits for the first reason. This solution will be termed "Magnitude" for comparison.

6.5 Comparison of saturation strategies

The distortion introduced by the different methods will depend both on the saturation level and the type of loads present in the system. A grid forming scenario has been used to test the described alternatives. Fig. 6.3 shows a three-phase inverter with an output LC filter, an unbalanced three-phase linear load, and a non-linear load. The main system parameters can be found in Table 6.1. The linear and non-linear loads draw about 40 % and 35 % of the rated power respectively.

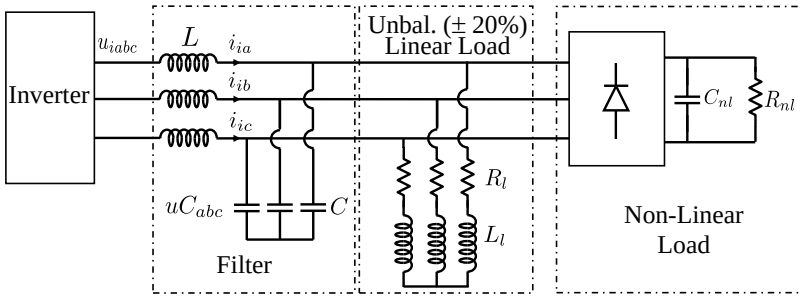

Figure 6.3: Test system: Grid forming scenario including unbalanced and non-linear loads.

Table 6.1: System Parameters

Rated voltage	V_r	400 V_{rms}
Rated current	I_r	144 A_{rms}
Filter	L	260 µH
Filter	C	270 µF
Linear load	R_l	3.36 Ω
Linear load	L_l	6.6 mH
Linear load	Unbalance	±20 %
Non-linear load	C_{nl}	1 mF
Non-linear load	R_{nl}	8.35 Ω

The inverter control goal is to obtain a balanced three-phase voltage at the filter output. The quality of this voltage will be used to benchmark the different methods. The necessary current to achieve this goal can be easily calculated by

replacing the inverter and the filter inductor L by an ideal three-phase source. Fig. 6.4(a) shows the current (i_{iqd}) needed to obtain the voltage trajectory at the filter capacitor (uC_{qd}) shown in Fig. 6.4(c). It is also possible to calculate the inverter voltage trajectory (u_{iqd}) to achieve both the inverter current and the capacitor voltage, as seen in Fig. 6.4(b).

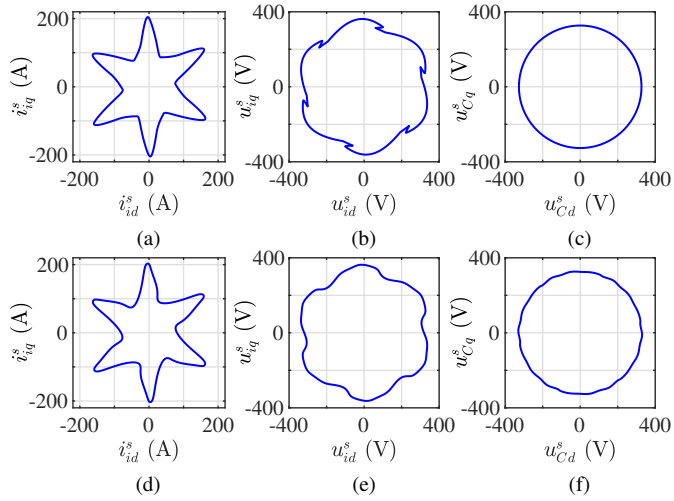

Figure 6.4: Current and voltage trajectories for the system under test. (a),(d): Inverter current. (b),(e): Inverter voltage. (c),(f): Capacitor voltage. (a)-(c): Unlimited bandwidth. (d)-(f): Considering fundamental and six main harmonics.

An unrealistic bandwidth would be needed for the current controller to produce the trajectories seen in Fig. 6.4(a)-(c). Assuming a parallel controller structure composed of a fundamental current controller, a negative sequence current controller, and five harmonic controllers the modified trajectories seen in Fig. 6.4(d)-(f) are considered. They include the fundamental voltage at 50 Hz and harmonics at -250, 350, -50, -550, 650, -850 Hz in decreasing order of magnitude. The resulting capacitor voltage shown in Fig. 6.4(f) has a small THD of 0.74 % and a magnitude error of -0.01 %. If only the fundamental component of the inverter voltage seen in Fig. 6.4(b) were injected, the THD would be 6.85 %, the magnitude error -0.1 %, and the phase-voltage unbalance 0.58 %.

If voltage saturation occurs, the previous trajectories will be distorted. The following discussion will analyze the resulting capacitor voltage trajectory when the different methods described in the previous section are used. First, open-

loop analysis using the voltage trajectory seen in Fig. 6.4(e) will be carried out. This avoids the interaction on the current controller and the time to recover from saturation to better understand the different saturation options. Later, closed-loop current control will be enabled to analyze the interaction of the current controller and the validity of the proposed realizable reference implementation, described in Section 6.3. Three levels of saturation are imposed assuming DC-link voltages of 600, 570, and 540 V. The corresponding hexagon limits can be seen in Fig. 6.5.

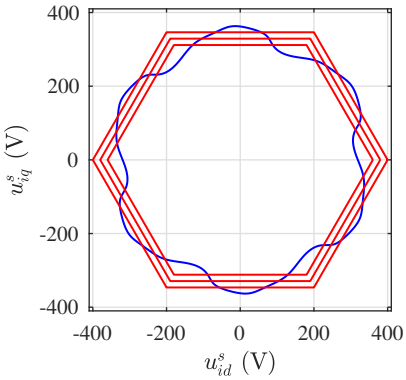

Figure 6.5: Non-saturated inverter voltage trajectory (blue) and hexagon voltage limits (600, 570, 540 V).

6.5.1 Open-loop analysis

The different saturation strategies described in Section 6.4 are analyzed in simulation. The inverter shown in Fig. 6.3 is simplified by using a linear voltage source to speed up the simulations. The voltage trajectory in Fig. 6.5 is the inverter voltage command before saturation. The measured capacitor voltage THD, fundamental voltage magnitude error, the fundamental voltage phase angle, and the phase unbalance are taken as figures of merit for the different methods. The phase angle is given with respect to the non-saturated capacitor voltage, whose trajectory is seen in Fig. 6.4(f). The phase unbalance is calculated as the difference between the fundamental peak of the highest and smallest phase voltages normalized by the mean phase voltage.

Table 6.2 summarizes the obtained results. Focusing first in the direct saturation methods, it can be seen that the "Group" strategy [see Fig. 6.2(d)] gives both

low THD and magnitude error. The "Global" strategy [see Fig. 6.2(a)] offers the second-best results for THD and magnitude errors, and the best for angle phase distortion and unbalance; in addition, it has the benefit of being the simplest for computer implementation. The "Incremental" strategies [see Fig. 6.2(b,c)] do not provide good results; this, in addition to their increased complexity, discards them for the closed-loop analysis. All methods have been tested using both the hexagon a circle limits. As expected, a better THD is obtained in all cases with the circle limit, but at the cost of a higher magnitude error and unbalance.

Voltage trajectories fitting the hexagon limit were synthesized from the original trajectory with three different strategies: decreasing the overall voltage (global), canceling harmonics until the trajectory fits in the hexagon (incremental 1 and 2), and reducing first the grouped harmonic components (group). As can be seen in Table 6.2 the global strategy preserves the original (i.e. unsaturated) THD, but the magnitude error is larger than in other methods. The small voltage margin left by the fundamental component makes the other two strategies have worst THD than non-trajectory methods. Their advantage is that they preserve better the fundamental magnitude under light saturation and the fundamental voltage phase under heavy saturation. It must be remarked that these are best-case results trying to resemble the behavior of trajectory-based methods. In practice, tracking of the feasible trajectory is not straightforward and worst results should be expected. The preservation of THD shown by the global trajectory method makes this strategy ideal for grid supporting applications, but grid forming applications require both harmonic quality and preservation of the fundamental voltage. A weighting algorithm could be implemented to trade-off THD and fundamental voltage reduction. However, that is far beyond the scope of this paper.

The "Magnitude" strategy [see Fig. 6.2(e)], shows similar results to trajectory-based methods. However, in the case of the global strategy, the worst voltage utilization by both using the circle limit and neglecting the component phases, makes the fundamental magnitude error to be significantly higher.

6.5.2 Closed-loop analysis

The validity of the proposed anti-windup algorithm is analyzed in combination with some saturation strategies selected from the previous discussion. The "Global" and "Group" strategies are selected for their implementation simplicity and good results, respectively. The online adaptation of the current commands

Table 6.2: Capacitor Voltage Distortion Using Different Saturation Strategies for Open-loop Inverter Voltage Command

	600 V				570 V				540 V			
Method	THD (%)	Mag. Error (%)	Angle (deg)	Unbal. (%)	THD (%)	Mag. Error (%)	Angle (deg)	Unbal. (%)	THD (%)	Mag. Error (%)	Angle (deg)	Unbal. (%)
Global (circle)	2.15	1.27	0	0.14	2.98	4.34	0	0.22	3.84	8.45	-0.01	0.29
Global (hexagon)	2.17	0.99	0	0.10	4.1	3.25	0.01	0.17	5.04	6.43	0	0.21
Incremental 1 (circle)	4.47	1.27	0.32	0.25	3.35	4.34	0.53	0.41	6.32	8.44	0.13	0.57
Incremental 1 (hexagon)	4.01	1.02	0.22	0.19	3.71	3.20	0.41	0.31	5.9	5.91	0.41	0.40
Incremental 2 (circle)	3.04	1.96	0.28	0.27	3.35	4.34	0.53	0.42	6.32	8.44	0.13	0.57
Incremental 2 (hexagon)	3.39	1.63	0.22	0.22	3.62	3.22	0.44	0.31	5.9	6.22	0.43	0.46
Group (circle)	1.87	1.26	0.25	0.21	2.59	4.57	0.57	0.42	2.54	10.06	0.61	0.58
Group (hexagon)	2.07	0.97	0.14	0.15	3.71	3.18	0.47	0.30	4.94	6.47	0.59	0.35
Trajectory (global)	0.74	4.58	0	0	0.74	9.35	0	0	0.74	14.13	0	0
Trajectory (incremental)	6.35	-0.07	-0.03	0.59	6.85	3.33	-0.03	0.55	6.85	8.42	-0.03	0.50
Trajectory (group)	5.45	-0.07	-0.02	0.44	6.85	3.33	-0.03	0.55	6.85	8.42	-0.03	0.50
Magnitude (global)	0.74	8.19	0	0	0.74	12.78	0	0	0.74	17.37	0	0
Magnitude (incremental)	6.35	-0.07	-0.03	0.59	6.85	3.33	-0.03	0.59	6.85	8.42	-0.03	0.59

proposed by trajectory methods is beyond the scope of this paper and they have not been implemented. However, the open-loop vs. closed-loop comparison shown in this section can be extrapolated to other methods.

The current trajectory shown in Fig. 6.4(d) is commanded to a current controller using a parallel structure (see Fig. 5.16) composed of seven complex vector PI controllers [224] for the fundamental, negative sequence, and main five harmonic components. Each controller is independently tuned in its own reference frame. In addition, the measured capacitor voltage is used as a feedforward term. This feedforward signal and the output of the fundamental current controller will be considered as the fundamental voltage component for the saturation strategy implementation. It is noted the feedforward term can also contain harmonic content during transients and also in steady-state if low harmonic distortion is not achieved.

The capacitor voltage THD using this controller and assuming no saturation is 1.03 %, the fundamental voltage component magnitude error is 0.1 %, and the phase unbalance 0.04 %. Linear sources are first used in simulation to separate the effects of the current controller bandwidth and anti-windup method from the inverter non-linear behavior. When inverter voltage saturation is introduced the results shown in Table 6.3 are obtained. Slightly increased THD and magnitude distortion values compared to those obtained for the open-loop inverter voltage are obtained. This is explained by the bandwidth limitation of the controllers. Nevertheless, the comparative results are similar to the case of open-loop voltage injection meaning than the proposed anti-windup implementation is working as expected.

To prove the validity of the described anti-windup technique, the "Group" hexagon saturation strategy was also implemented without the proposed anti-windup algorithm in two cases. One, calculating the individual output voltages after saturation according to the given strategy (see "State saturation" in Table 6.3); the second, limiting only the global controller output according to the same strategy but not calculating the individual outputs (see "No state saturation (SS)" in Table 6.3). The results are clearly worst than for the case in which the proposed anti-windup technique is enabled. However, the THD and magnitude error for the particular case of 540 V are better in case of only state saturation ("State saturation"). This is explained by the largely increased capacitor voltage phase lag respect the target value.

The same simulations were repeated with a three-phase switching inverter showing slightly increased THD values and magnitude error under low saturation

Table 6.3: Capacitor Voltage Distortion Using Different Saturation Strategies for Closed-Loop Inverter Current Injection

	600 V				570 V				540 V			
Method	THD (%)	Mag. Error (%)	Angle (deg)	Unbal. (%)	THD (%)	Mag. Error (%)	Angle (deg)	Unbal. (%)	THD (%)	Mag. Error (%)	Angle (deg)	Unbal. (%)
Global (circle)	2.99	2.16	-0.17	0.52	5.84	6.8	-1.1	0.8	7.75	11.18	-2.38	1.17
Global (hexagon)	3	1.54	-0.03	0.56	6.28	6.24	-0.53	1.08	9.46	10.81	-1.51	1.52
Group (circle)	1.99	2	0.95	0.54	4.30	6.24	0.94	1.10	7.50	10.39	-0.62	0.79
Group (hexagon)	2.21	1.48	0.669	0.4	4.2	5.2	2.16	0.84	6.32	9.26	2.47	0.97
State saturation	6.09	0.02	-2.87	0.52	7.25	4.53	-4.58	3.43	5.78	8.78	-5.71	1.39
No state saturation	8.30	-6.73	-3.34	1.16	9.78	0.48	-0.64	1.18	Unstable			

(600 V), similar at 570 V, and slightly better under large saturation (540 V).

6.6 Experimental results

The experimental setup is the one from Fig. 1.5, consisting of an interleaving DC/DC converter and a grid-forming DC/AC converter. Although the DC/DC converter is intended to interface the $LiFePO_4$ battery pack, in this work it is used to force DC-link voltage variations. The DC/DC converter control is detailed in Section 7.2.1. An LC filter is used to smooth the output voltage to supply the loads, with the structure shown in Fig. 6.3.

The proposed realizable reference anti-windup implementation along with the "Group" saturation strategy was experimentally tested. Due to laboratory power constraints, the inverter LC filter (which is the original one installed in the power converter and the one used for the simulations of the open and closed loop analysis in this chapter) and the load shown in Table 6.1 were resized to the values shown in Table 6.4 to allow voltage saturation within the lab's current limits.

The current controller can be seen in Fig. 6.6. The controller is composed of eight complex vector PI controllers for the fundamental, DC component, negative sequence, and the main five harmonic components(-250, 350, -550, 650 and 950 Hz). The DC component controller is required in practice to compensate for inverter non-idealities when a feedforward term is used. Each controller is independently tuned in its own reference frame. The measured capacitor voltage (uC_{qd}) is used as feedforward signal. The sum of the feedforward signal and the fundamental and DC current controllers' outputs will be considered as the main voltage component for the "Group" saturation strategy.

The measured inverter current, i_{iqd}, is compared to the current trajectory command, i^*_{iqd}, seen in Fig. 6.7(a). This trajectory is obtained in simulation using the experimental setup parameters as described in Section 6.5. Fig. 6.7(b) shows the corresponding theoretical non-saturated inverter voltage trajectory, and 6.7(c) the resulting capacitor voltage when the described harmonics are injected. This must be taken as the best output voltage trajectory achievable by the implemented controller structure. The THD in the capacitor voltage is 3.28 % due to the strong non-linear load selected. To decrease the THD below 1 %, five additional parallel harmonic controllers would be required. The resulting voltage u_{iqd} from the control loop, after proper saturation, is commanded to the inverter.

Fig. 6.8 shows the trajectory of the actual non-saturated inverter voltage

Table 6.4: Experimental System Parameters

Rated voltage	V_r	400 V_{rms}
Rated current	I_r	16 A_{rms}
Filter	L	2 mH
Filter	C	16 µF
Linear load	R_l	35 Ω
Linear load	L_l	2.4 mH
Linear load	Unbalance	±25 %
Non-linear load	C_{nl}	500 µF
Non-linear load	R_{nl}	106 Ω

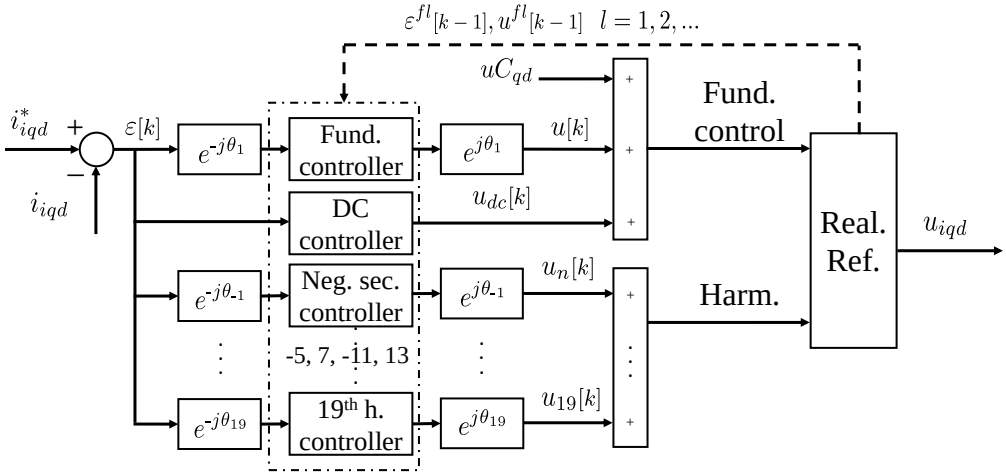

Figure 6.6: Current controller including realizable reference anti-windup.

command when the current trajectory seen in Fig. 6.7(a) is commanded. The differences with the theoretical trajectory shown in Fig. 6.7(b) are due to the inverter non-idealities. Voltage hexagon limits for DC-links voltages of 750, 570 and 500 V are also shown in Fig. 6.8. While a 750 V DC-link voltage ensures non-saturated operation, both 570 and 500 V impose increasing levels of saturation. These DC-link voltage levels will be used to test the proposed method performance.

Fig. 6.9 compares the behavior of the proposed realizable reference (RR)

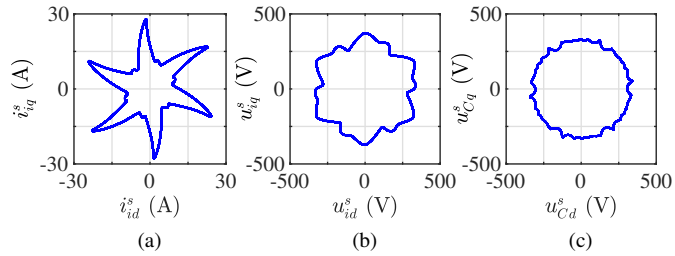

Figure 6.7: Current commands and predicted voltage trajectories for the experimental system. (a) Inverter current. (b) Inverter voltage. (c) Capacitor voltage.

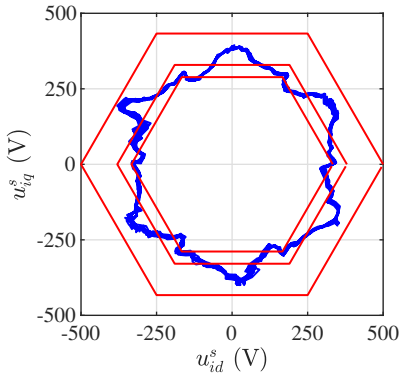

Figure 6.8: Experimental non-saturated inverter voltage trajectory and voltage hexagon limits under test: 500, 570, and 750 V.

method versus a simple state saturation (SS). In the last case, when the controller output exceeds the voltage hexagon limits, it is limited following the "Group" strategy, the corresponding individual controller outputs are calculated, but the realizable reference (i.e. error) is not computed. This prevents from windup but does not ensure a bumpless transition from the saturated to the non-saturated state. Fig. 6.9(a) shows a DC-link voltage transition from 570 V to 750 V. Fig. 6.9(b,d) show the inverter output current commands and actual phase currents. It can be observed that the current during saturation cannot accurately follow the command, but the distortion is small for RR, while in the case of SS there is noticeable distortion. Moreover, when the DC-link voltage is restored, the RR algorithm ensures a fast transition to the correct signal tracking (less that 1 fundamental cycle). SS transition is slower, needing 7 fundamental cycles

for complete recovery (not shown in the graph). The current command tracking also impacts the output voltage waveform. The output voltage can be seen in Fig. 6.9(c,e). In the case of RR, the distortion is low during voltage saturation, while a greatly distorted signal is seen for SS. Table 6.5 summarizes THD and fundamental component magnitude error for different DC-link levels analyzed. It must be noted that the THD in the non-saturated case is higher in the experimental results compared with simulation, due to the non-linearities of the real setup and the scaled-down load. A higher DC-link voltage is also needed to avoid saturation. However, the distortion increment during saturation aligns with the results obtained in simulation (Table 6.3).

Table 6.5: Experimental Capacitor Voltage Distortion Using Realizable Reference (RR) and State Saturation (SS)

Vdc (V)	Method	THD (%)	Magnitude error (%)
750	RR	3.15	0
	SS	3.15	0
570	RR	3.96	8.6
	SS	19.84	8.35
500	RR	4.93	17.46
	SS	-	-

A deeper saturation situation is shown in Fig. 6.10. In this case, the converter is initially operated with 500 V of DC-link voltage. This deep saturation level makes SS inoperative, making the system unstable. RR is able to keep a low distortion in the current tracking, as can be seen in 6.10(b). This allows to keep a low harmonic distortion in the capacitor voltage during saturation, as seen in 6.10(c) and Table 6.5. However, the large saturation level unavoidably decreases the fundamental component magnitude. Again, once the voltage is restored a fast transition to regular operation is achieved.

6.7 Conclusions

This chapter develops and demonstrates a simple way of implementing the realizable reference anti-windup technique for parallel controllers in multiple reference frames. The proposed implementation allows to use any kind of controller and, if required, seamless modification of single controller outputs during saturation. Different saturation options are available and can be easily applied.

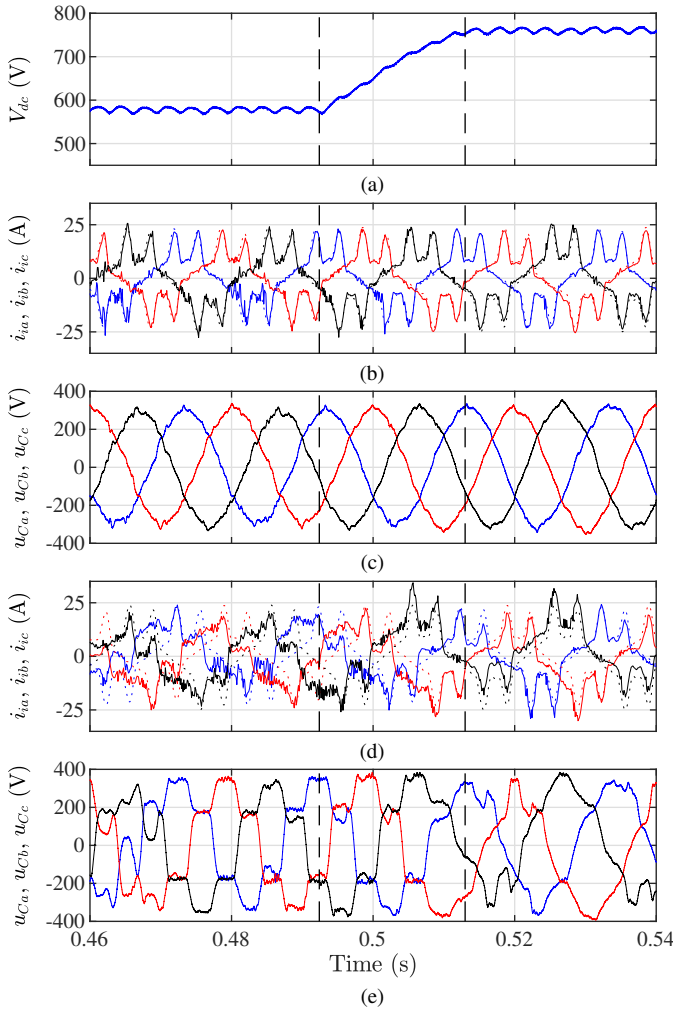

Figure 6.9: Experimental anti-windup performance during saturation (DC-link voltage: 570V) and transition to non-saturated state. (a): DC-link voltage. (b)-(d): Phase currents (solid line) and current commands (dashed line). (c)-(e): Capacitor voltages. (b)-(c): Realizable reference. (d)-(e): State saturation. Blue: phase-a; red: phase-b; black: phase-c.

The selection will depend on the final application (e.g. grid support, grid form, etc.). Grouping the harmonic controllers' outputs shows excellent results in grid-forming applications. Simulation and experimental results demonstrate the feasi-

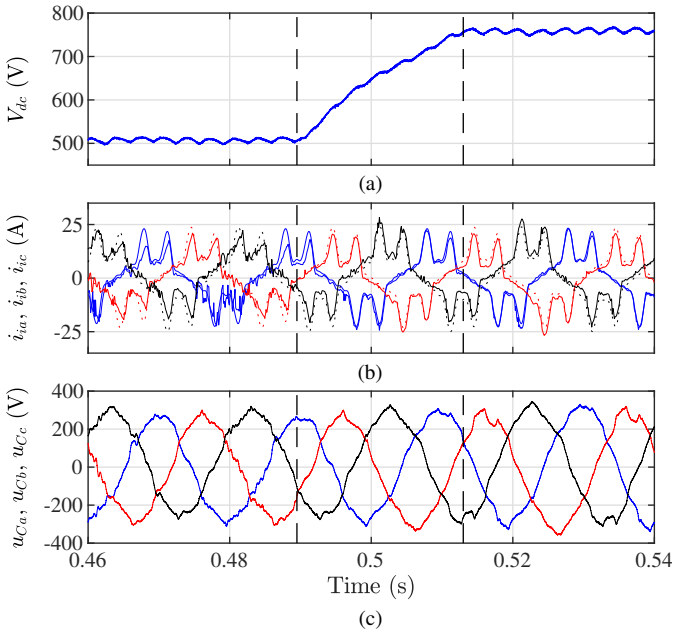

Figure 6.10: Experimental realizable reference anti-windup performance during saturation (DC-link voltage: 500V) and transition to non-saturated state. (a): DC-link voltage. (b): Phase currents (solid line) and current commands (dashed line). (c): Capacitor voltages. Blue: phase-a; red: phase-b; black: phase-c.

bility and performance of the proposed anti-windup implementation, even under deep DC-link voltage drops. It is noted that the proposed realizable reference implementation can be applied to any type of controller (e.g. voltage controller), although the choice of saturated value will depend on the application.

Chapter 7

Control of converters for smartgrids: DC/DC and 3P4L

7.1 Introduction

As explained in Section 1.2, the building's power stage is formed by two different converters, a DC/DC to boost the battery pack voltage and a DC/AC converter which generates the grid (see Fig. 1.5).

To reduce the current ripple in the batteries, the DC/DC converter is composed of three interleaved branches. In order to distribute the neutral wire, the DC/AC converter has an extra 4^{th} leg, which makes it a 3P4L converter (see Section 5.3.1).

The battery pack is made of $LiFePO_4$ cells as the ones in Section 2.2.4. They are stack in series and parallel in a 15x15 matrix to increase both the current and voltage capability. This way, Table 2.4 becomes Table 7.1. These stacks of 48 V are then further stacked to reach the desired input voltage, in this case, 7 stacks will be series connected to reach a nominal voltage of 336 V.

In this chapter, both converters are analyzed and the basics for their control is presented. The chapter is organized as follows: the DC/DC converter is explained

Table 7.1: $LiFePO_4$ Parameters of the Stack for the Building

Nominal voltage	48 V
Nominal current	48 A
Maximum charge current	1C
Maximum discharge current	3C
Battery capacity	48000 mAh

in Section 7.2. The basics of the control are explained in Section 7.2.1, the simulation results are shown in Section 7.2.2 and finally the experimental results are shown in Section 7.2.3. The DC/AC converter is explained in Section 7.3. Practical considerations related to this converter are explained in Section 7.3.1. The basics of the control are explained in Section 7.3.2, the simulation results are shown in Section 7.3.3 and finally the experimental results are shown in Section 7.3.4.

7.2 Boost converter

From the different converter topologies in Section 2.2.5, the DC/DC converter that interfaces the batteries for this project was selected to be a bidirectional boost converter with 3 interleaved branches, since there was no need for galvanic isolation. In the case of needing galvanic isolation, a DAB could be a good alternative due to its good efficiency. The scheme for this converter is the same as the part to the left from the DC-link capacitor in Fig. 1.5, represented again and alone in Fig. 7.1. The *load* in the final connection would be the DC/AC converter.

In this setup there are five different sensors (marked in Fig. 7.1):

- **Inductors currents:** Currents through each inductor (i_{Lu}, iL_{Lv} and iL_{Lw}).
- **Input voltage:** battery voltage, V_{in} .
- **Output voltage:** voltage at DC-link capacitor, V_{DC}.

Main parameters of the DC/DC converter can be seen in Table 7.2.

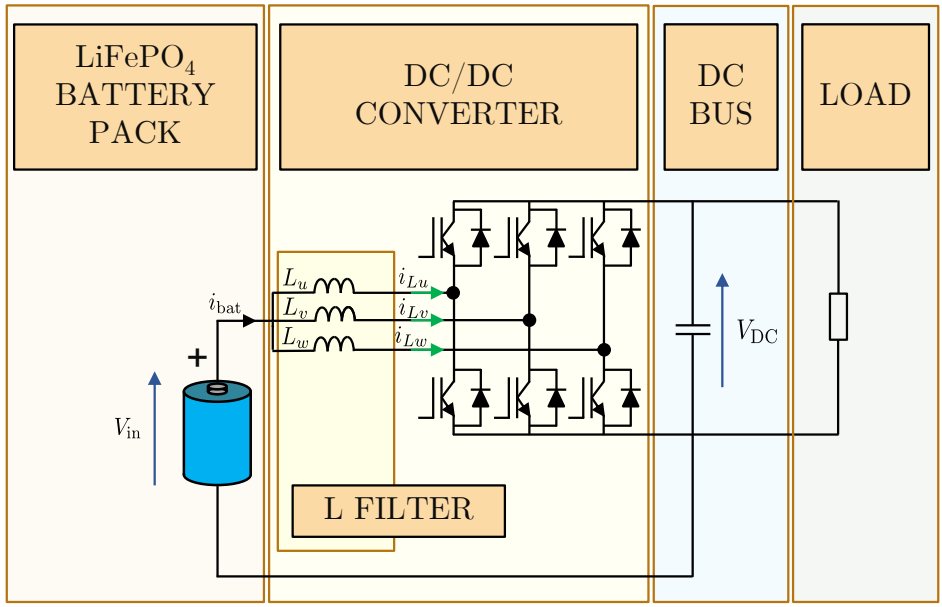

Figure 7.1: DC/DC converter interfacing the battery with the system.

Table 7.2: DC/DC System Parameters

DC-link voltage	V_{DC}	700 V
Input voltage	V_{in}	325 V
Switching frequency	f_{sw}	15 kHz
DC-link capacitor	C_{DC}	1 mF
Boost inductor	L_u, L_v, L_w	3 mH

7.2.1 Control of the boost converter

The boost converter is controlled with a simple cascade control [225] for current and voltage, paying attention to the interleaved technology. In this case, since there are three different branches, currents will be 120° phase-shifted in a switching cycle to minimize the ripple.

The complete control loop is shown in Fig. 7.2. The desired voltage at the DC link (V_{DC}) is compared with the measured voltage and the error (ε_v) is controlled

with a simple PI (PI_v) controller (see Section 5.7.3.1). The commanded current (i^*_{bat}) is then divided into three (i^*_{Lu}, i^*_{Lv} and i^*_{Lw}), so ideally each branch of the interleaved topology will carry the same amount of current. In reality, and due to small mismatches in construction of both the converter and the inductor, these three currents will not be identical. The current error (ε_{iLu}, ε_{iLv} and ε_{iLw}) will be then controlled with one PI (PI_i) for each branch, the same for the three branches. Finally the commanded voltage for each branch (v^*_{Lu}, v^*_{Lv} and v^*_{Lw}) will be converted into duty cycle (not shown in Fig. 7.2) by means of (7.1) and generated with the converter. $G_i(s)$ ((7.2)) and $G_v(s)$ ((7.3)) represent the system plant for current and voltage control, respectively.

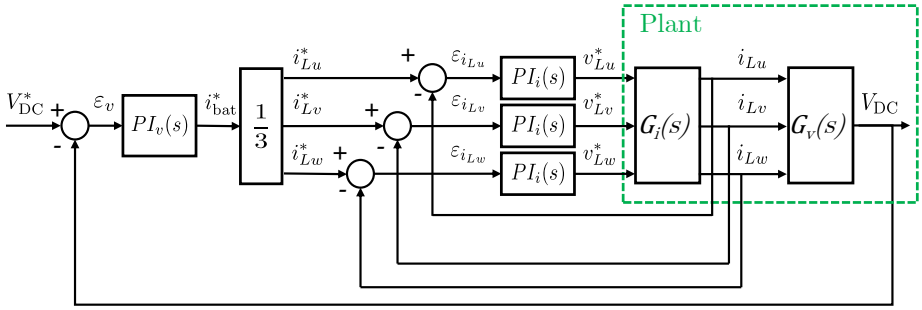

Figure 7.2: DC/DC converter control loop.

$$d = \frac{V_{\text{in}} - V^*_L}{V_{\text{DC}}} \tag{7.1}$$

$$G_i(s) = \frac{1}{Ls} \tag{7.2}$$

$$G_i(s) = \frac{1}{Cs} \tag{7.3}$$

Although not shown in Fig. 7.2, it is important to limit the currents to those allowed by the battery pack to avoid excess heat generation and premature aging. This limits will be different depending on the sign of the current and can be seen in Table 7.1 for the final design.

7.2.2 Simulation

The simulations were carried out using Matlab/Simulink. The scheme from Fig. 7.1 were represented using the powerlib library. The control was programmed using a C caller instead of Simulink blocks. This has several advantages:

1. Faster simulation.
2. Easier organization.
3. Easier to convert to control code in the real setup: the C code programmed this way can be directly transferred to the microcontroller. Then, only the microcontroller directly related configurations would be needed.

A step in the DC bus voltage command is shown in Fig.7.3a. The step goes from a bit over 300 V to 700 V. The step cannot start from zero because of the diodes in the IGBT module (antiparallel connected with the switch); as soon as there is voltage at the input (V_{in}), current flows through them and charges the DC-link capacitor to the input voltage value.

As it can be seen, the voltage increases constantly and without oscillations. This is due to the current limitation in the current loop. For this simulation, the current limit during discharge of the battery was set to 30 A, due to future limitations in the laboratory in terms of maximum power capability. This is shown in Fig. 7.3b, where the battery current is seen to reach 30 A right after the beginning of the step (at t=0.05 s). Fig. 7.3c shows the currents through each boost inductor. Since there is no load in the simulation, once the voltage reaches the desired command the current provided by the battery pack drops almost to zero, maintaining just the losses from parasitic resistances in the capacitor.

A closed view from Fig. 7.3b and Fig. 7.3c can be seen in Fig. 7.4 to show and compare the ripples. The first remark is that, as expected, the current through the battery has a ripple around three times smaller than the current through each inductor in the interleave configuration.

The other remark comes from the offset than can be seen between the three currents in Fig. 7.4b, although the 120° phase shift is clearly seen. This has to do with the synchronous sampling (see Section 5.5) and is expected to happen also in the real setup. Since there is only one sampling point per cycle but three currents 120° shifted, only one of the currents (i_{Lu}) is sampled at its mean value. The other two are sampled higher or lower respect to this mean value. This results in

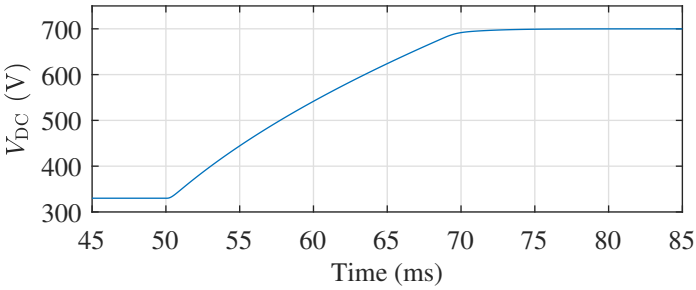

(a) DC bus voltage.

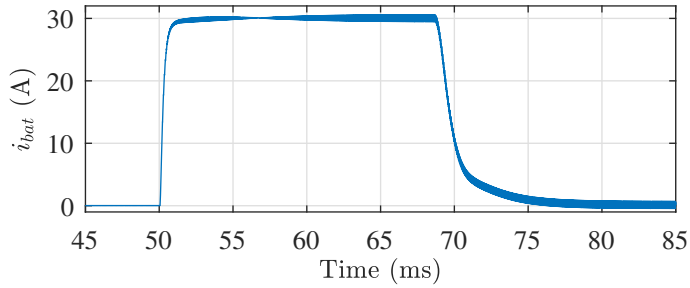

(b) Battery current.

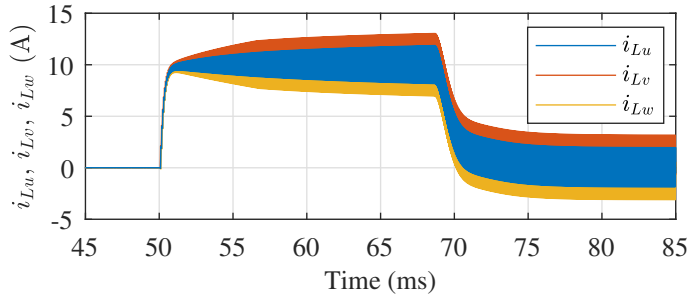

(c) Currents through each inductor.

Figure 7.3: Step in the DC-bus voltage command.

the controller seeing a higher or lower current than the one in reality, thus over-controlling or under-controlling. However, this difference is not too high and in practice it will result in one of the branches being slightly more loaded than the other two, without any real implications in the system behavior.

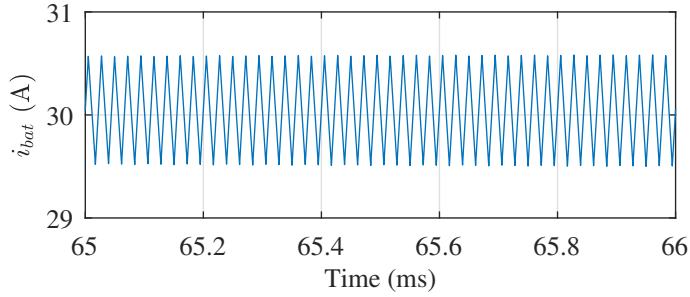

(a) Battery current.

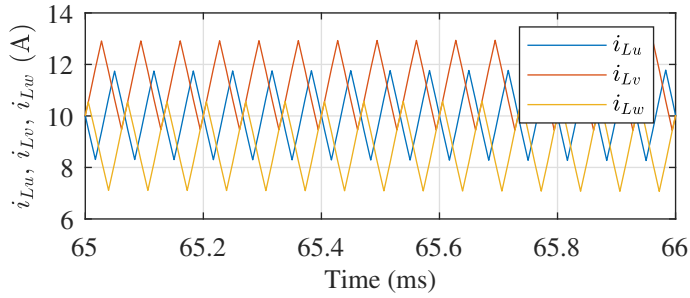

(b) Inductors current.

Figure 7.4: Zoom of the currents through the DC/DC converter.

7.2.3 Experimental results

The C code used to simulate the DC/DC converter was transfer without modifications to the DSP in the control board from Fig. 1.7. After the corresponding peripheral configurations, the same voltage step as in the previous section was captured. The voltage results are shown in Fig. 7.5. This resulting voltage (in red) is compared with the one in Fig. 7.3a, represented here again in blue. As shown, the response is practically the same as the one in simulations. The small difference between the steady-state values come from some unavoidable offsets in the voltage sensors.

Due to physical constraints in the design of the power modules it was not possible to measure the currents through each inductor with current probes. However, inspecting them with the Code Composer Studio, the program used to program and debug the DSP, it could be possible to see that they were all similar in quantities, yielding similar results as in Section 7.2.2.

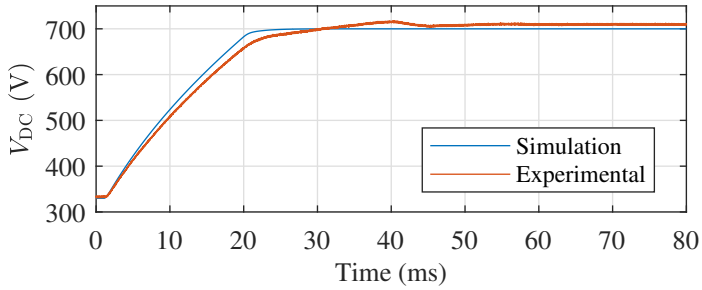

Figure 7.5: Comparative results between simulation and experimental.

7.3 3P4L converter

From the different options shown in Section 5.3, the DC/AC converter for the building was selected to have a 3P4L topology (see Section 5.3.1.2) because it is the best option to control the homopolar component that appears when there are single-phase loads. The scheme for this converter is the same as the part to the right from the DC-link capacitor in Fig. 1.5, represented again and alone in Fig. 7.6. The part after the output LC filter can be the loads of the building and/or the connection to the grid.

Different currents and voltages are marked in the figure, but not all of them are measured. Voltage sensors are marked in blue and current sensors are marked in green. In total, there are eight different sensors:

- **Inductors currents:** Currents through each inductor (i_a, i_b and i_c).
- **Capacitor current:** one current sensor to measure the sum of the currents through the filters capacitors (i_{cf}).
- **Input voltage:** voltage at the DC-link capacitor (V_{DC}).
- **Output voltage:** voltage at each filter capacitor (V_{an}, V_{bn} and V_{cn}).

The main parameters of the DC/AC converter can be seen in Table 7.3.

Based on (5.2) with the values of the LC filter's inductor and capacitor, the resonance frequency of the filter will be ≈ 600 Hz.

7.3.1 Practical considerations

Before advancing further into the control of the 3P4L converter, several practical considerations had to be analyzed, related to the connection of the neutral

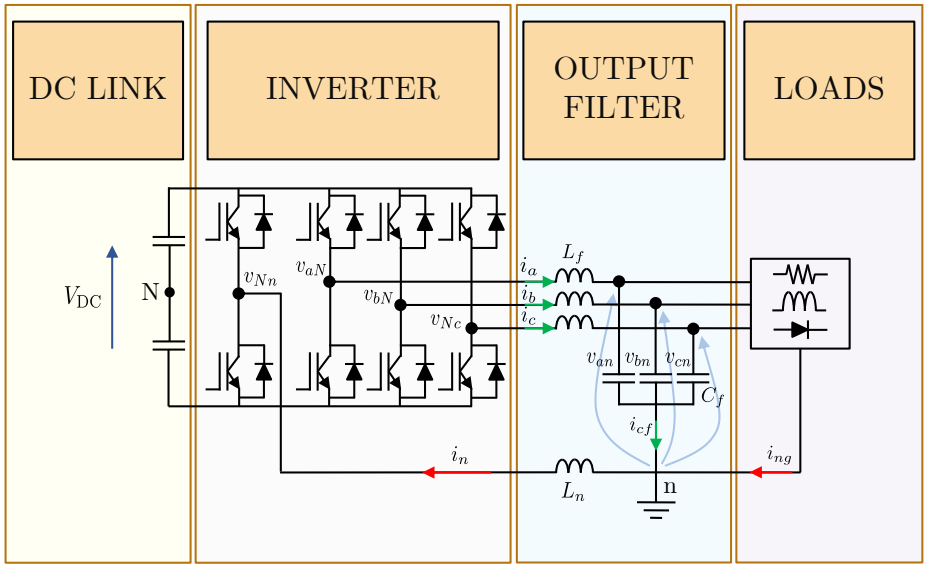

Figure 7.6: DC/AC building converter.

Table 7.3: DC/AC System Parameters

DC-link voltage	V_{DC}	700 V
Switching frequency	f_{sw}	10 kHz
DC-link capacitor	C	1 mF
Output filter inductor	L_f	260 μH
Output filter capacitor	C_f	270 μF

wire and switching patterns of the two parts forming the 3P4L inverter: the 3-phase system and the 4^{th} leg.

7.3.1.1 Neutral inductor connection

The original connection was set as in Fig. 7.7 following [170]. As mentioned in Section 5.3.1.3, these authors claim that this solution is easier to control.

To try this connection, the system was connected to a fixed input voltage (without the DC/DC converter, as in Fig. 7.7) of around 500 V. With this, the

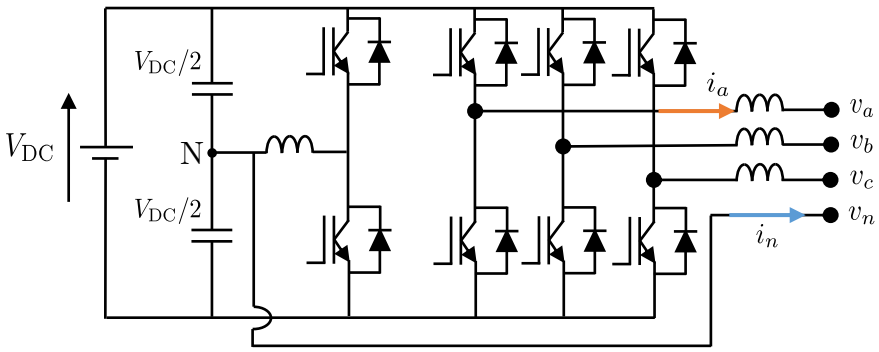

Figure 7.7: 3-phase 4-leg converter connecting the middle point of the DC-link voltage to the middle point of the 4^{th} leg by means of the neutral inductor.

system was powered and the open-loop voltage command was set to zero. The 4^{th} leg was kept from switching (both switches in open state). The system configured like this resulted in an unstable situation with a current through the neutral line (i_n) reaching 300 A and a phase current (i_a) almost reaching 100 A. This can be seen in Fig. 7.8, showing the current through one of the output inductors and the neutral inductor. The frequency of the waveforms is the same as the switching frequency: 10 kHz. This happens because switching harmonics in this connection have a really low impedance path to circulate.

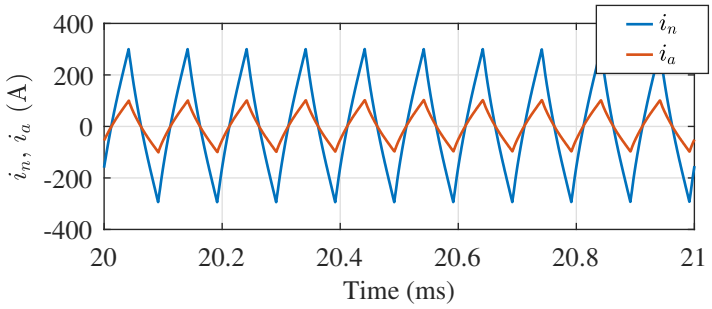

Figure 7.8: Current through the filter inductor in phase A (i_a) and through the neutral inductor (i_n) in the system from Fig. 7.7 (experimental results).

If the system works in open-loop with a commanded output voltage of 50 V these results change. If the 4^{th} leg does not switch (both switches are kept open), the results in terms of peak current are still high but slightly reduced, with a peak

current of 250 A for the neutral current and 85 A for the phase current. This can be seen in blue in Fig. 7.9. If the 4^{th} leg is made to switch at a 50 %, the peak current is dramatically reduced, as seen in Fig. 7.9 in orange, both for the neutral current (Fig. 7.9a) and for the phase current (Fig. 7.9b).

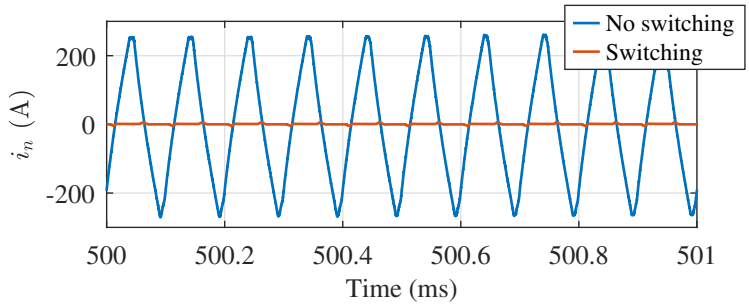

(a) Neutral current.

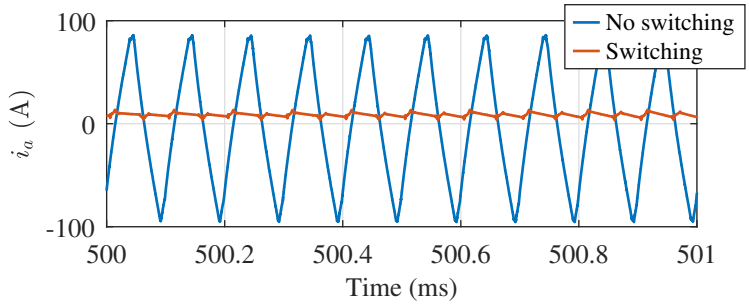

(b) Phase current.

Figure 7.9: Current through the phase and neutral inductor when the switches of the 4^{th} leg switch and when they stay open.

These results were checked in simulations with the same setup and conditions that were set to obtained Fig. 7.8. Simulation results are shown in Fig. 7.10.

Although unstable, the peak current for both i_n (84 A) and i_a (28 A) is smaller in simulation case (Fig. 7.10) than in the experimental case (Fig. 7.8). The difference between both cases is around 3.5 higher for experimental results than for simulations. This has to do with the inductor's saturation, which is not modeled in the simulation.

From the equation of the inductor (7.4), the value of the inductor can be obtained. For this, voltage and current across one of the inductors is required. This is shown in Fig. 7.11 for both the open-loop without 4^{th} leg connection

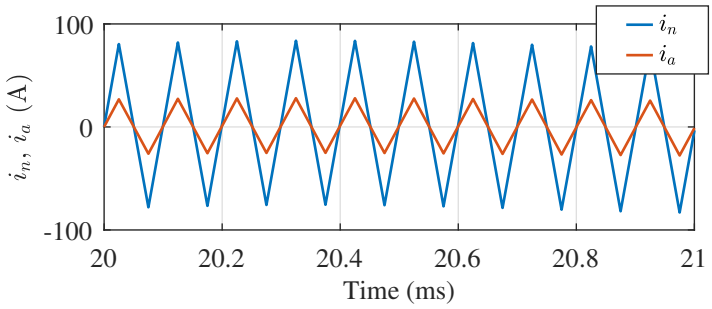

Figure 7.10: Current through the filter inductor in phase A (i_a) and through the neutral inductor (i_n) in the system from Fig. 7.7 (simulation results).

(Fig. 7.11a) and with 4^{th} leg connection (Fig. 7.11b) but no switching, in the experimental setup.

$$\Delta I = \frac{1}{L} \cdot \Delta T \cdot \Delta V \tag{7.4}$$

Applying (7.4) to the waveforms in Fig. 7.11a, the inductor value obtained is 235 μH. Repeating the process with the waveforms in Fig. 7.11b, the inductor value obtained is 62.5 μH, around 3.7 times smaller than in the first case. This matches the difference in peak currents when comparing the simulation to the experimental results.

Different simulations were carried out to check the suitability of different connections and switching techniques. For all the simulations, the DC-link voltage was set to 800 V since it represents the worst-case scenario. In addition, a 3-phase balanced load composed of a series resistance (20 Ω) and inductor (0.1 μH) was connected.

1. **Case 1:** Scheme from Fig. 7.7 and not switching the 4^{th} leg.
   - **Case 1a:** Commanding 0 V at the output.
   - **Case 1b:** Commanding 400 V at the output.
2. **Case 2:** Scheme from Fig. 7.7 and switching the 4^{th} leg at 50 %.
   - **Case 2a1:** Triangular carrier for both converters in phase. Commanding 0 V at the output.

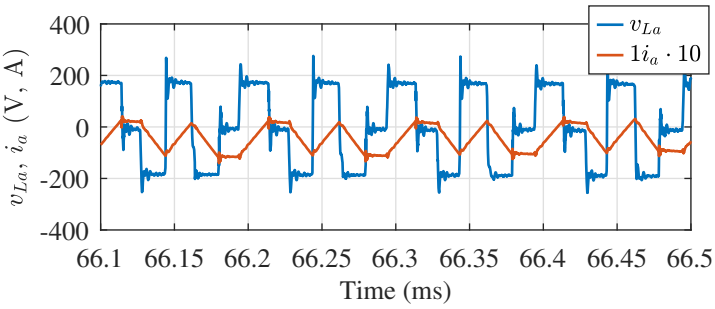

(a) 4^{th} leg not connected.

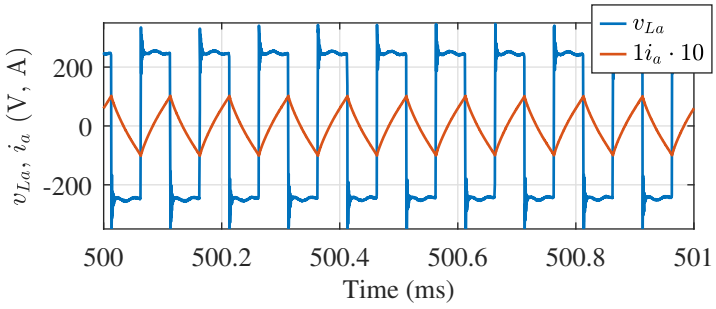

(b) 4^{th} connected but not switching.

Figure 7.11: Current and voltage across one of the phase inductors in open-loop.

- **Case 2a2:** Triangular carrier for both converters 180° phase-shifted. Commanding 0 V at the output.
- **Case 2b1:** Triangular carrier for both converters in phase. Commanding 400 V at the output.
- **Case 2b2:** Triangular carrier for both converters 180° phase-shifted. Commanding 400 V at the output.

3. **Case 3:** Same conditions as in cases 1 and 2 with the scheme from Fig. 7.6.

Table 7.4 summarizes the results obtained for the different cases, indicating the peak value of the different currents of interest. In orange it is represented the real case from Figures 7.8 and 7.10, while shaded in green are the most favorable cases.

From Figures 7.8 and 7.10 and Table 7.4 it is clear that the system cannot be connected like Fig. 7.7. Even if the system would improve when switching the 4^{th} (orange waveforms in Fig. 7.9 and cases 2a1 and 2b1 from Table 7.4),

Table 7.4: Simulation Results for Different open-loop Configurations

Case	$i_n(A)$	$i_{cf}(A)$	$i_a(A)$
Real case (Fig. 7.8)	300	300	100
Sim of real case (Fig. 7.10)	84	84	28
1a	516	116	172
1b	70	70	124
2a1	0	0	0
2a2	58	58	0.015
2b1	16	16	109
2b2	44	44	109
3-1a	424	0	142
3-1b	414	0	256
3-2a1	0	0	0
3-2a2	30	0	10
3-2b1	8.2	0	127
3-2b2	22.5	0	121.5

the fact that the current gets unstable just as it is powered means it could result in serious safety issues, thus the connection from Fig. 7.6 with all the triangular carriers synchronized was finally employed.

7.3.1.2 Phase shift between modules

In the scheme of Fig. 7.6, if the system is made to work in open-loop (commanding at the output 50 V in one axis) and the 4^{th} leg switches at 50 % duty cycle, i_n has the shape shown in Fig. 7.12. It is observed a two-level current around zero. This is due to a phase shift between the voltage generated in the 3-phase module and the single-phase module. The phase A output voltage in the three-phase power module is compared with the single-phase converter output voltage in Fig. 7.13. There is a difference of $\approx 1.8°$ (500 ns). This may lead to aliasing when sampling, resulting in an offset of the mean value of the current.

In order to test if this phase shift can affect the control, several simulations were carried out. The parameters for the simulation are:

- System from Fig. 7.6.

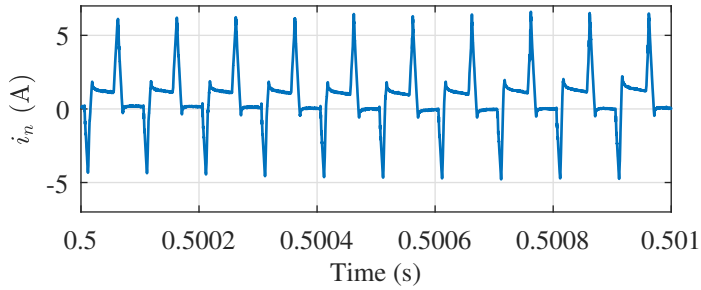

Figure 7.12: Current through the neutral wire when the 3-phase converter works in open-loop and the 4^{th} leg switches at 50 % duty cycle (experimental results).

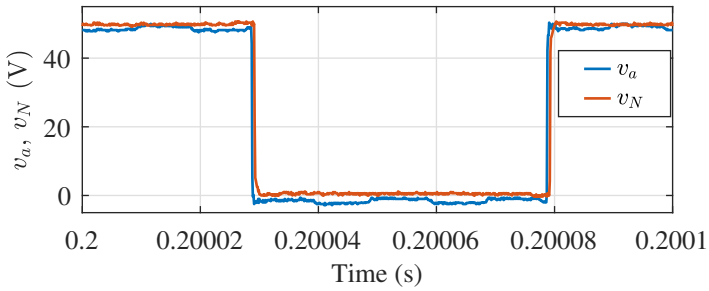

(a) Phase and neutral voltages.

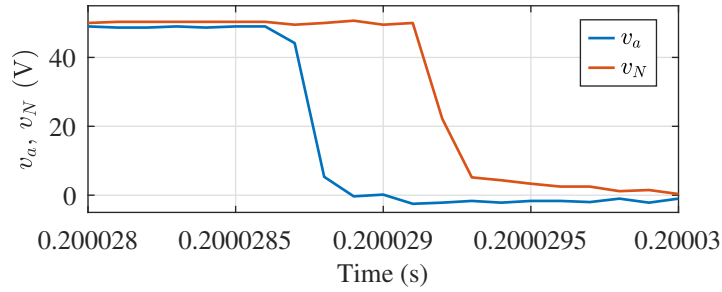

(b) Phase and neutral voltages zoom.

Figure 7.13: Comparison of phase and neutral output voltages at the output of the inverter (experimental results).

- System in open-loop: output commanded voltage of 100, 200, 300 and 400 V.
- 4^{th} leg switches at 50 % duty cycle.
- Phase shift between triangular carriers for 3-phase module and single-phase

module of 3°.

- Output load of 18 Ω and 10 μH.
- Dead time of 4 μs.

The current was both sampled and sampled and filtered (with a 905 Hz filter) and the error between them and the original neutral current were compared. The option where the current is filtered and sampled represents the case in which the acquisition system includes an analog anti-aliasing filter. Neutral current for the three cases is shown in Fig. 7.14 for the case of commanding 200 V as the output voltage in open-loop. As expected, the original current has the two levels around zero. The rest of the voltages (100, 300 and 400 V) all have a similar behavior, although the peak neutral current increases as the voltage increases.

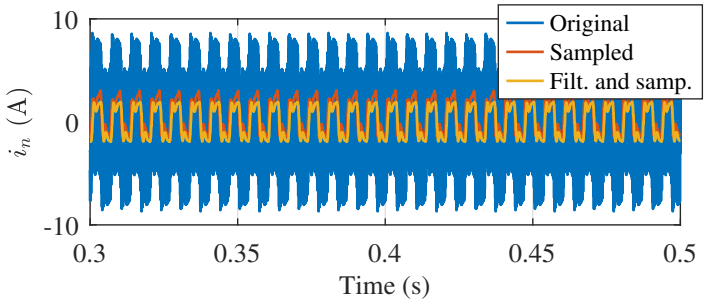

(a) Neutral current.

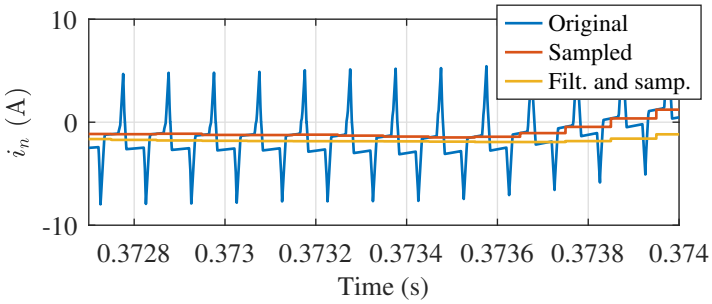

(b) Zoom of the neutral current.

Figure 7.14: Neutral current when commanding 200 V in open-loop: real current (blue), current sampled (orange) and current filtered and sampled (yellow) in simulation.

It is expected for the neutral current to include different harmonics, so the error must be checked for different frequencies. In order to do so, the FFT of the current in Fig. 7.14 is performed, which can be seen in Fig. 7.15. From this, the

most relevant points can be seen to be the frequencies at 150, 450 and 750 Hz.

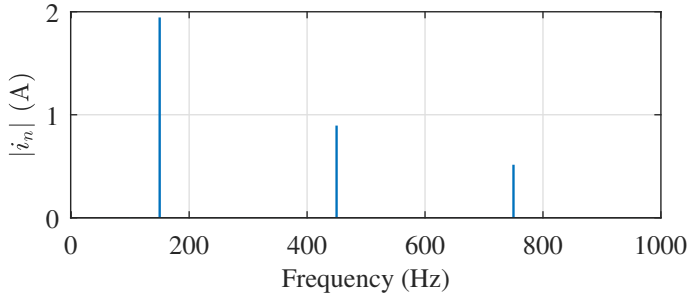

Figure 7.15: FFT of the blue current waveform (neutral current) in Fig. 7.14.

Checking those frequency points at different voltages yields to Fig. 7.16. In the figure, the first row shows the real current (blue), the same current after been sampled (orange) and the same current after been filtered and sampled (yellow). The second row represents the absolute error of subtracting the real waveform in the previous row from either the sampled current (blue) or the filtered and sampled current (orange). The last row represents the same as the second raw, but instead of absolute error is relative error. Each column shows the results for a different frequency.

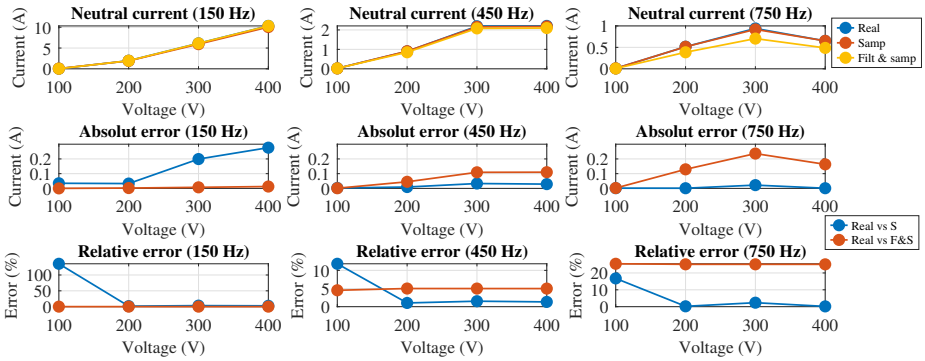

Figure 7.16: Simulated neutral current (i_n) at different output voltages commanded in open-loop.

As it can be seen from Fig. 7.16, at low frequencies the relative error for the case sampled and filtered is the best. As the frequency increases, so does this error, because it gets closer to the cut-off frequency of the anti-aliasing filter. On

the other hand, having no filter causes higher error at low output voltages of the converter. Since the system is thought for working at an output voltage of 325 V of a normal grid, the option where there is no filter appears to be better if higher frequencies are to be controlled. Besides, it allows for synchronous sampling (see Section 5.5). Another option, if high frequencies are to be properly identified, will be increasing the cut-off frequency of the anti-aliasing filter. A similar analysis can be carried out with the three-phase currents, resulting in similar conclusions.

Summarizing, it can be concluded that a difference in phase between the carrier of the 3-phase and the single-phase controller will not affect significantly to the controllability of the system.

7.3.2 Control of the 3P4L converter

The control objective is the generation of a 3-phase nanogrid with 230 V_{RMS} line-to-neutral output voltage, keeping the harmonic content of this generation among the limits required by the regulations [40] (see Section 5.7.1). Harmonics expected in the grid will be the negative sequence component (-50 Hz) due to three-phase unbalances and the ones produced due to the connection of the non-linear loads, as the -5^{th} (-250 Hz) and 7^{th} (350 Hz) (see Section 5.7.1). Since the resonance frequency of the filter is in the range of 600 Hz, higher-order harmonics are expected to be of less importance or highly attenuated by the filter. In addition, zero-sequence components will be expected when connecting single-phase loads.

There are many control techniques for 3P4L in the literature [45]. In this thesis, the control of this converter was divided into two. By means of the Clarke or Park transformation (see Appendix B) the abc quantities will be converted into stationary ($\alpha\beta$0) or synchronous (dq0) quantities. $\alpha\beta$ or dq components can be separated from the zero-sequence component and controlled independently. This will be further explained in the following sections. By doing so, the 4^{th} leg can be disabled at first to prepare and test the control for the 3-phase DC/AC converter. Once that is working, the control of the 4^{th} leg can be added to the system.

7.3.2.1 3-phase converter control

As in the case of the DC/DC converter, this part of the system is controlled with a cascade control [225] for current and voltage. Fig. 7.17 shows the complete

control scheme, which will be identical for the d and q axes. The control strategy would be a control in mixed single reference frames, where the positive and negative sequence component will be controlled in its own reference frame using a PI controller while the different harmonics would be controlled with PR controllers to avoid having a large number of Park transformations (see Appendix B).

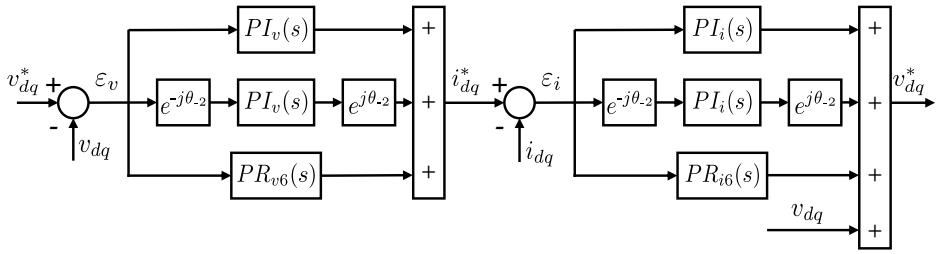

Figure 7.17: 3-phase DC/AC converter control loop.

The desired output voltage, v^*_{dq} (400 V, 50 Hz) is compared with the measured voltage, obtaining the voltage error (ε_v) between both signals. This magnitude is in the synchronous reference frame with the positive sequence and it is the common error that will be used for the different controllers in the system, as done in chapter 6 (see also Section 5.7.2). As already mentioned, there are three different controllers in the system: one PI for the positive sequence, another for the negative sequence and a PR to control the -5^{th} and 7^{th} harmonics at the same time. Note that two coordinate rotations using Park's transformation (see Appendix B) must be performed to control the negative sequence component with a PI: one to get the common error in the synchronous reference frame with the negative sequence component and another one to get the resulting current from the controller back in the synchronous reference frame with the positive sequence component.

The sum of the output of all these controllers is the current reference for the current control loop. In the same way as for the voltage loop, the current command is compared to the real current measured in the system to extract the current error (ε_i). The same arrangement of controllers is then employed, with a higher bandwidth for this inner loop. The sum of the output of all the current controllers, including a feedforward term from the measured voltage, is the voltage that must be commanded to the converter to obtain the desired output voltage from the beginning of the loop (v^*_{dq}). Finally, this voltage command is converter back to an abc reference frame and used to calculate the duty cycle needed to

drive the power converter.

7.3.2.2 4^{th} leg control

In a 3P4L system, the sum of the 3 phase currents through a 3-phase load returns through the neutral conductor. In a 3-phase balanced system with the currents phase-shifted 120°, currents get canceled and ideally, the current through the neutral conductor is zero. In case of an unbalance, currents do not longer get canceled. In this case, there is a current through the neutral wire because the triplen harmonics (3^{rd}, 9^{th}...) add cumulatively in the neutral conductor and can reach a 173 % of the phase current at 150 Hz (3^{rd} harmonic) [197].

The 4^{th} leg will control the homopolar component, the zero sequence component resulting from the Park transformation (see Appendix B). The electric circuit can be express as the homopolar-circuit version in Fig. 7.18. The load here is considered to be a single-phase resistive load, but it does not affect the following explanation.

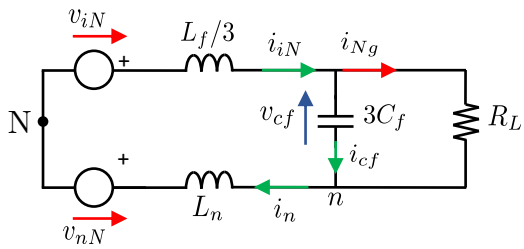

Figure 7.18: Homopolar circuit for the analysis and control of the homopolar component.

The different elements in Fig. 7.18 are:

- $\boldsymbol{L_f}$: filter inductance.
- $\boldsymbol{C_f}$: filter capacitor.
- $\boldsymbol{L_n}$: nuetral inductance.
- $\boldsymbol{R_L}$: single-phase load.
- $\boldsymbol{i_{iN}}$: homopolar current through L_f.
- $\boldsymbol{i_{cf}}$: homopolar current through C_f.
- $\boldsymbol{i_{Ng}}$: homopolar current through the load.

- $\boldsymbol{i_N}$: neutral current, expressed as:

$$i_n = i_{iN} = i_a + i_b + i_c \tag{7.5}$$

$$i_n = i_{iN} = i_{cf} + i_{Ng} \longrightarrow i_{Ng} = i_n - i_{cf} \tag{7.6}$$

- $\boldsymbol{v_{iN}}$: voltage generated by the 3-phase converter
- $\boldsymbol{v_{nN}}$: voltage generated by the 4^{th} leg.
- $\boldsymbol{v_{cf}}$: homopolar equivalent from the filter's capacitors, expressed as:

$$v_{cf} = \frac{1}{3}(v_{an} + v_{bn} + v_{cn}) \tag{7.7}$$

As seen from (7.6), the homopolar current through the filter's inductor in the phase is the same as the neutral current through the neutral wire. Due to this, Fig. 7.18 can be re-drawn as Fig. 7.19, changing the position of the phase-inductor.

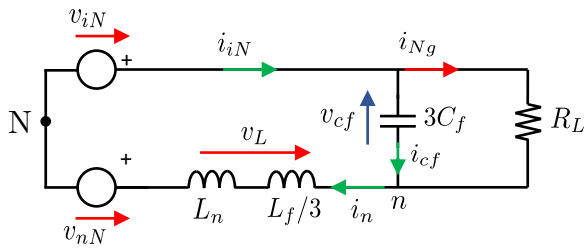

Figure 7.19: Homopolar circuit for the analysis and control of the homopolar component changing the position of the phase inductor.

The idea is controlling the homopolar voltage/current through the load. In this regard, the homopolar voltage at the load will be the same as in the filter's capacitors (v_{cf}) because they are connected in parallel. Applying Kirchhoff's law to the circuit in Fig. 7.19, the v_{cf} can be expressed as:

$$v_{cf} = v_{iN} - v_L - v_{nN} \tag{7.8}$$

From this equation, it can be seen that there are two degrees of freedom for controlling the homopolar voltage; either using the 3-phase converter (v_{iN}) or alternative using the 4^{th} leg (v_{nN}). If the 3-phase converter is selected, the voltage

generated by the 4^{th} leg must be set to zero (switching at 50 % duty cycle). If the 4^{th} leg is selected, the zero-sequence component in the 3-phase control must be set to zero. Anyhow, both options lead to the same results. Here, the 4^{th} leg is selected because the voltage utilization can be increased [170, 171, 176].

In principle, controlling the homopolar current through the capacitors to be zero should result in zero homopolar voltage. Thus, and taking into account (7.5) and (7.6), the initial control loop will look as the one in Fig. 7.20.

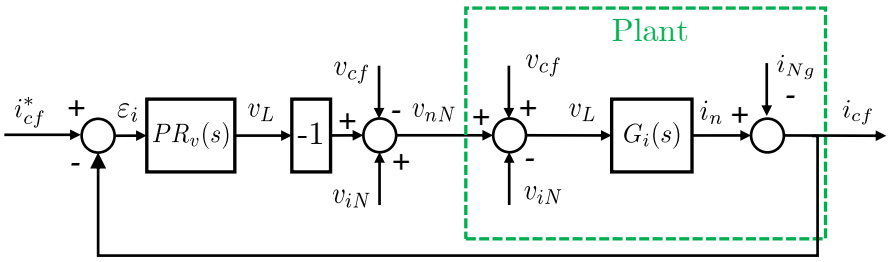

Figure 7.20: Homopolar current control.

In this control there will be as many current PR regulators in parallel as frequencies of interest to be controlled. These frequencies will be analyzed in the following sections. $G_i(s)$ represents the plant for the current control:

$$G_i(s) = \frac{1}{(L_n + \frac{L_f}{3})s} \tag{7.9}$$

As will be shown later, there is also a DC component in the homopolar voltage that cannot be eliminated just by controlling the current. Thus, a voltage control has to be cascaded to the current control. The final control loop for the homopolar component is shown in Fig. 7.21.

As explained in Chapter 6, saturation plays an important role in these kind of multifrequency systems. Integrating the method developed for 3-phase systems to a system with a 4^{th} was still an ongoing research at the moment of writing this thesis.

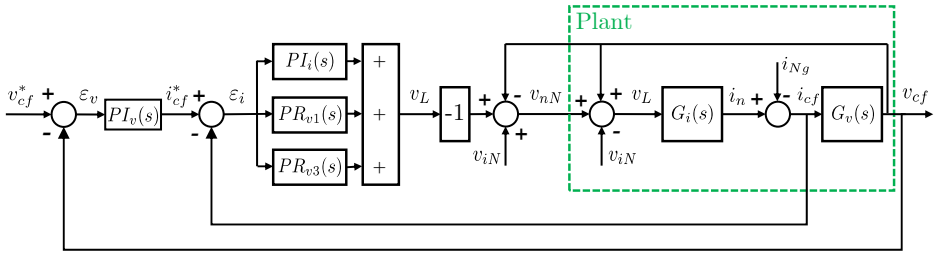

Figure 7.21: Homopolar voltage and current control.

7.3.3 Simulation results

Simulations were carried out similarly as in Section 7.2.2. Unless specified otherwise, the parameters for the simulation are the ones from Table 7.3. In addition, the loads are shown in Table 7.5.

Table 7.5: 3P4L Loads

Linear load	18 Ω
Unbalance in one phase	10 Ω
Single-phase load	18 Ω
Non-linear load	1 mF || 5 Ω

7.3.3.1 3-phase converter

7.3.3.1.1 open-loop analysis

The first simulation is used to compare the system's response when there is or there is no dead time. In some cases, the effect of the dead time can be neglected and, thus, get a faster simulation. Commanding 325 V in the d-axis as peak phase-to-neutral voltage, voltages and currents with no dead time can be seen in Fig. 7.22. The current is shown both before (middle plot) and after (lower plot, i_{ag}, i_{bg} and i_{cg}) of the LC filter, and it can be seen that the filter is working as expected, filtering the high-frequency ripple in the current.

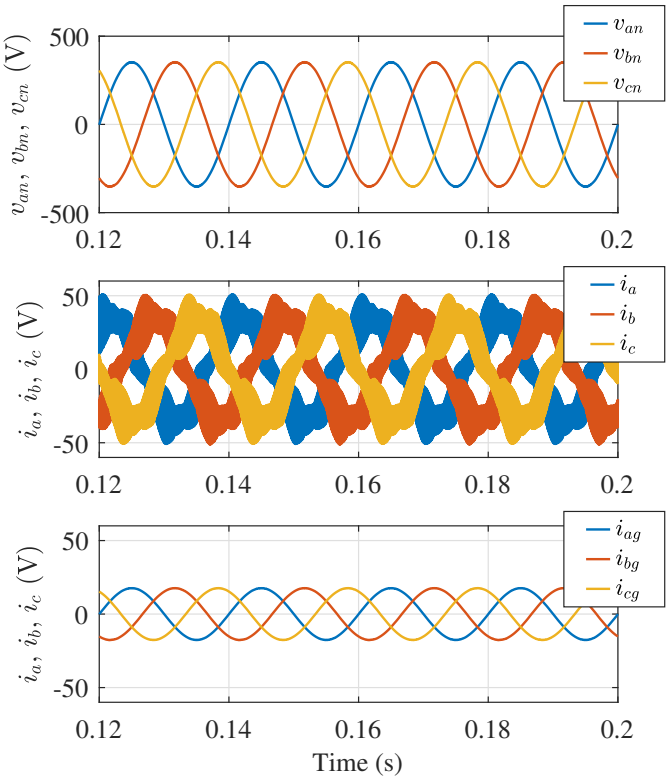

Figure 7.22: Three-phase output voltages and currents when there is no dead time in the inverter.

The voltage response in dq synchronous reference frame with the fundamental component (50 Hz) can be seen in Fig. 7.23 (no dead time, THD = 0.21 %). The figure also shows the complex FFT of the voltages.

Fig. 7.24 shows the same waveforms when the dead time is included in the commutation of the IGBTs (THD = 1.39 %).

As expected [226], in the case with dead time the ±6 and ±12 harmonics appear. This can be seen in the FFT of both complex vectors and also in the dq representation. Compared with the case without dead time, in the case with dead time there are oscillations in the dq quantities, which means there are going to be other visible frequencies in the spectrum. Due to the importance of the harmonics in this analysis, the rest of the simulations were carried out including the dead time.

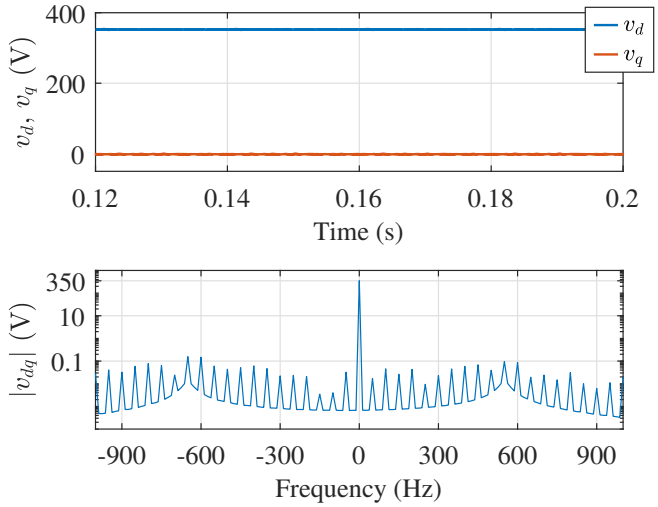

Figure 7.23: Output voltage when there is no dead time in the inverter. Synchronous reference frame with the fundamental component.

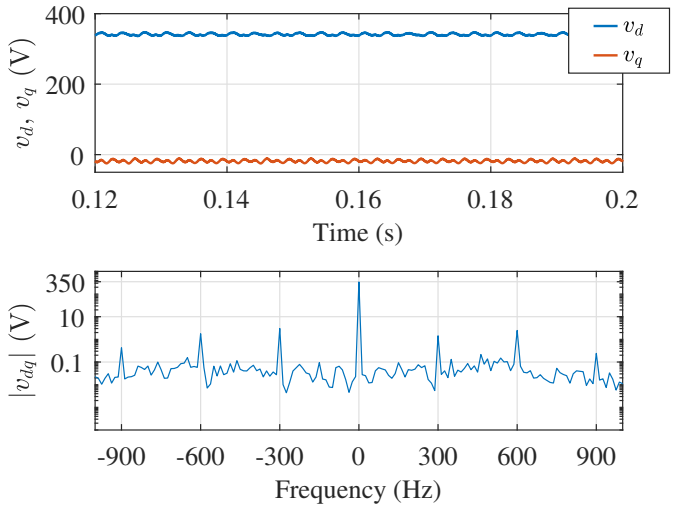

Figure 7.24: Output voltage when there is dead time in the inverter. Synchronous reference frame with the fundamental component.

7.3.3.1.2 Positive sequence control

The result of controlling the output voltage when the load is a 3-phase balance load and the positive sequence component control is enabled is shown in Fig. 7.25. The THD is 1.22 %. Compared with Fig. 7.24, it can be seen a positive shift in the y-axis on the whole FFT spectrum, resulting from the control loop.

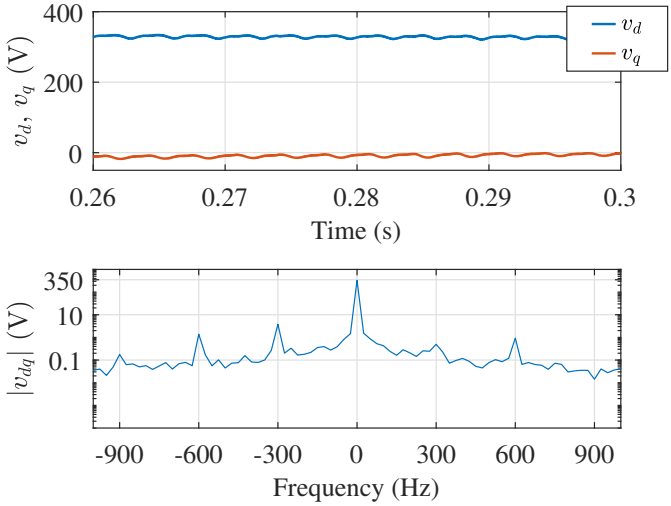

Figure 7.25: Output voltage when controlling the positive sequence. Synchronous reference frame with the fundamental component.

7.3.3.1.3 Negative sequence control

As explained in Chapter 5, a 3-phase unbalance load results in a negative sequence component (-50 Hz in this case). Fig. 7.26 shows the change in the system from a 3-phase balance load to a 3-phase unbalance load.

Fig. 7.27 shows the voltage response in the synchronous reference frame when the load is unbalanced. Since there is only a positive sequence controller, the new component is not controlled and can be seen in the figure at -100 Hz (with an absolute value of 46 V) in synchronous reference frame with the positive sequence. The THD in this case becomes 11.43 %, which is not acceptable according to the standards explained in Section 5.7.1.

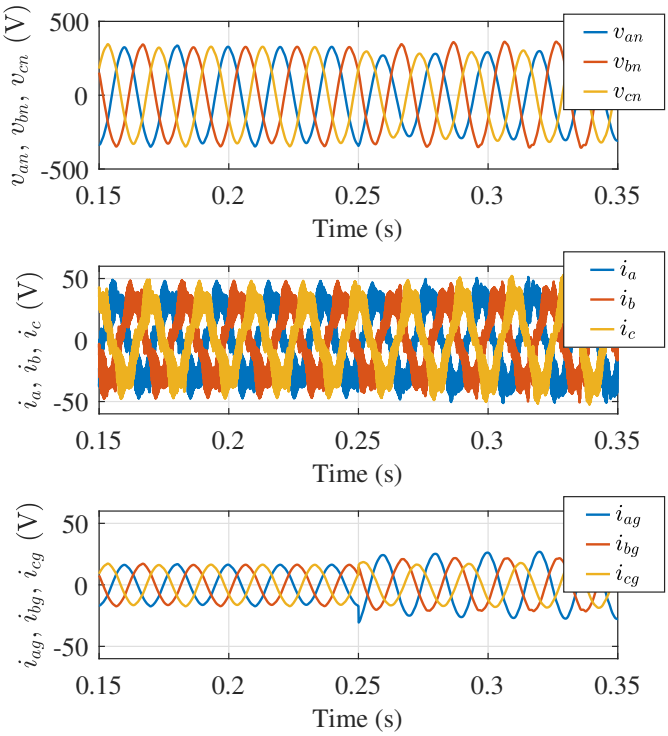

Figure 7.26: Three-phase output voltages and currents when the load changes from being 3-phase balanced to 3-phase unbalanced (t=0.25 s).

If the controller is enabled, the absolute value of the negative sequence component is reduced to 1.6 V and the THD to 1.9 %, which complies with the regulations, as shown in Fig. 7.28.

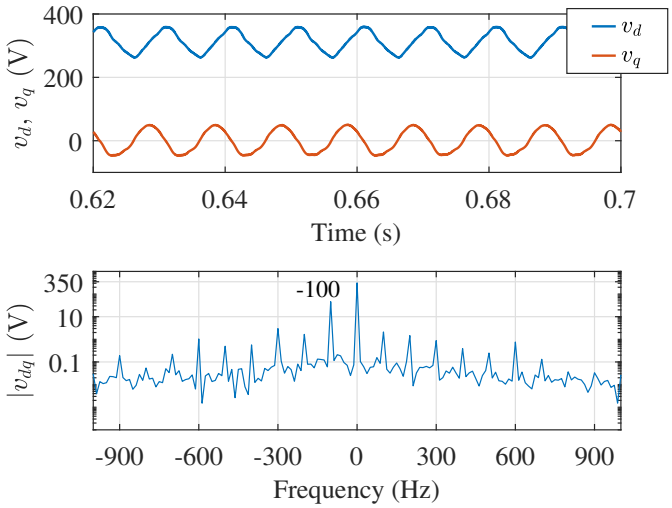

Figure 7.27: Output voltage when controlling the positive sequence component, being the load a 3-phase unbalanced one. Synchronous reference frame with the fundamental component.

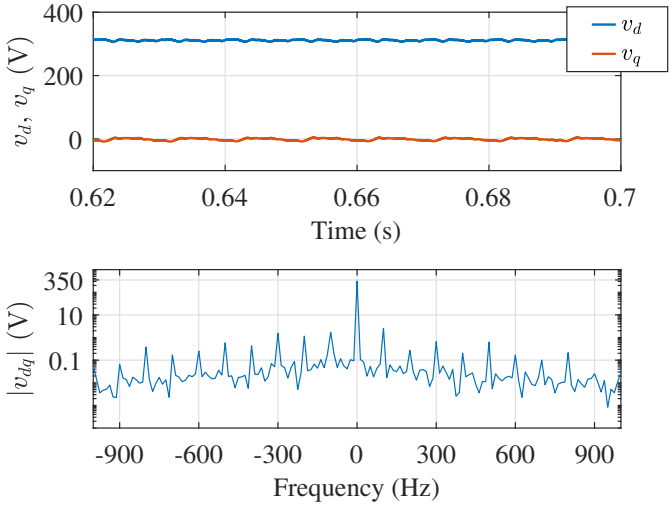

Figure 7.28: Output voltage when controlling the positive and negative sequence components, being the load a 3-phase unbalanced one. Synchronous reference frame with the fundamental component.

7.3.3.1.4 Harmonics control

Similarly as with the negative sequence component, the non-linear load will provoke the appearance of harmonics in the voltages and currents. The system response when a non-linear load is connected to the system at t=0.25 s, in parallel with the existing 3-phase balanced load, is shown in Fig. 7.29.

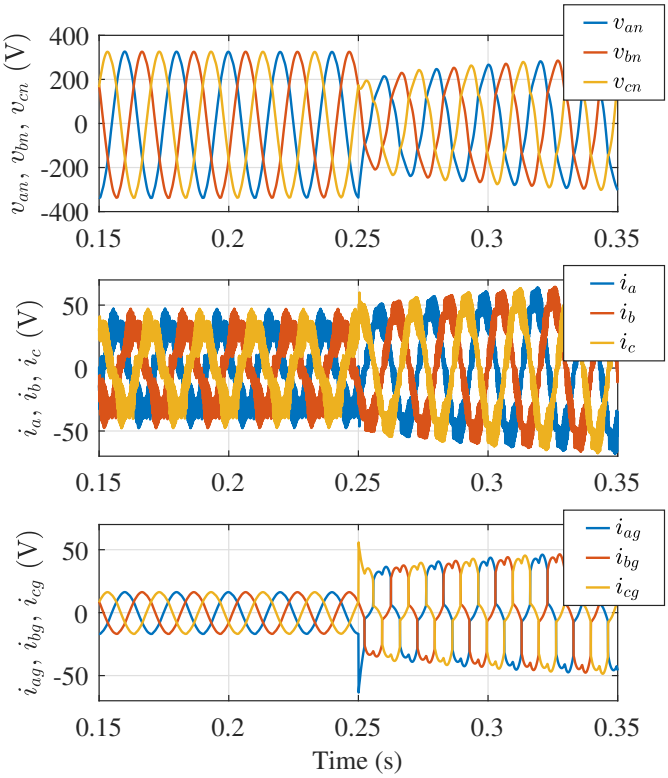

Figure 7.29: Three-phase output voltages and currents when the load changes from being 3-phase balanced to 3-phase balanced + a non-linear load (t=0.25 s).

The frequency response of this is shown in Fig. 7.30. In this case, the ±6, ±12 and so on harmonics appear, as explained in Section 5.7.1. The THD of this voltage is 6.7 %, mainly due to an absolute value of 20.45 V in the -6^{th} harmonic and 5.23 V in the 6^{th} harmonic. The ±12 harmonics are in the range of 2 V each.

Enabling the harmonics control of the ±6 component, Fig. 7.31 shows how the ±6 harmonics almost disappear, and the THD becomes 1.83 %, complying

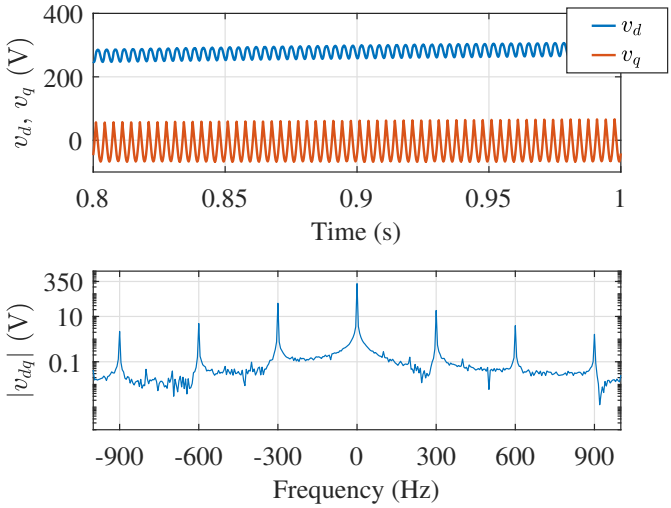

Figure 7.30: Output voltage when controlling the positive and negative sequence components when the load is non-linear. Synchronous reference frame with the fundamental component.

with the regulations.

7.3.3.1.5 Conclusions

The different cases presented in this section for the 3-phase controller are summarized in Table 7.6. It can be seen how adding the positive, negative and $\pm 6^{th}$ harmonic control is enough to get the required THD by the regulations explained in Section 5.7.1.

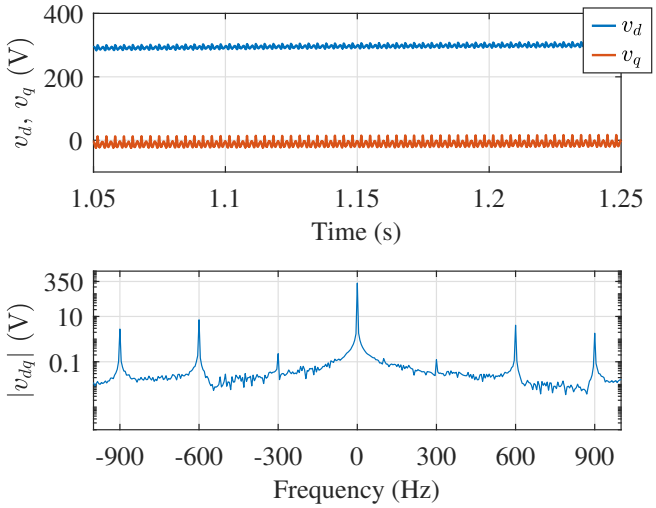

Figure 7.31: Output voltage when controlling the positive and negative sequence components and the ±6 harmonics when the load is non-linear. Synchronous reference frame with the fundamental component.

Table 7.6: Summary of Simulations for the 3-Phase System

Case	$\|V_{dq}\|$ **(V)**	**THD (%)**
Open-loop (no dead time)	327.8	0.21
Open-loop (dead time)	318.0	1.39
Positive sequence control	325.4	1.22
Unbalance 3-phase load (only pos. control)	325.4	11.43
Unbalance 3-phase load (pos. & neg. control)	325.4	1.9
Non linear load (pos. & neg. control)	325.4	6.7
Non linear load (pos., neg., & h. control)	325.1	1.83

7.3.3.2 4^{th} leg integration

The homopolar voltage/current control can be added to the control system without modifying anything from the 3-phase control system explained in the previous section.

7.3.3.2.1 Analysis of the harmonic components

For the first analysis, the neutral wire was connected switching at a 50 % duty cycle. Connected to a 3-phase balanced load, the resulting output voltages and currents are shown in Fig. 7.32.

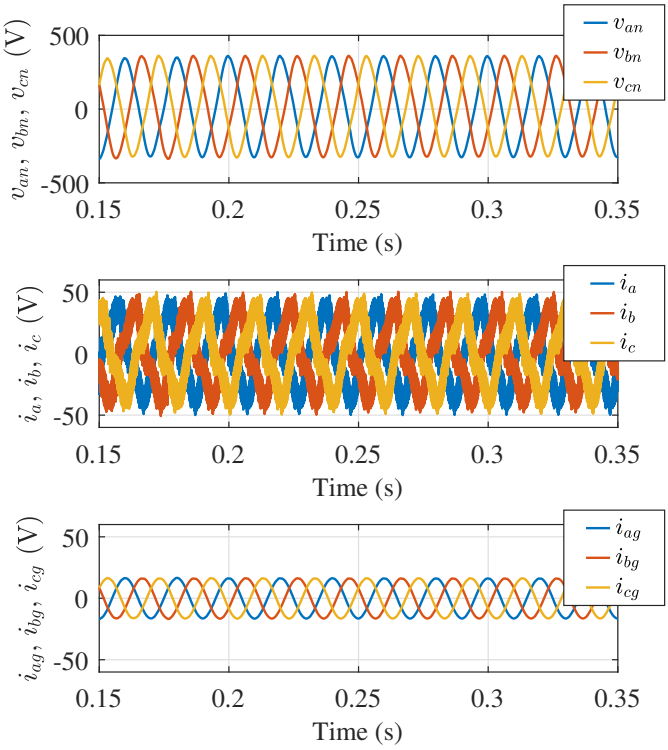

Figure 7.32: Three-phase output voltages and currents when the load is balanced and the 4^{th} leg is connected and switching at a 50 % duty cycle.

Although it is not easy to appreciate it from the figure, the voltages are shifted all by the same DC quantity (≈20 V). This would not be an acceptable voltage in a grid. However, this is not reflected in the THD, which is around 1.9 %. This is because the THD is computed from the dq complex voltage vector, but it does not take into account the zero-sequence component. This is shown in Fig. 7.33, where dq components are almost DC in the synchronous reference frame with the fundamental component with no other remarkable harmonics.

In order to analyze the homopolar components it is useful to look at the current through the capacitors in the filter (i_{cf} in Fig. 7.6 and Fig. 7.18). This is shown in Fig. 7.34. This figure also shows the FFT of the current.

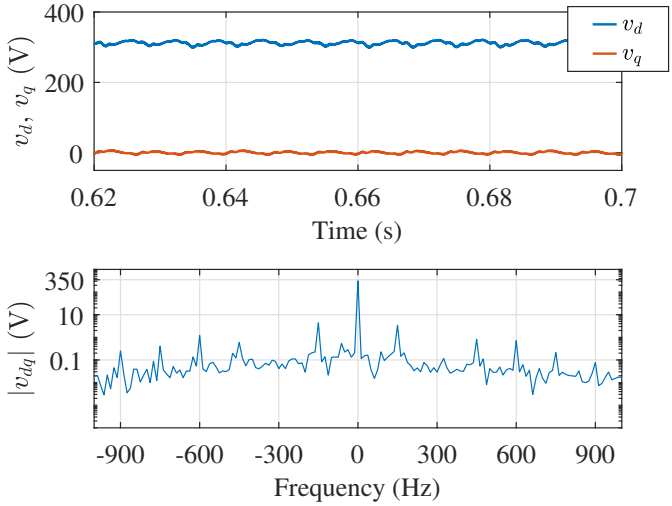

Figure 7.33: Output voltage when the load is balanced and the 4^{th} leg is connected and switching at a 50 % duty cycle. Synchronous reference frame with the fundamental component.

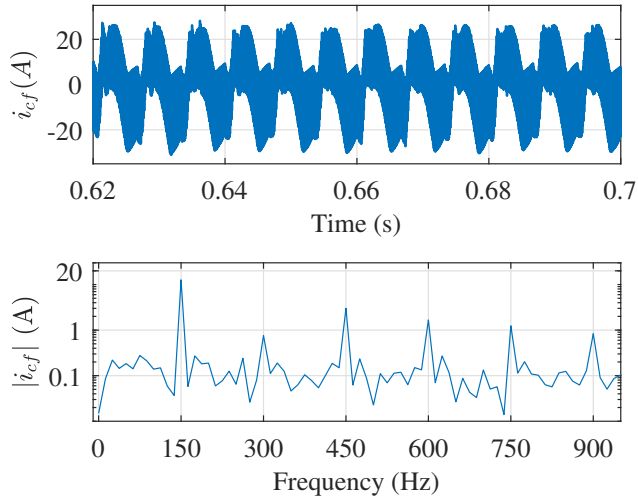

Figure 7.34: icf when the load is balanced and the 4^{th} leg is connected and switching at a 50 % duty cycle.

It can be seen how the highest harmonic component is the 3^{th} (150 Hz) with an amplitude of 12.67 V. The next harmonic in importance would be the 9^{th} (450 Hz), with an amplitude of 3 V. In the same way, the output voltage zero-sequence component can be analyzed, extracted from the upper plot in Fig. 7.32 by means of the Park's transformation (v_{cf} in Fig. 7.18). Fig. 7.35 shows the voltage response and the FFT of this voltage. As expected, there is a DC component of ≈20 V. In addition to this DC-component, there are also the same harmonics as in i_{cf}.

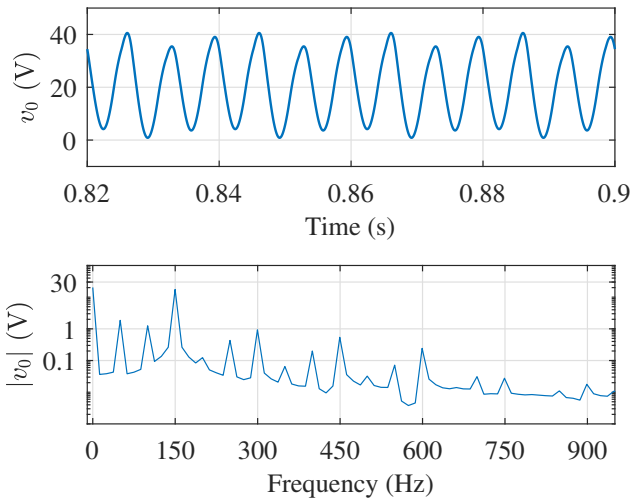

Figure 7.35: Homopolar voltage when the load is balanced and the 4^{th} leg is connected and switching at a 50 % duty cycle.

If a single-phase load is connected in addition to the 3-phase balanced one, the currents and voltages get unbalanced (Fig. 7.36). However, and as in the previous case, this almost does not show in the FFT or THD (2.73 %) of the complex vector (Fig. 7.37) because it reflects on the homopolar component.

Checking the current through the capacitors (Fig. 7.38), it can be seen how now the most important component is now the 1^{st} harmonic (50 Hz, 24.45 A) followed by the 3^{rd} harmonic (150 Hz, 9.67 A). Analyzing the homopolar voltage component (Fig. 7.39), yields to the same results, the DC component is reduced (≈6 V) compared with the case without single-phase loads but there is the new component at 50 Hz that reaches 30 V. The component at 150 Hz is also big, with a value of (≈20 V).

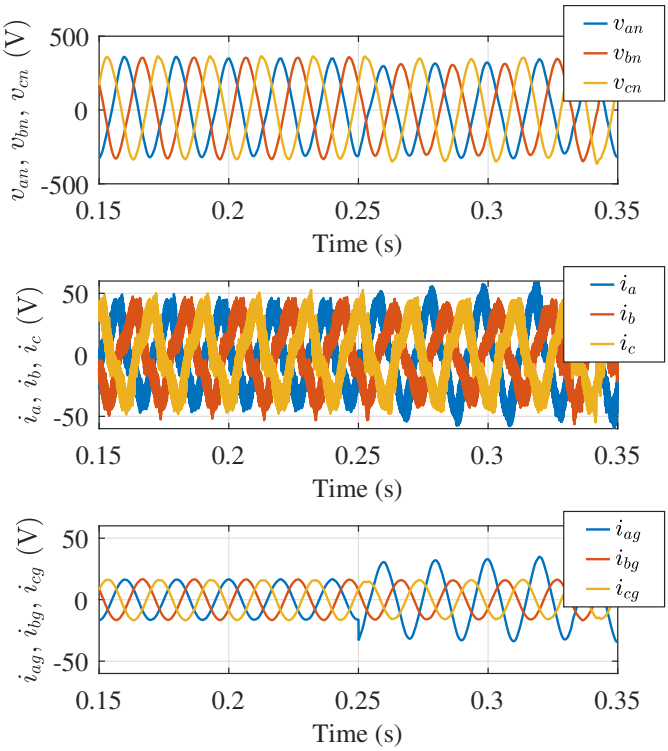

Figure 7.36: Three-phase output voltages and currents when a single-phase load is connected (t=0.25 s) and the 4^{th} leg is connected and switching at a 50 % duty cycle.

From the figures shown in this section, it can be seen that the most important harmonics to be controlled from the zero-sequence component are the DC component and the 1^{st} and 3^{rd} harmonics, as was already shown in Fig. 7.21.

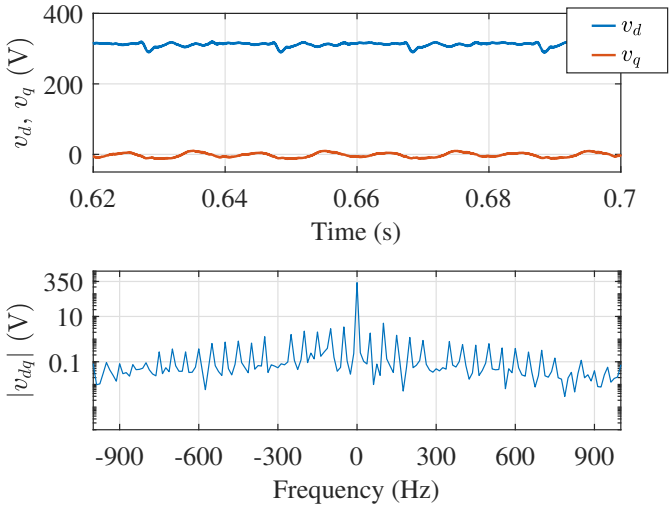

Figure 7.37: Output voltage when the load includes a single-phase load and the 4^{th} leg is connected and switching at a 50 % duty cycle. Synchronous reference frame with the fundamental component.

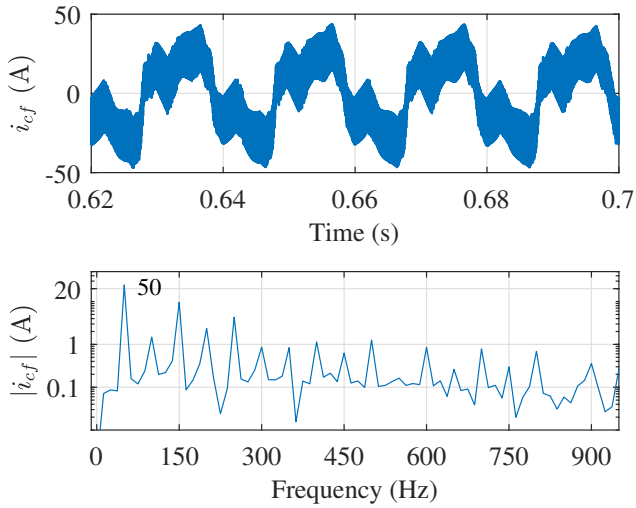

Figure 7.38: icf when the load includes a single-phase load and the 4^{th} leg is connected and switching at a 50 % duty cycle.

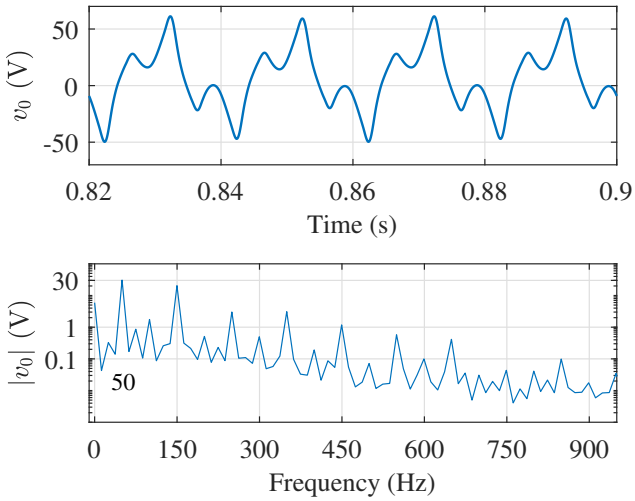

Figure 7.39: Homopolar voltage when the load includes a single-phase load and the 4^{th} leg is connected and switching at a 50 % duty cycle.

7.3.3.2.2 Homopolar voltage and current control

The results from the implementation of the control in Fig. 7.21 is shown Fig. 7.40. When the load is connected the currents get unbalanced, but the voltage keeps the expected waveform. The THD in this case is 1.73 %.

Analyzing the capacitor's current (Fig. 7.41) and the zero-sequence voltage component (Fig. 7.42) it can be seen how the controlled components have disappeared from the FFT; there is no DC component in the zero-sequence voltage and no 1^{st} nor 3^{rd} harmonics both in the zero-sequence voltage component and in the current through the filter capacitors.

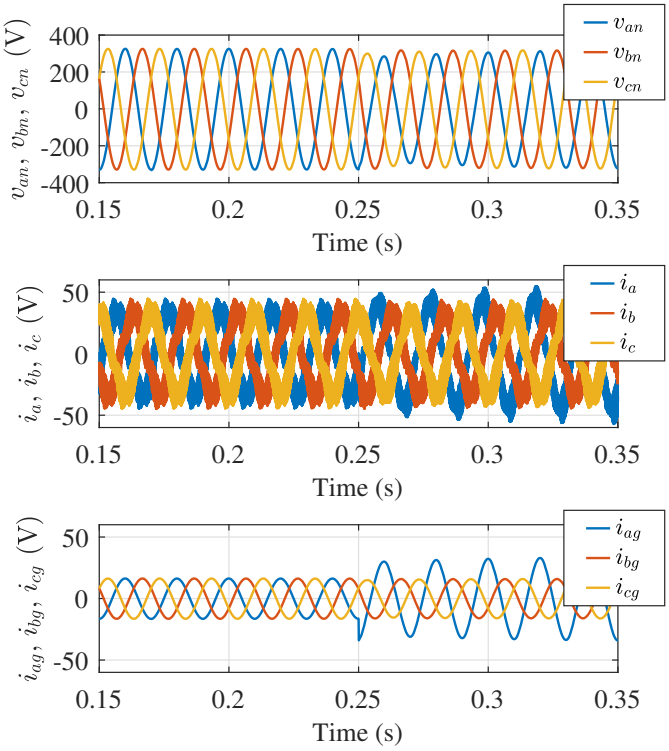

Figure 7.40: Three-phase output voltages and currents when a single-phase load is connected (t=0.25 s) and the 4^{th} leg is connected and the homopolar control is active.

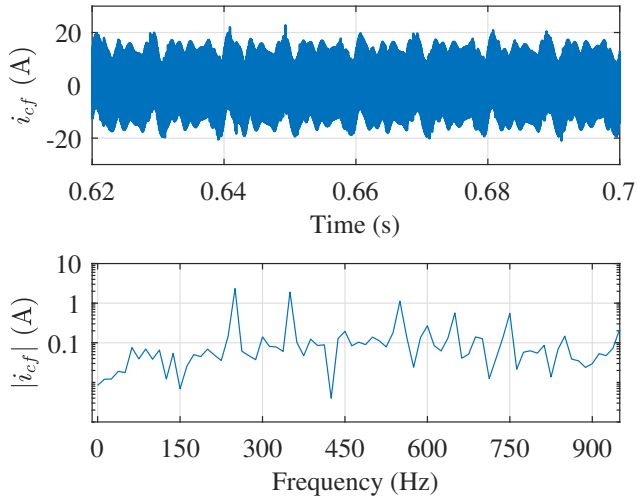

Figure 7.41: icf when the load includes a single-phase load and the homopolar control is active.

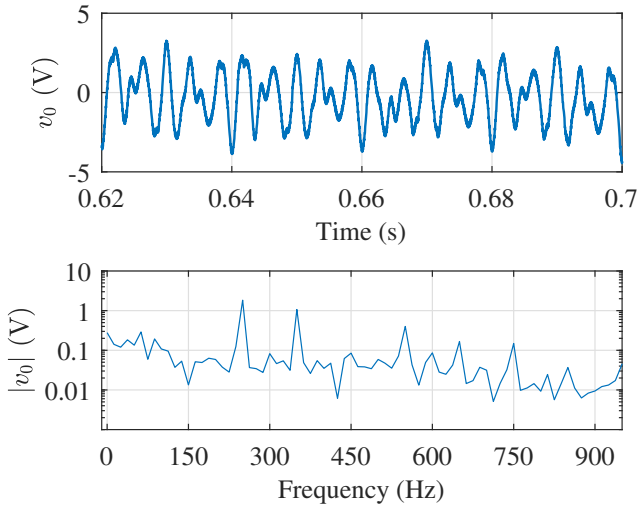

Figure 7.42: Homopolar voltage when the load includes a single-phase load and the homopolar control is active.

7.3.4 Experimental results

The control proposed in Fig. 7.18 is validated in the following section through experimental results, following the same analysis as in the previous section.

7.3.4.1 3-phase control

Fig. 7.43 shows the voltage and current waveforms when all the controls are enabled and the load is balanced. The dq representation of the output voltage is shown in Fig. 7.44. The THD is 1.63 % so it complies with the regulations.

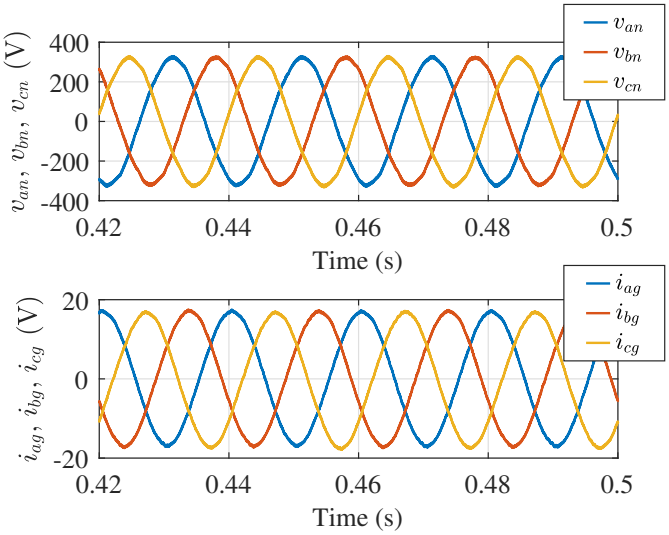

Figure 7.43: Three-phase output voltages when the load is balanced and the 4^{th} leg is connected and all the controls are enabled.

If the non-linear load is added (see Fig. 7.45), the system has a THD of 1.4 % and the voltages FFT (see Fig. 7.46) does not reveal any significant harmonic, been the highest one at -150 Hz with a value of 2 V.

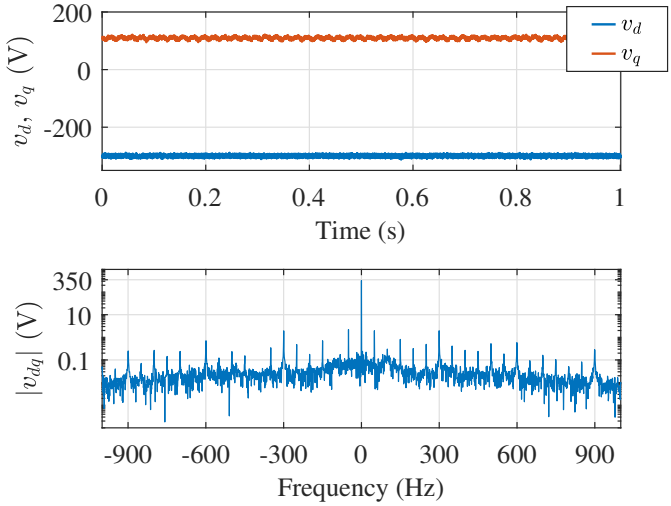

Figure 7.44: Output voltage when the load is balanced and the 4^{th} leg is connected and all the controls are enabled. Synchronous reference frame with the fundamental component.

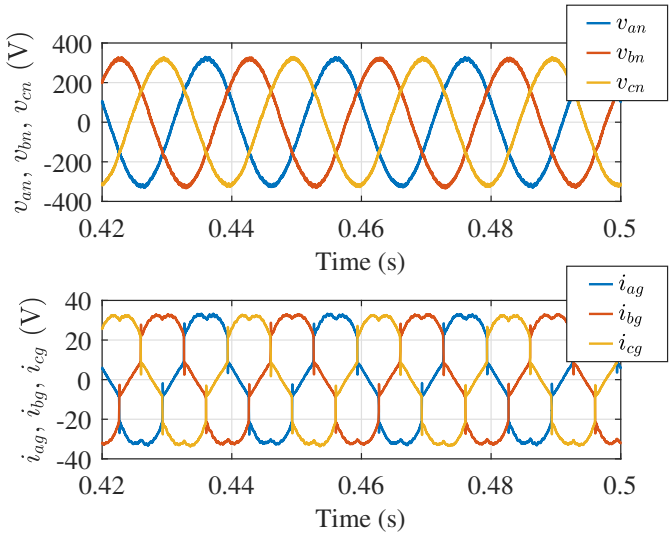

Figure 7.45: Three-phase output voltages and currents when the load includes a non-linear load and the 4^{th} leg is connected and all the controls are enabled.

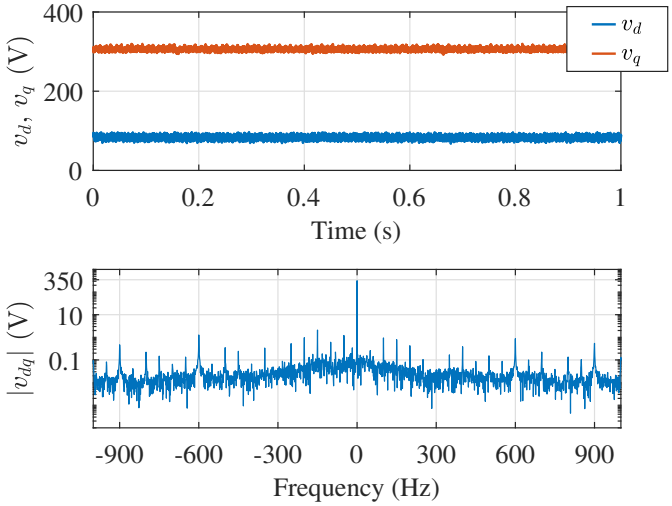

Figure 7.46: Output voltage when the load includes a non-linear load and the 4^{th} leg is connected and switching at a 50 % duty cycle. Synchronous reference frame with the fundamental component.

7.3.4.2 Homopolar control

Fig. 7.47 shows the current through the capacitors when the load includes a single-phase load. All the harmonics controlled are under 0.5 A. Complete control is not possible, because the resolution of the current sensors is limited. Fig. 7.48 shows the zero-sequence voltage. Again, the harmonics under control are below 2 V. The limited resolution of the voltage sensors makes it impossible to completely control said harmonics.

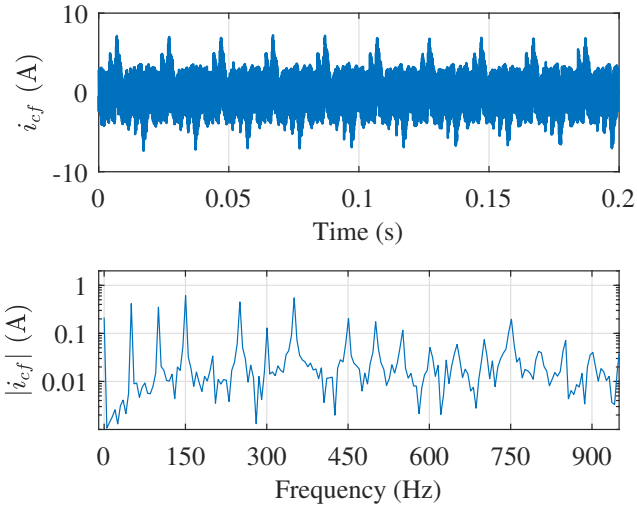

Figure 7.47: icf when the load includes a single-phase load and the homopolar control is active.

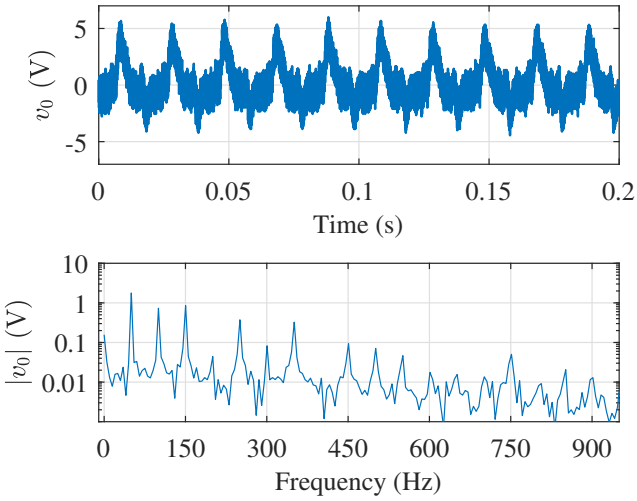

Figure 7.48: Homopolar voltage when the load includes a single-phase load and the homopolar control is active.

7.4 Conclusions

A 3P4L converter is a good alternative to line transformers to manage homopolar currents and voltages. By adding a 4^{th} leg and an extra inductor, they occupy less space and add great controllability to the system. As it has been shown, the system's control can be divided into two different blocks, the 3-phase classical system and the homopolar control. This technique allows an easier tune process for the regulators. As has been shown, both with simulations and experimental results, the controllers work appropriately and the THD is kept below the requirements of the standard at all times.

Part IV

Conclusions

Chapter 8

Conclusions and future work

8.1 Conclusions

Motivated by the need of abandoning highly pollutant fossil-fuel based generation, the electric system is gradually changing to a distributed generation system, which is formed by small generation units based on renewable energy sources, as solar panels or wind turbines. In this scenario, massive ESS are a key piece due to the intermittence of renewable generation. The integration of RES with ESS and the possibility of connecting to the grid generates a series of issues that have been only partially solved.

This thesis has shown the development and control of an autonomous building which can work connected to the grid or isolated from it, with $LiFePO_4$ batteries as the main ESS. This thesis is divided into two blocks, a first part dealing with the selection and handling of the energy storage system for the building and a second one dealing with the power converter selection and control.

The ESS was selected after an extensive review of the possible storage methods available in the literature, from the most classical and established systems, as pumped hydro, to the last research trends, as superconductive materials. After a deep analysis of the pros and cons of each different method, a battery storage system was selected as the main energy storage system in the building. Their low size compared to other methods, in addition to the fast response, makes them a great choice to be the main ESS in an autonomous zero-energy building.

Since there are a lot of possible battery chemistries, a study of them was

carried out. $LiFePO_4$ batteries were considered the most attractive due to a number of reasons including safety, long cycle life and low toxicity. However, LIBs in general are very sensitive to temperature variations, due to the chemistry and the different elements forming the cell. Due to this, an effort to monitor cell temperature must be done.

LIB temperature can be directly measured using temperature sensors, but they add cost and complexity and can compromise the system reliability as there are more elements susceptible to failure. Alternatively, LIB temperature can be estimated. There are several methods to estimate battery temperature, but the most interesting one is based on battery parameters, since they require less knowledge of the cell than other methods.

In this thesis, specifically in Chapters 3 and 4, two different methods to monitor cell temperature are proposed. They are based on two different power converters that are normally find combined together with batteries: the power converter connecting the battery pack to the rest of the system and the equalizer that keeps the batteries' voltages at the same level. In both cases, signals produced by the normal operation of the converters are used to estimate the internal resistance of the battery, without any additional sensors or signal injection.

In the first case, the cell voltage and current at the switching frequency are used to estimate the high frequency equivalent impedance of the cell. From this, the real part of the impedance is extracted and its change with temperature is analyzed. This relationship can be then used to estimate cell temperature.

In the second case, voltage and current at the cell are also used, but in this case the waveforms are different, corresponding to the normal operation of an SCE. Once the resistance is estimated, it can be used to track temperature changes in the same manner as in the previous case.

Regarding the second block of the thesis, the power converter of the building was analyzed and control. First, the selection of a 3P4L converter was justified by the need to control single-phase loads. These loads generate a homopolar component in the voltage and/or current which cannot be controlled with typical 3-phase systems without neutral distribution. Although a line-frequency transformer could be used instead, they are big and heavy and do not provide the required controllability.

The different loads that can be connected to the converter generate different components (harmonics) in the voltage and currents. These harmonics must be correctly handled in order to comply with the regulations regarding the maximum

THD allowed in a grid. Due to this, several controllers are connected in parallel, generally one for each harmonic component or one for each pair of harmonics, depending on the type of controller. All these paralleled connected controllers increase the chance of saturation in the converter, limited by the DC-link available voltage.

There are several proposals in the literature that address the importance of a correct saturation technique, but the majority are complex or require special formulations. Besides, they tend to reduce in equal ways the fundamental component and the harmonics of the voltage, which is not a good practice in some scenarios, as grid forming converters (the case in this thesis). Due to this, in Chapter 6, there is a proposal of a realizable reference frame anti-windup implementation for parallel controllers in multiple reference frames. The proposed implementation does not require a particular type of controllers nor special formulations. The proposed method preserves the fundamental component (magnitude and angle) as long as possible, and groups the harmonics in a different vector. In this way, lower priority harmonics are disabled as the saturation increases instantaneously, and are enabled when the available voltage increases again.

Finally, chapter 7 proposes the analysis and control of the 3P4L converter for the building. The system is analyzed and different scenarios are considered. The different harmonics under different types of loads are analyzed and the whole control scheme is validated using simulations and experimental results. It is concluded that the most important harmonics in the system are the negative sequence and the $\pm 6^{th}$ harmonics in the synchronus reference frame with the fundamental component. For the homopolar current and voltage, the system is analyzed employing a simplified homopolar circuit. It is concluded that the homopolar component could be controlled using either the 3-phase converter or the single-phase (4^{th} leg). The most important harmonics to be controlled in this case are the 1^{st} and 3^{th}.

8.2 Contributions

The contributions made during the development of this thesis are summarized as follows:

- An extensive state of the art regarding energy storage systems and battery chemistries has been provided.

- A method to estimate cell temperature when it is connected to a DC/DC converter has been developed. It uses the internal resistance of the cell to estimate its temperature. Unlike previously proposed methods, the one proposed here does not need to inject additional signals and works with the ones naturally produced by the commutation of the converter.

- A method to estimate cell temperature when it is connected to a switched capacitor equalizer has been developed. As the previous method, it uses the intrinsic waveform to the operation of the equalizer to estimate the operating temperature without needing extra sensors or extra signal injections.

- A realizable reference frame anti-windup implementation for parallel controllers in multiple reference frames has been proposed for 3-phase systems without neutral connection. Unlike previously proposed methods, under a situation of saturation the method is simpler to apply and keeps the fundamental component from degrading the maximum possible, only saturating it when the rest of the harmonics has been already discarded. The proposed implementation does not require a particular type of controllers nor special formulations.

- The control algorithm for a 3P4L converter in grid forming operation is proposed and validated. The system can be controlled as a 3-phase classical system independently of the extra leg. For the analysis of the homopolar path, a single-phase circuitry is employed. This extra control can be implemented in any of the two converters, both the 3-phase converter or the single-phase branch, provided that the other one keeps this homopolar value at zero.

Several scientific papers have been published in international journals and international conferences derived from the work of this dissertation (see Section 8.2.1 and Section 8.2.2). Moreover, other contributions have been made during the development of this dissertation (see Section 8.2.3 and Section 8.2.4).

8.2.1 Contributions of the dissertation published in international journals

1. **C. G. Moral**, D. Fernandez, J. M. Guerrero, D. Reigosa, C. Rivas and F. Briz, "Thermal monitoring of $LiFePO_4$ batteries using switching harmonics," in IEEE Transactions on Industry Applications (early access), 2020.

8.2.2 Contributions of the dissertation published in international conferences

2. J. M. Guerrero, **C. G. Moral**, D. Fernández, D. Reigosa, C. Rivas and F. Briz, "Realizable References Anti-Windup Implementation for Parallel Controllers in Multiple Reference Frames," IEEE Energy Conversion Congress and Exposition (ECCE), Portland, OR, pp. 3142-3149, Sept. 2018.

3. **C. G. Moral**, D. Fernandez, J. M. Guerrero, D. Reigosa and F. Briz, "Thermal monitoring of $LiFePO_4$ batteries using switching harmonics," IEEE Energy Conversion Congress and Exposition (ECCE), Portland, OR, pp. 2734-2740, Sept. 2018.

4. **C. G. Moral**, D. F. Laborda, L. S. Alonso, J. M. Guerrero, D. Fernandez, C. Rivas and D. Reigosa, "Battery internal resistance estimation using a battery balancing system based on switched capacitors," IEEE Energy Conversion Congress and Exposition (ECCE), Baltimore, MD, USA, pp. 2516-2522, Oct. 2019.

8.2.3 Other contributions published in international journals

5. D. Reigosa, D. Fernandez, **C. G. Moral**, S. B. Lee and F. Briz, "Permanent Magnet Synchronous Machine Drive Control Using Analog Hall-Effect Sensors," in IEEE Transactions on Industry Applications, vol. 54, no. 3, pp. 2358-2369, May-June 2018.

6. C. Lumbreras, J. M. Guerrero, D. Fernandez, D. D. Reigosa, **C. G. Moral** and F. Briz, "Analysis and Control of the Inductorless Boost Rectifier for Small-Power Wind-Energy Converters," in IEEE Transactions on Industry Applications, vol. 55, no. 1, pp. 689-700, Jan.-Feb. 2019.

8.2.4 Other contributions published in international conferences

7. D. Reigosa, D. Fernandez, **C. G. Moral**, S. B. Lee and F. Briz, "Permanent magnet synchronous machine drive control using analog hall-effect sensors,"

IEEE Energy Conversion Congress and Exposition (ECCE), Cincinnati, OH, pp. 3966-3971, 2017.

8.3 Future work

Several points could be addressed in the future to continue the research line of this dissertation:

- It has been shown how the resistance of the battery at high frequencies (≈10 kHz) is related to the cell's temperature. However, measurements were calibrated using a temperature sensor placed in contact with the cell's surface. Some works suggest that the internal battery temperature can be as higher as 20 % [142] when compared with the external one during transients. To check the influence of this on the proposed methods, it would be interesting to place a temperature sensor inside the cell.

- Explore the possibility of designing a battery equalizer that equalizes in terms of energy and not voltage. This would imply some kind of SOC estimation and more controllability in the system than the ones in SCE, but would increase the equalization in cells with specially flat SOC characteristics, as LIFePO_4 cells.

- Implement together the methods proposed for cell temperature estimation, both with the power converter and the equalizer. They are not mutually exclusive and could improve the temperature estimation at no cost, since the system would not be modified.

- Integrate the algorithms proposed for cell temperature estimation using a DC/DC converter in the DC/DC converter of the autonomous building to estimate the battery pack temperature.

- Try different modulation techniques for the 3P4L converter to extend its operating range.

- Extend the realizable reference anti-windup implementation for parallel controllers proposed to 3P4L converters.

- Add harmonics control to the DC/DC converter in the power converter of the building to protect the batteries.

8.4 Dissertation funding

This work was funded in part by the Research, Technological Development and Innovation Programs of the Spanish Ministry Economy and Competitiveness of the Spanish Government under the project MINECO-17-ENE2016-80047-R, in part by the Government of the Principality of Asturias under the project IDI/2018/000188, in part by the Oviedo Siembra Talento program of the Oviedo City Council and in part by FEDER funds.

Chapter 8

Conclusiones y trabajo futuro

8.1 Conclusiones

La necesidad de abandonar la producción eléctrica basada en combustibles fósiles altamente contaminantes está propiciando un cambio en el sistema eléctrico mundial, moviéndose de un sistema centralizado hacia una generación distribuida formada por generadores basados en energías renovables (paneles solaras, turbinas eólicas...). En este nuevo escenario, los sistemas de almacenamiento de energía masivos constituyen un punto esencia, debido a la intermitencia de la generación basada en energías renovables. Integrar generación y almacenamiento, unidos a la posibilidad de conectar esta producción distribuida a la red, genera una serie de problemas que aún no han sido completamente resueltos.

En esta tesis se muestra el desarrollo y control de un edificio autónomo que puede funcionar conectado o aislado de la red general, cuyo sistema principal de almacenamiento son baterías de $LiFePO_4$. La tesis se encuentra divida en dos partes. La primera parte muestra la elección y control del sistema de almacenamiento, mientras que la segunda parte muestra la selección y control del sistema de potencia.

La selección de las baterías como sistema de almacenamiento principal tuvo lugar tras una extensa revisión de los métodos disponibles en la literatura, desde los sistemas clásicos y ya altamente establecidos, como por ejemplo los sistemas

hidráulicos, a las últimas tendencias en investigación, como por ejemplo aquellos basados en materiales superconductores. Tras un profundo análisis de ventajas e inconvenientes de cada sistema, las baterías fueron seleccionadas por tener un tamaño inferior a otros sistemas y tener una respuesta más rápida.

Existe un gran número de composiciones químicas utilizadas en baterías, por lo que se realizó un estudio sobre ellas para seleccionar la más conveniente para esta aplicación concreta. Se concluyó que las baterías de $LiFePO_4$ son unas de las más atractivas debido a sus altos niveles de seguridad, larga vida útil y baja toxicidad. Sin embargo, las baterías de litio son bastante sensibles a cambios de temperatura por su composición, y por ello su temperatura tiene que ser cuidadosamente monitorizada.

La temperatura de estas baterías se puede medir directamente utilizando sensores de temperatura, pero añaden coste y complejidad al sistema y aumenta el número de elementos susceptibles de fallo. De forma alternativa, su temperatura se puede estimar utilizando diferentes métodos, siendo el más interesante aquel basado en parámetros de la batería, puesto que es el que menos conocimiento sobre la celda requiere.

En la tesis, específicamente en los Capítulos 3 y 4, se proponen dos métodos distintos para estimar temperatura. Cada método se aplica a un convertidor diferente, pudiendo encontrarse ambos normalmente relacionados con distintas configuraciones de baterías. El primero sería un convertidor de potencia que permite conectar las baterías al resto del sistema. El segundo sería el ecualizador que mantiene todas las tensiones de las celdas a un valor igualado. En ambos casos, las señales que se utilizan para estimar temperatura se producen de forma natural en los convertidores debido a su funcionamiento normal, sin necesidad de inyectar señales adicionales o añadir sensores nuevos.

En el primer caso, el voltaje y la corriente de la celda a la frecuencia de conmutación se usan para estimar la impedancia equivalente de la celda a alta frecuencia. De esta impedancia se extrae la parte real y su variación con la temperatura se usa para estimar temperatura en la celda.

En el segundo caso también se usan el voltaje y la corriente de la celda, aunque las formas de ondas cambian al cambiar el convertidor, correspondiendo éstas al funcionamiento normal de un ecualizador basado en condensadores conmutados. Una vez que la resistencia se ha estimado con estos parámetros, ésta puede usarse para estimar temperatura, de una forma similar al caso anterior.

En el segundo bloque de la tesis se analiza y controla el convertidor de po-

tencia del edificio autónomo. Primero se justifica la selección del convertidor 3P4L por la necesidad de controlar un sistema que incluya cargas monofásicas. Estas cargas generan componentes homopolares en el voltaje y/o la corriente que no pueden ser controlados en los sistemas clásicos trifásicos sin distribución de neutro. Aunque se podría utilizar un transformador a frecuencia de red para bloquear estas componentes, pero se descarta debido a un elevado tamaño y peso, además de perderse parte de la controlabilidad.

Las distintas cargas que pueden conectarse al convertidor generan diferentes componentes (armónicos) tanto en tensión como en corriente. El control de estos armónicos es esencial para cumplir las normativas de regulación sobre el máximo THD permitido en una red. Por este motivo es necesario paralelizar distintos reguladores, generalmente uno por componente o por cada dos componentes, dependiendo del tipo de regulador empleado. El aumento de reguladores conlleva un aumento de las probabilidades de saturación de la tensión del convertidor, limitada por la máxima tensión en cada momento en el bus de continua.

Existen numerosas propuestas en la literatura que demuestran la importancia de manejar correctamente la saturación de los convertidores, aunque la mayoría son complejas o requieren formulaciones especiales. Además, estos métodos tienen a reducir de manera similar la componente fundamental y los armónicos de tensión ante una saturación, lo que no sería una práctica recomendable en ciertos escenarios, como por ejemplo en convertidores generadores de red, caso que nos ocupa. Por todo ello, en el Capítulo 6 se propone una implementación anti-windup en referencias realizables utilizando múltiples sistemas de referencias que no requiere formulaciones especiales ni estructuras concretas de los reguladores. El método propuesto preserva la componente fundamental (magnitud y ángulo) siempre que sea posible y primero satura los armónicos, que se agrupan en otra componente diferente. De esta manera, los armónicos de más baja prioridad se deshabilitan de forma instantánea según va aumentando la saturación, y vuelven a habilitarse cuando el voltaje disponible crece de nuevo.

Finalmente, en el capítulo 7 se propone un análisis y control del convertidor 3P4l del edificio autónomo. El sistema se analiza ante varios posibles escenarios de cargas y se estudian los distintos armónicos que podrían aparecer. El control propuesto se valida por medio de simulaciones y experimentales. Se concluye que los armónicos más importantes serían la secuencia negativa y los armónicos $\pm 6^{th}$ en referencia síncrona con la componente fundamental. En cuanto a la componente homopolar, se analiza el sistema en base a un circuito homopolar simplificado. Se concluye que componente homopolar puede controlarse tanto

utilizando el convertidor trifásico como el convertidor monofásico (que corresponde a la cuarta rama). Las componentes armónicas más importantes en ese caso serían los armónicos primero y tercero.

8.2 Contribuciones

Las contribuciones de esta tesis se pueden resumir de la siguiente manera:

- Extenso desarrollo del estado del arte en relación con los sistemas de almacenamiento de energía y los distintos tipos de químicas de baterías.
- Desarrollo de un sistema de estimación de temperatura en baterías de litio cuando se conectan a un convertidor DC/DC. Se usa la resistencia interna de la celda para estimar su temperatura. Al contrario que otros métodos previos de la literatura, el método propuesto no necesita inyectar señales adicionales y trabaja con las generadas de forma natural por la conmutación del convertidor.
- Desarrollo de un sistema de estimación de temperatura en baterías de litio cuando se conectan a un convertidor ecualizador de celdas basado en condensadores conmutados. Al igual que en el método anterior, utiliza las señales intrínsecas al funcionamiento del ecualizador para estimar la temperatura de las celdas sin necesidad de sensores ni inyecciones extra de señales.
- Se ha propuesto una implementación de un anti-windup en referencias realizables utilizando múltiples sistemas de referencias para un sistema trifásico sin neutro. Al contrario que las propuestas previas, en caso de saturación el método se aplica de forma sencilla y evita degradar la componente fundamental el máximo posible, solo saturándola cuando ya se han eliminado el resto de los armónicos. El método propuesto no requiere formulaciones especiales ni estructuras concretas de los reguladores.
- Se propone y valida un algoritmo de control para convertidores 3P4L operando en formación de red. El sistema puede controlarse como un sistema trifásico clásico independiente de la cuarta rama. Para el análisis de la cuarta rama se utiliza el circuito homopolar simplificado. El control homopolar se puede implementar tanto en el convertidor trifásico como en el de la cuarta rama, siempre que el otro convertidor mantenga su componente homopolar a cero.

El trabajo realizado durante la elaboración de esta tesis resultó en la publicación de varios trabajos, tanto en conferencias como en revistas internacionales (Secciones 8.2.1 y 8.2.2). También se colaboró en la publicación de otros trabajos sin relación directa con los contenidos de la tesis (Secciones 8.2.3 y 8.2.4).

8.2.1 Contribuciones de la tesis publicadas en revistas internacionales

1. **C. G. Moral**, D. Fernandez, J. M. Guerrero, D. Reigosa, C. Rivas and F. Briz, "Thermal monitoring of $LiFePO_4$ batteries using switching harmonics," in IEEE Transactions on Industry Applications (early access), 2020.

8.2.2 Contribuciones de la tesis publicadas en conferencias internacionales

2. J. M. Guerrero, **C. G. Moral**, D. Fernández, D. Reigosa, C. Rivas and F. Briz, "Realizable References Anti-Windup Implementation for Parallel Controllers in Multiple Reference Frames," IEEE Energy Conversion Congress and Exposition (ECCE), Portland, OR, pp. 3142-3149, Sept. 2018.

3. **C. G. Moral**, D. Fernandez, J. M. Guerrero, D. Reigosa and F. Briz, "Thermal monitoring of $LiFePO_4$ batteries using switching harmonics," IEEE Energy Conversion Congress and Exposition (ECCE), Portland, OR, pp. 2734-2740, Sept. 2018.

4. **C. G. Moral**, D. F. Laborda, L. S. Alonso, J. M. Guerrero, D. Fernandez, C. Rivas and D. Reigosa, "Battery internal resistance estimation using a battery balancing system based on switched capacitors," IEEE Energy Conversion Congress and Exposition (ECCE), Baltimore, MD, USA, pp. 2516-2522, Oct. 2019.

8.2.3 Otras contribuciones publicadas en revistas internacionales

5. D. Reigosa, D. Fernandez, **C. G. Moral**, S. B. Lee and F. Briz, "Permanent Magnet Synchronous Machine Drive Control Using Analog Hall-Effect

Sensors," in IEEE Transactions on Industry Applications, vol. 54, no. 3, pp. 2358-2369, May-June 2018.

6. C. Lumbreras, J. M. Guerrero, D. Fernandez, D. D. Reigosa, **C. G. Moral** and F. Briz, "Analysis and Control of the Inductorless Boost Rectifier for Small-Power Wind-Energy Converters," in IEEE Transactions on Industry Applications, vol. 55, no. 1, pp. 689-700, Jan.-Feb. 2019.

8.2.4 Otras contribuciones publicadas en conferencias internacionales

7. D. Reigosa, D. Fernandez, **C. G. Moral**, S. B. Lee and F. Briz, "Permanent magnet synchronous machine drive control using analog hall-effect sensors," IEEE Energy Conversion Congress and Exposition (ECCE), Cincinnati, OH, pp. 3966-3971, 2017.

8.3 Trabajo futuro

A raíz del trabajo realizado en la presente tesis doctoral, existen varias líneas de investigación abiertas para su estudio futuro:

- Se ha demostrado como la resistencia de la batería a altas frecuencias (≈10 kHz) está relacionada con la temperatura de una batería. Sin embargo, las medidas se calibraron con un sensor de temperatura en contacto con la superficie de la celda. Algunos trabajos sugieren que la temperatura interna de la batería podría ser de un 20 % superior comparada con el exterior durante los transitorios [142]. Para comprobar la influencia de esto en los métodos propuestos, sería interesante colocar un sensor en el interior de la celda.

- Explorar la posibilidad de diseñar un sistema de ecualización de celdas basado en energía y no en voltaje. Para ello sería necesario algún tipo de estimador de SOC y más controlabilidad en el ecualizador que en el caso de la ecualización usando condensadores conmutados. Esto incrementaría la ecualización en las celdas, sobre todo en aquellos casos con curvas de SOC planas, como las baterías $LIFePO_4$.

- Implementar de manera conjunta los métodos de estimación de temperatura de celda propuestos, tanto el que usa el convertidor de potencia como el que usa el ecualizador. Estos dos métodos no son mutuamente excluyentes y podrían mejorar la estimación de temperatura sin coste asociado, ya que el sistema no sufriría ninguna modificación.
- Integrar el método de estimación de temperatura de celda utilizando un convertidor DC/DC en el control del DC/DC del edificio autónomo para estimar la temperatura del pack de baterías.
- Probar nuevos métodos de control del 3P4L para extender su rango de operación.
- Extender la implementación anti-windup desarrollada para controladores en paralelo a sistemas 3P4L.
- Añadir control de armónicos al convertidor DC/DC del edificio autónomo para proteger las baterías.

8.4 Financiación

Este trabajo fue financiado en parte por el programa de Investigación, Desarrollo Tecnológico e Innovación del Ministerio de Economía y Competitividad del Gobierno de España bajo el proyecto MINECO-17-ENE2016-80047-R, en parte por el Gobierno del Principado de Asturias con el proyecto IDI/2018/000188, en parte por el programa Oviedo Siembra Talento del Ayuntamiento de Oviedo y en parte por las becas del Fondo Europeo de Desarrollo Regional (FEDER).

Bibliography

[1] NASA, "NOAA Analyses Reveal 2019 Second Warmest Year on Record". https://www.giss.nasa.gov/research/news/20200115/, accessed 17-February-2020.

[2] Asociación de Empresas de Energías Renovables (APPA), "Renovables en España," 2019. https://www.appa.es/energias-renovables/renovables-en-espana/, accessed 12-April-2020.

[3] European Commission, "Paris Agreement," Dec. 2015. https://ec.europa.eu/clima/policies/international/negotiations/paris_en, accessed 17-February-2020.

[4] BP, "Statistical Review of World Energy," June 2019. https://www.bp.com/content/dam/bp/business-sites/en/global/corporate/pdfs/energy-economics/statistical-review/bp-stats-review-2019-full-report.pdf, accessed 17-February-2020.

[5] M. Liserre, T. Sauter, and J. Y. Hung, "Future Energy Systems: Integrating Renewable Energy Sources into the Smart Power Grid Through Industrial Electronics," *IEEE Industrial Electronics Magazine*, vol. 4, no. 1, pp. 18–37, Mar. 2010.

[6] M. I. Ojovan, W. E. Lee, and S. N. Kalmykov, *"An Introduction to Nuclear Waste Immobilisation"*. Elsevier, Apr. 2019.

[7] D. Gielen, F. Boshell, D. Saygin, M. D. Bazilian, N. Wagner, and R. Gorini, "The role of renewable energy in the global energy transformation," *Energy Strategy Reviews*, vol. 24, pp. 38–50, Apr. 2019.

[8] U.S. Energy Information Administration,"Annual Energy Outlook 2020 with projections to 2050," Jan. 2020. https://www.eia.gov/outlooks/aeo/, accessed 17-February-2020.

[9] International Energy Agency (IEA), "Global CO_2 emissions in 2019," 2020. https://www.iea.org/articles/global-co2-emissions-in-2019, accessed 17-February-2020.

[10] International Hydropower Association (IHA), "2019 Hydropower status report," 2019. https://www.hydropower.org/status2019, accessed 17-February-2020.

[11] International Energy Agency (IEA), "Snapshot of global photovoltaic markets," 2019. http://www.iea-pvps.org/?id=266, accessed 17-February-2020.

[12] World Wind Energy Association (WWEA), "Wind Power Capacity Worldwide Reaches 597 GW, 50,1 GW added in 2018," June, 2019. https://wwindea.org/blog/2019/02/25/wind-power-capacity-worldwide-reaches-600-gw-539-gw-added-in-2018/, accessed 17-February-2020.

[13] H. Polatidis, D. A. Haralambopoulos, G. Munda, and R. Vreeker, "Selecting an appropriate multi-criteria decision analysis technique for renewable energy planning," *Energy Sources, Part B: Economics, Planning, and Policy*, vol. 1, no. 2, pp. 181–193, 2006.

[14] M. Khalil, "Geological survey energy and wildlife research annual report for 2019," *U.S. Geological Survey*, vol. 1458, pp. 1–108, Sept. 2019.

[15] P. Denholm, E. Ela, B. Kirby, and M. Milligan, "Role of energy storage with renewable electricity generation," *National Renewable Energy Laboratory*, Jan. 2010.

[16] B. Scrosati and J. Garche, "Lithium batteries: Status, prospects and future," *Journal of Power Sources*, vol. 195, no. 9, pp. 2419–2430, May 2010.

[17] S. Rehman, L. M. Al-Hadhrami, and M. M. Alam, "Pumped hydro energy storage system: A technological review," *Renewable and Sustainable Energy Reviews*, vol. 44, pp. 586–598, Apr. 2015.

[18] M. Valavi and A. Nysveen, "Variable-Speed Operation of Hydropower Plants: A Look at the Past, Present, and Future," *IEEE Industry Applications Magazine*, vol. 24, no. 5, pp. 18–27, Sept. 2018.

[19] M. I. Daoud, A. S. Abdel-Khalik, A. Massoud, S. Ahmed, and N. H. Abbasy, "On the development of flywheel storage systems for power system applications: A survey," in *XXth International Conference on Electrical Machines*, pp. 2119–2125, Sept. 2012.

[20] M. Bragard, N. Soltau, S. Thomas, and R. W. De Doncker, "The Balance of Renewable Sources and User Demands in Grids: Power Electronics for Modular Battery Energy Storage Systems," *IEEE Transactions on Power Electronics*, vol. 25, no. 12, pp. 3049–3056, Dec. 2010.

[21] Red Eléctrica de España (REE), "Demanda y producción en tiempo real," February, 2020. https://demanda.ree.es/visiona/peninsula/demanda/total/2020-02-05, accessed 07-March-2020.

[22] H. Chen, T. N. Cong, W. Yang, C. Tan, Y. Li, and Y. Ding, "Progress in electrical energy storage system: A critical review," *Progress in Natural Science*, vol. 19, no. 3, pp. 291–312, Mar. 2009.

[23] International Hydropower Association (IHA), "The world's water battery: Pumped hydropower storage and the clean energy transition," Dec. 2018. https://www.hydropower.org/publications/the-world%E2%80%99s-water-battery-pumped-hydropower-storage-and-the-clean-energy-transition, accessed 17-February-2020.

[24] D. J. Swider, "Compressed Air Energy Storage in an Electricity System With Significant Wind Power Generation," *IEEE Transactions on Energy Conversion*, vol. 22, no. 1, pp. 95–102, Mar. 2007.

[25] R. Strzelecki and G. Benysek, *"Power Electronics in Smart Electrical Energy Networks"*. Pringer-Verlag, 2008.

[26] Z. Yang and S. V. Garimella, "Thermal analysis of solar thermal energy storage in a molten-salt thermocline," *Solar Energy*, vol. 84, no. 6, pp. 974–985, June 2010.

[27] J. Carrasco, L. Franquelo, J. Bialasiewicz, E. Galvan, R. PortilloGuisado, M. Prats, J. Leon, and N. Moreno-Alfonso, "Power-Electronic Systems for the Grid Integration of Renewable Energy Sources: A Survey," *IEEE Transactions on Industrial Electronics*, vol. 53, pp. 1002–1016, June June 2006.

[28] K. Hashimoto, N. Kumagai, K. Izumiya, H. Takano, and Z. Kato, "The production of renewable energy in the form of methane using electrolytic hydrogen generation," *Energy, Sustainability and Society volume*, vol. 4, no. 17, pp. 1–9, Jan. 2014.

[29] M. T. Lawder, B. Suthar, P. W. C. Northrop, S. De, C. M. Hoff, O. Leitermann, M. L. Crow, S. Santhanagopalan, and V. R. Subramanian, "Battery Energy Storage System (BESS) and Battery Management System (BMS) for Grid-Scale Applications," *Proceedings of the IEEE*, vol. 102, no. 6, pp. 1014–1030, Jun. 2014.

[30] D. W. Gao, *"Energy Storage for Sustainable Microgrid"*. Elsevier, 2015.

[31] P. Ribeiro, B. Johnson, M. Crow, A. Arsoy, and Y. Liu, "Energy storage systems for advanced power applications," *Proceedings of the IEEE*, vol. 89, no. 12, pp. 1744–1756, Dec. 2001.

[32] D. Linden and T. B. Reddy, *"Handbook of Batteries", Fourth Edition*. New York: McGraw-Hill Professional, Jan. 2011.

[33] D. Anseán, M. González, V. M. García, J. C. Viera, J. C. Antón, and C. Blanco, "Evaluation of $LiFePO_4$ Batteries for Electric Vehicle Applications," *IEEE Transactions on Industry Applications*, vol. 51, no. 2, pp. 1855–1863, Mar. 2015.

[34] L.Wilson, "Shades of Green: Electric Cars' Carbon Emissions Around the Globe," 2013. http://shrinkthatfootprint.com/electric-car-emissions, accessed 17-February-2020.

[35] J. Tollefson, "Car industry: Charging up the future," *Nature*, vol. 456, p. 436–440, Nov. 2008.

[36] P. Hernandez and P. Kenny, "From net energy to zero energy buildings: Defining life cycle zero energy buildings (LC-ZEB)," *Energy and Buildings*, vol. 42, no. 6, pp. 815–821, Jun. 2010.

[37] Q. Wang, P. Ping, X. Zhao, G. Chu, J. Sun, and C. Chen, "Thermal runaway caused fire and explosion of lithium ion battery," *Journal of Power Sources*, vol. 208, pp. 210–224, June 2012.

[38] H. Rahimi-Eichi, U. Ojha, F. Baronti, and M.-Y. Chow, "Battery Management System: An Overview of Its Application in the Smart Grid and

Electric Vehicles," *IEEE Industrial Electronics Magazine*, vol. 7, no. 2, pp. 4–16, Jun. 2013.

[39] F. Blaabjerg, R. Teodorescu, M. Liserre, and A. V. Timbus, "Overview of Control and Grid Synchronization for Distributed Power Generation Systems," *IEEE Transactions on Industrial Electronics*, vol. 53, no. 5, pp. 1398–1409, Oct. 2006.

[40] "IEEE Recommended Practice and Requirements for Harmonic Control in Electric Power Systems," *IEEE Std 519-2014 (Revision of IEEE Std 519-1992)*, pp. 1–29, June 2014.

[41] S. Santoso, F. McGranaghan, R. G. Dugan, and W. Rand, Beaty, *"Electrical Power Systems Quality," Third Edition.* McGraw-Hill Education, 2012.

[42] Y. W. Li and J. He, "Distribution System Harmonic Compensation Methods: An Overview of DG-Interfacing Inverters," *IEEE Industrial Electronics Magazine*, vol. 8, no. 4, pp. 18–31, Dec. 2014.

[43] F. Wang, J. L. Duarte, and M. A. M. Hendrix, "Pliant Active and Reactive Power Control for Grid-Interactive Converters Under Unbalanced Voltage Dips," *IEEE Transactions on Power Electronics*, vol. 26, no. 5, pp. 1511–1521, May 2011.

[44] M. Saeed, M. R. Rogina, M. López, A. Rodríguez, M. Arias, and F. Briz, "Design and construction of a DAB using SiC MOSFETs with an isolation of 24 kV for PET applications," in *19th European Conference on Power Electronics and Applications (EPE'17 ECCE Europe)*, pp. P.1–P.10, Sept. 2017.

[45] M. R. Miveh, M. F. Rahmat, A. A. Ghadimi, and M. W. Mustafa, "Control techniques for three-phase four-leg voltage source inverters in autonomous microgrids: A review," *Renewable and Sustainable Energy Reviews*, vol. 54, pp. 1592–1610, Feb. 2016.

[46] Texas Instruments, "TMS320F2833x, TMS320F2823x Digital Signal Controllers (DSCs)," June 2007. https://www.ti.com/lit/ds/symlink/tms320f28335.pdf?&ts=1588972438647, accessed 08-May-2020.

[47] K. T. Møller, T. R. Jensen, E. Akiba, and H.-w. Li, "Hydrogen - A sustainable energy carrier," *Progress in Natural Science: Materials International*, vol. 27, no. 1, pp. 34–40, Feb. 2017.

[48] M. E. Nazari, M. M. Ardehali, and S. Jafari, "Pumped-storage unit commitment with considerations for energy demand, economics, and environmental constraints," *Energy*, vol. 35, no. 10, pp. 4092–4101, Oct. 2010.

[49] G. Genta, *"Kinetic energy storage: theory and practice of advanced flywheel systems"*. Butterworth-Heinemann, 1985.

[50] S. Mukoyama, K. Nakao, H. Sakamoto, T. Matsuoka, K. Nagashima, M. Ogata, T. Yamashita, Y. Miyazaki, K. Miyazaki, T. Maeda, and H. Shimizu, "Development of Superconducting Magnetic Bearing for 300 kW Flywheel Energy Storage System," *IEEE Transactions on Applied Superconductivity*, vol. 27, no. 4, pp. 1–4, June 2017.

[51] AcivePower, "Understanding Flywheel Energy Storage: Does High-Speed Really Imply a Better Design?". www.activepower.com, accessed 19-February-2020.

[52] S. M. Hasnain, "Review on sustainable thermal energy storage technologies, Part I: heat storage materials and techniques," *Energy Conversion and Management*, vol. 39, no. 11, pp. 1127–1138, Aug. 1998.

[53] H. Ibrahim, A. Ilinca, and J. Perron, "Energy storage systems—Characteristics and comparisons," *Renewable and Sustainable Energy Reviews*, vol. 12, no. 5, pp. 1221–1250, June 2008.

[54] I. Sarbu and C. Sebarchievici, "A Comprehensive Review of Thermal Energy Storage," *Sustainability*, vol. 10, no. 1, p. 191, Jan. 2018.

[55] A. D. Smith, P. J. Mago, and N. Fumo, "Benefits of thermal energy storage option combined with CHP system for different commercial building types," *Sustainable Energy Technologies and Assessments*, vol. 1, pp. 3–12, Mar. 2013.

[56] I. Buchmann, *"Batteries in a Portable World - A Handbook on Rechargeable Batteries for Non-Engineers"*. Cadex Electronics Inc., 2016.

[57] J. Garche, E. Karden, P. T. Moseley, and D. A. J. Rand, *"Lead-Acid Batteries for Future Automobiles"*. Elsevier, 2017.

[58] M. Götz, J. Lefebvre, F. Mörs, A. McDaniel Koch, F. Graf, S. Bajohr, R. Reimert, and T. Kolb, "Renewable Power-to-Gas: A technological and economic review," *Renewable Energy*, vol. 85, pp. 1371–1390, Jan. 2016.

[59] H. Barthelemy, M. Weber, and F. Barbier, "Hydrogen storage: Recent improvements and industrial perspectives," *International Journal of Hydrogen Energy*, vol. 42, no. 11, pp. 7254–7262, Mar. 2017.

[60] M. Einhorn, F. V. Conte, C. Kral, and J. Fleig, "Comparison, Selection, and Parameterization of Electrical Battery Models for Automotive Applications," *IEEE Transactions on Power Electronics*, vol. 28, no. 3, pp. 1429–1437, Mar. 2013.

[61] S. Buller, M. Thele, E. Karden, and R. W. De Doncker, "Impedance-based non-linear dynamic battery modeling for automotive applications," *Journal of Power Sources*, vol. 113, no. 2, pp. 422–430, Jan. 2003.

[62] A. E. Mejdoubi, H. Gualous, H. Chaoui, and G. Alcicek, "Experimental investigation of calendar aging of lithium-ion batteries for vehicular applications," in *EMC Conference, Turkiye, Ankara*, pp. 1–5, Sept. 2017.

[63] I. Alsaidan, W. Gao, and A. Khodaei, "Optimal design of battery energy storage in stand-alone brownfield microgrids," in *North American Power Symposium (NAPS)*, pp. 1–6, Sept. 2017.

[64] Z. Miao, L. Xu, V. R. Disfani, and L. Fan, "An SOC-Based Battery Management System for Microgrids," *IEEE Transactions on Smart Grid*, vol. 5, no. 2, pp. 966–973, Mar. 2014.

[65] J. P. Fellner, G. J. Loeber, S. P. Vukson, and C. A. Riepenhoff, "Lithium-ion testing for spacecraft applications," *Journal of Power Sources*, vol. 119-121, pp. 911–913, June 2003.

[66] M. Sayegh, C. Forgez, T.-H. Tran, and G. Cherouvrier, "$LiFePO_4$/graphite battery modelling for an aeronautical application," in *IEEE 24th International Symposium on Industrial Electronics (ISIE)*, pp. 1278–1283, June 2015.

[67] G. Pistoia, *"Battery Operated Devices and Systems"*. Elsevier, Amsterdam, 2009.

[68] Z. Liao, S. Zhang, K. Li, G. Zhang, and T. G. Habetler, "A survey of methods for monitoring and detecting thermal runaway of lithium-ion batteries," *Journal of Power Sources*, vol. 436, p. 226879, Oct. 2019.

[69] D. A. González, "High power Li-ION battery performance: A mechanistic analysis of aging." PhD thesis, University of Oviedo, 2015. http://hdl.handle.net/10651/34551, accessed 16-January-2018.

[70] C. D. Rahn and C.-Y. Wang, *"Battery Systems Engineering", First Edition.* United Kingdom: John Wiley & Sons, Ltd, 2013.

[71] K. W. E. Cheng, B. P. Divakar, H. Wu, K. Ding, and H. F. Ho, "Battery-management system (BMS) and SOC development for electrical vehicles," *IEEE Transactions on Vehicular Technology*, vol. 60, no. 1, pp. 76–88, Jan. 2011.

[72] E. Chemali, M. Preindl, P. Malysz, and A. Emadi, "Electrochemical and electrostatic energy storage and management systems for electric drive vehicles: State-of-the-art review and future trends," *IEEE Journal of Emerging and Selected Topics in Power Electronics*, vol. 4, no. 3, pp. 1117–1134, Sept. 2016.

[73] B. Scrosati, K. M. Abraham, W. V. Schalkwijk, and J. Hassoun, *"Lithium batteries: Advanced Technologies and Applications"*. John Wiley & Sons, Inc., 2016.

[74] Y. Sato, S. Takeuchi, and K. Kobayakawa, "Cause of the memory effect observed in alkaline secondary batteries using nickel electrode," *Journal of Power Sources*, vol. 93, no. 1, pp. 20–24, Feb. 2001.

[75] Panasonic, "Litihum Ion Batteries Technical Handbook". https://eu.industrial.panasonic.com/sites/default/pidseu/files/downloads/files/panasonic_li-ion_handbook.pdf, accessed 27-February-2020.

[76] Q. Wang, L. Jiang, Y. Yu, and J. Sun, "Progress of enhancing the safety of lithium ion battery from the electrolyte aspect," *Nano Energy*, vol. 55, pp. 93–114, Jan. 2019.

[77] B. Scrosati, F. Croce, and S. Panero, "Progress in lithium polymer battery R&D," *Journal of Power Sources*, vol. 100, no. 1, pp. 93–100, Nov. 2001.

[78] C.-H. Dustmann, "Advances in ZEBRA batteries," *Journal of Power Sources*, vol. 127, no. 1, pp. 85–92, Mar. 2004.

[79] C. Delmas, "Sodium and Sodium-Ion Batteries: 50 Years of Research," *Advanced Energy Materials*, vol. 8, no. 17, p. 1703137, 2018.

[80] P. Alotto, M. Guarnieri, and F. Moro, "Redox flow batteries for the storage of renewable energy: A review," *Renewable and Sustainable Energy Reviews*, vol. 29, pp. 325–335, Jan. 2014.

[81] W. Wang, Q. Luo, B. Li, X. Wei, L. Li, and Z. Yang, "Recent progress in redox flow battery research and development," *Advanced Functional Materials*, vol. 23, no. 8, pp. 970–986, 2013.

[82] L. Wei, T. S. Zhao, G. Zhao, L. An, and L. Zeng, "A high-performance carbon nanoparticle-decorated graphite felt electrode for vanadium redox flow batteries," *Applied Energy*, vol. 176, pp. 74–79, Aug. 2016.

[83] P. Zhao, H. Zhang, H. Zhou, J. Chen, S. Gao, and B. Yi, "Characteristics and performance of 10kW class all-vanadium redox-flow battery stack," *Journal of Power Sources*, vol. 162, no. 2, pp. 1416–1420, Nov. 2006.

[84] P. Van den Bossche, F. Vergels, J. Van Mierlo, J. Matheys, and W. Van Autenboer, "SUBAT: An assessment of sustainable battery technology," *Journal of Power Sources*, vol. 162, no. 2, pp. 913–919, Nov. 2006.

[85] Z. M. Salameh and B. G. Kim, "Advanced lithium polymer batteries," in *IEEE Power Energy Society General Meeting*, pp. 1–5, July 2009.

[86] B. Weißhar and W. G. Bessler, "Model-based degradation assessment of lithium-ion batteries in a smart microgrid," in *International Conference on Smart Grid and Clean Energy Technologies (ICSGCE)*, pp. 134–138, Oct. 2015.

[87] J. C. Koo, S. K. Lee, and W. Ra, "Lithium-ion battery design for the hybrid satellite in the geostationary orbit," in *International Telecommunications Energy Conference (INTELEC), Incheon*, pp. 1–6, Dec. 2009.

[88] J. Vetter, P. Novák, M. R. Wagner, C. Veit, K. C. Möller, J. O. Besenhard, M. Winter, M. Wohlfahrt-Mehrens, C. Vogler, and A. Hammouche, "Ageing mechanisms in lithium-ion batteries," *Journal of Power Sources*, vol. 147, no. 1, pp. 269–281, Sept. 2005.

[89] G. Zubi, R. Dufo-López, M. Carvalho, and G. Pasaoglu, "The lithium-ion battery: State of the art and future perspectives," *Renewable and Sustainable Energy Reviews*, vol. 89, pp. 292–308, June 2018.

[90] S. Zhang, M. S. Ding, K. Xu, J. Allen, and T. R. Jow, "Understanding solid electrolyte interface film formation on graphite electrodes," *Electrochemical and Solid-State Letters*, vol. 4, no. 12, pp. A206–A208, Jan. 2001.

[91] N. S. Spinner, C. T. Love, S. L. Rose-Pehrsson, and S. G. Tuttle, "Expanding the Operational Limits of the Single-Point Impedance Diagnostic for Internal Temperature Monitoring of Lithium-ion Batteries," *Electrochimica Acta*, vol. 174, pp. 488–493, Aug. 2015.

[92] Markets and markets, "Lithium Ion Battery Market - Global Forecast to 2025". Jan. 2019. https://www.marketsandmarkets.com/Market-Reports/lithium-ion-battery-market-49714593.html, accessed 26-February-2020.

[93] M. A. Roscher and D. U. Sauer, "Dynamic electric behavior and open-circuit-voltage modeling of $LiFePO_4$-based lithium ion secondary batteries," *Journal of Power Sources*, vol. 196, no. 1, pp. 331–336, Jan. 2011.

[94] AA Portable Power Corp, "$LiFePO_4$/$LiFeMnPO_4$ Batteries". https://www.batteryspace.com/LiFePO4/LiFeMnPO4-Batteries.aspx, accessed 15-January-2020.

[95] R. Schwarz, K. Semmler, M. Wenger, V. R. H. Lorentz, and M. März, "Sensorless battery cell temperature estimation circuit for enhanced safety in battery systems," in *Annual Conference of the IEEE Industrial Electronics Society (IECON), Yokohama*, pp. 001536–001541, Nov. 2015.

[96] P. Chanthevee, S. Hirai, V. Lailuck, Y. Laoonual, P. Sriam, S. Rompho, N. Chanurai, and M. Masomtob, "A simplified approach for heat generation due to entropy change in cylindrical lco battery," in *IEEE Transportation Electrification Conference and Expo, Asia-Pacific (ITEC Asia-Pacific)*, pp. 1–5, June 2018.

[97] J. M. Blanes, R. Gutiérrez, A. Garrigós, J. L. Lizán, and J. M. Cuadrado, "Electric Vehicle Battery Life Extension Using Ultracapacitors and an FPGA Controlled Interleaved Buck–Boost Converter," *IEEE Transactions on Power Electronics*, vol. 28, no. 12, pp. 5940–5948, Dec. 2013.

[98] J. Dixon, I. Nakashima, E. F. Arcos, and M. Ortuzar, "Electric Vehicle Using a Combination of Ultracapacitors and ZEBRA Battery," *IEEE Transactions on Industrial Electronics*, vol. 57, no. 3, pp. 943–949, Mar. 2010.

[99] B. Miwa, D. Otten, and M. Schlecht, "High efficiency power factor correction using interleaving techniques," in *APEC Seventh Annual Applied Power Electronics Conference and Exposition*, pp. 557–568, Feb. 1992.

[100] J. Rosas-Caro, J. Ramirez, F. Peng, and A. Valderrabano, "A DC-DC multilevel boost converter," *IET Power Electronics*, vol. 3, no. 1, pp. 129–137, Jan. 2010.

[101] R. W. Erickson and D. Maksimovic, *"Fundamentals of Power Electronics"*. Kluwer Academic, 2001.

[102] J. Zhang, X. Huang, X. Wu, and Z. Qian, "A high efficiency flyback converter with new active clamp technique," *IEEE Transactions on Power Electronics*, vol. 25, no. 7, pp. 1775–1785, July 2010.

[103] A. R. Rodríguez Alonso, J. Sebastian, D. G. Lamar, M. M. Hernando, and A. Vazquez, "An overall study of a dual active bridge for bidirectional DC/DC conversion," in *IEEE Energy Conversion Congress and Exposition*, pp. 1129–1135, Sept. 2010.

[104] Z. Zhang, Y.-Y. Cai, Y. Zhang, D.-J. Gu, and Y.-F. Liu, "A distributed architecture based on microbank modules with self-reconfiguration control to improve the energy efficiency in the battery energy storage system," *IEEE Transactions on Power Electronics*, vol. 31, no. 1, pp. 304–317, Jan. 2016.

[105] M. Shen, F. Z. Peng, and L. M. Tolbert, "Multilevel DC–DC power conversion system with multiple DC sources," *IEEE Transactions on Power Electronics*, vol. 23, no. 1, pp. 420–426, Jan. 2008.

[106] J. Cao, N. Schofield, and A. Emadi, "Battery balancing methods: A comprehensive review," in *IEEE Vehicle Power and Propulsion Conference*, pp. 1–6, Sept. 2008.

[107] F. Feng, R. Lu, G. Wei, and C. Zhu, "Identification and analysis of model parameters used for $LiFePO_4$ cells series battery pack at various ambient temperature," *IET Electrical Systems in Transportation*, vol. 6, no. 2, pp. 50–55, 2016.

[108] W. Bentley, "Cell balancing considerations for lithium-ion battery systems," in *The Twelfth Annual Battery Conference on Applications and Advances*, pp. 223–226, Jan. 1997.

[109] M. Einhorn, W. Roessler, and J. Fleig, "Improved performance of serially connected li-ion batteries with active cell balancing in electric vehicles," *IEEE Transactions on Vehicular Technology*, vol. 60, no. 6, pp. 2448–2457, July 2011.

[110] S. W. Moore and P. J. Schneider, "A Review of Cell Equalization Methods for Lithium Ion and Lithium Polymer Battery Systems," SAE Technical Paper 2001-01-0959, SAE International, Warrendale, PA, Mar. 2001.

[111] M.-Y. Kim, C.-H. Kim, J.-H. Kim, and G.-W. Moon, "A Chain Structure of Switched Capacitor for Improved Cell Balancing Speed of Lithium-Ion Batteries," *IEEE Transactions on Industrial Electronics*, vol. 61, no. 8, pp. 3989–3999, Aug. 2014.

[112] C. Pascual and P. Krein, "Switched capacitor system for automatic series battery equalization," in *APEC - Applied Power Electronics Conference*, vol. 2, pp. 848–854 vol.2, Feb. 1997.

[113] Y. Ye, K. W. E. Cheng, Y. C. Fong, X. Xue, and J. Lin, "Topology, Modeling, and Design of Switched-Capacitor-Based Cell Balancing Systems and Their Balancing Exploration," *IEEE Transactions on Power Electronics*, vol. 32, no. 6, pp. 4444–4454, June 2017.

[114] A. C. Baughman and M. Ferdowsi, "Double-Tiered Switched-Capacitor Battery Charge Equalization Technique," *IEEE Transactions on Industrial Electronics*, vol. 55, no. 6, pp. 2277–2285, June 2008.

[115] Y. Shang, N. Cui, B. Duan, and C. Zhang, "Analysis and Optimization of Star-Structured Switched-Capacitor Equalizers for Series-Connected Battery Strings," *IEEE Transactions on Power Electronics*, vol. 33, no. 11, pp. 9631–9646, Nov. 2018.

[116] Y. Shang, C. Zhang, N. Cui, and C. C. Mi, "A Delta-Structured Switched-Capacitor Equalizer for Series-Connected Battery Strings," *IEEE Transactions on Power Electronics*, vol. 34, no. 1, pp. 452–461, Jan. 2019.

[117] Y. Yuanmao, K. W. E. Cheng, and Y. P. B. Yeung, "Zero-Current Switching Switched-Capacitor Zero-Voltage-Gap Automatic Equalization System for Series Battery String," *IEEE Transactions on Power Electronics*, vol. 27, no. 7, pp. 3234–3242, July 2012.

[118] M. Muneeb Ur Rehman, F. Zhang, R. Zane, and D. Maksimovic, "Design and control of an integrated BMS/DC-DC system for electric vehicles," in *2016 IEEE 17th Workshop on Control and Modeling for Power Electronics (COMPEL)*, pp. 1–7, June 2016.

[119] M. Chen and G. Rincon-Mora, "An accurate electrical battery model capable of predicting runtime and I-V performance," *IEEE Transactions on Energy Conversion*, vol. 21, no. 2, pp. 504–511, June 2006.

[120] R. Ahmed, *"Modeling and State of Charge Estimation of Electric Vehicle Batteries"*. Thesis, 2014.

[121] B. Schweighofer, K. Raab, and G. Brasseur, "Modeling of high power automotive batteries by the use of an automated test system," *IEEE Transactions on Instrumentation and Measurement*, vol. 52, no. 4, pp. 1087–1091, Aug. 2003.

[122] C. Birkl and D. Howey, "Model identification and parameter estimation for $LiFePO_4$ batteries," in *IET Hybrid and Electric Vehicles Conference (HEVC), London*, pp. 1–6, Nov. 2013.

[123] Y. F. Pulido, C. Blanco, D. Anseán, M. González, J. C. Viera, and V. M. García, "Effect of aging on C/LFP battery impedance: Operating conditions to which the impedance has minimal variations," in *IEEE International Conference on Environment and Electrical Engineering and IEEE Industrial and Commercial Power Systems Europe (EEEIC / I&CPS Europe), Milan*, pp. 1–5, June 2017.

[124] J. Kowal, J. B. Gerschler, C. Schäper, T. Schoenen, and D. U. Sauer, "Efficient battery models for the design of EV drive trains," in *14th International Power Electronics and Motion Control Conference EPE-PEMC*, pp. S11–31–S11–38, Sept. 2010.

[125] B. Pattipati, C. Sankavaram, and K. Pattipati, "System Identification and Estimation Framework for Pivotal Automotive Battery Management System Characteristics," *IEEE Transactions on Systems, Man, and Cybernetics, Part C (Applications and Reviews)*, vol. 41, no. 6, pp. 869–884, Nov. 2011.

[126] D. Wong, B. Shrestha, D. A. Wetz, and J. M. Heinzel, "Impact of high rate discharge on the aging of lithium nickel cobalt aluminum oxide batteries," *Journal of Power Sources*, vol. 280, pp. 363–372, Apr. 2015.

[127] M. J. Newman, D. N. Zmood, and D. G. Holmes, "Stationary frame harmonic reference generation for active filter systems," *IEEE Transactions on Industry Applications*, vol. 38, no. 6, pp. 1591–1599, Nov. 2002.

[128] L. Gagneur, A. L. Driemeyer-Franco, C. Forgez, and G. Friedrich, "Modeling of the diffusion phenomenon in a lithium-ion cell using frequency or time domain identification," *Microelectronics Reliability*, vol. 53, no. 6, pp. 784–796, June 2013.

[129] J. G. Zhu, Z. C. Sun, X. Z. Wei, and H. F. Dai, "A new lithium-ion battery internal temperature on-line estimate method based on electrochemical impedance spectroscopy measurement," *Journal of Power Sources*, vol. 274, pp. 990–1004, Jan. 2015.

[130] Digatron Power Electronics, "Electrochemical Impedance Spectroscopy EIS-Meter". http://www.digatron.com/en/cells-packs/, accessed 17-January-2018.

[131] R. Srinivasan, B. G. Carkhuff, M. H. Butler, and A. C. Baisden, "Instantaneous measurement of the internal temperature in lithium-ion rechargeable cells," *Electrochimica Acta*, vol. 56, no. 17, pp. 6198–6204, Jul. 2011.

[132] L. H. J. Raijmakers, D. L. Danilov, J. P. M. van Lammeren, M. J. G. Lammers, and P. H. L. Notten, "Sensorless battery temperature measurements based on electrochemical impedance spectroscopy," *Journal of Power Sources*, vol. 247, pp. 539–544, Feb. 2014.

[133] M. Takahashi, S.-i. Tobishima, K. Takei, and Y. Sakurai, "Reaction behavior of $LiFePO_4$ as a cathode material for rechargeable lithium batteries," *Solid State Ionics*, vol. 148, no. 3, pp. 283–289, Jun. 2002.

[134] L. W. Juang, P. J. Kollmeyer, T. M. Jahns, and R. D. Lorenz, "Improved modeling of lithium-based batteries using temperature-dependent resistance and overpotential," in *IEEE-ITEC, Dearborn, MI*, pp. 1–8, June 2014.

[135] ENIX Energies, "Specification approval sheet: ACL9012 -3.3Ah datasheet. Document Number S470XLB029," Apr. 2012. Version A0.

[136] C. Alaoui, "Solid-State Thermal Management for Lithium-Ion EV Batteries," *IEEE Transactions on Vehicular Technology*, vol. 62, no. 1, pp. 98–107, Jan. 2013.

[137] K. Zaghib, K. Striebel, A. Guerfi, J. Shim, M. Armand, and M. Gauthier, "$LiFePO_4$/polymer/natural graphite: low cost Li-ion batteries," *Electrochimica Acta*, vol. 50, no. 2, pp. 263–270, Nov. 2004.

[138] Mitsubishi Intelligent Power Modules, "PM200CLA120 datasheet," Jul. 2005. https://www.mitsubishielectric-mesh.com/products/pdf/pm200cla120_e.pdf, accessed 20-March-2020.

[139] R. R. Richardson, P. T. Ireland, and D. A. Howey, "Battery internal temperature estimation by combined impedance and surface temperature measurement," *Journal of Power Sources*, vol. 265, pp. 254–261, Nov. 2014.

[140] J. Zhu, Z. Sun, X. Wei, and H. Dai, "Battery Internal Temperature Estimation for $LiFePO_4$ Battery Based on Impedance Phase Shift under Operating Conditions," *Energies*, vol. 10, no. 1, p. 60, Jan. 2017.

[141] R. Srinivasan, "Monitoring dynamic thermal behavior of the carbon anode in a lithium-ion cell using a four-probe technique," *Journal of Power Sources*, vol. 198, pp. 351–358, Jan. 2012.

[142] J. P. Schmidt, S. Arnold, A. Loges, D. Werner, T. Wetzel, and E. Ivers-Tiffée, "Measurement of the internal cell temperature via impedance: Evaluation and application of a new method," *Journal of Power Sources*, vol. 243, pp. 110–117, Dec. 2013.

[143] L. H. J. Raijmakers, D. L. Danilov, J. P. M. V. Lammeren, T. J. G. Lammers, H. J. Bergveld, and P. H. L. Notten, "Non-Zero Intercept Frequency: An Accurate Method to Determine the Integral Temperature of Li-Ion Batteries," *IEEE Transactions on Vehicular Technology*, vol. 63, no. 5, pp. 3168–3178, May 2016.

[144] R. R. Richardson and D. A. Howey, "Sensorless Battery Internal Temperature Estimation Using a Kalman Filter With Impedance Measurement," *IEEE Transactions on Vehicular Technology*, vol. 6, no. 4, pp. 1190–1199, Oct. 2015.

[145] H. S. Fogler, *"Elements of Chemical Reaction Engineering. Fifth edition"*. Prentice Hall, 2016.

[146] J. A. A. Qahouq and Z. Xia, "Single-Perturbation-Cycle Online Battery Impedance Spectrum Measurement Method With Closed-Loop Control of Power Converter," *IEEE Transactions on Industrial Electronics*, vol. 64, no. 9, pp. 7019–7029, Sep. 2017.

[147] C. Gonzalez Moral, D. Fernandez, J. M. Guerrero, D. Reigosa, C. Rivas, and F. Briz, "Thermal monitoring of LiFePO4 batteries using switching harmonics," *IEEE Transactions on Industry Applications (early acccess)*, pp. 1–1, 2020.

[148] R. Soares, A. Bessman, O. Wallmark, G. Lindbergh, and P. Svens, "Measurements and analysis of battery harmonic currents in a commercial hybrid vehicle," in *IEEE Transportation Electrification Conference and Expo (ITEC), Chicago, IL*, pp. 45–50, June 2017.

[149] K. Uddin, A. D. Moore, A. Barai, and J. Marco, "The effects of high frequency current ripple on electric vehicle battery performance," *Applied Energy*, vol. 178, pp. 142–154, Sept. 2016.

[150] B. Widrow, I. Kollar, and M. C. Liu, "Statistical theory of quantization," *IEEE Transactions on Instrumentation and Measurement*, vol. 45, no. 2, pp. 353–361, Apr. 1996.

[151] Infineon, "IRFR3607PbF datasheet," Apr. 2010.

[152] Texas Instruments, "LM35 precision centigrade temperature sensors datasheet," Aug. 1999. Revised Dec. 2017.

[153] B. Wu, Z. Li, and J. Zhang, "Thermal design for the pouch-type large-format lithium-ion batteries i. thermo-electrical modeling and origins of temperature non-uniformity," *J. Electrochem. Soc.*, vol. 162, no. 1, pp. A181–A191, Jan. 2015.

[154] J. Matthey, "Automotive lithium-ion batteries - developments for passenger car applications," *Johnson Matthey Technology Review*, vol. 59, no. 1, pp. 4–13, 2015.

[155] C. G. Moral, D. Fernández Laborda, L. S. Alonso, J. Manuel Guerrero, D. Fernández, C. Rivas, and D. D. Reigosa, "Battery internal resistance estimation using a battery balancing system based on switched capacitors," in *IEEE Energy Conversion Congress and Exposition (ECCE)*, pp. 2516–2522, Sept. 2019.

[156] KEMET, "Tantalum Surface Mount Capacitors – Standard Tantalum: T491 Industrial Grade MnO_2," Feb. 2020. https://content.kemet.com/datasheets/KEM_T2005_T491.pdf, accessed 04-April-2020.

[157] INFINEON, "IRLB8314PbF datasheet," Aug. 2018. https://www.infineon.com/dgdl/irlb8314pbf.pdf?fileId=5546d462533600a4015356604d6f258f, accessed 04-April-2020.

[158] Y. Ye and K. W. E. Cheng, "Modeling and analysis of series–parallel switched-capacitor voltage equalizer for battery/supercapacitor strings," *IEEE Journal of Emerging and Selected Topics in Power Electronics*, vol. 3, no. 4, pp. 977–983, Dec. 2015.

[159] Y. Zou, X. Hu, H. Ma, and S. E. Li, "Combined State of Charge and State of Health estimation over lithium-ion battery cell cycle lifespan for electric vehicles," *Journal of Power Sources*, vol. 273, pp. 793–803, Jan. 2015.

[160] R. Lasseter, "MicroGrids," in *IEEE Power Engineering Society Winter Meeting*, vol. 1, pp. 305–308, Jan. 2002.

[161] N. Hatziargyriou, H. Asano, R. Iravani, and C. Marnay, "Microgrids," *IEEE Power and Energy Magazine*, vol. 5, no. 4, pp. 78–94, July 2007.

[162] F. Katiraei, R. Iravani, N. Hatziargyriou, and A. Dimeas, "Microgrids management," *IEEE Power and Energy Magazine*, vol. 6, no. 3, pp. 54–65, May 2008.

[163] A. Hirsch, Y. Parag, and J. Guerrero, "Microgrids: A review of technologies, key drivers, and outstanding issues," *Renewable and Sustainable Energy Reviews*, vol. 90, pp. 402–411, July 2018.

[164] D. Burmester, R. Rayudu, W. Seah, and D. Akinyele, "A review of nanogrid topologies and technologies," *Renewable and Sustainable Energy Reviews*, vol. 67, pp. 760–775, Jan. 2017.

[165] F. Martin-Martínez, A. Sánchez-Miralles, and M. Rivier, "A literature review of Microgrids: A functional layer based classification," *Renewable and Sustainable Energy Reviews*, vol. 62, pp. 1133–1153, Sept. 2016.

[166] J. W. Kolar, T. Friedli, J. Rodriguez, and P. W. Wheeler, "Review of three-phase PWM AC–AC converter topologies," *IEEE Transactions on Industrial Electronics*, vol. 58, no. 11, pp. 4988–5006, Nov. 2011.

[167] N. S. Hasan, N. Rosmin, D. A. A. Osman, and A. H. Musta'amal@Jamal, "Reviews on multilevel converter and modulation techniques," vol. 80, pp. 163–174, Dec. 2017.

[168] A. Hintz, U. R. Prasanna, and K. Rajashekara, "Comparative study of the three-phase grid-connected inverter sharing unbalanced three-phase and/or single-phase systems," *IEEE Transactions on Industry Applications*, vol. 52, no. 6, pp. 5156–5164, Nov. 2016.

[169] P. Mattavelli, "Synchronous-frame harmonic control for high-performance AC power supplies," *IEEE Transactions on Industry Applications*, vol. 37, no. 3, pp. 864–872, May 2001.

[170] Q.-C. Zhong, T. Green, J. Liang, and G. Weiss, "H^∞ control of the neutral point in 3-phase 4-wire DC-AC converters," in *28th Annual Conference of the Industrial Electronics Society. IECON 02*, vol. 1, pp. 520–525 vol.1, Nov. 2002.

[171] A. Mora, R. Cardenas, M. Urrutia, M. Espinoza, and M. Diaz, "A vector control strategy to eliminate active power oscillations in 4-leg grid-connected converters under unbalanced voltages," *IEEE Journal of Emerging and Selected Topics in Power Electronics. Early access*, pp. 1–1, 2019.

[172] J. Chen, L.-J. Diao, L. Wang, H. Du, and Z. Liu, "Distributed auxiliary inverter of urban rail train—the voltage and current control strategy under complicated load condition," *IEEE Transactions on Power Electronics*, vol. 31, no. 2, pp. 1745–1756, Feb. 2016.

[173] P. Verdelho and G. Marques, "Four-wire current-regulated PWM voltage converter," *IEEE Transactions on Industrial Electronics*, vol. 45, no. 5, pp. 761–770, Oct. 1998.

[174] R. Zhang, D. Boroyevich, V. Prasad, H.-C. Mao, F. Lee, and S. Dubovsky, "A three-phase inverter with a neutral leg with space vector modulation," in *Applied Power Electronics Conference APEC*, vol. 2, pp. 857–863 vol.2, Feb. 1997.

[175] Z. Lin, X. Ruan, L. Jia, W. Zhao, H. Liu, and P. Rao, "Optimized design of the neutral inductor and filter inductors in three-phase four-wire inverter with split DC-link capacitors," *IEEE Transactions on Power Electronics*, vol. 34, no. 1, pp. 247–262, Jan. 2019.

[176] A. Bellini and S. Bifaretti, "A simple control technique for three-phase four-leg inverters," in *International Symposium on Power Electronics, Electrical Drives, Automation and Motion, SPEEDAM*, pp. 1143–1148, May 2006.

[177] D. G. Holmes and T. A. Lipo, *"Pulse Width Modulation for Power Converters: Principles and Practice"*. John Wiley & Sons, 2003.

[178] B. Mwinyiwiwa, Z. Wolanski, and B.-T. Ooi, "Microprocessor-implemented SPWM for multiconverters with phase-shifted triangle carriers," *IEEE Transactions on Industry Applications*, vol. 34, no. 3, pp. 487–494, May 1998.

[179] A. Hava, R. Kerkman, and T. Lipo, "Simple analytical and graphical methods for carrier-based PWM-VSI drives," *IEEE Transactions on Power Electronics*, vol. 14, no. 1, pp. 49–61, Jan. 1999.

[180] A. Hava, R. Kerkman, and T. Lipo, "Carrier-based PWM-VSI overmodulation strategies: analysis, comparison, and design," *IEEE Transactions on Power Electronics*, vol. 13, no. 4, pp. 674–689, July 1998.

[181] K. Zhou and D. Wang, "Relationship between space-vector modulation and three-phase carrier-based PWM: a comprehensive analysis [three-phase inverters]," *IEEE Transactions on Industrial Electronics*, vol. 49, no. 1, pp. 186–196, Feb. 2002.

[182] J. A. Houldsworth and D. A. Grant, "The use of harmonic distortion to increase the output voltage of a three-phase PWM inverter," *IEEE Transactions on Industry Applications*, vol. IA-20, no. 5, pp. 1224–1228, Sept. 1984.

[183] T. D. Nguyen, N. Patin, and G. Friedrich, "Extended double carrier PWM strategy dedicated to RMS current reduction in DC link capacitors of three-phase inverters," *IEEE Transactions on Power Electronics*, vol. 29, no. 1, pp. 396–406, Jan. 2014.

[184] M. Rizo, M. Liserre, E. J. Bueno, F. J. Rodríguez, and A. Rodríguez, "Distortion-Free Saturators for Power Converters Under Unbalanced Conditions," *IEEE Transactions on Power Electronics*, vol. 30, no. 6, pp. 3364–3375, June 2015.

[185] C. Klarenbach and J. O. Krah, "Fast and high precision motor control for high performance servo drives," in *PCIM Europe*, 2010.

[186] M. Liserre, F. Blaabjerg, and S. Hansen, "Design and control of an LCL-filter-based three-phase active rectifier," *IEEE Transactions on Industry Applications*, vol. 41, no. 5, pp. 1281–1291, Sept. 2005.

[187] J. M. Sosa, G. Escobar, P. R. Martínez-Rodríguez, G. Vázquez, M. A. Juárez, and M. Diosdado, "Comparative evaluation of l and LCL filters in transformerless grid tied converters for active power injection," in *IEEE International Autumn Meeting on Power, Electronics and Computing (ROPEC)*, pp. 1–6, Nov. 2014.

[188] P. C. Loh and D. Holmes, "Analysis of multiloop control strategies for LC/CL/LCL-filtered voltage-source and current-source inverters," *IEEE Transactions on Industry Applications*, vol. 41, no. 2, pp. 644–654, Mar. 2005.

[189] D. A. González, "Synchronization, islanding detection and power quality improvement in distributed power generation systems" PhD thesis, University of Oviedo, June, 2015. http://hdl.handle.net/10651/33942, accessed 18-March-2020.

[190] L. Harnefors, L. Zhang, and M. Bongiorno, "Frequency-domain passivity-based current controller design," *IET Power Electronics*, vol. 1, no. 4, pp. 455–465, Dec. 2008.

[191] Y. Tang, W. Yao, P. C. Loh, and F. Blaabjerg, "Design of LCL filters with LCL resonance frequencies beyond the nyquist frequency for grid-connected converters," *IEEE Journal of Emerging and Selected Topics in Power Electronics*, vol. 4, no. 1, pp. 3–14, Mar. 2016.

[192] R. Teodorescu, F. Blaabjerg, M. Liserre, and P. C. Loh, "Proportional-resonant controllers and filters for grid-connected voltage-source converters," *IEE Proceedings - Electric Power Applications*, vol. 153, no. 5, pp. 750–762, Sept. 2006.

[193] P. Mattavelli, "A closed-loop selective harmonic compensation for active filters," *IEEE Transactions on Industry Applications*, vol. 37, no. 1, pp. 81–89, Jan. 2001.

[194] C. A. Busada, S. Gomez Jorge, A. E. Leon, and J. A. Solsona, "Current Controller Based on Reduced Order Generalized Integrators for Distributed Generation Systems," *IEEE Transactions on Industrial Electronics*, vol. 59, no. 7, pp. 2898–2909, July 2012.

[195] L. R. Limongi, R. Bojoi, G. Griva, and A. Tenconi, "Digital current-control schemes," *IEEE Industrial Electronics Magazine*, vol. 3, no. 1, pp. 20–31, Mar. 2009.

[196] C. Blanco, D. Reigosa, J. C. Vasquez, J. M. Guerrero, and F. Briz, "Virtual Admittance Loop for Voltage Harmonic Compensation in Microgrids," *IEEE Transactions on Industry Applications*, vol. 52, no. 4, pp. 3348–3356, July 2016.

[197] Nikunj Shah, "Harmonic in Power Systems: Causes, effects and control," Siemens Whitepaper. May 2013. https://assets.new.siemens.com/siemens/assets/api/uuid:8ab2a02e-ad94-41cb-a362-438f016aa704/version:1570302838/drive-harmonics-in-power-systems-whitepaper.pdf, accessed 26-April-2020.

[198] M. El-Habrouk, M. Darwish, and P. Mehta, "Active power filters: a review," *IEE Proceedings - Electric Power Applications*, vol. 147, no. 5, pp. 403–413, Sept. 2000.

[199] J. Moriano, M. Rizo, E. Bueno, J. R. Sendra, and R. Mateos, "Distortion-Free Instantaneous Multifrequency Saturator for THD Current Reduction," *IEEE Transactions on Industrial Electronics*, vol. 66, no. 7, pp. 5310–5320, July 2019.

[200] I. Etxeberria-Otadui, A. Lopez De Heredia, H. Gaztanaga, S. Bacha, and M. Reyero, "A single synchronous frame hybrid (SSFH) multifrequency controller for power active filters," *IEEE Transactions on Industrial Electronics*, vol. 53, no. 5, pp. 1640–1648, Oct. 2006.

[201] M. Ochoa-Gimenez, S. D'Arco, and J. A. Suul, "Voltage saturation anti-windup for harmonic controllers in multiple reference frames," in *2015 IEEE International Conference on Industrial Technology (ICIT)*, pp. 2139–2144, Mar. 2015.

[202] J. Karttunen, S. Kallio, J. Honkanen, P. Peltoniemi, and P. Silventoinen, "Partial Current Harmonic Compensation in Dual Three-Phase PMSMs Considering the Limited Available Voltage," *IEEE Transactions on Industrial Electronics*, vol. 64, no. 2, pp. 1038–1048, Feb. 2017.

[203] Springer-Verlag, *"Practical PID Control"*. Elsevier, 2006.

[204] G. F. Franklin, J. D. Powell, and A. Emami-Naeini, *"Feedback Control of Dynamic Systems"*. Pearson Education Limited, 2006.

[205] S. A. Richter and R. W. De Doncker, "Digital proportional-resonant (PR) control with anti-windup applied to a voltage-source inverter," in *Proceed-*

ings of the 2011 14th European Conference on Power Electronics and Applications, pp. 1–10, Aug. 2011.

[206] A. G. Yepes, F. D. Freijedo, J. Doval-Gandoy, O. Lopez, J. Malvar, and P. Fernandez-Comesana, "Effects of discretization methods on the performance of resonant controllers," *IEEE Transactions on Power Electronics*, vol. 25, no. 7, pp. 1692–1712, July 2010.

[207] J. Roldán-Pérez, A. García-Cerrada, J. L. Zamora-Macho, P. Roncero-Sánchez, and E. Acha, "Troubleshooting a digital repetitive controller for a versatile dynamic voltage restorer," *International Journal of Electrical Power & Energy Systems*, vol. 57, pp. 105–115, May 2014.

[208] J. Roldan-Perez, M. Prodanovic, A. Rodriguez-Cabero, J. M. Guerrero, and A. Garcia-Cerrada, "Finite-gain repetitive controller for harmonic sharing improvement in a VSM microgrid," *IEEE Transactions on Smart Grid*, vol. 10, no. 6, pp. 6898–6911, Nov. 2019.

[209] A. Lidozzi, C. Ji, L. Solero, F. Crescimbini, and P. Zanchetta, "Load-adaptive zero-phase-shift direct repetitive control for stand-alone four-leg VSI," *IEEE Transactions on Industry Applications*, vol. 52, no. 6, pp. 4899–4908, Nov. 2016.

[210] T. C. Y. Wang and X. Yuan, "Design of multiple-reference-frame PI controller for power converters," in *IEEE 35th Annual Power Electronics Specialists Conference (IEEE Cat. No.04CH37551)*, vol. 5, pp. 3331–3335, June 2004.

[211] I. J. Gabe, F. F., K. Palha, and H. Pinheiro, "Grid connected voltage source inverter control during voltage dips," in *2009 35th Annual Conference of IEEE Industrial Electronics*, pp. 4571–4576, Nov. 2009.

[212] B. P. McGrath and D. G. Holmes, "Anti-windup control for stationary frame current regulators using digital conditioning architectures," in *2017 IEEE Energy Conversion Congress and Exposition (ECCE)*, pp. 5744–5751, Oct. 2017.

[213] B. P. McGrath, D. G. Holmes, and L. McNabb, "A Signal Conditioning Antiwindup Approach for Digital Stationary Frame Current Regulators," *IEEE Transactions on Industry Applications*, vol. 55, no. 6, pp. 6036–6046, Nov. 2019.

[214] M. Rizo, A. Rodríguez, F. J. Rodríguez, E. Bueno, and M. Liserre, "Different approaches of stationary reference frames saturators," in *IECON - 38th Annual Conference on IEEE Industrial Electronics Society*, pp. 2245–2250, Oct. 2012.

[215] L. Harnefors, A. G. Yepes, A. Vidal, and J. Doval-Gandoy, "Reduction of saturation-induced distortion and antiwindup in multifrequency current control," in *17th European Conference on Power Electronics and Applications (EPE'15 ECCE-Europe)*, pp. 1–7, Sept. 2015.

[216] L. Harnefors, A. G. Yepes, A. Vidal, and J. Doval-Gandoy, "Multifrequency Current Control With Distortion-Free Saturation," *IEEE Journal of Emerging and Selected Topics in Power Electronics*, vol. 4, no. 1, pp. 37–43, Mar. 2016.

[217] A. G. Yepes, J. Doval-Gandoy, and H. A. Toliyat, "Multifrequency Current Control Including Distortion-Free Saturation and Antiwindup With Enhanced Dynamics," *IEEE Transactions on Power Electronics*, vol. 33, no. 9, pp. 7309–7313, Sept. 2018.

[218] A. G. Yepes, J. Doval-Gandoy, and H. A. Toliyat, "Multifrequency Current Control for n-Phase Machines Including Antiwindup and Distortion-Free Saturation With Full DC-Bus Utilization," *IEEE Transactions on Power Electronics*, vol. 34, no. 10, pp. 9891–9905, Oct. 2019.

[219] J. Serrano, J. Moriano, M. Rizo, and F. J. Dongil, "Enhanced current reference calculation to avoid harmonic active power oscillations," *Energies*, vol. 12, no. 21, Oct. 2019.

[220] J. M. Guerrero, C. González-Moral, D. Fernández, D. Reigosa, C. Rivas, and F. Briz, "Realizable References Anti-Windup Implementation for Parallel Controllers in Multiple Reference Frames," in *IEEE Energy Conversion Congress and Exposition (ECCE)*, pp. 3142–3149, Sept. 2018.

[221] Y. Peng, D. Vrancic, and R. Hanus, "Anti-windup, bumpless, and conditioned transfer techniques for PID controllers," *IEEE Control Systems Magazine*, vol. 16, no. 4, pp. 48–57, Aug. 1996.

[222] J. M. Guerrero, F. Briz, A. Diez, and J. C. Alvarez, "Design and tuning of PI velocity regulators for high performance AC drives," *IFAC Workshop on Digital Control - Past, Present and Future of PID Control (PID 00)*, vol. 33, pp. 101–106, Apr. 2000.

[223] K. Ogata, *"Discrete-Time Control Systems," 2nd edition.* Prentice Hall, 1995.

[224] F. B. d. Blanco, M. W. Degner, and R. D. Lorenz, "Dynamic analysis of current regulators for AC motors using complex vectors," *IEEE Transactions on Industry Applications*, vol. 35, no. 6, pp. 1424–1432, Nov. 1999.

[225] W. Bolton, *"Intrumentation and Control Systems. Second Edition"*. Elsevier, 2015.

[226] S.-H. Hwang and J.-M. Kim, "Dead time compensation method for voltage-fed PWM inverter," *IEEE Transactions on Energy Conversion*, vol. 25, no. 1, pp. 1–10, Mar. 2010.

[227] Mitsubishi Intelligent Power Modules, "PM200DV1A120 datasheet," Nov. 2011. http://www.mitsubishielectric-mesh.com.cn/products/pdf/PM200DV1A120_N1.pdf, accessed 20-March-2020.

[228] Murata Power Solutions, "OKI-78SR Series: Fixed Output 1.5 Amp SIP DC/DC Converters," 2014. https://uk.rs-online.com/webdocs/12b2/0900766b812b22d9.pdf, accessed 23-March-2020.

[229] Murata Power Solutions, "MEV1 Series: 3kVDC Isolated 1W Single & Dual Output DC-DC Converters," 2018. https://power.murata.com/pub/data/power/ncl/kdc_mev.pdf, accessed 23-March-2020.

[230] Broadcom, "ACPL-M46T: Automotive Intelligent Power Module," Dec. 2011. https://docs.broadcom.com/docs/AV02-0822EN, accessed 23-March-2020.

[231] Broadcom, "HFBR-0500Z Series, Versatile Link: The Versatile Fiber Optic Connection," March 2020. https://docs.broadcom.com/docs/AV02-1501EN, accessed 23-March-2020.

[232] Avago Technologies, "ACPL-M49U: Wide Operating Temperature R2CouplerTM 20kBd Digital Optocoupler," Oct. 2012. https://docs.broadcom.com/docs/AV02-0822EN, accessed 23-March-2020.

[233] Electronics notes, "Tantalum Capacitor". https://www.electronics-notes.com/articles/electronic_components/capacitors/tantalum.php, accessed 24-March-2020.

[234] T. A. Novotny, D. W.and Lipo, *"Vector control and dynamics of AC drives"*. Oxford Science Publications, 1996.

[235] R. Teodorescu, M. Liserre, and P. Rodriguez, *"Grid converters for photovoltaic and wind power systems"*. John Wiley & Sons, 2011.

[236] A. K. Chakraborty and B. Bhattachaya, "Determination of α, β and γ-components of a switching state without clarke transformation," in *2^{nd} International Conference on Control, Instrumentation, Energy Communication (CIEC)*, pp. 260–263, Jan. 2016.

Appendix A

Power Converter design

A.1 Introduction

This appendix shows the design of two drivers for the control of two different power modules, one is a 3-phase module and the other is a single-phase module. There will be two units of the 3-phase modules in the design, one for the interleaved DC/DC converter and the other for the DC/AC. The single-phase module will be used for the 4^{th} leg of the DC/AC converter (see Fig. 1.5). The most important specifications for the design are:

- Input voltage: 24 V
- Components in only one size of the PCB
- Measurements of the PCB limited to the size of the power module.

A.2 Power modules

The modules are from Mitsubishi Electric, both Intelligent Power Modules (IPMs) with a maximum voltage of 1200 V and 200 A as maximum current:

- 3-phase module: IPM PM200CLA120 (Fig. A.1) [138].
- single-phase module: IPM PM200DV1A120 (Fig. A.2) [227].

Figure A.1: Three-phase module: PM200CLA120.

Figure A.2: Single-phase module: PM200DV1A120.

Being from the same family of devices, the general design concepts are the same, changing only some aspects related to components placement and connections.

A.3 Design aspects

Both IPMs consist of IGBTs connected in a 3-phase or single-phase bridge. They include an internal driver that simplifies the control stage. For each IGBT there are three different signals applied between 4 different pins: power supply, ground, control and error. The three different signals are:

- **Supply voltage (V_D):** between power pins (power supply and ground).
- **Control (V_{CIN}):** Between control pin and ground.
- **Error (V_{FO}):** Between error pin and ground. Maximum current in the error pin (I_{-FO}) is 20 mA.

All the voltage levels for these pins must be below 20 V. For the design, standard 15 V were selected.

A.3.1 Logic

The logic of the modules is reversed, meaning a logic one (15 V in V_{CIN}) will open the IGBT and a zero will close it, provided that there is supply voltage (V_D). This was taken into account when designing the hardware and can be seen in Fig.A.3 [138].

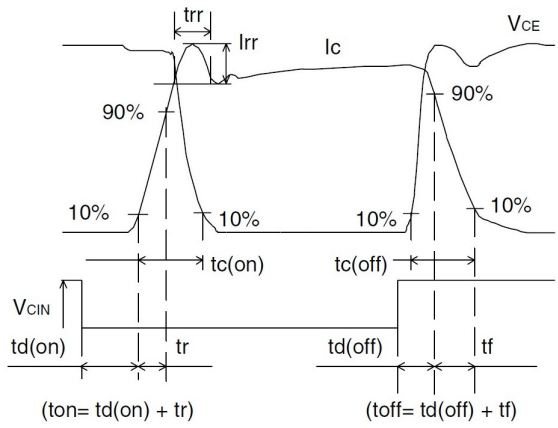

Figure A.3: Logic of the modules.

A.4 Driver components

Both PCBs (3-phase and single-phase versions) have two main parts:

- First part: common voltages part to all the circuits, sharing the ground plane.
- Second part: isolated voltages. There will be one per IGBT in the IPM, with different ground planes that can be visually identified.

A.4.1 Power supply

Both PCBs have an input voltage of 24 V.

A.4.1.1 Power supply for the non-isolated circuit

Input voltage (24 V) is too high for the majority of the component in the non-isolated zone. A buck converter is used to reduce the voltage from 24 V to 5 V [228]. A linear regulator, although simpler, is not advisable due to the different between the input and the output voltage, that will imply dissipating around 4 W in the form of heat, reducing the efficiency of the system and heating up the PCB unnecessarily.

A.4.1.2 Power supply for the isolated circuit

Due to design requirements in the IPM, each IGBT must have its control isolated from the rest of the system, including the power supply.

This is achieved by means of isolated voltage sources (1 W, 3 kV_{DC} isolation) [229], directly fed from the 24 V at the input and generating 15 V at the output.

A.4.2 Control signals

These signals get to the module through fiber optic receptors. Each PCB has as many receptors as IGBTs in the IPM; six for the three-phase module and two for the single-phase one. There is also an optocoupler per IGBT to isolate the signal coming from the receptors with a common ground, getting it to the isolated part of the PCB.

It was important to take into account here the reversed logic of the module, so if there are no fiber optic signals or the converter is not switching the switches are forced to stay open (i.e. with 15 V at V_{CIN}), avoiding a short circuit between the branches.

A.4.2.1 Components of the control part

The receptor is fed from the output of the buck converter, i.e. 5 V. The receptor employed inverts the signal, so if there is light in the receptor (a logic one), its output will be a logic zero.

The optocoupler [230] was selected to be fast enough when switching, so there are no noticeable delays. The signal coming from the receptor cannot be directly connected to the LED in the optocoupler because the current levels in the receptor, limited by its internal resistance [231], are not powerful enough for it. In the worst case, the current would be in the range of 3 mA, while the optocoupler requires a minimum current of 10 mA [230]. Due to this, a non-inverting buffer is placed to amplify this current.

A.4.3 Error signal

The error signal is sent via fiber optics to the control system from the driver. There as many error signals as IGTBs in the power module.

A.4.3.1 Components in the control part

The error signal circuitry is similar to the control one. There is also an optocoupler [232] which allows for the voltage change from the isolated control part to the common ground part.

As in the control signal case, it is not possible to directly connect the output signal of the optocoupler with the fiber optics emitter, because the emitter requires higher currents [231] than the ones available from the optocoupler [232]. In this case, an AND gate is used to amplify the power of the signal, with one of its inputs permanently connected to the feeding voltage.

A.5 Other components

A.5.1 Capacitors

All the electrolytic capacitors are substitute by tantalum capacitors. The main motivation for this substitution is increasing safety regarding material and life expectancy. Electrolytic capacitors lose capacity during its life time due to problems related with gases. Tantalum capacitors occupy less space than aluminum ones because they have higher capacity per volume and have low Equivalent Series Resistant (ESR). They also work well at high temperatures and in a higher range of frequencies. One of their drawbacks is that they cannot stand high voltages, so at the input voltage in the PCB (24 V) there is still an electrolytic capacitor. In addition, as electrolytic capacitors, they are polarized and cannot be reversed biased. Another drawback is that their prices are higher than in electrolytic capacitors [233].

A.5.2 Connectors

The different connector in the PCB are:

- **Power connectors:** for the input DC voltage (24 V).
- **Signals:** Fiber optics connectors, two per IGBT, one for the control signal and the other for the error signal.
- **IPM connector:** connects the driver PCB to the IPM.

A.6 Driver design

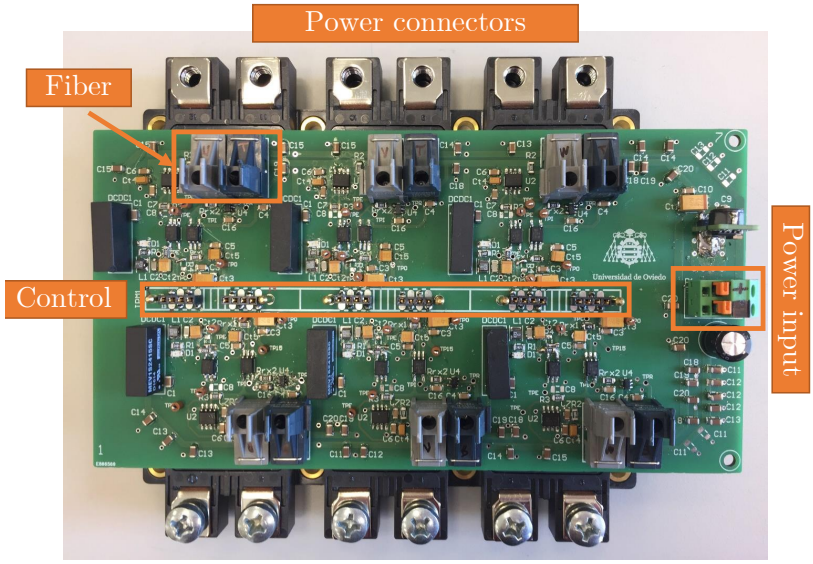

Figure A.4: 3-phase driver on top of the IPM.

A.6.1 Three-phase module

The 3-phase IPM has the control connectors placed in the same line in the middle of the module (see Fig. A.1). The PCB of the driver of this module was designed as a rectangular piece, in such a way that it can be inserted into the IPM. Fig. A.4 shows the final design with the designed PCB on top of the IPM. Power connectors are twelve, six in each side of the IPM, and they correspond to the collector or the emitter of each IGBT.

A.6.2 Single-phase module

The single-phase IPM has the control connectors in the same line in a side of the module, as seen in Fig. A.2. Fig. A.5 shows the final result with the single-phase PCB driver on top of the IPM. Power connectors are three and corresponds

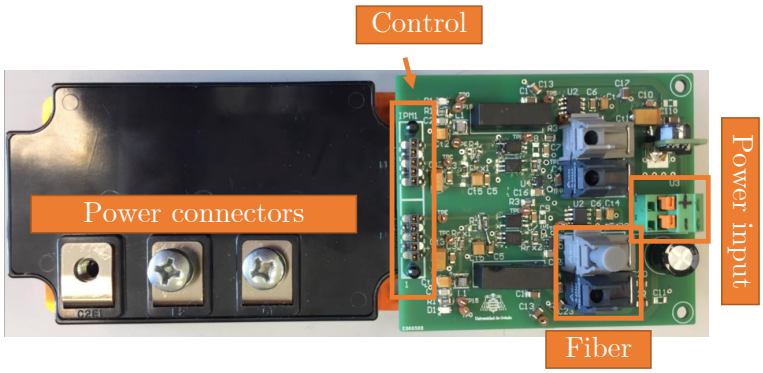

Figure A.5: Single-phase driver on top of the IPM.

to the upper IGBT (C1), the emitter (E2) or the point of connection of the two IGBTs (C2E1).

Appendix B

Complex vectors: reference frame transformation

B.1 Clarke transformation

In this thesis, rotating vectors will be used (also known as space vectors), because of the simplicity they bring allowing a better performance in the control [234]. Three-phase systems (X_{abc}) can be represented in an arbitrary stationary reference frame ($X_{\alpha\beta 0}$) by using the Clarke transformation, where x represents any electric variable, as voltage or current:

$$\begin{bmatrix} x_\alpha \\ x_\beta \\ x_0 \end{bmatrix} = \frac{2}{3} \begin{bmatrix} 1 & -\frac{1}{2} & -\frac{1}{2} \\ 0 & \frac{\sqrt{3}}{2} & -\frac{\sqrt{3}}{2} \\ \frac{1}{2} & \frac{1}{2} & \frac{1}{2} \end{bmatrix} \begin{bmatrix} x_a \\ x_b \\ x_c \end{bmatrix} \tag{B.1}$$

Expressed in this form, the transformation is conservative with respect to the amplitude, but not respect to the power (power calculations must take this into account). This is the transformation used in this thesis. If the transformation needs to be conservative respect to the power, this transformation should be used instead [235]:

$$\begin{bmatrix} x_\alpha \\ x_\beta \\ x_0 \end{bmatrix} = \sqrt{\frac{2}{3}} \begin{bmatrix} 1 & -\frac{1}{2} & -\frac{1}{2} \\ 0 & \frac{\sqrt{3}}{2} & -\frac{\sqrt{3}}{2} \\ \frac{1}{\sqrt{2}} & \frac{1}{\sqrt{2}} & \frac{1}{\sqrt{2}} \end{bmatrix} \begin{bmatrix} x_a \\ x_b \\ x_c \end{bmatrix} \tag{B.2}$$

The transformation in (B.1) can be reversed as:

$$\begin{bmatrix} x_a \\ x_b \\ x_c \end{bmatrix} = \begin{bmatrix} 1 & 0 & 1 \\ -\frac{1}{2} & \frac{\sqrt{3}}{2} & 1 \\ -\frac{1}{2} & -\frac{\sqrt{3}}{2} & 1 \end{bmatrix} \begin{bmatrix} x_\alpha \\ x_\beta \\ x_0 \end{bmatrix} \tag{B.3}$$

The transformation in (B.2) can be reversed as:

$$\begin{bmatrix} x_a \\ x_b \\ x_c \end{bmatrix} = \sqrt{\frac{2}{3}} \begin{bmatrix} 1 & 0 & \frac{1}{\sqrt{2}} \\ -\frac{1}{2} & \frac{\sqrt{3}}{2} & \frac{1}{\sqrt{2}} \\ -\frac{1}{2} & -\frac{\sqrt{3}}{2} & \frac{1}{\sqrt{2}} \end{bmatrix} \begin{bmatrix} x_\alpha \\ x_\beta \\ x_0 \end{bmatrix} \tag{B.4}$$

The Clarke reference frame can be seen in Fig. B.1. If the system is balanced ($X_a + X_b + X_c = 0$), the orthogonal component to the complex plane is zero, but this component appears if the system is unbalanced (aligned with the space diagonal of the abc reference frame) [235]. In 3-phase systems without a neutral distribution, as the one in Fig. 5.1 or the majority of the electric motors, the zero-sequence component (x_0) is usually disregarded [236] and the vectors are represented in a 2D plane (see Fig. B.2).

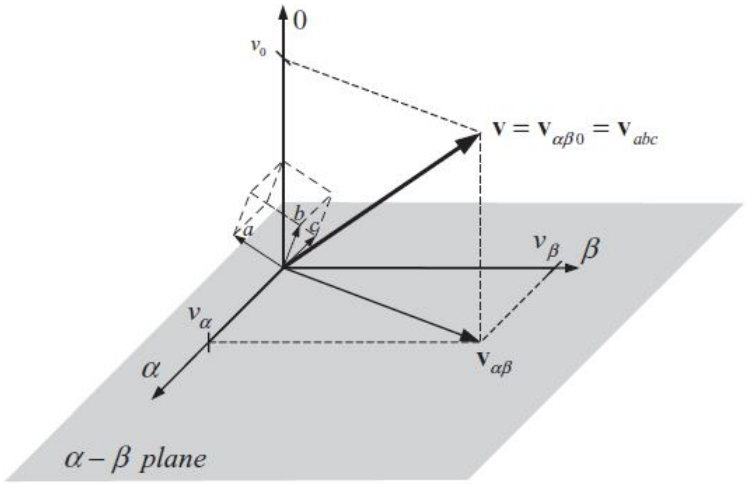

Figure B.1: Graphical representation of the $\alpha\beta 0$ reference frame [235].

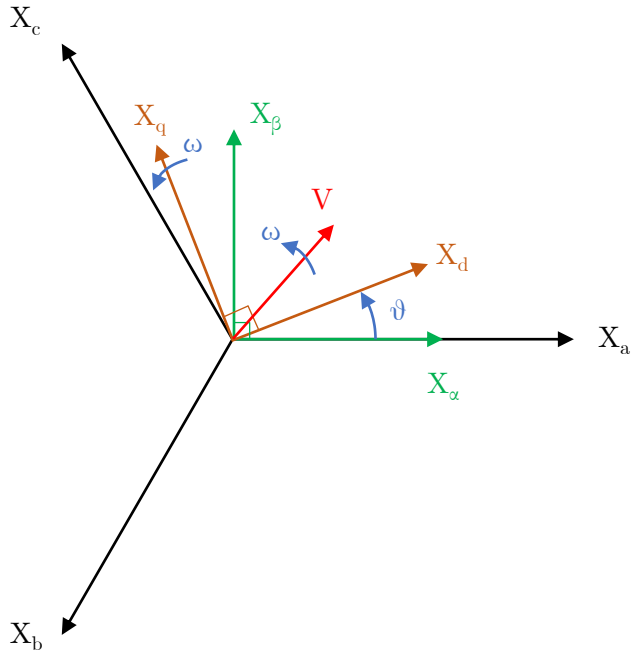

Figure B.2: Different reference frames: abc, $\alpha\beta 0$, $dq0$.

B.2 Park transformation

If vectors are in an arbitrary reference frame, signals are still changing in steady state. The reference frame can be made to rotate at the same speed (ω) as the complex vector, becoming constant signals at steady state (see Fig. B.2). This is done by means of the Park transformation, which converters the $\alpha\beta 0$ reference frame into the dq0 reference frame, also known as the synchronous reference frame. The dq axes are placed at $\theta = \omega t$ angular position on the $\alpha\beta$ plane [235]. In Fig. B.2, the d-axis is the real axis and the q-axis the imaginary axis. The set of axis is also typically used rotating the 90°, clockwise direction. If the q-axis is considered the real axis, the Park transformation would be:

$$\begin{bmatrix} x_d \\ x_q \\ x_0 \end{bmatrix} = \begin{bmatrix} sin(\theta) & -cos(\theta) & 0 \\ cos(\theta) & sin(\theta) & 0 \\ 0 & 0 & 1 \end{bmatrix} \begin{bmatrix} x_\alpha \\ x_\beta \\ x_0 \end{bmatrix} \tag{B.5}$$

If the d-axis is considered the real axis:

$$\begin{bmatrix} x_d \\ x_q \\ x_0 \end{bmatrix} = \begin{bmatrix} cos(\theta) & sin(\theta) & 0 \\ -sin(\theta) & cos(\theta) & 0 \\ 0 & 0 & 1 \end{bmatrix} \begin{bmatrix} x_\alpha \\ x_\beta \\ x_0 \end{bmatrix} \tag{B.6}$$

As seen from (B.5) and (B.6), from Clarke to Park, the zero-sequence remains the same. The inverse of (B.5) would be:

$$\begin{bmatrix} x_\alpha \\ x_\beta \\ x_0 \end{bmatrix} = \begin{bmatrix} cos(\theta) & -sin(\theta) & 0 \\ sin(\theta) & cos(\theta) & 0 \\ 0 & 0 & 1 \end{bmatrix} \begin{bmatrix} x_d \\ x_q \\ x_0 \end{bmatrix} \tag{B.7}$$

Analogously, the inverse of (B.6) would be:

$$\begin{bmatrix} x_\alpha \\ x_\beta \\ x_0 \end{bmatrix} = \begin{bmatrix} sin(\theta) & cos(\theta) & 0 \\ -cos(\theta) & sin(\theta) & 0 \\ 0 & 0 & 1 \end{bmatrix} \begin{bmatrix} x_d \\ x_q \\ x_0 \end{bmatrix} \tag{B.8}$$

B.3 abc-dq0 transformation

The two transformations can be joint so the conversion from abc to dq0 is done in only one step. If the q-axis is considered the real axis:

$$\begin{bmatrix} x_d \\ x_q \\ x_0 \end{bmatrix} = \frac{2}{3} \begin{bmatrix} sin(\theta) & sin(\theta - \frac{2\pi}{3}) & sin(\theta - \frac{4\pi}{3}) \\ cos(\theta) & cos(\theta - \frac{2\pi}{3}) & cos(\theta - \frac{4\pi}{3}) \\ \frac{1}{2} & \frac{1}{2} & \frac{1}{2} \end{bmatrix} \begin{bmatrix} x_a \\ x_b \\ x_c \end{bmatrix} \tag{B.9}$$

Alternatively, if the d-axis is considered the real axis (as in Fig. B.2):

$$\begin{bmatrix} x_d \\ x_q \\ x_0 \end{bmatrix} = \frac{2}{3} \begin{bmatrix} cos(\theta) & cos(\theta - \frac{2\pi}{3}) & cos(\theta - \frac{4\pi}{3}) \\ -sin(\theta) & -sin(\theta - \frac{2\pi}{3}) & -sin(\theta - \frac{4\pi}{3}) \\ \frac{1}{2} & \frac{1}{2} & \frac{1}{2} \end{bmatrix} \begin{bmatrix} x_a \\ x_b \\ x_c \end{bmatrix} \tag{B.10}$$

The power invariant version of (B.9) and (B.10) would be obtained in an analogous way.

The Clarke transformation can be considered as an specific case of the Park transformation occurring when $\theta = 0$.